A Study on Flow Regime Identification in Microgravity Gas-Liquid Flows Using a Capacitance Sensor

A Thesis

Submitted to the College of Graduate Studies and Research

in Partial Fulfillment of the Requirements for

the Degree of

Master of Science

in

the Department of Mechanical Engineering

University of Saskatchewan

by

Devin C. Lowe

September, 1997

PERMISSION TO USE

In presenting this thesis in partial fulfillment of the requirements for a Postgraduate degree from the University of Saskatchewan, I agree that the Libraries of this University may make it freely available for inspection. I further agree that permission for copying of this thesis in any manner, in whole or in part, for scholarly purposes may be granted by the professor who supervised my thesis work or, in his absence, by the Head of the Department or the Dean of the College in which my thesis work was done. It is understood that any copying or publication or use of this thesis or parts thereof for financial gain shall not be allowed without my written permission. It is also understood that due recognition shall be given to me and to the University of Saskatchewan in any scholarly use which may be made of any material in my thesis.

Requests for permission to copy or to make other use of material in this thesis in whole or part should be addressed to:

Head of the Department of Mechanical Engineering

University of Saskatchewan

Saskatoon, Saskatchewan

S7N 5A9

ABSTRACT

Microgravity two-phase flow is becoming increasingly important in space-based technologies. Research into microgravity two-phase flows, in addition to providing data on the behavior of such flows in a near weightless environment, serves to further research into normal gravity two-phase flow by changing one of the major variables affecting the flow, namely gravity. Gravitational force plays a major role in two-phase flows, and has a great influence on the flow regimes. Depending on the liquid and gas flow rates, the fluid properties, the tube size, and the gravity field, the flow will assume one of the following flow regimes: bubbly flow, where the gas flows as discrete bubbles in the liquid medium; slug flow, where the gas is contained in long Taylor bubbles separated by liquid slugs; transitional flow, where the gas flows in the center of the tube and the liquid generally flows along the circumference of the tube with frequent bridging; and annular flow, where the liquid forms an annulus around the circumference of the tube and the gas flows uninterrupted through the core. One of the important parameters of two-phase flow is the void fraction, which is the ratio of the volume of gas flowing in the tube to the total flow volume. This thesis investigates the use of void fraction signals to determine a more objective method of microgravity flow regime identification than what is possible through examining video images.

The first objective of this study was to design, build, and test a void fraction sensor for measuring microgravity two-phase flows. To this end, a capacitance type sensor was built. It has a two tube diameter sensing length as a compromise between obtaining a local measurement and the greater sensitivity achieved with a longer sensor. Calibration of the sensor was done using quick closing valves.

Void fraction data was collected for water-air two-phase flow in a 3/8 in. (9.525 mm) tube on board the NASA Lewis DC-9 microgravity aircraft. Void fraction data was compared against that of Elkow (1995) and Bousman (1995), and was found to be in excellent agreement.

The microgravity void fraction data was used in the form of probability density functions to determine a more objective method of identifying the flow regimes and their transitions than what is possible from examining video images. This, in turn, minimizes the errors and complexity associated with the use of subjective methods such as two dimensional video images.

Once the flow regimes were identified, the data was compared against microgravity flow regime transition models in the literature. The Drift-Flux model, originally developed by Zuber and Findlay (1965) and later modified for microgravity flows by Bousman (1995), separated the bubbly and slug flow regimes well when evaluated with the transition void fraction determined from this data set. The slug-to-annular transition model suggested by Bousman (1995) resulted in a transition line which fell in the transitional flow region. The Weber number model for the transition from slug to transitional and from transitional to annular flow, originally suggested by Zhao and Rezkallah (1993), separated the slug and transitional flows perfectly. The transitional-to-annular boundary was slightly over-predicted. It was concluded that the Weber number model is of more use than the slug-to-annular transition model suggested by Bousman (1995) since it delineates both the slug-to-transitional and transitional-to-annular flow regime boundaries.

ACKNOWLEDGEMENTS

I would like to thank the following people for their assistance throughout my thesis work. First of all, I would like to thank my supervisor Dr. K.S. Rezkallah for all his hard work to obtain the space and funding for our experiment to fly on the NASA Lewis microgravity aircraft, and for giving me the incredible opportunity to fly along with it. I would also like to thank him for all his guidance and help throughout my thesis work. I would like to express sincere thanks to Mr. D. Deutscher of the Thermodynamics-Fluids Laboratory and Mr. H. Berg and his staff at engineering shops for all their help in developing my sensor and in preparing the two-phase flow apparatus for the flight campaign. The efforts and advice of the author's committee members, Dr. J.D. Bugg and Dr. L.G. Watson, is also appreciated. Finally, I would like to thank my colleague Ken Elkow for all his help and advice at the start of this project, along with the summer students Greg Schmidt and Glen Mooney for their help over the past two summers, and all the other graduate students who lent a hand when I needed it.

I would like to thank the Canadian Space Agency for funding the microgravity flights, and the National Science and Engineering Research Council of Canada for their funding of the experiment and for their generous scholarship. I would also like to thank the College of Engineering for its financial contributions to this project.

I would also like to thank my parents for encouragement and financial support throughout my university years, without which I would have never gotten this far.

Finally, I would like to give very special thanks to my fiancé Selina for all her patience, understanding, and support throughout my work on this project. She was always there when I needed her to motivate and encourage me in my work.

TABLE OF CONTENTS

LIST OF TABLES

LIST OF FIGURES

NOMENCLATURE

$\langle F \rangle$	cross-sectional average of a parameter F
a	acceleration [m/s^2] in Equation (6.12)
A	area of an electrode [m^2] in Equation (2.1)
A	cross-sectional area of tube [m^2] in Equation (2.3) and (6.1)
A_g	area occupied by the gas phase [m^2] in Equation (1.1)
A_l	area occupied by the liquid phase [m^2] in Equation (1.1)
C	constant in Equation (1.3)
C	capacitance [F] in Equation (2.1)
C	constant in Equation (6.25)
C_D	drag coefficient
C_0	velocity and void distribution coefficient
d	distance between electrodes [m] in Equation (2.1)
D	inside tube diameter [m]
D	drag force [N] in Equation (6.12)
d_b	bubble diameter [m]
f	sampling frequency [Hz]
f_G	single phase gas friction factor
f_i	interfacial friction factor
f_w	wall friction factor
g	gravitational acceleration [m/s^2]
$\bar{h}$	average film thickness [m]
j	total volumetric flux [m^3/s]
K	dielectric constant
m	mass [kg] in Equation (6.12)
n	constant in Equation (6.25)
N	number of points sampled in Equations (4.2) and (4.3)
P	absolute pressure [Pa] in Equation (2.4)
P_0	standard pressure [kPa] Equation (A.1)
P_{abs}	absolute pressure [kPa]
P_g	inlet pressure of the gas [kPa] in Equation (A.1)

Q	mass flow rate [kg/s] in Equation (2.3)
Q_g	actual gas volumetric flow rate [m^3/s] in Equation (A.1)
Q_m	measured gas volumetric flow rate [m^3/s] in Equation (A.1)
r	radius of gas bubble [m] in Equation (6.14)
R	specific gas constant [J/kg K]
R^2	coefficient of determination
Re_D	Reynolds number based on bubble diameter in Equation (6.16)
Re_{TP}	two-phase Reynolds number
s	standard deviation in Equation (4.1)
t	time [s]
T	absolute temperature [K] in Equation (2.4)
T	total sampling period [s] in Equation (4.4)
T_g	inlet temperature of the gas [K] in Equation (A.1)
T_0	standard temperature [K] in Equation (A.1)
U_S	slug velocity [m/s] in Equation (1.6)
V^*	normalized void fraction sensor voltage output
V_a	all air void fraction sensor voltage output [V] in Equation (2.5)
V_b	bubble velocity [m/s]
$\forall_g$	volume occupied by the gas phase [m^3] in Equation (1.1)
V_G	actual gas velocity [m/s]
V_{Gj}	gas drift velocity [m/s]
$\forall_l$	volume occupied by the liquid phase [m^3] in Equation (1.1)
V_L	actual liquid velocity [m/s]
V_{lb}	difference between fluid velocity and bubble velocity [m/s] in Equation (6.15)
V_m	measured void fraction sensor voltage output [V] in Equation (2.5)
V_{SG}	superficial gas velocity [m/s]
V_{SL}	superficial liquid velocity [m/s]
V_w	all water void fraction sensor voltage output [V] in Equation (2.5)
We_{SG}	superficial gas Weber number
We_{SL}	superficial liquid Weber number
$\bar{x}$	sample average in Equation (4.1)

x	position of gas bubble [m] in Equation (6.13)

Greek Symbols:

α	void fraction
$\overline{\alpha}$, α_{ave}	average void fraction
$\Delta\alpha$	class interval in Equation (4.2) and (4.3)
δ_{actual}	actual film thickness [m] in Equation (5.1)
$\delta_{meas.}$	measured film thickness [m] in Equation (5.1)
δV	error in velocity [m/s]
$\delta\tau$	error in time delay [s]
ε	permitivity of a dielectric [C^2/Nm^2]
ε_0	permitivity of a vacuum [C^2/Nm^2]
μ_G	gas viscosity [N s/m^2]
μ_L	liquid viscosity [N s/m^2]
ν_G	kinematic gas viscosity [m^2/s]
ν_L	kinematic liquid viscosity [m^2/s]
ρ	density [kg/m^3] in Equation (2.3) and (2.4)
ρ_G	gas density [kg/m^3]
ρ_L	liquid density [kg/m^3]
ρ_M	mixture density [kg/m^3]
σ	surface tension [N/m]
τ	time delay between two signals [s] in Equation (4.4)
τ_i	interfacial shear stress [N/m^2]
τ_w	wall shear stress [N/m^2]
ζ	center of a class interval in Equation (4.2) and (4.3)

LIST OF ACRONYMS

A	Annular Flow
ACF	Autocorrelation Function
ADAC	American Data Acquisition Company
A/D	Analog-to-Digital
B	Bubbly Flow
B-S	Bubbly-Slug
CC	Cross-Correlation
cv	sample coefficient of variation
DMA	Direct Memory Access
D/A	Digital-to-Analog
F.S.	Full Scale
FT	Film Thickness
HSV	High Speed Video
I/0	Input/Output
LPM	Liters Per Minute
NASA	National Aeronautics and Space Administration
PDF	Probability Density Function
PSDF	Power Spectral Density Function
RMS	Root Mean Square
RTD	Resistance Temperature Detector
S	Slug Flow
SLM	Standard Liters per Minute
SNR	Signal-to-Noise Ratio
S-T	Slug-Transitional
T	Transitional Flow
T-A	Transitional-Annular
VDC	Volts Direct Current

1. INTRODUCTION

Two-phase flow is becoming increasingly important as the industrial world moves into new and more aggressive technologies in the twenty-first century. Some of its many applications include the design of efficient heat transport systems, the transfer and storage of cryogenic fluids, and condensation and flow boiling processes in heat exchangers and energy storage/transport systems.

Over the past forty years, much research has been done on two-phase flow at normal (earth) gravity conditions where the phenomena is highly influenced by gravitational forces. On the other hand, under microgravity conditions the research has been limited, with most of it only emerging in the past ten years. This is largely due to the strict availability of microgravity platforms and the difficulty in acquiring data during the short duration of near zero-gravity conditions. Examples of such areas in microgravity two-phase flow which need further research include the development of a more objective method of flow regime identification, evaluation and refinement of flow regime transition models, and the measurement of various flow parameters.

1.1 Motivation

There are several reasons for investigating two-phase flow under microgravity conditions. First, it provides data on the aforementioned processes for the design and testing of space based hardware. It also lends to a better understanding of the flow. The virtual absence of gravity allows the influence of other forces, such as surface tension, to

be investigated. On earth, buoyancy forces play a major role in the transport of both phases due to the significant difference in phase densities.

One of the areas in microgravity two-phase flow which needs more research is the development of a reliable method of flow regime identification. Reasons for this include:

1. Just as flow regime plays an important role in determining flow parameters for single phase flow, two-phase flow parameters are strongly related to their flow regimes. For example, heat transfer rates and pressure drop can vary substantially from one flow regime to another.

2. It has also been found that heat transfer and pressure drop models work best if they are developed for a particular flow regime.

3. A more reliable, more objective method of flow regime identification would allow greater consistency in flow regime identification between research groups than what is possible using two-dimensional flow images.

Void fraction is a key parameter in two-phase flow, and it is of great importance in modeling parameters used in predicting heat transfer rates and pressure drops. In addition, it is has been shown that it has a strong relationship with flow regimes, and may be used as a flow regime identifier.

1.2 Microgravity Two-Phase Flow Regimes

Just as single phase pipe flows experience laminar or turbulent flow regimes which depend on the fluid velocities and properties, two-phase flow takes on flow regimes which are dependent on flow conditions such as liquid and gas flow rates, tube diameter, and fluid properties. As the gas and liquid flow rates are changed, two-phase flow will

transition between several flow regimes. Zhao & Rezkallah (1993) categorized two-phase flow into four main flow regimes: bubbly, slug, frothy slug-annular and annular. Figure 1.1 shows a schematic and video images of each flow regime highlighting the important features. The approximate areas occupied by each flow regime are shown in Figure 1.2 on a flow regime map with the liquid and gas superficial velocities (V_{SL} and V_{SG}, respectively) as the coordinates. The superficial velocity of a phase is the average velocity that the phase would have if it were flowing alone in the tube at the same mass flow rate.

At high liquid flow rates (typically V_{SL} greater than 0.4 m/s) and low gas flow rates (typically V_{SG} less than 0.8 m/s), bubbly flow is encountered. Bubbly flow is recognized by discrete gas bubbles flowing in a continuous liquid medium. These bubbles are generally spherical in shape, and typically have diameters less than the tube diameter.

With an increase in the gas flow rate (or a decrease in the liquid flow rate), bubbly flow transitions to slug flow. This flow regime is characterized by long Taylor bubbles of gas separated by a stable liquid slug, which may or may not contain small bubbles. The Taylor bubbles have a diameter close to that of the inside tube diameter, and a length that ranges from 2 D (two tube diameters) up to 40 D (Zhao and Rezkallah, 1995).

If the gas flow rate is increased further, transitional flow develop. In transitional flow, the liquid flows mainly as a film along the wall and the gas phase flows through the center with frequent appearances of unstable slugs. At high liquid flow rates the unstable slugs are frothy with highly aerated areas in which the liquid film collapses and is pushed up again by the incoming gas flow. At lower liquid flow rates, the unstable slugs are not as chaotic, but rather distorted with frequent occurrences of liquid bridging the tube. In this study, the transition regime between slug and annular flow will be referred to as transitional flow, regardless of whether the slugs are frothy or not. In

addition, transitional flow will be divided into two sub-regimes called frothy slug-annular and distorted slug, according to whether or not the unstable slugs are frothy.

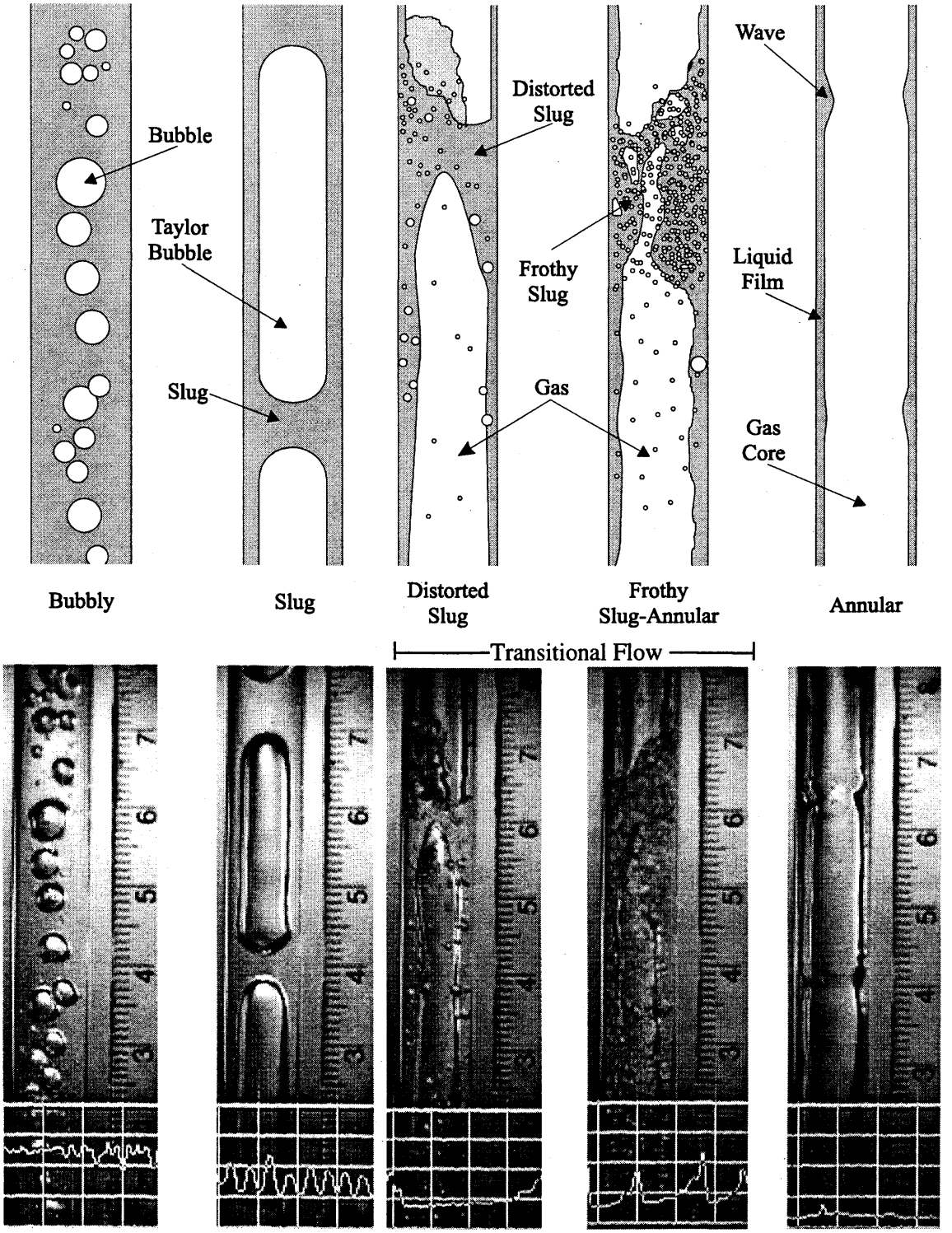

Figure 1.1 - Microgravity two-phase flow regimes.

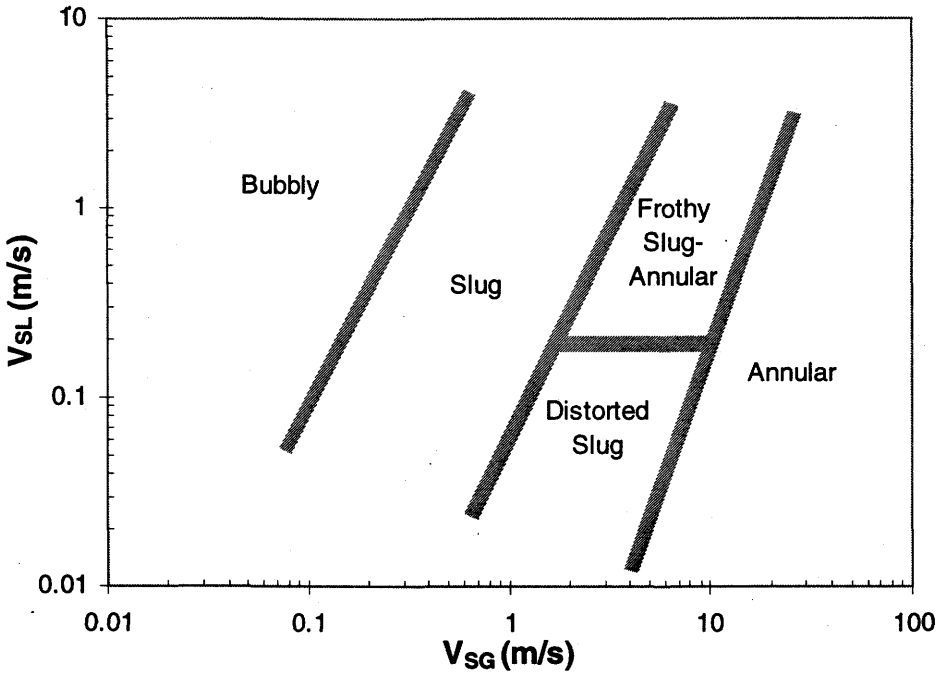

Figure 1.2 - Dimensional microgravity flow regime map showing approximate flow regime locations.

Transitional flow becomes annular flow with further increase in the gas velocity. This is characterized by the liquid film flowing along the tube wall, and the gas flowing uninterrupted in the center. The liquid film may contain gas bubbles, and is generally smooth with occasional large amplitude waves. The gas core could also carry liquid droplets that are entrained from the film near the wall.

1.3 Void Fraction

Void fraction, α, is defined as the volume of the gas normalized by the total flow volume for a two-phase flow, calculated as:

$$\alpha = \frac{\forall_g}{\forall_g + \forall_l} \text{ or } \alpha = \frac{A_g}{A_g + A_l}. \tag{1.1}$$

In Equation (1.1) $\forall_g$ and $\forall_l$ are the volumes of the gas and liquid flowing in the tube, respectively, and A_g and A_l are the time averaged cross-sectional areas occupied by the gas and the liquid, respectively.

The following section outlines some of the research work that was previously done to use void fraction signals as a flow identifier, with emphasis on work done at microgravity conditions. As well, microgravity flow regime transition models in the literature are reviewed.

1.4 Previous Work

Over the past forty years, many researchers have used void fraction to identify flow regimes, to determine flow regime transition criteria, and to infer other flow parameters. Much of the work has been done on the ground using vertical, horizontal, and inclined configurations. It has been only in the past decade that some efforts were made to investigate microgravity two-phase flows. The following section summarizes what has been done, and what still remains to be done.

1.4.1 Flow Regime Identification

1.4.1.1 Microgravity

In searching the literature, it appears that some minor effort has been put into determining an objective method of identifying two-phase flow regimes and their transitions at microgravity. Research by Bousman *et al.* (1996), Rezkallah and Zhao (1995), Bousman and Dukler (1994), Colin and Fabre (1995), Zhao and Rezkallah (1993), Colin *et al.* (1991), and Dukler *et al.* (1988) have mainly used video or two-dimensional photographic images to determine the flow regimes. This process is very subjective and may account for discrepancies between reported data.

One of the few efforts to add some objectivity to the flow regime identification was done by Bousman *et al.* (1996). In a study of air-water, air-water/glycerin, and air-water/Zonyl in 12.7 mm and 25.4 mm tubes, film thickness time traces were used in conjunction with video images to identify the flow. The following three flow regimes were defined: bubble, where the gas phase was distributed as discrete bubbles which were no longer than one tube diameter (1 D); slug, characterized by the presence of Taylor bubbles longer than 1 D; and annular flow, where the gas core of a liquid annulus remains continuous without bridging. Two transitional flow regimes were also defined: bubble-slug flow and slug-annular flow. Bubble-slug flow was characterized by short Taylor bubbles appearing in an otherwise bubble flow, and slug-annular flow was defined as annular flow with large amplitude waves that momentarily bridge the tube diameter and then rupture.

In order to classify the flow into one of these five flow regimes, Bousman *et al.* (1996) used time-series film thickness measurements to help characterize the flow. Bubble flow was characterized by a film thickness trace that spanned a large portion of the entire range of the measurement with no discernible features. Bousman (1996) reports that bubble flow could, in general, be easily identified by photograph. Slug flow could be identified from the time-series film thickness trace which had periods of film thickness at or near the tube diameter (indicating liquid slugs) followed by long periods where the film thickness was at a low value (indicating a Taylor bubble). The bubble-slug transition flow could not be identified from the film thickness time-series, as they exhibited no features that differentiated them from bubbly flow. Therefore, Bousman *et al.* (1996) identified bubble-slug flow strictly from photography. This makes one wonder how bubble flow can be discerned from bubble-slug flow with regards to the film thickness trace. Annular flow was identified when the film thickness trace indicated a thin liquid substrate with numerous waves. Film thickness time-series and high-speed photography had to be employed to identify slug-annular flow. Bousman *et al.* (1996) determined that if wave amplitudes exceeded 70% of the tube diameter, analysis of the film usually showed bridging events, indicating slug-annular flow.

Elkow and Rezkallah (1997) used void fraction probability density functions (PDF) to compare microgravity and normal gravity two-phase flows. They showed that there were discernable differences in the PDF between flow regimes. However, it was found that the void fraction sensor length of 10 tube diameters and a sample rate of 70 Hz did not allow for using the PDF as a flow regime identifier. Regardless, the results that were obtained did show that there is some promise in using PDF plots to objectively determine the flow regimes.

1.4.1.2 Normal Gravity

Under normal gravity conditions much research has been done in the area of flow regime identification in vertical and horizontal two-phase flows. In general, the methods for flow regime identification involve the use of PDF plots of void fraction signals. One of the earliest studies of this nature was conducted by Jones and Zuber (1975), while some of the more recent efforts have been reported by Song *et al.* (1995) and Costigan and Whalley (1997).

Jones and Zuber (1975) investigated two-phase air-water flow in a vertical square channel 0.498 cm deep by 6.350 cm wide. Void fraction was measured using an X-ray system. They classified the flows into one of three general flow regimes: bubble flow consisting of discrete bubbles in the liquid; annular flow in which the liquid flows in a thin film along the channel wall with a gas core; and slug flow defined as a combination of annular and bubble flows. Flow regime identification was then achieved by making PDF plots of each flow setting. The results of this study showed that slug flow was characterized by a double peaked PDF and bubble and annular flow had single peaked PDF plots at low and high void fractions, respectively. That study served as a basis for much of the work that was later done in this area.

More recently Song *et al.* (1995) examined air-water flow in a 25 mm inside diameter vertical tube. Void fraction was measured using an impedance sensor, and the data was used to determine several statistical parameters. These included signal-to-noise ratio

(SNR), power spectral density functions (PSDF), autocorrelation functions (ACF), and PDF plots. Through visual observations and examination of the PDF, SNR, and the time traces of the void signals, they discerned three flow regimes for the range of flow rates tested: bubbly flow, churn-type flow, and slug flow. Bubbly flow was broken into two sub-regimes called discrete bubbly, where the gas phase is distributed as discrete bubbles, and clustered bubbly, characterized by bubble clusters flowing in the center of the flow channel and discrete bubbles flowing near the channel wall and between clusters. Churn-type flow was identified as closely packed bubbles suddenly forming large distorted structures of the gas phase. Slug flow was given the usual definition of Taylor bubbles separated by slugs of water.

Song *et al.* (1995) found that strong indicators of the bubble-to-slug transition are the shape of the PDF, a sharp increase in the SNR as gas flow is increased, and the distinct change in apparent time scales calculated from the ACF. These apparent time scales are defined as the time required for the ACF, calculated either from the instantaneous signal or from the fluctuating portion of the signal, to reach half its maximum.

Costigan and Whalley (1997) investigated vertical air-water flow in a 32 mm inner diameter tube. In that study, void fraction data from a conductance probe in the form of time traces and PDF plots was used to identify flow regimes. Six flow regimes were identified; these are: discrete bubbly flow consisting of small bubbles uniformly distributed in liquid, spherical cap bubble flow representing a transition between bubble and slug flow, stable slug flow characterized by aerated liquid slugs separated by Taylor bubbles of varying lengths, unstable slug flow representing a transitional flow between slug and churn flow characterized by many collapsing slugs while others maintain their shape (this regime is often classified as churn), churn flow defined as fundamentally annular in nature with occasional waves that bridge the tube (or fall within it), and annular flow which is characterized by an annulus of water with a continuous gas core.

Based on examination of the void fraction time trace and PDF plots, Costigan and Whalley (1997) reported an objective set of criteria for determining flow regimes. Discrete bubble flow was characterized by a void fraction which was always less than 0.45. The flow was considered to be spherical cap bubble flow if the void fraction time trace appeared as discrete bubble flow with narrow void fraction peaks between 0.4 to 0.8 (due to large bubbles) superimposed on it. Stable slug flow was said to occur when liquid slugs with a void fraction less than 0.4 were separated by Taylor bubbles with a void fraction greater than 0.8. Unstable slug flow occurs when the void fraction in the slugs is greater than 0.4 and merge with Taylor bubbles whose void fraction is less than 0.8. When the void fraction is less than 0.8, but there are no low void fraction slugs, churn flow is said to occur. Finally, annular flow is defined when void fraction is greater than 0.8.

Clearly, with all the success in flow regime identification for two-phase flows at normal gravity conditions, it must be feasible to determine a largely objective method of determining flow regimes under microgravity conditions. This would help to achieve more commonality in flow regime identification between different researchers.

1.4.2 Transition Models

While very little work has been done on flow regime identification at microgravity, there have been several attempts to define flow regime transition models. Research into the bubble-to-slug transition has been reported by Dukler *et al.* (1988), Bousman *et al.* (1996), Colin *et al.* (1991), Bousman (1995), Elkow and Rezkallah (1997), Colin and Fabre (1995,1996), and Bousman and Dukler (1994).

Much of the above research focused on determining a critical void fraction at which the flow transition occurs. Early work such as Dukler *et al.* (1988), Colin *et al.* (1991) and Zhao and Rezkallah (1993) calculated the average void fraction $\overline{\alpha}$ as:

$$\overline{\alpha} = \frac{V_{SG}}{V_{SG} + V_{SL}}. \tag{1.2}$$

A critical void fraction was then chosen which best separated the bubble and slug flow regimes. This results in an expression for V_{SL} in terms of V_{SG} such that:

$$V_{SL} = CV_{SG}, \tag{1.3}$$

where C depends on the critical void fraction chosen. Several empirical values have been determined for C ranging from 1.2 to 4.6 corresponding to critical void fractions ranging from 0.45 to 0.18 (Rezkallah and Zhao, 1995).

More recently, Bousman *et al.* (1996), Bousman (1995), Bousman and Dukler (1994) and Colin and Fabre (1995) used the drift-flux model (Zuber and Findlay, 1965) to develop a transition model. If the gas drift velocity in the drift-flux model is set to zero, which has been observed in films of bubble and slug flows, the resulting equation relating the superficial velocities is:

$$V_{SL} = \frac{(1 - C_0\overline{\alpha})}{C_0\overline{\alpha}} V_{SG} \tag{1.4}$$

(Bousman *et al.*, 1996). In Equation (1.4), C_0 is the distribution coefficient as defined by Zuber and Findlay (1965), and represents the radial distribution of the void and velocity profiles. A C_0 greater than one indicates a profile which is maximum at the center and minimum near the walls, while a C_0 less than one indicates a profile which peaks near the wall. A C_0 equal to one indicates a uniform velocity and void profiles. Several experimental values of C_0 for water-air flows at microgravity have been reported in the literature. Bousman and Dukler (1994) reported a C_0 of 1.25, Bousman *et al.* (1996) reported a C_0 of 1.21 for a 12.7 mm tube. Bousman (1995) also reported a value of 1.27 for the 12.7 mm tube when a different method of calculating C_0 was used. However, Bousman (1995) felt that the 1.21 value was most accurate. Colin and Fabre (1995) report a C_0 of 1.20 for 6, 10, 19, and 40 mm tubes, and Elkow and Rezkallah

(1997) report a value of 1.25 for a 9.525 mm tube. Clearly there is some discrepancy between researchers, but all the values fall within the range of 1.2 to 1.27.

To complete the transition criteria set by Equation (1.4), a transition void fraction must be selected. Bousman and Dukler (1994), Bousman (1995), and Bousman *et al.* (1996) chose a transition void fraction of 0.4 for a 12.7 mm tube. Colin and Fabre (1995), on the other hand, found a transition void fraction of 0.45 for 6, 10, and 19 mm tubes. Bousman *et al.* (1996) found a transition void fraction of 0.23 for a 25.4 mm tube. A similar transitional void fraction of 0.2 was found for a 40 mm tube by Colin and Fabre (1995). It is generally acknowledged that the transitional void fraction is dependent on tube diameter.

The slug-to-annular transition has also received attention, and two predominant models have been suggested. Zhao and Rezkallah (1993) suggested a transition model based on the balance between inertia and surface tension forces represented by the Weber number. The Weber number, defined as the ratio of inertia forces to surface tension forces, is expressed in terms of V_{SG} and V_{SL} as:

$$We_{SG} = \frac{\rho_G V_{SG}^2 D}{\sigma} \text{ and } We_{SL} = \frac{\rho_L V_{SL}^2 D}{\sigma}, \tag{1.5}$$

where ρ is the phase density, σ is surface tension, and D is the inside tube diameter. Zhao and Rezkallah (1993) suggested that the transition between slug and frothy slug-annular (transitional flow) occurs when inertia forces become of similar magnitude to the surface tension forces. This occurs when $We_{SG} = 1$. However, at low liquid flow rates (i.e. $V_{SL} < 0.09$ m/s) the transition happens at a flow rate slightly less than $We_{SG} = 1$. Zhao and Rezkallah (1993) attributed this to residual gravity levels on the aircraft. As the gas flow rate increases, the transitional regime develops into annular flow. Fully annular flow occurs at $We_{SG} = 20$. At this point, inertial forces are most dominant compared to body forces such as those due to surface tension.

Rezkallah and Zhao (1995) refined the Weber number model. It was determined that at higher We_{SL} ($We_{SL} \approx 10$), We_{SG} at the slug-to-transitional flow boundary begins to trend slightly upwards. It was also determined that a slightly upwards sloping transition line beginning at $We_{SG} = 20$ better separated the transitional and annular flow regimes. Rezkallah and Zhao (1995) suggested that this may be due to the decreasing role of gas inertia as the liquid flow rate is increased. Rezkallah (1996) showed that the flow regimes were well separated by lines with a slope of approximately 1:4 on a We_{SG} versus We_{SL} flow regime map.

Bousman (1995) proposed a void fraction matching slug-to-annular transition model. Bousman (1995) used a force balance approach to determine a void fraction relationship for annular flow and then equated this with a void fraction expression developed using the drift-flux model. When both phases are turbulent, this model predicted a line of constant void fraction equal to 0.8 as the transition criteria for a 12.7 mm tube. This model over-predicted the void fraction in the turbulent liquid region, possibly due to problems in accurately determining the pressure gradient in the unstable transitional region (Bousman *et al.*, 1996). Bousman (1995) found that a line of constant void fraction at $\alpha = 0.75$ separated the data better.

Clearly, applying new data to the aforementioned transition models would be beneficial to two-phase flow research. Not only would it help to prove or disprove these models, it could result in some new insights.

1.4.3 Flow Parameters

Some research has been done at normal gravity conditions to use void fraction signals to measure flow parameters such as slug and Taylor bubble velocities and lengths. A recent study by Costigan and Whalley (1997) reports using cross-correlation of void fraction signals from two probes to determine slug velocities. Slug and Taylor bubble lengths were then calculated from the void fraction time trace by determining the

amount of time it took for a slug or Taylor bubble to pass a void sensor. Costigan and Whalley (1997) found that the slug velocities agreed well with the commonly accepted correlation for slug velocity:

$$U_S = 1.2(V_{SL} + V_{SG}) + 0.35\sqrt{gD}\,. \tag{1.6}$$

In Equation (1.6), U_S is the slug velocity and g is gravity. Good agreement with:

$$U_S = \frac{V_{SG}}{\bar{\alpha}} \tag{1.7}$$

was also found.

1.5 Objectives

After a review of the relevant literature, it is clear that there are a number of areas where the data collected in this study may serve to further research in microgravity two-phase flow. The following objectives have been defined for this study:

1. To design, build and test a "short" sensor for measuring void fraction in two-phase flow, and to use this sensor to acquire microgravity void fraction data.

2. To examine the void fraction time traces and PDF plots to develop a more objective method of flow regime determination for microgravity two-phase flow than what is possible through the use of video images.

3. To test and compare flow regime transition models presented in the literature using the new data set.

2. VOID FRACTION SENSOR DESIGN AND CALIBRATION

The following chapter describes the objectives for the design and the actual sensor developed. The calibration procedures and results are also discussed.

2.1 Design Objectives

The design objectives are for the void fraction sensor to be:

- Capable of precisely measuring void fraction;
- non-intrusive;
- independent of flow regime;
- capable of measuring the entire range of void fractions;
- safe and reliable to operate; and
- able to withstand vibrations and pressure fluctuations in the flow.

Obviously, the first objective of the design was to build a sensor that is capable of precisely measuring void fraction. The sensor is to be non-intrusive in order to avoid any changes to the flow characteristics or trigger an early transition from one regime to another. In addition, the sensor's calibration must be completely independent of flow regime, and span the widest possible range of void fractions. The sensor must be safe and reliable because it is designed to take measurements on board the NASA DC-9 microgravity aircraft. This requires that it successfully meet NASA's safety requirements for flying on board the zero-gravity aircraft. It must also be extremely reliable as opportunities to fly on the aircraft are scarce. In addition, the sensor must be

insensitive to vibrations and able to withstand the pressure fluctuations usually encountered in the flow. Finally, it must be robust enough to withstand the harsh conditions encountered during flights.

2.2 Sensor Design

There are several methods for measuring void fraction in two-phase flow. These include radiation traversing techniques, conductance sensors, quick closing valves, and capacitance sensors. Each of these methods have positive and negative attributes. Radiation traversing techniques are non-intrusive and are capable of giving much information about the flow, however they do not meet the safety requirements for flying onboard the NASA DC-9. Conductance sensors have been constructed in a variety of configurations and are capable of measuring the area averaged void fraction (Elkow, 1995), however they are often intrusive probes and their calibration can be sensitive to the flow regime. Quick closing valves are probably the simplest and most accurate method of determining void fraction. Their disadvantage, however, is that the measurement can not be continuous and it requires a long isolation section for best accuracy. On the other hand, capacitance sensors can be constructed so that they can non-intrusively measure volumetric void fraction. However, this type of sensor can be sensitive to temperature changes in the fluid and stray capacitance from its environment. Elkow (1995) presents an excellent review of the various techniques of void fraction measurement and their capabilities.

For this study a capacitance type void fraction sensor was chosen. These sensors measure the change in the dielectric of a two-phase mixture as the void fraction changes. The measurement is affected by two major factors: (a) the geometry of the sensor and (b) the dielectric between the electrodes. For a simple parallel plate capacitor, as shown in Figure 2.1, the capacitance C is given by:

$$C = \varepsilon \frac{A}{d}, \tag{2.1}$$

where ε is the permitivity of the dielectric, A is the area of each electrode, and d is the distance between electrodes. The permitivity of the dielectric is determined by the type and temperature of the fluids flowing through the sensor. It is defined as:

$$\varepsilon = K\varepsilon_0, \tag{2.2}$$

where ε_0 is the permitivity of a vacuum and K is the dielectric constant for the material between the electrodes. In this research, distilled, deionized water and air are the two fluids used in the experiments. The dielectric constant of air is relatively constant at 1.00059, but the dielectric constant of the water changes with temperature, as shown in Table 2.1; taken from Lide (1992-1993). The permitivity of water also changes as impurities contaminate the water.

Table 2.1 - Properties of water from 0 to 50 °C.

Temp (°C)	ρ (kg/m^3)	K	σ (mN/m)
0	999.84	87.90	75.64
10	999.70	83.96	74.23
20	998.21	80.20	72.75
30	995.65	76.60	71.20
40	992.22	73.17	69.60
50	998.03	69.88	67.94

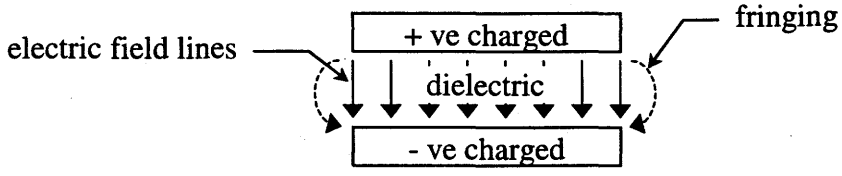

Figure 2.1 - Parallel plate capacitor showing electric field lines and fringing.

One of the problems associated with capacitance measurement is fringing. This is when the electric field lines travel outside of the area between the electrodes, as shown in Figure 2.1. The distance between the electrodes will determine how much fringing of the electrical field occurs. If the separation distance is kept small relative to the electrode area, fringing is minimal, and therefore it is not a problem. However, in a void

fraction sensor the distance between electrodes is determined by the tube diameter. Thus, guard electrodes need to be installed to reduce fringing. The purpose of the guard electrodes is to 'drain' off the fringing electric field lines so that they do not affect the capacitance measurement.

The sensor design chosen was based on work by Elkow and Rezkallah (1996). They designed a concave parallel plate capacitance sensor which proved to meet many of the design objectives listed previously. Results from that sensor showed that the calibration was linear over its entire range and independent of flow regime. It was also found that it was possible to identify flow regimes with the sensor using PDF plots. However the sensing length of 10 D was too long to provide much information about the fluctuating void fraction signal. As well, the sampling rate on the data acquisition system was too slow to acquire sufficient data for statistical analysis.

The sensor design for this research is shown in Figure 2.2. This sensor has a measuring length of 2 D, as compared to 10 D. A measuring length of 2 D was chosen as a compromise between obtaining a localized measurement while maintaining sufficient sensitivity for an accurate measurement. Observation of flow images also showed that in slug flow, the Taylor bubbles and slugs generally have a length greater than 2 D, and the disturbances or bridging events in transitional flow are generally greater than 2 D in length. In bubbly and annular flow, the 2D sensing length does not allow a large change in capacitance due to the passing of bubbles or waves; thus differentiating them from flow structures encountered in slug and transitional flows. In summary, the sensor is sufficiently short to pick up the characteristics of slug and transitional flow regimes, yet not so short as to confuse them with bubbly and annular flows.

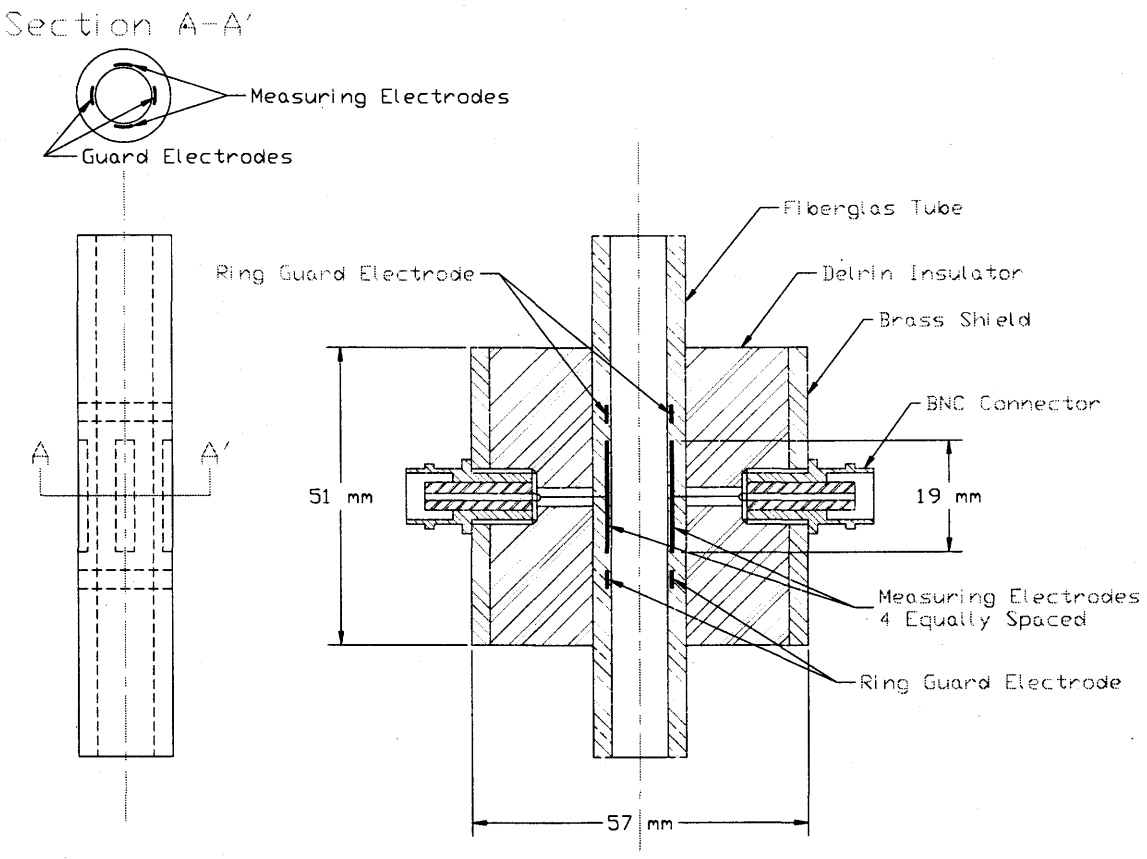

Figure 2.2 - Void fraction sensor design.

The sensor consists of a fiberglass tube (3/8 in. (9.525 mm) inner diameter, 5/8 in. (15.875 mm) outer diameter) surrounded by a Delrin insulator (50.8 mm in diameter) which is sheathed by a brass shield (1/8 in. (3.175 mm) thick). Built into the fiberglass tube at 0.5 mm from the inside wall are four measuring electrodes and two ring guard electrodes; all made of brass. The four measuring electrodes are 19 mm long and 5.5 mm wide (each covers a 60 degree arc), equally spaced around the circumference. Each of the four measuring electrodes are connected to a BNC connector mounted on the brass shield. Two opposing BNC connectors are connected to the measuring electronics, while two are grounded to the brass shield. Thus, the two measuring electrodes grounded to the brass shield act as guard electrodes separating the two active electrodes. This ensures that the electric field lines run directly across the tube and do not experience fringing, resulting in a 'short circuit' around the circumference of the tube. The guard electrodes are especially important in slug and annular flows where the electric field lines have a greater tendency to take a path around the tube in the liquid

film. The two ring guard electrodes, which are 3 mm wide and cover the circumference of the tube, are placed 3 mm from each end of the measuring electrodes. These guard electrodes are grounded to the brass shield to prevent fringing at each end of the measuring electrodes. The Delrin insulator and the brass shield act as guards against stray capacitance created by other electrical components located in the apparatus.

The sensor was constructed by the author, and machining was done at the University of Saskatchewan Central Shops. The fiberglass tube was constructed by wrapping fiberglass and resin around a steel rod with a diameter just under 9.525 mm to allow machining of the inside surface later in the construction. After a layer of fiberglass and resin were built up to a thickness greater than 0.5 mm, the exterior was machined down to a diameter of 10.5 mm, leaving 0.5 mm of fiberglass. Next, brass electrodes were cut for the four measuring electrodes and the two ring guard electrodes. Each of these were then glued to the surface of the fiberglass. Copper leads were then soldered to each of the electrodes. Fiberglass and resin were then wrapped onto the tube until a diameter greater than 16 mm was achieved. At this time, the surface, including the exposed copper leads, was machined down to 15.9 mm. The fiberglass tube was then removed from the steel rod, and the interior was finished.

The Delrin insulator and brass shield were then machined to fit over the fiberglass tube. The Delrin insulator was machined in two pieces, so that one piece can be removed, allowing the BNC connectors to be soldered to the electrode leads via a short fine wire. Set screws passing through the shield and insulator into the fiberglass tube ensure that the fiberglass tube is held firmly in place.

2.3 Capacitance Sensing Electronics

The electronics used to measure the void fraction sensor capacitance are the same as those used by Elkow (1995). The circuit was designed by Siemens (1992) and is based on work by Huang *et al.* (1988). It uses a charge/discharge principle of capacitance measurement which is immune to stray capacitance.

Huang *et al.* (1988) developed a capacitance measuring circuit, which is shown in Figure 2.3, that can operate at frequencies in the range of approximately100 kHz to 5 MHz. The circuit uses four CMOS switches; operated as shown in Figure 2.3. A summary of the switching process described by Huang *et al.* (1988) is as follows. The switching process begins by closing switches S1 and S2 to connect one electrode (point B) to ground and the other (point A) to V_c, thus charging the sensor capacitance C_x. At this

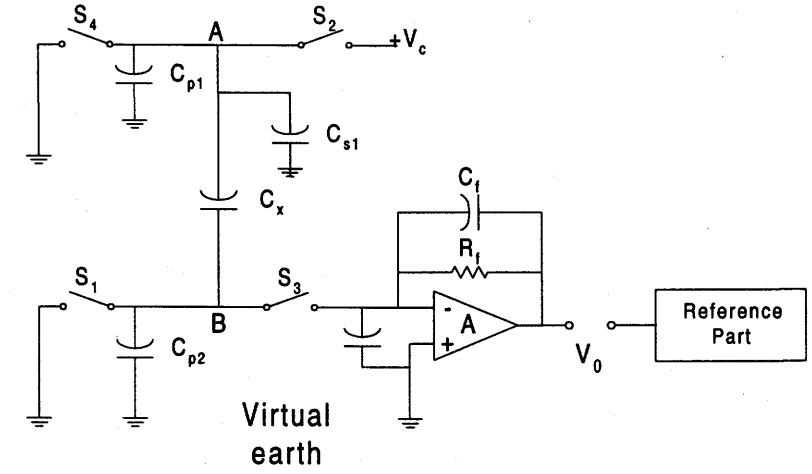

(a)

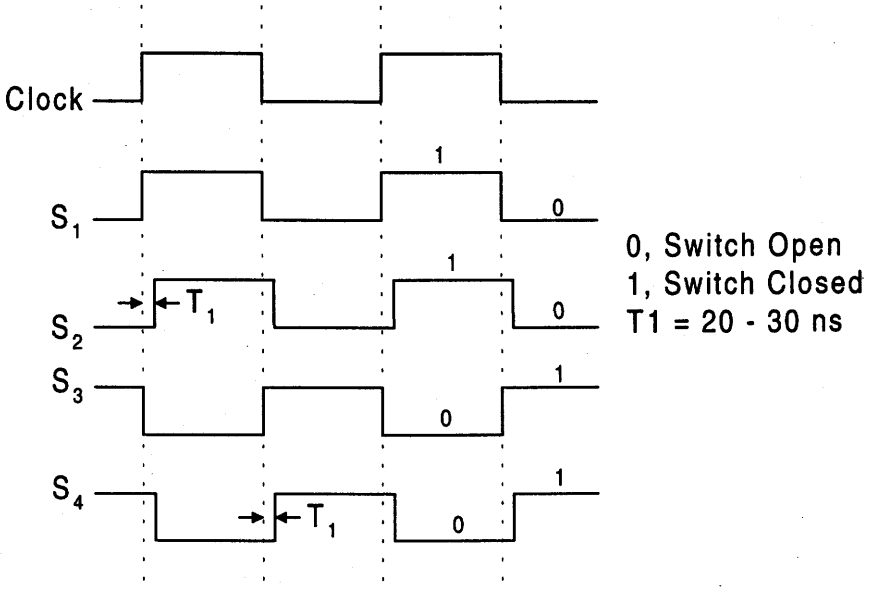

(b)

Figure 2.3 - Capacitance measuring circuit. (a) Circuit diagram; (b) Switching control signals (Huang *et al.*, 1988).

time the stray capacitance in the circuit from switches S1 and S4 is also charged to V_c. On discharge, S1 and S2 are opened, and S3 is closed, connecting point B to the charge detector which is at virtual earth (ground) potential. A short time later, S4 closes to discharge C_x to ground. This process results in a capacitance measuring circuit in which the stray capacitance is negligible.

2.4 Calibration Loop

The flow loop used for calibrating the void fraction sensor is shown in Figure 2.4. It consists of a positive displacement pump which pumps distilled, deionized water (conductivity of water ranges between 8 and 9.5 μS/cm due to changes in the purity of the water) from a 151.4 liter (40 US gallon) tank through a heat exchanger and a liquid flow meter to the mixer at the bottom of the vertical section. At the mixer, air is injected radially into the flow. The two-phase mixture flows up through the 9.525 mm (3/8 in.) inner diameter tube, through the void fraction sensor located 3.00 m (315 D) from the mixer outlet. Absolute pressure is measured prior to the void fraction sensor with a Validyne 0-414 kPa (0-60 psia) absolute pressure transducer. Following the void fraction sensor are the quick closing valves, the first of which located 3.50 m (368 D) and the second 5.00 m (525 D) from the mixer. The flow then returns to the storage tank, where the water is recycled and the air is allowed to escape. The fluid mixture temperature is measured with a thermocouple at the tank inlet.

The water flow rate is controlled by adjusting a needle valve that allows flow into the calibration section, and a ball valve which controls the amount of water bypassing the calibration section. A poppet valve set at 862 kPa (125 psi) is located upstream of both valves to limit the pressure in the system. The water flow rate is measured with one of two OMEGA turbine flow meters. These meters have ranges of 0.3-9 LPM (liters per minute, corresponding to V_{SL} = 0.07-2.1 m/s) and 0.5-15 LPM (corresponding to V_{SL} = 0.12-3.5 m/s). These flow meters generate a square wave signal from an infrared electro-optical transmitter, which is then converted to a voltage through an OMEGA

FLSC-28 Signal Conditioner. Specifications for the flow meters can be found in Appendix A.

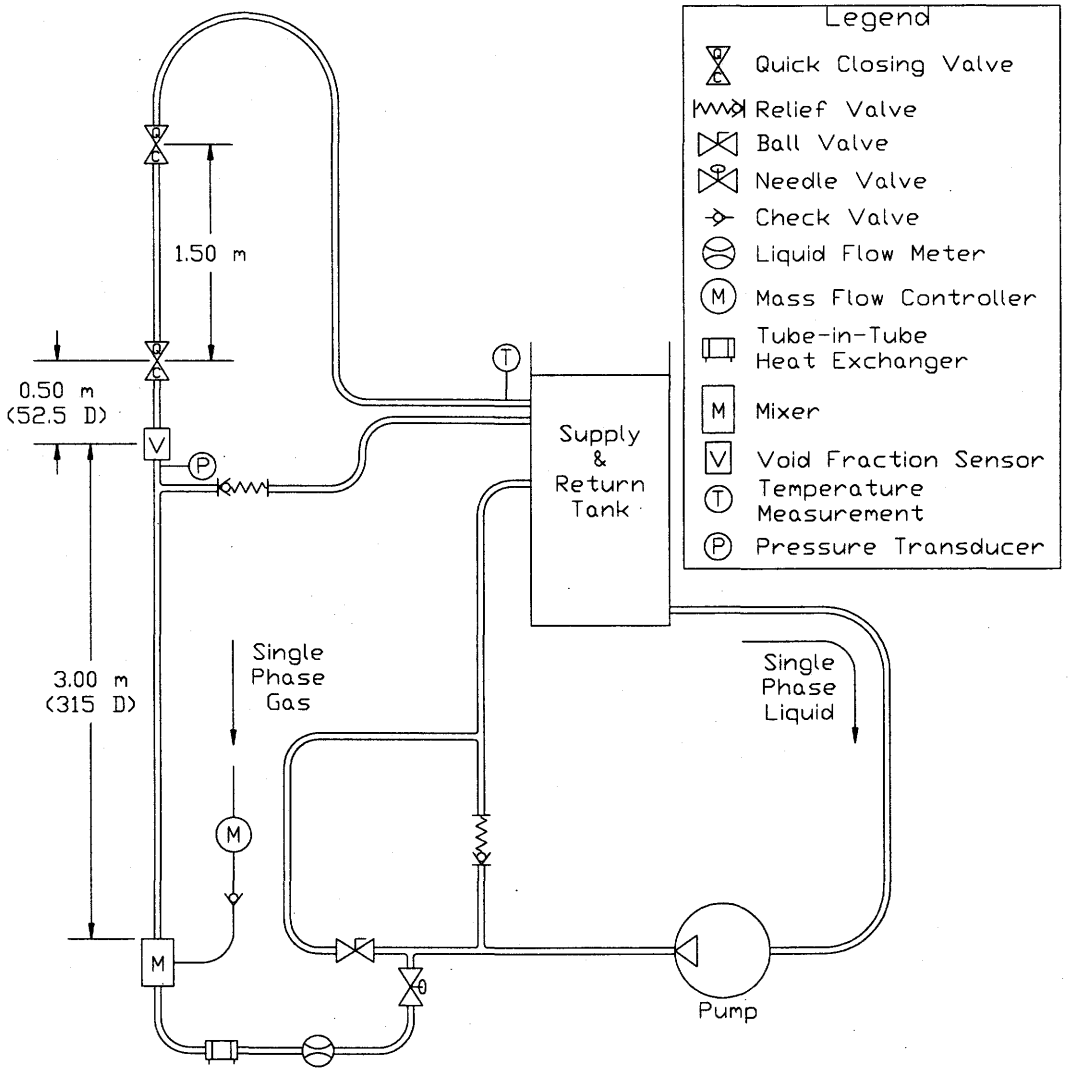

Figure 2.4 - A schematic diagram of the calibration flow loop.

Air is supplied to the calibration loop from a 272.8 liter (60 Imperial gallon) air compressor. The air is filtered for oil, dust, and moisture before entering a pressure regulator followed by a computer controlled mass flow controller. Following the mass flow controller, the air passes through a check valve (to prevent water from entering the mass flow controller) and into the mixer. Two mass flow controllers are used, one with a range of 0-20 SLM (standard liters per minute), and the other with a range of 0-100 SLM. The mass flow controllers are based on the principle that the uniform surface heat

flux required to maintain a fixed temperature profile along a tube carrying a fully developed laminar flow is a function of the mass flow rate in the tube. The mass flow controllers branch a small amount of the flow into a small tube in which laminar flow develops. The mass flow rate is then determined by how much uniform surface heat flux is required to maintain a certain temperature profile. The specifications of the mass flow controllers can be found in Appendix A. The computer calculates V_{SG} from the mass flow rate Q using the simple equation:

$$V_{SG} = \frac{Q}{\rho A} \tag{2.3}$$

and the ideal gas law to calculate the gas density ρ:

$$\rho = \frac{P}{RT}. \tag{2.4}$$

In Equation (2.4) P is the absolute pressure of the flow (measured at a location immediately before the void fraction sensor), R is the specific gas constant for air, and T is the absolute temperature of the two-phase mixture measured at the outlet of the test section. The mass flow rate is then adjusted by the computer to maintain the proper V_{SG} setting.

The quick closing valves were designed by the author and were built at the University of Saskatchewan Central Shops. Figure 2.5 shows an assembly drawing of one of the valves. The valve is opened by pushing the sliding gate in, aligning the hole in the gate with the holes in the valve and creating an unobstructed flow passage. In the open position a spring at the bottom of the gate is compressed so that the gate must be held open with a pin. The two valves are closed simultaneously by removing the pin from both valves at the same time via a mechanical linkage. The spring pushes the gate quickly into the closed position thereby trapping the flow. The closing time of the

valves was measured to be less than 0.01 seconds, which was the time determined by Dounan *et al.* (1985) required to make experimental errors negligible. When the valves are closed, a relief valve set at 105 kPa (15.2 psi) gauge pressure, located prior to the void fraction sensor, allows flow to bypass to the return tank. In addition, if the absolute pressure in the test section exceeds 310 kPa (45 psi), the computer shuts off the gas flow to reduce the pressure and protect the flow loop.

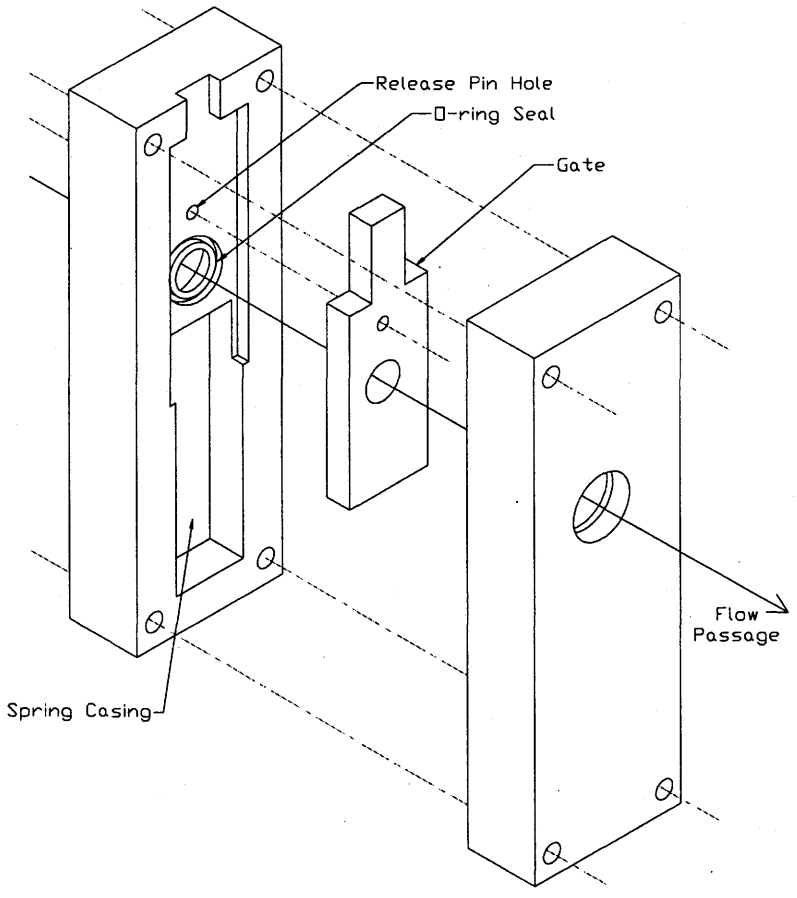

Figure 2.5 - Assembly drawing of a quick-closing gate valve (spring omitted).

Data acquisition and control was performed by a 12 bit ADAC 5550MF multi-function board in a 486/66 MHz computer. Water and air flow rates, absolute pressure, void fraction data, and ambient and fluid temperatures were recorded at approximately 200 Hz with the 12 bit A/D (analog-to-digital) converter on the multi-function board. The

mass flow controllers were controlled via the 12 bit D/A (digital-to-analog) converter on the multi-function board. The software used to control the data acquisition and control was developed by the author in the laboratory using Borland Turbo C++© and ADLIBPC I/O© drivers.

2.5 Calibration

The calibration was designed to cover the full range of void fractions to be measured by the sensor, and also to test the sensor for insensitivity to the liquid flow rate and flow regimes at all set points. Table 2.2 shows the range of flow settings used for the calibrations. The calibration procedure was to first set the liquid flow rate, and then to set the gas flow rate at each of the points shown in Table 2.2.

Table 2.2 - Calibration flow settings.

V_{SL} (m/s)	V_{SG} (m/s)
0.10	0.05, 0.30, 0.85, 2.03, 3.22, 4.23, 7.3, 10.3, 14.6
0.33	0.06, 0.12, 0.32, 0.84, 1.97, 3.09, 3.99, 6.57, 8.95
0.60	0.13, 0.23, 0.63, 1.89, 2.9, 3.79, 5.93, 7.89
1.00	0.06, 0.12, 0.23, 0.33, 0.43, 0.62, 1.26, 1.76, 2.68, 3.48, 3.83, 5.01
1.30	0.06, 0.12, 0.23, 0.33, 0.43, 0.62, 0.80, 1.00, 1.20
1.70	0.10, 0.20, 0.30, 0.37, 0.83, 1.43, 2.66
2.00	0.25, 0.35, 0.50, 0.80, 1.10, 1.40
2.40	0.25, 0.33, 0.47, 0.90

After a flow rate was set and the system was given enough time to reach steady state conditions, the quick closing valves were activated and the flow was trapped. The void fraction in the trapped section was then obtained by dividing the height of the column of air by the total separation between the valves (1.5 m). For each flow setting, no less than four trappings were averaged before data was recorded from the void fraction sensor. Typically, the void fractions obtained from separate trappings fell within 5% of the average reading, with differences of less than 2% common. Each recording of the sensor output was approximately 12 seconds long (or 2500 samples).

To obtain the calibration curve, the void fraction from the quick closing valves is plotted against the normalized voltage output of the void fraction sensor. The normalized sensor output voltage, V^* is calculated from:

$$V^* = \frac{V_w - V_m}{V_w - V_a}, \tag{2.5}$$

where V_w and V_a are the voltage outputs when the sensor is filled with all water and all air, respectively. In Equation (2.5), V_m is the voltage measured for a particular set point. All air and all water readings are taken before and after each calibration run, as well as whenever the liquid flow rate is changed. This is done in order to keep track of changes in the permitivity of the fluids due to changes in temperature or conductivity of the water. The conductivity of the water was measured before and after the calibration and was found to change by 8.7% (the conductivity before testing was 8.4 μS/cm and 9.2 μS/cm after).

The calibration results, shown in Figure 2.6, indicate that the sensor is linear over most of the range of void fraction, and is independent of flow regime. The best fit line through the calibration data is given by the equation:

$$\alpha = 0.091\left[1 - \exp\left(-\frac{V^*}{0.061}\right)\right] + 0.841V^*, \tag{2.6}$$

where α is the void fraction obtained from the quick closing valves. The coefficient of determination (R^2) for this line is 0.9983 and the standard error is 0.011, indicating an excellent fit. The precision error of the instrument was determined to be 0.022 with a 95% confidence level. The best fit line is not linear since it includes an exponential term, however, this term has virtually no effect after a void fraction of 0.24 and the calibration becomes essentially linear for the rest of the range. In practical terms, the

exponential in Equation (2.6) only has a significant effect at void fractions less than 0.06. The scatter in the calibration between void fractions of 0.6 to 0.8 is a reflection of the highly chaotic churn flow present in this region. Churn flow is characterized by an annular film of liquid which falls back down the tube until sufficient liquid collects and the gas pushes the liquid back up the tube. Other important things to note about the calibration is that it is independent of flow regime, and is continuous over the entire range of void fraction.

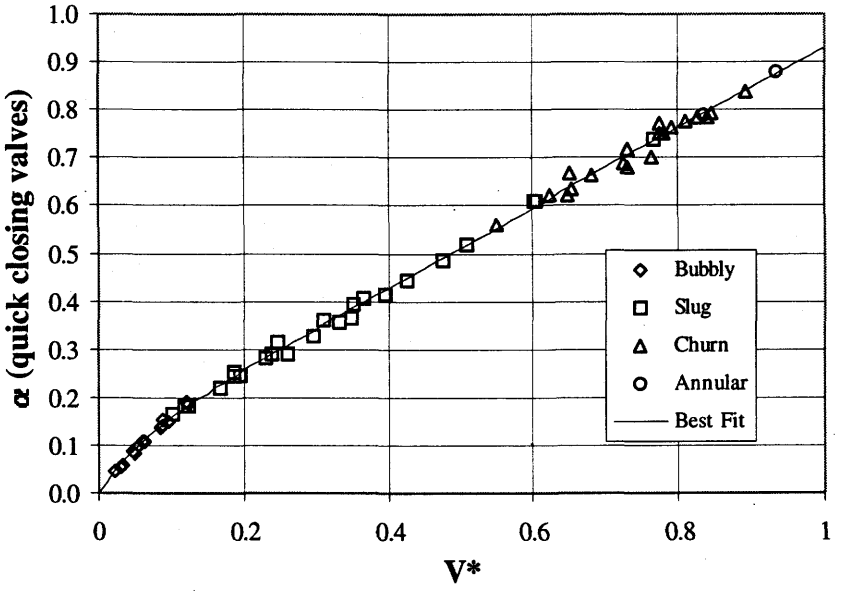

Figure 2.6 - Void fraction sensor calibration results.

2.6 Other Tests

2.6.1 Drift

To confirm that the electronics were stable, and to determine the required warm-up period for the sensor, several drift tests were performed. These were done by leaving the sensor and its electronics unplugged for several hours before plugging them in and taking readings every minute while the sensor and the electronics warmed up. Readings were taken for at least four hours to determine the warm-up period, and the stability of the reading after the sensor had warmed up. Figure 2.7 shows the results of two drift

tests taken several days apart. It was determined that the electronics needed approximately 100 minutes before they stabilized. Once the signal leveled out, it remained nearly constant for the duration of the test.

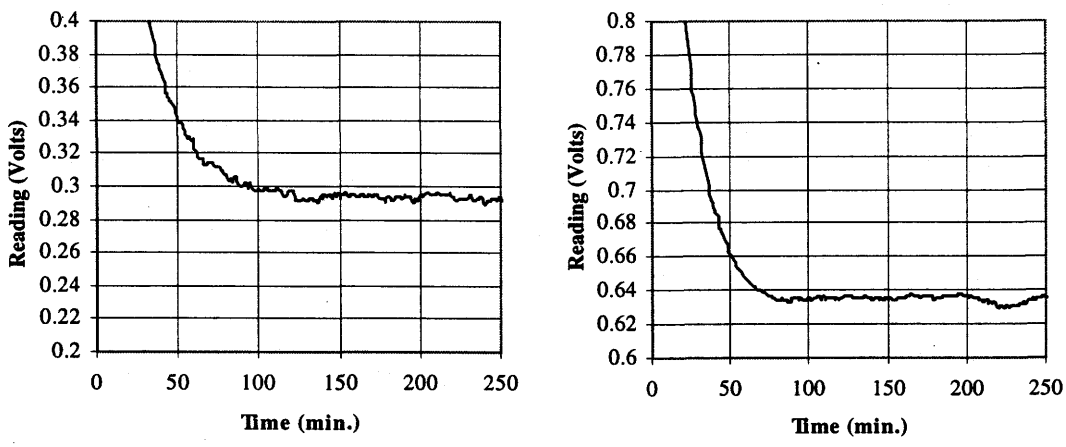

(a) (b)

Figure 2.7 - Drift test results.

2.6.2 Repeatability

In order to ensure that the sensor is reliable, tests to check its repeatability were performed. Ground tests of repeatability were performed by running flow settings which covered the complete range that the flight apparatus is capable of maintaining. Each flow setting was repeated on three separate occasions and the results are shown in Figure 2.8. It is clear that for the most part, the readings were very consistent. The points which show some scatter are once again located in the churn flow regime, where the flow is very chaotic, resulting in larger discrepancies between tests. Table 2.3 presents the results of the repeatability tests in the form of the root mean square (RMS) of the percent difference between tests, with test 1 as the reference. The results indicate that the variation in void fraction between test 1 and test 2 is 2.6% and between test 3 and test 1 is 3.6%. If the flow settings were identical for each test, this would represent the repeatability of the sensor. However, there are clearly variations in V_{SL} of the same order as α, and slightly smaller variations in V_{SG}, indicating that some of the variation in α is likely, at least in part, due to the differences in flow settings between tests.

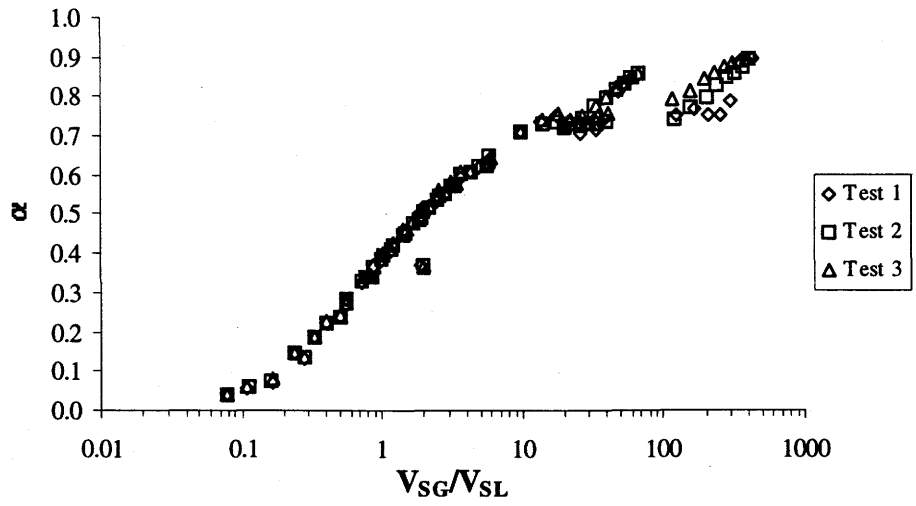

Figure 2.8 - Ground repeatability test results.

Table 2.3 - RMS percent difference between flow settings and void fraction for repeatability tests.

	RMS Percent Difference	
	Test 2 vs. Test 1	Test 3 vs. Test 1
V_{SG}	0.958	1.414
V_{SL}	2.789	4.027
α	2.602	3.642

A number of flow settings were also repeated during microgravity flights onboard the NASA Lewis DC-9 microgravity aircraft. In this case V_{SL} had a RMS difference 2.7% and V_{SG} had an RMS difference of 0.2% for all the repeated set points, while the void fraction had an RMS difference of 1.9%. Again, the differences between the void fractions is likely partly due to the differences in the flow settings. Figure 2.9 shows the results of the in-flight repeatability tests.

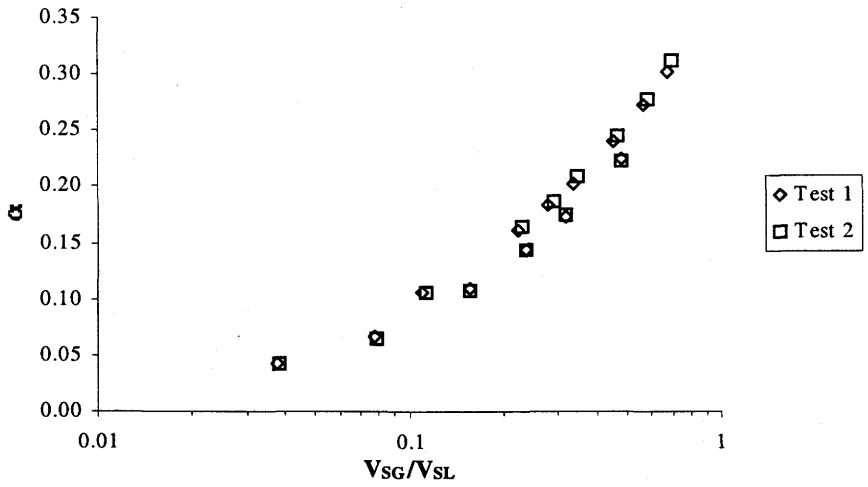

Figure 2.9 - Microgravity repeatability test results.

2.7 Summary

Table 2.4 presents a summary of the void fraction sensor specifications presented in this chapter.

Table 2.4 - Summary of void fraction sensor specifications.

Physical Characteristics of the Sensor	
Construction Material:	Fiberglass, Brass, and Delrin
Wetted Material:	Fiberglass only
Inside Diameter:	9.525 mm (3/8 in.)
Outside Diameter (maximum):	57.15 mm (2.25 in.)
Overall Length:	101.6 mm (4 in.)
Active Electrode Length:	19.05 mm (3/4 in.)
Calibration	
Calibration Relation:	$\alpha = 0.091\left[1-\exp\left(-\frac{V^*}{0.061}\right)\right]+0.841V^*$
Coefficient of Determination:	0.9983
Standard Error:	0.011
Precision Error:	0.022 (95 % confidence level)
Repeatability	
Normal Gravity:	less than 3.7 % difference between repeated flow settings
Microgravity:	less than 1.9 % difference between repeated flow settings

3. EXPERIMENTAL APPARATUS

The Microgravity Research Group at the University of Saskatchewan has been involved with the study of two-phase flow at microgravity for several years. Several flight campaigns have been undertaken and improvements to the apparatus have been made after each campaign. The original apparatus was designed by Huckerby (1991), with improvements made over the past several years by Elkow (1995), Rite (1995), and the author. This chapter describes the flight apparatus and the microgravity platform upon which it was flown.

3.1 Flight Apparatus

The apparatus used to acquire microgravity two-phase flow data is shown schematically in Figure 3.1. The apparatus consists of four major components: the test section where void fraction, film thickness, and pressure drop measurements are made, and video images of the flow are recorded; the liquid and gas supply and metering section; the data acquisition and control; and the separation tanks. Each of these are described in the following sections.

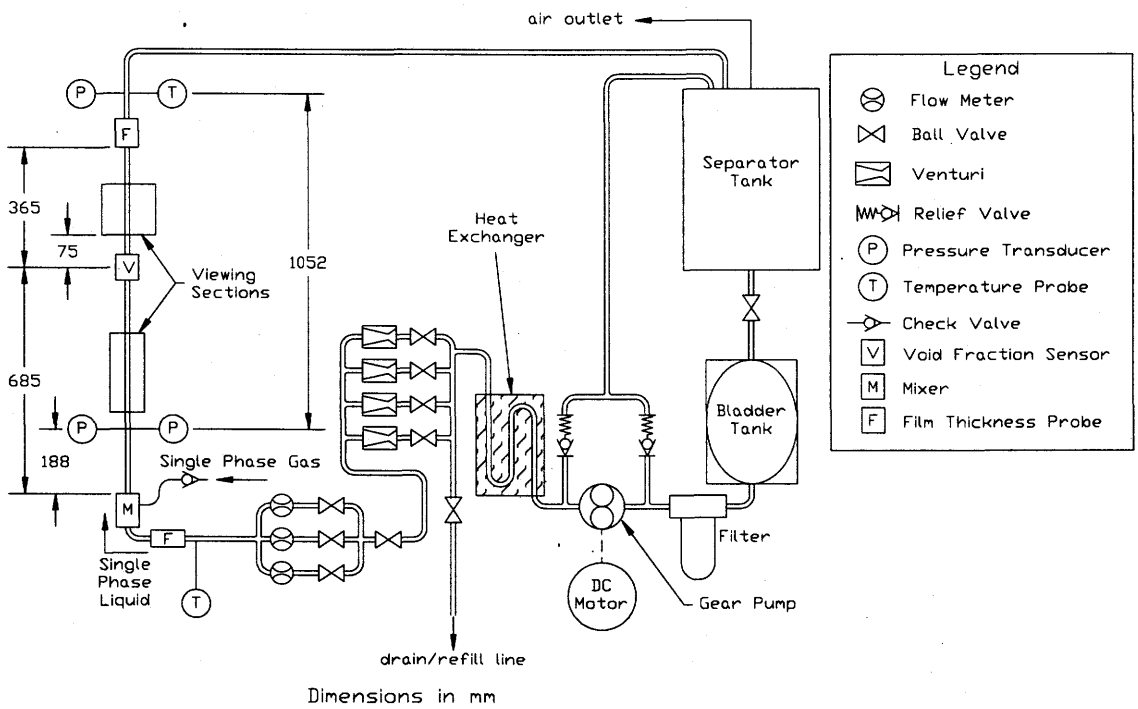

Figure 3.1 - Schematic diagram of the flight apparatus.

3.1.1 Test Section

The 3/8 in. (9.525 mm) inner diameter test section begins with a mixer in which the liquid phase enters axially, and the gas phase is injected radially. Absolute pressure measurements are made 18.8 cm (19.7 D) downstream of the mixer outlet using a Validyne 0-414 kPa (0-60 psia) absolute pressure transducer. A viewing section is placed immediately after the absolute pressure transducer. The center of the void fraction sensor is placed 68.5 cm (72 D) from the mixer and is followed 7.5 cm (8 D) downstream by a second viewing section. Following the viewing section are two film thickness probes separated by 3 D, the first of which is located 105 cm (110 D) from the mixer.

Pressure drop measurements in the test section are obtained using two Druck PDCR 820 differential pressure transducers, the first located 18.8 cm (19.7 D), and the second 124 cm (130 D) from the mixer outlet. The clear acrylic pressure taps are purged periodically to ensure that no air bubbles are trapped inside them. Since each transducer

has only a ±6.9 kPa (±1 psi) range, it is necessary to supply a back pressure to avoid over pressurization. An MKS pressure controller is computer controlled to supply a back pressure to each transducer which maintains the bottom pressure transducer at zero differential pressure.

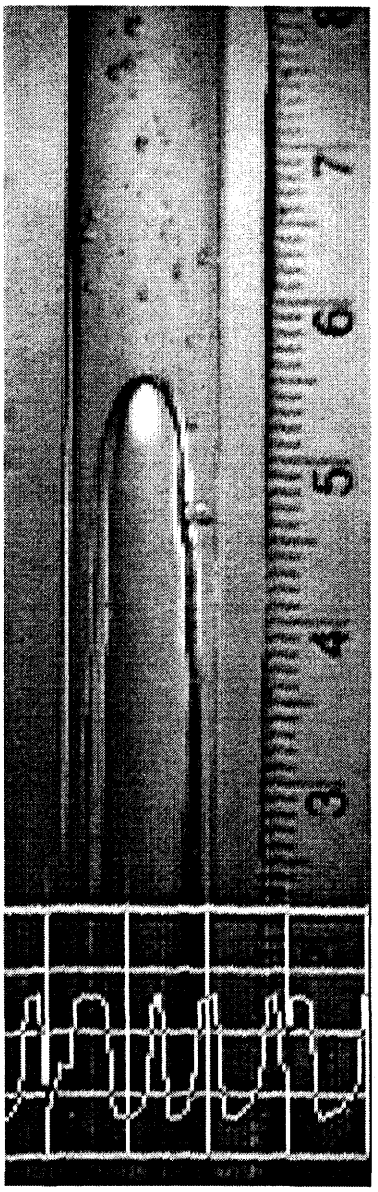

Figure 3.2 - Video image showing wave inserter signal.

Flow temperature measurements are made using RTD (Resistance Temperature Detector) probes on the single phase liquid before it enters the venturis as well as prior to entering the mixer, and on the two-phase flow at the top differential pressure transducer. Ambient temperature is also measured using an RTD.

Both viewing sections are made of acrylic and filled with glycerol to provide a clear image (glycerol has a refractive index of 1.46, while that of acrylic is 1.43, and thus distortion of the images is reduced). The first viewing section is designed for use with a Sony Hi-8 video camera operating at 60 f.p.s., with shutter speeds adjustable to 1/10000 of a second. The second viewing section is designed for a NAC HSV-1000 color high speed video system. The HSV-1000 is the primary video source and is used for visual flow regime identification and other video analysis. In addition, the HSV-1000 has the unique capability of superimposing up to two analog voltage signals on top of the flow images. This allows the researcher the opportunity to directly see how a flow parameter, such as void fraction, responds to various changes in the flow. An example of a void fraction signal

superimposed on the video signal is shown in Figure 3.2. In this case, a low reading corresponds to a high void fraction, and a high reading to a low void fraction. In Figure 3.2 the change in the void fraction signal can be clearly seen as Taylor bubbles and liquid slugs pass through the sensor. On the most recent flight campaign (November, 1996) the void fraction signal was superimposed on the video.

The film thickness probes consist of two thin wires strung across the tube diameter. Each wire is insulated from the wall to the tube centerline on one end, and in contact with the flow on the other end. The conductance between the two wires is then measured and compared to values obtained from calibration to determine the film thickness. Since the film thickness probe data are not the subject of this thesis, no further details will be given here. Some minor details on the film thickness sensors can be found in Appendix A.

3.1.2 Separation Tanks

Since the liquid phase must be recirculated, it is necessary to separate the two phases after the flow leaves the test section. This is done in two stages. During the first stage the two-phase flow enters a separation tank, which physically separates the two phases, then in the next stage the liquid is drawn off into a flexible bladder tank for recirculation.

The separator tank, which performs the first stage of separation is shown in Figure 3.3. It is designed to dissipate the inertia of the flow and then trap the liquid while allowing the gas to escape, a difficult task in the absence of gravity. Dissipation of the flow inertia is achieved by having the flow mixture enter tangential to the tank wall with an approximately 30° down inclination. The flow energy is then dissipated by wall friction as it flows around the circumference of the tank. In addition, the downward inclination of the inlet tube directs the liquid phase towards the nylon screen which covers stainless steel mesh filling the bottom third of the separation tank. The nylon screen and the stainless steel mesh effectively trap the liquid in the bottom of the tank by surface

tension. The gas phase is allowed to escape through the center of the tank lid. In order to prevent liquid loss (since there may still be droplets of liquid floating in the tank), the air outlet is surrounded by a baffle and covered with a 1 mm by 1 mm Nylon screen, as shown in Figure 3.3. After leaving the separation tank, the gas phase passes through another tank filled with water absorbing material before it is allowed to vent into the aircraft cabin.

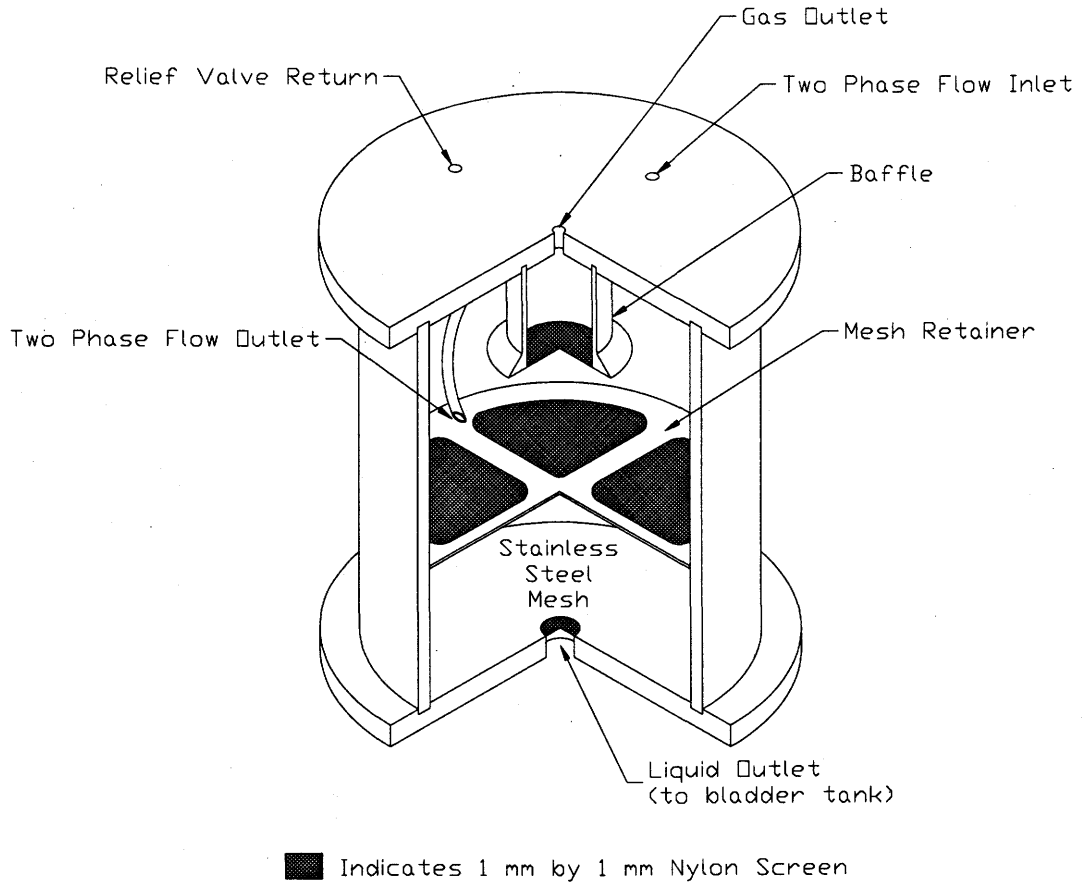

Figure 3.3 - Cutaway of separator tank (stainless steel mesh omitted for clarity).

The second stage of separation is to draw the liquid phase from the separator tank for recirculation. To ensure complete separation of the phases, this is done only during the high gravity (1.8-g) portions of the flight (see Section 3.2 for a description of microgravity flights). Immediately after the plane enters the high-g portion of the parabola, a ball valve at the bottom of the separator tank is opened to allow the liquid to

gravity feed into a specially designed flexible bladder tank. A flexible bladder tank is used so that as liquid is pumped out of the tank, the tank can collapse. This prevents air from entering the tank, or a failure due to the large negative pressure that would be caused by the removal of water from a rigid tank. This separation process ensures that only single phase liquid is contained in the bladder tank which feeds the gear pump for recirculation.

3.1.3 Liquid and Gas Metering and Control

Single phase liquid is supplied to the mixer from the flexible bladder tank, as shown in Figure 3.1. The liquid is pumped from the tank through a filter by a positive displacement gear pump. The pump is driven by a variable speed dc motor controlled by a variable transformer. Liquid flow rate is controlled by adjusting the speed of the motor, thus changing the speed of the pump. After the pump, the flow passes through a heat exchanger and then through any combination of four different cavitating venturis. The venturis allow further control of the liquid flow rate by creating pressure downstream of the pump. This allows higher pump speeds at low liquid flow rates, which results in a steadier flow. Next, the liquid enters one of three manually selected OMEGA turbine flow meters similar to the ones used in the calibration loop. The flow meters have ranges of 0.1-2 LPM, 0.3-9 LPM, and 0.5-15 LPM (corresponding to V_{SL} of 0.02-.47 m/s, 0.07-2.1 m/s, and 0.12-3.5 m/s, respectively). The specifications of each flow meter can be found in Appendix A. The liquid flow rate is set before each micro-g period, and then the output of the selected flow meter is recorded throughout the micro-g portion of the parabola.

Single phase gas is supplied to the mixer from either a compressed air cylinder (provided onboard the NASA DC-9) or an air compressor (during ground tests). The supply air is regulated to 690 kPa (100 psi) before it enters a computer controlled air mass flow controller, similar to those used in the calibration loop. Depending on the gas flow rates required, one of three mass flow controllers are used, having ranges of 0-10 SLM, 0-20 SLM, and 0-100 SLM, corresponding to superficial gas velocities (at

standard conditions) of 0-2.34 m/s, 0-4.68 m/s, and 0-23.4 m/s, respectively. The computer calculates V_{SG} as described in Chapter 2, and adjusts the mass flow rate to maintain the proper V_{SG} setting. Specifications on the mass flow controllers can be found in Appendix A. After leaving the mass flow controller, the gas passes through a check valve and into the mixer.

3.1.4 Data Acquisition and Control

The data acquisition and control system consists of two 486-66MHz computers operating several data acquisition cards. One computer system is dedicated to the high speed data acquisition of the void fraction and film thickness signals, while the other performs control operations and acquires data at low rates.

The main control computer allows the user to monitor and control all of the variables in the experiment. It also has built-in automatic shutdowns to ensure that no parameter exceeds a user set limit. This system records and displays gas and liquid flow rates, pressures, temperatures, pump speed, and gravity levels in the x, y, and z directions with a 12 bit analog-to-digital converter. Data is recorded at approximately 70 Hz. The same computer also controls the air mass flow controller and back pressure controller through a 12 bit digital-to-analog converter. As well, this system monitors the g-level in the z direction (perpendicular to the floor of the aircraft) and activates data recording for both computers when the g-level is below a preset threshold, and then stops recording when gravity levels rise again. This system also turns on a light visible to the high speed video camera to indicate when microgravity conditions exist and data is being recorded.

The high speed data acquisition system recorded the void fraction and film thickness data through a separate 12 bit analog-to-digital converter. This system begins taking data when it reads a high signal output from the parallel port of the main computer. The data is recorded in buffers using DMA to ensure a steady sampling rate, and between buffers the computer checks for a low signal from the other computer to determine when

data acquisition should be stopped. The user has the option of setting the sampling rate, and in this study these measurements were recorded at 1024 Hz.

3.2 Microgravity Platform

There are few facilities in which investigators can perform microgravity experiments. These are drop towers, sounding rockets, aircraft flying parabolic trajectories, and space flights and stations. Space flights and space stations offer the longest duration and best quality microgravity, however it is very expensive and availability is very limited. Drop towers offer the shortest duration of microgravity, typically between 5 and 10 seconds, while sounding rockets offer approximately 5 to 15 minutes of microgravity as they travel through the atmosphere. Parabolic flight is the most cost effective approach, offering approximately 20 seconds of microgravity per parabola with up to 60 parabolas per flight, depending on the type of aircraft and weather patterns. This method also has the added advantage that the researchers can fly with the experiments to monitor and control them throughout the flight.

The apparatus described previously was flown most recently on the NASA Lewis DC-9 microgravity aircraft. This aircraft follows a flight path similar to the one shown in Figure 3.4. The aircraft starts by pulling up at an angle of approximately 45° during which time the g level is approximately 1.8-g. Next the pilot pushes the nose of the plane over and flies the aircraft in a large arc until it is pointing down at an angle of approximately 45°, keeping the g levels in all three axis near zero. A plot of the gravity level in the z direction (perpendicular to the floor of the plane) for a typical parabola is shown in Figure 3.5. The microgravity portion lasts approximate 20 seconds before the pilot begins to pull out of the dive, again subjecting the contents of the plane to approximately 1.8 g for about 60 seconds. This process is repeated between 45 and 60 (the record is 67) times per flight, depending on the weather conditions. During the November 1996 flight campaign, more than two hundred parabolas were flown over the course of four days, for approximately 70 minutes of cumulative microgravity time. Figure 3.6 is a photo of the author enjoying his work on the DC-9.

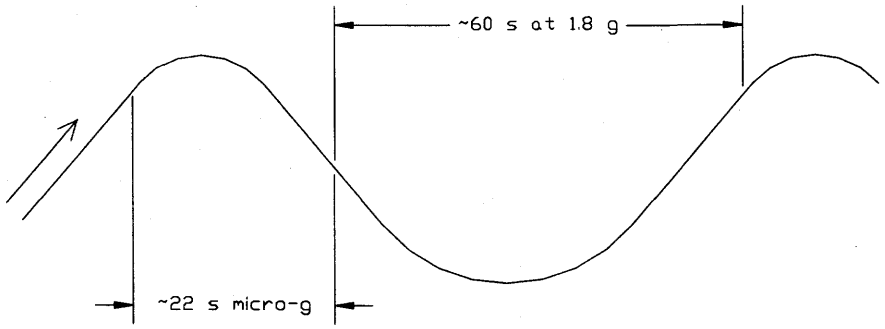

Figure 3.4 - Typical parabolic trajectory.

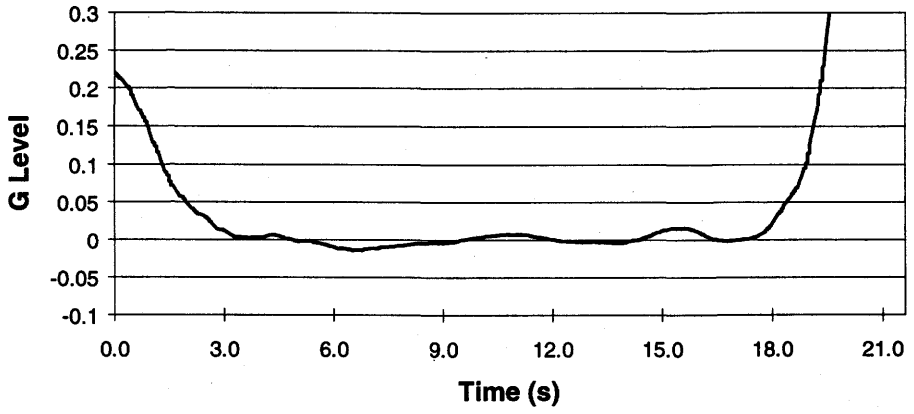

Figure 3.5 - Typical microgravity period on the NASA DC-9 microgravity aircraft.

Figure 3.6 - The author enjoying his work during a microgravity period.

3.3 Experimental Procedure

This section gives a description of the procedure followed to take the data onboard the microgravity aircraft. Before take-off the apparatus was examined and tested to ensure that all instrumentation was working correctly, and that the separator tank had the appropriate amount of water. After take-off and during the microgravity portions of the flight, the following procedure was followed:

1. Before the first parabola the equipment is again checked to ensure everything is operating correctly. The first liquid and gas flow rates are set at this time. The Hi-8 video camera is set to record.

2. At the start of a parabola, just prior to the onset of microgravity, the ball valve between the separator tank and the bladder tank is closed to seal the bladder tank. The HSV-1000 video camera is set to record.

3. During the microgravity portion of the parabola the liquid flow rate is maintained at the proper setting by the operator, and the gas flow rate is computer controlled to remain at the proper rate. Data is recorded to the two computers.

4. At the end of the microgravity portion the ball valve between the separator tank and the bladder tank is opened to allow the bladder tank to refill under the 1.8-g conditions. The HSV-1000 video camera is paused.

5. During the 1.8-g portion of the parabola the computer sets the gas flow rate to the next setting, and the operator adjusts the liquid flow rate to the proper setting. Any other required adjustments to the instrumentation or to the video cameras is done at this time as well.

6. At the end of the flight the instrumentation and cameras are shut off and the data is backed up to a portable disk drive.

The data is taken in a manner which allows the liquid flow setting to remain constant, while the gas flow setting is incremented, for several parabolas. This relieves the operator of making large adjustments to the liquid flow setting after each parabola.

4. DATA ANALYSIS

This chapter discusses in detail the various methods used to analyze the data presented in the next two chapters. First, the method by which the data is chosen for analysis is discussed. This is followed by the definition of the probability density function used in Chapter 5, along with a discussion on the effects of noise on the probability density function. Also presented in this chapter are two methods of measuring bubble velocity from the void fraction and film thickness data. In addition, the void fraction data taken in this study is compared with microgravity data reported by Elkow (1995) and Bousman (1995).

4.1 Data Selection Procedures

Since reduced gravity conditions on the plane did not always provide true zero-gravity, largely due to large fluctuations in g-level induced by air turbulence, and since each flow setting is run only once, it is necessary to select a window of good data from the total data set for each parabola. The data window is selected based on a set of criteria for V_{SG} and V_{SL}, to ensure that the flow rates were steady, and for the g-level in all three directions to ensure that they did not exceed a pre-set maximum.

The criteria used for ensuring that the flow rates maintained a steady value was the sample coefficient of variation, cv, defined as:

$$cv = \left(\frac{s}{\bar{x}} \right) \times 100\%, \tag{4.1}$$

where s is the sample standard deviation, and $\bar{x}$ is the sample average. Data windows were selected when the sample coefficient of variation was less than 2% for V_{SG} and less than 7% for V_{SL}. As well, the g-level in all three directions had to be between ± 0.03, for the window to be accepted.

4.2 Probability Density Functions

In order to clarify what a PDF represents, this section presents a brief description of probability density functions, and how they are calculated. A probability density function gives the probability that a variable will fall within a certain range of the variable. For example, given that α varies over the range 0 to 1, which can be split into several non-overlapping sub-ranges $\Delta\alpha$, called class intervals, the PDF will give the probability of α falling within each of the class intervals $\Delta\alpha$. The results are then plotted to show the probability of α falling within each $\Delta\alpha$. Bendat and Piersol (1971, 1980) give more details on the PDF.

To calculate the PDF of a function $\alpha(n)$, the range over which $\alpha(n)$ varies is first broken up into a number of narrow class intervals, $\Delta\alpha$. The probability that $\alpha(n)$ will fall within $\Delta\alpha$ is then given by:

$$Prob\left[\alpha(n) \in \Delta\alpha_{\xi}\right] = \lim_{N \to \infty} \frac{N\left[\alpha(n) \in \Delta\alpha_{\xi}\right]}{N}, \tag{4.2}$$

where ξ is the center of $\Delta\alpha$, $N\left[\alpha(n) \in \Delta\alpha_{\xi}\right]$ is the number of times $\alpha(n)$ falls within the sub-range $\Delta\alpha$, and N is the total number of points. The probability density function is then obtained by dividing Equation (4.2) by $\Delta\alpha$.

For a continuous random variable, sampled a finite number of times N, the probability function is given by:

$$p(\alpha) = \lim_{\substack{N\to\infty \\ \Delta\alpha_i \to 0}} \left[\frac{n_i}{N\Delta\alpha_i} \right], \tag{4.3}$$

where n_i is the number of times $\alpha(n)$ falls within the range $\Delta\alpha_i$.

If Equation (4.3) is plotted as a histogram, the area of each rectangle of the histogram represents the probability that $\alpha(n)$ will fall within the range $\Delta\alpha$ for that rectangle. Thus, if each $\Delta\alpha$ is the same, then dividing by $\Delta\alpha$ in Equation (4.3) is redundant and the probability can be directly represented on the ordinate of the histogram. This is the practice used in the PDF plots to follow.

In this study, each PDF represents all the data acquired for a single flow setting. In each case N was between 3000 and 20 000 points, thus Equation (4.3) gives an approximation of the PDF if a small $\Delta\alpha_i$ is used. All the PDF plots to follow use a $\Delta\alpha_i$ equal to 0.01.

4.3 Effects of Noise

In the PDF plots presented in Chapter 5, there are often instances where the PDF shows a negative void fraction. This of course is not possible, but is instead a result of noise in the void fraction signal. Figure 4.1 shows a PDF and a time trace for an all water void fraction reading. The all water time trace shows the void fraction reading fluctuating about an average value of zero. The fluctuations are not the result of changes in void fraction, rather they are from random noise in the reading. The effect of random noise on the PDF is to cause the histogram to spread slightly to each side of the zero reading.

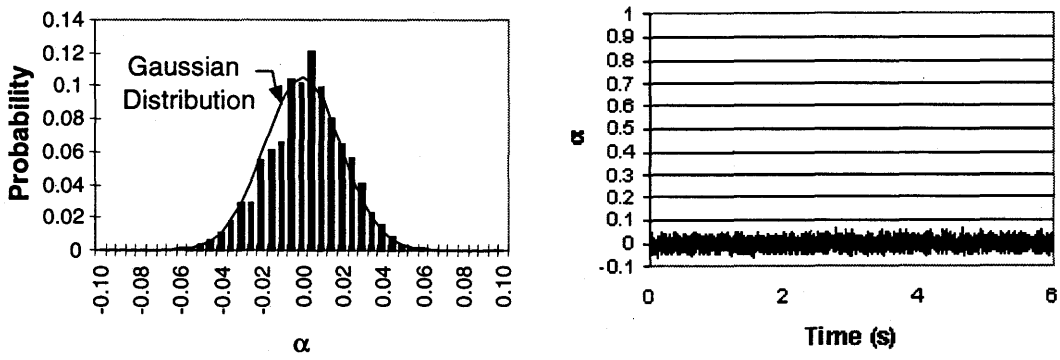

Figure 4.1 - PDF and time trace for an all water flow setting.

To further show that the spreading of the PDF is the result of random noise, a Gaussian distribution is also plotted in Figure 4.1. Clearly, the shape of the PDF closely follows that which would be produced by Gaussian noise. To quantify how closely the all water PDF fits the Gaussian distribution, we look at the skew and the kurtosis of the PDF. The skew presents a measure of how symmetric the PDF is, and the kurtosis is a measure of how peaked the PDF is. If the PDF is a Gaussian distribution, both the skew and kurtosis will be zero. The PDF in Figure 4.1 has an average of 0.00004, a variance of 0.00036, a skew of –0.159, and a kurtosis of –0.036. While these parameters do not indicate a perfect fit, they are sufficiently small to say that the distribution is essentially Gaussian. Therefore, in the following analysis, any PDF plots or time traces which indicate a negative void fraction are not due to measurement error, but rather due to the random noise in the void fraction signal.

4.4 Bubble Velocity Measurement

4.4.1 Bubble Velocity from Film Thickness Probes

One of the advantages of having two similar probes separated by a short distance in the test section is that it allows the determination of bubble velocities. Since the two sensors will give similar responses to the passage of a bubble, the time trace from the two sensors will be very similar, but phase shifted from each other. The time lag between the two time traces is then the time it takes for a flow structure to pass from one sensor

to the other. As the distance between the sensors is fixed, the velocity of the bubble can then be calculated. This method works best if there is little change in the flow structures as they pass from one sensor to the other. Examination of the flow images indicate that, at least in the viewing section, there is little change in bubble size and shape after travelling only 3 D (the separation between the film thickness probes is 29.62 mm, which is just over 3 D).

A convenient tool for determining the time lag between two signals is cross-correlation. The cross-correlation of two signals S_1 and S_2 is given by Bendat and Piersol (1980) as:

$$CC_{12}(\tau) = \frac{1}{T-\tau}\int_0^{T-\tau} S_1(t)S_2(t+\tau)dt, \tag{4.4}$$

where CC_{12} is the cross-correlation function, T is the total sampling period, t is time, and τ is the time delay between the two signals. The time delay at which the maximum in $CC_{12}(\tau)$ occurs represents the time difference when the two signals are most alike. Thus, it gives the average time it takes for a disturbance in the flow to pass from one sensor to the other, from which the velocity may be calculated.

The error in the velocity calculation is due mainly to the error imposed by the sampling rate. For a signal sampled at a sampling frequency f, the maximum resolution on τ is $\pm 1/f$. This error is propagated through the velocity calculation, so that the error in the velocity δV can be determined using the maximum possible error method as:

$$\delta V = \pm\frac{d}{\tau^2}\delta\tau, \tag{4.5}$$

where $\delta\tau = 1/f$ is the error in τ.

4.4.2 Bubble Velocity from Void Fraction Sensor

The 2 D sensing length of the void fraction sensor, along with the fixed void fraction sampling rate, offers a capability to measure the velocity of well defined Taylor bubbles. The finite length of the sensor makes it possible to measure the time it takes for a liquid/gas interface to pass through the sensor. The velocity can then be simply determined by dividing the sensing length by the time it takes for the interface to pass through the sensor.

The process for determining the liquid/gas interface velocity is illustrated in Figure 4.2, which shows the void fraction time trace for the passing of a liquid slug between two Taylor bubbles, along with the corresponding sketch of the Taylor bubbles. Point A in Figure 4.2 is when the bubble covers the entire sensor and the void fraction reads high. At point B, the tail of the Taylor bubble is just about to exit the sensor, which corresponds to the void fraction beginning to drop. As the tail of the bubble passes through the sensor, the void fraction quickly drops through point C to point D, where the tail is just exiting the sensor. At this point, the void fraction signal levels off at a low value, corresponding to the passing of the liquid slug, point E.

To determine the velocity of the Taylor bubble, the time required for the bubble to pass from point B to point D is determined from the void fraction signal. The velocity is then calculated by dividing the sensing length (2 D) by the passage time. A computer program was developed to do this for a number of slug flows. Two thresholds were determined by finding the center of each peak of the void fraction PDF for each flow setting; one corresponding to point B and the other corresponding to point D, as shown in Figure 4.3. The thresholds were then offset slightly towards each other so that the speed of most of the bubbles could be determined. Thus, each threshold was slightly below point B and slightly above point D. The computer program then measures the average time that is required for the liquid/gas interface to pass between points B and D.

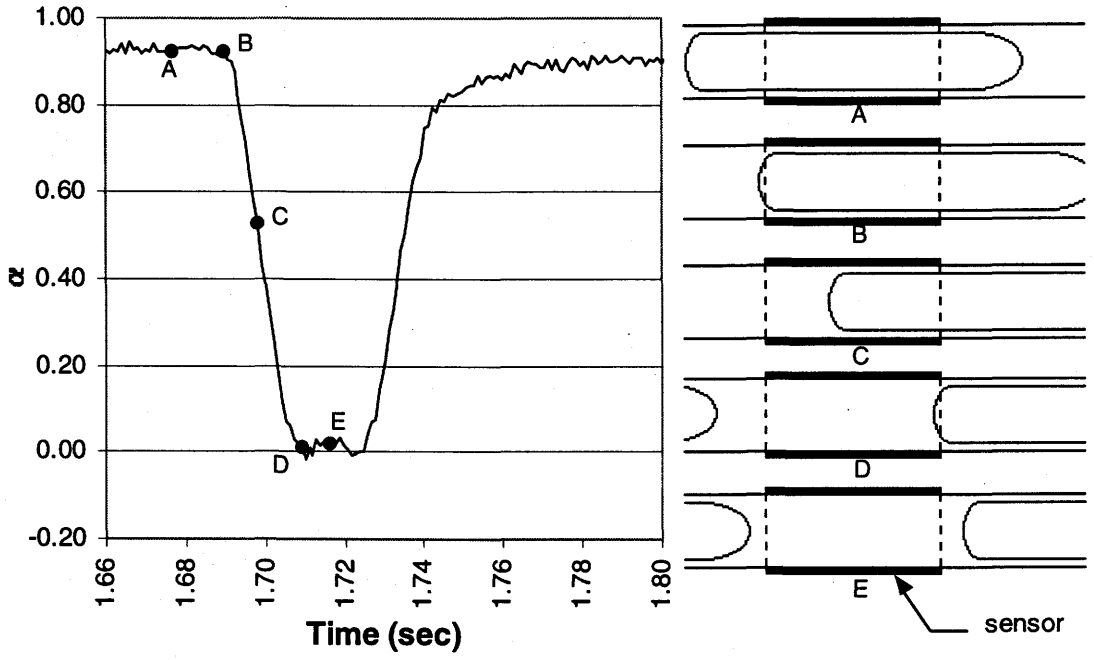

Figure 4.2 - Illustration of Taylor bubble velocity measurement.

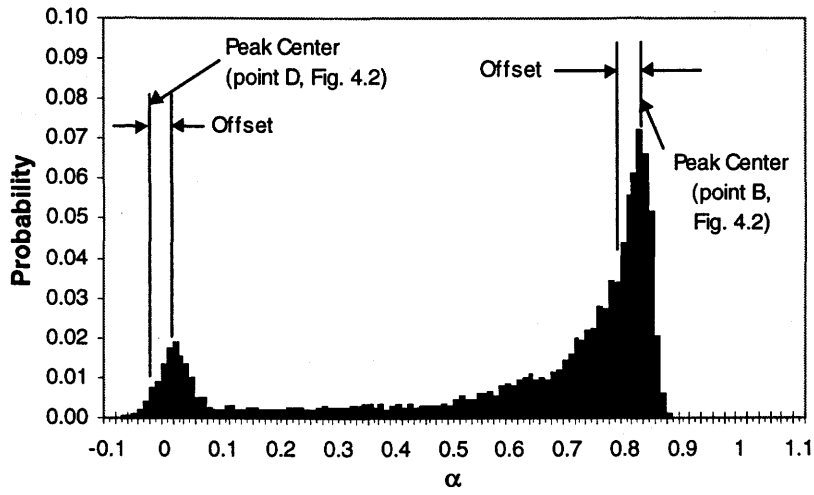

Figure 4.3 - Illustration of threshold determination.

In Figure 4.4 the results of this Taylor bubble velocity measurement technique, labeled Vg (time trace), are compared against velocities calculated from cross-correlation of the film thickness probes, labeled Vg (cross-correlation), and from the void fraction measurement, labeled Vsg/alpha (see Chapter 6). In Figure 4.4, the abscissa is labeled j,

which is the total volumetric flux, and is equal to the sum of V_{SG} and V_{SL}. The error bars on the velocities calculated using this technique, and those calculated from the cross-correlation of the film thickness probes are due to the finite sampling rate of 1024 Hz (i.e. each time measurement is only accurate to +/- 1/1024 seconds), and are calculated using Equation (4.5). The data compare quite well at low velocities with greater differences at higher velocities. The divergence at high velocities is mainly due to the fact that the tails of the bubbles become more deformed, making the change in the void fraction at point D more of a curve rather than a sharp corner. This results in a larger measured time, and thus a lower velocity. The points which do not compare very well at low velocities may be biased due to the inclusion in the average of a false measurement caused by an irregular bubble/slug combination. The algorithm attempted to exclude such false readings by averaging only the times which occurred most often (i.e. by averaging only the values which occur near the first mode of a histogram of the data).

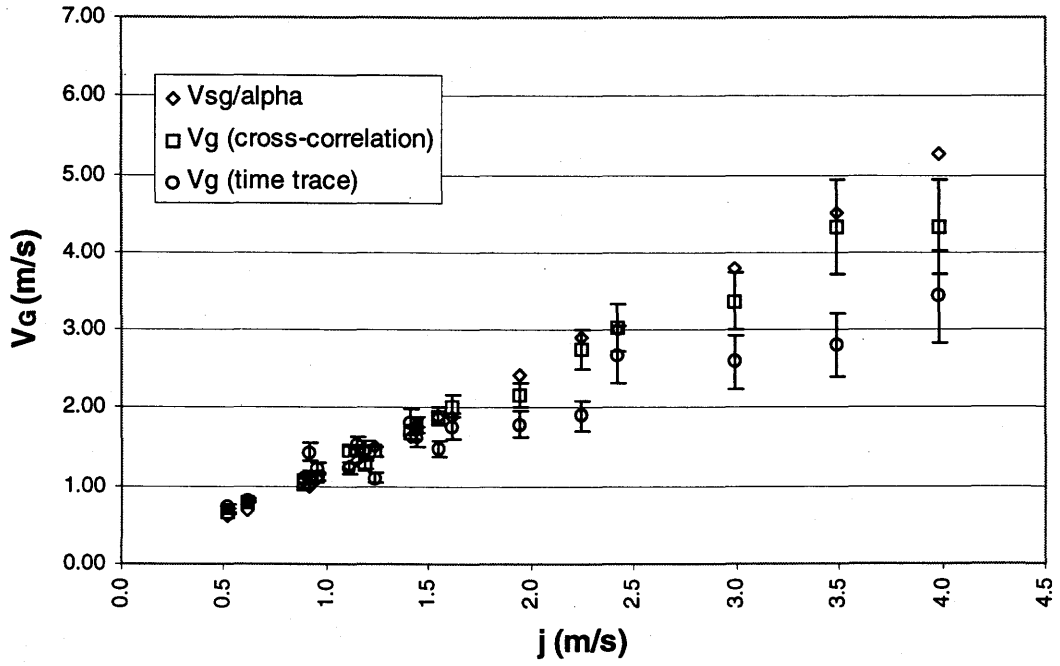

Figure 4.4 - Taylor bubble velocity measurements.

Overall, the velocities measured with this technique compare reasonably to the velocities determined from the cross-correlation of the film thickness with an RMS percent difference of 19%. While this is an acceptable difference, the method is limited to flows which contain well defined, well separated Taylor bubbles. For this method to work, the Taylor bubbles must be separated by at least 2 D, otherwise the signal does not represent the passage of a single interface, but rather it reflects the passage of one interface and the entrance of another. If the Taylor bubbles are not well defined, this method will give false readings due to curves in the void fraction signal at points B and D, rather than sharp corners. Due to these limitations, the author proposes that cross-correlation of two similar probes separated by a short distance is a more useful method of determining the actual bubble velocity.

4.5 Void Fraction Data Comparison

Since the void fraction sensor was calibrated on the ground under normal gravity conditions, a comparison with other reported microgravity data was performed to verify this microgravity data. The flow settings at which the current data set was taken are shown in Figure 4.5, along with the range of flow settings covered by Elkow (1995) and Bousman (1995). The results of the void fraction comparison are shown in Figure 4.6. The data from the present study shows excellent agreement with that of Elkow (1995) and Bousman (1995), with considerably less scatter. The scatter in the measurements of the other two studies could be attributed to the effect of other parameters, for example tube diameter, which are not represented in Figure 4.6. The important fact to note is that Figure 4.6 shows that the microgravity data from this sensor falls within the range of other accepted microgravity data.

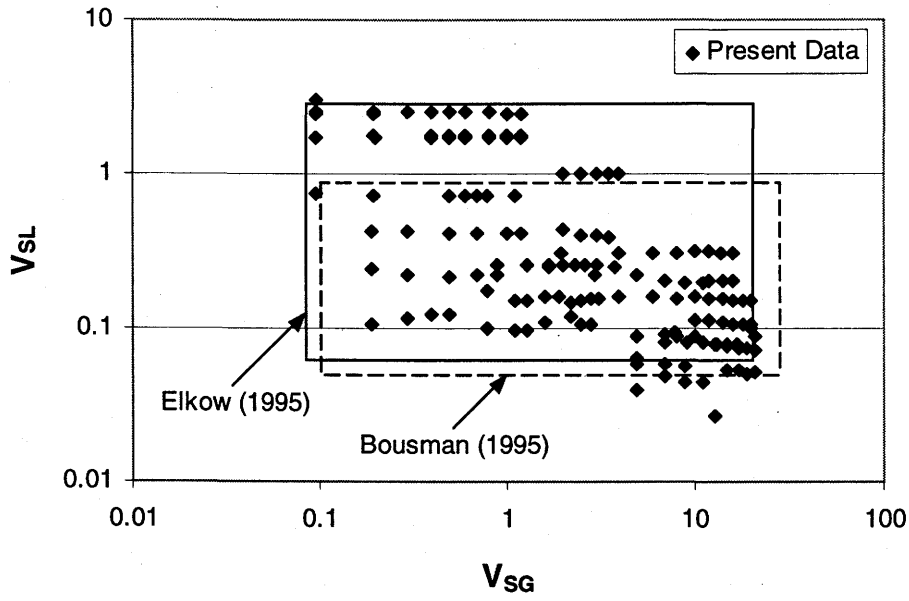

Figure 4.5 - Flow settings for the present data set.

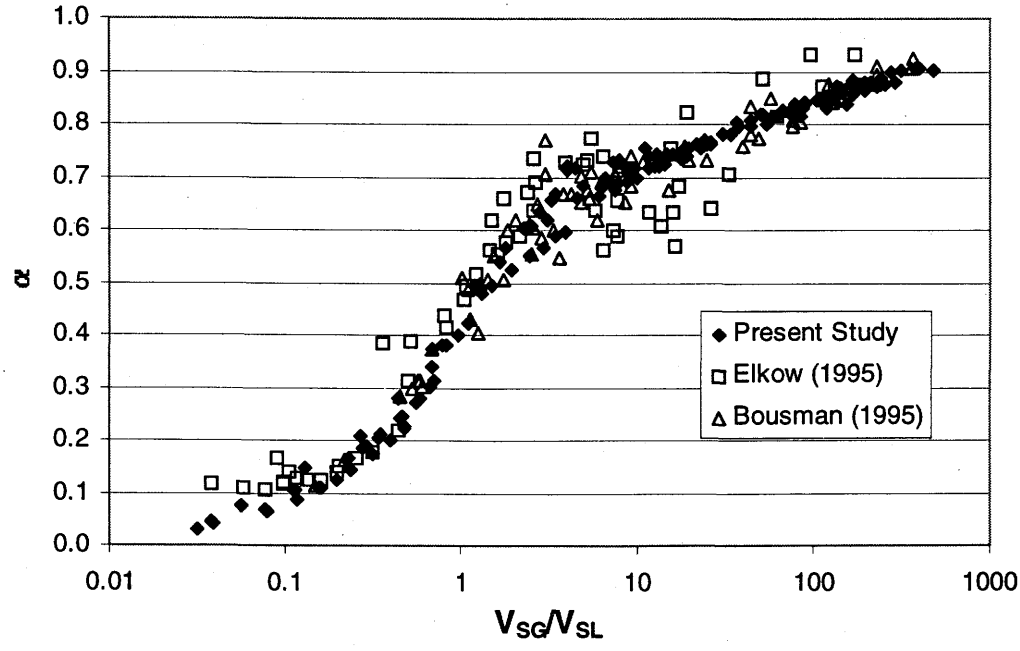

Figure 4.6 - Comparison of microgravity void fraction data.

5. FLOW REGIME IDENTIFICATION

As discussed in Chapter 1, void fraction is closely related to flow regime. Several researchers (see for example Jones and Zuber, 1975, or Costigan and Whalley, 1997) have shown that under normal gravity conditions, the void fraction probability density function is an excellent indicator of flow regime. However, few attempts have been made to add objectivity to flow regime identification through signal analysis of microgravity two-phase flow. Most researchers use flow images alone to identify flow regimes, a process which is very subjective and which can be misleading.

While the void fraction PDF is not the only tool which has been used to identify normal gravity flow regimes, the author proposes that it is perhaps the most useful. Song *et al.* (1995) reported that a good indicator of the bubbly-to-slug transition was a sharp increase in the void fraction signal-to-noise ratio. However, it was found that with the present data the signal-to-noise ratio did not show significant change as the flow transitioned from bubbly to slug flow. Song *et al.* (1995) also found that two time scales derived from the void fraction auto-correlation function could also be used to determine the transition from bubbly to slug flow. Again, the present data set did not show an appreciable change in these time scales as the flow transitioned. Another common tool used to identify flow regimes is the void fraction power spectral density function (see for example Song *et al.*, 1995 or Jones and Zuber, 1975). However, the power spectral density function does not appear to be as useful for determining flow regimes as the PDF.

This chapter presents a method of identifying the four microgravity flow regimes through analysis of the void fraction PDF. The reader is referred back to Figures 1.1 and 1.2 for definitions of the flow regimes and their approximate locations on a superficial velocity flow pattern map. In this chapter, the PDF which clearly identifies each flow regime is presented along with the corresponding flow image and void fraction time trace. This is followed by a discussion of how the PDF changes as the flow transitions between flow regimes. While this chapter presents an overview of the data, Appendix C contains the void fraction PDF for each flow setting and flow images for selected flow settings. The figures presented in this chapter are cross-referenced to the data tabulated in Appendix B by a code such as 96F3P28, which gives the year the data was taken (1996), the flight number (F3), followed by the parabola number (P28).

5.1 Typical Flow Regime Identifiers

Before any discussion on how to identify flow regime transitions can take place, we must first examine how each flow regime can be identified. This section presents typical void fraction time traces and their PDF along with video images for the four flow regimes. Each flow regime is represented by a flow setting which can be clearly identified through video images, and which does not fall near a transition area.

5.1.1 Bubbly Flow

Bubbly flow is characterized by the time trace and PDF as typically shown in Figure 5.1. Also shown in Figure 5.1 is an image grabbed from the high speed video system, which clearly shows that this is a bubbly flow. The void fraction time trace centers around a low average void fraction with small fluctuations corresponding to the passage of the bubbles. The PDF for bubbly flow has a single narrow peak at a low void fraction, indicative of the small fluctuations about a mean value. It was found that a PDF with a single peak at a void fraction typically less than 0.2 corresponded to bubbly flow.

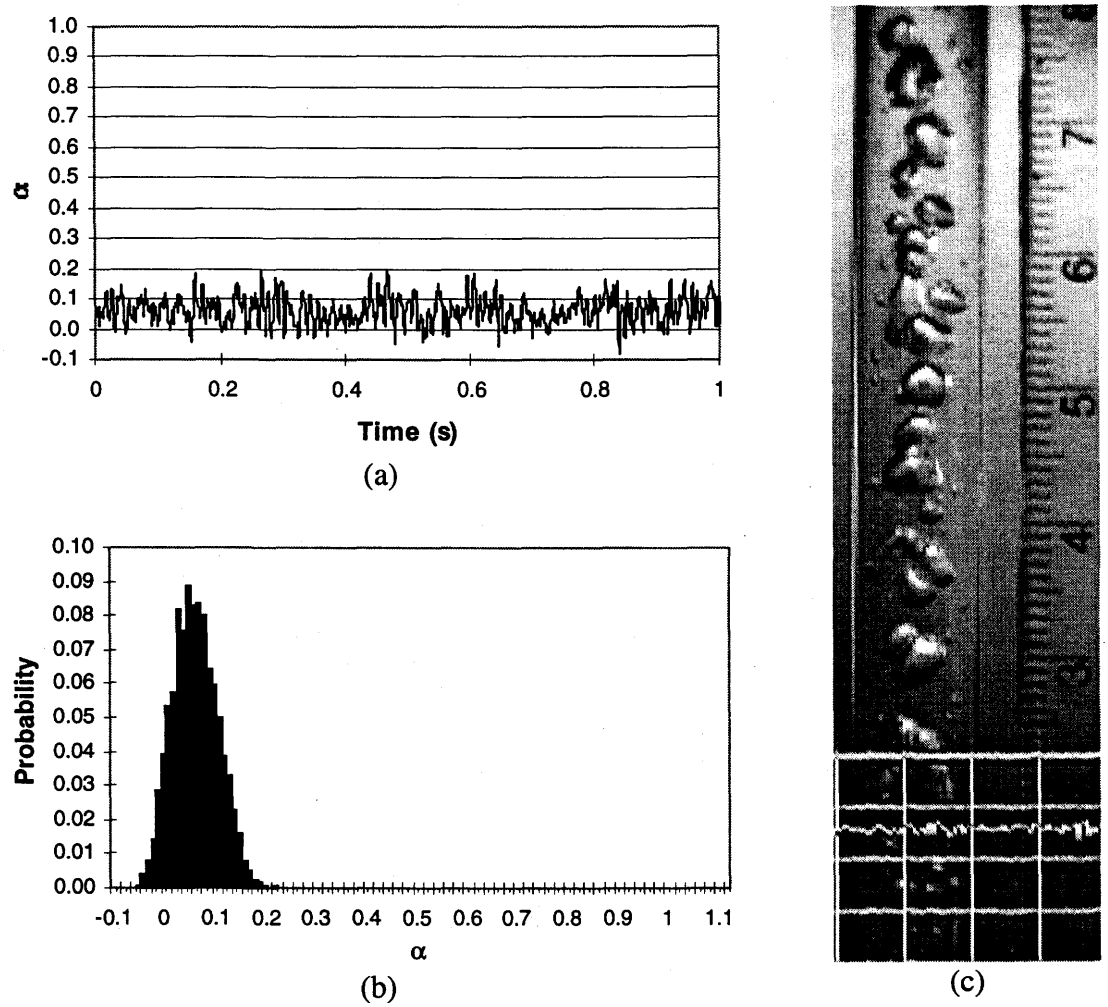

Figure 5.1 - Bubbly Flow run 96F3P13 with V_{SL} = 2.53 m/s and V_{SG} = 0.196 m/s, showing; (a) Time trace, (b) PDF, and (c) Flow image.

5.1.2 Slug Flow

A void fraction time trace, its PDF, and the flow image for a typical slug flow at the upper end of liquid and gas velocities is shown in Figure 5.2. The time trace for a slug flow is characterized by a void fraction signal which fluctuates between high and low values. The high void fraction corresponds to the passage of a Taylor bubble, while the low void fraction indicates the passage of a liquid slug. The flow image shows the passage of a liquid slug, with the tail of the preceding Taylor bubble exiting at the top, and the nose of the next Taylor bubble entering at the bottom. The small bubbles at the tail of the top bubble are the result of a small amount of slip between the liquid and gas (slip is discussed in more detail in Chapter 6) induced at higher gas velocities. The slug

flow PDF has two peaks, one at a high void fraction and the other at a low void fraction corresponding to the passage of Taylor bubbles and liquid slugs, respectively.

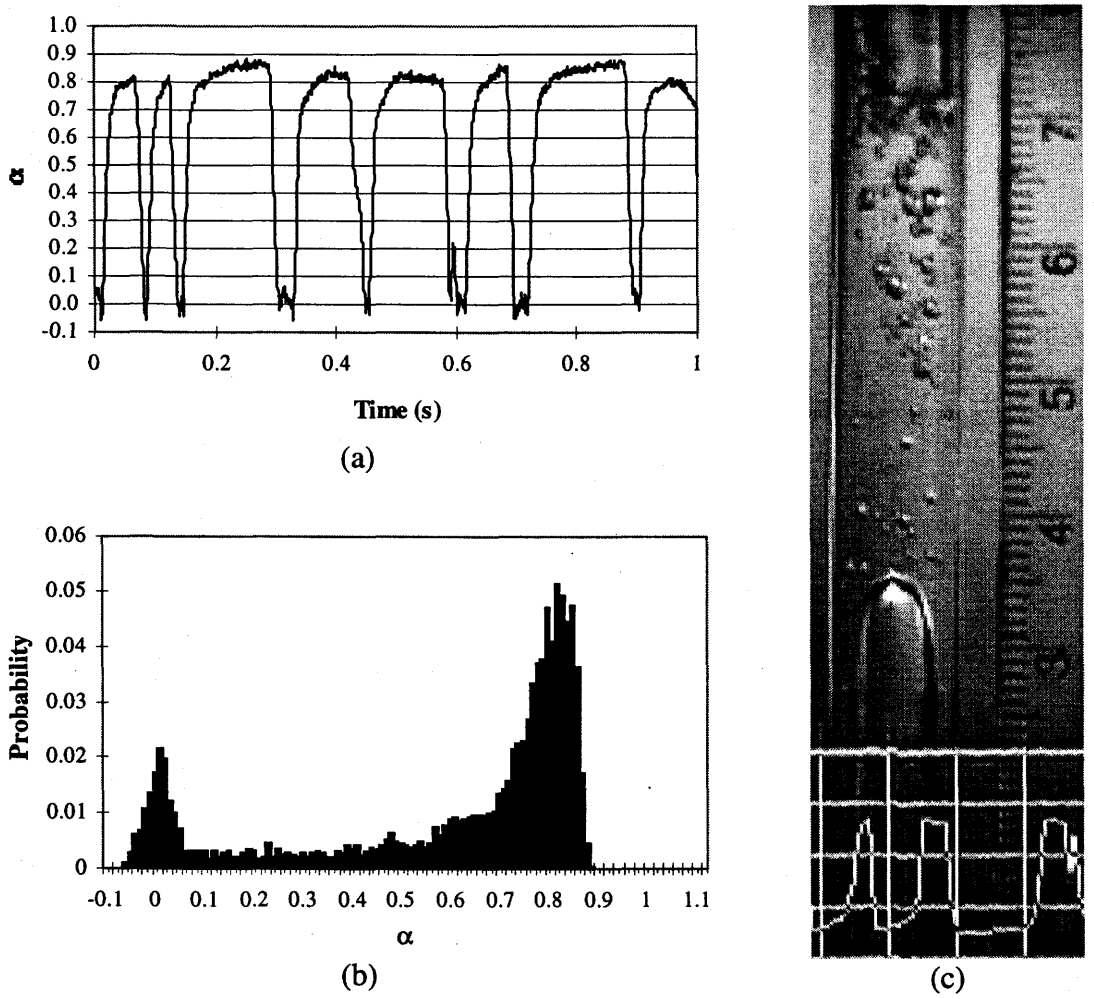

Figure 5.2 - Slug Flow run 96F4P46 with V_{SL} = 0.42 m/s and V_{SG} = 0.99 m/s, showing; (a) Time trace, (b) PDF, and (c) Flow image.

At lower liquid and gas velocities, the shape of the PDF changes slightly, as shown in Figure 5.3. In this case the flow image shows Taylor bubbles with nearly spherical noses and tails separated by short slugs. Since the Taylor bubbles are so close together, the sensor rarely reads only a liquid slug. There is always either the tail of the preceding bubble or the nose of the following bubble in the sensor with the liquid slug. This results in the time trace and void fraction PDF shown in Figure 5.3. The time trace shows an almost sinusoidal shape, and the double peaks of the PDF move closer together. However, there is clearly a PDF that represents slug flow.

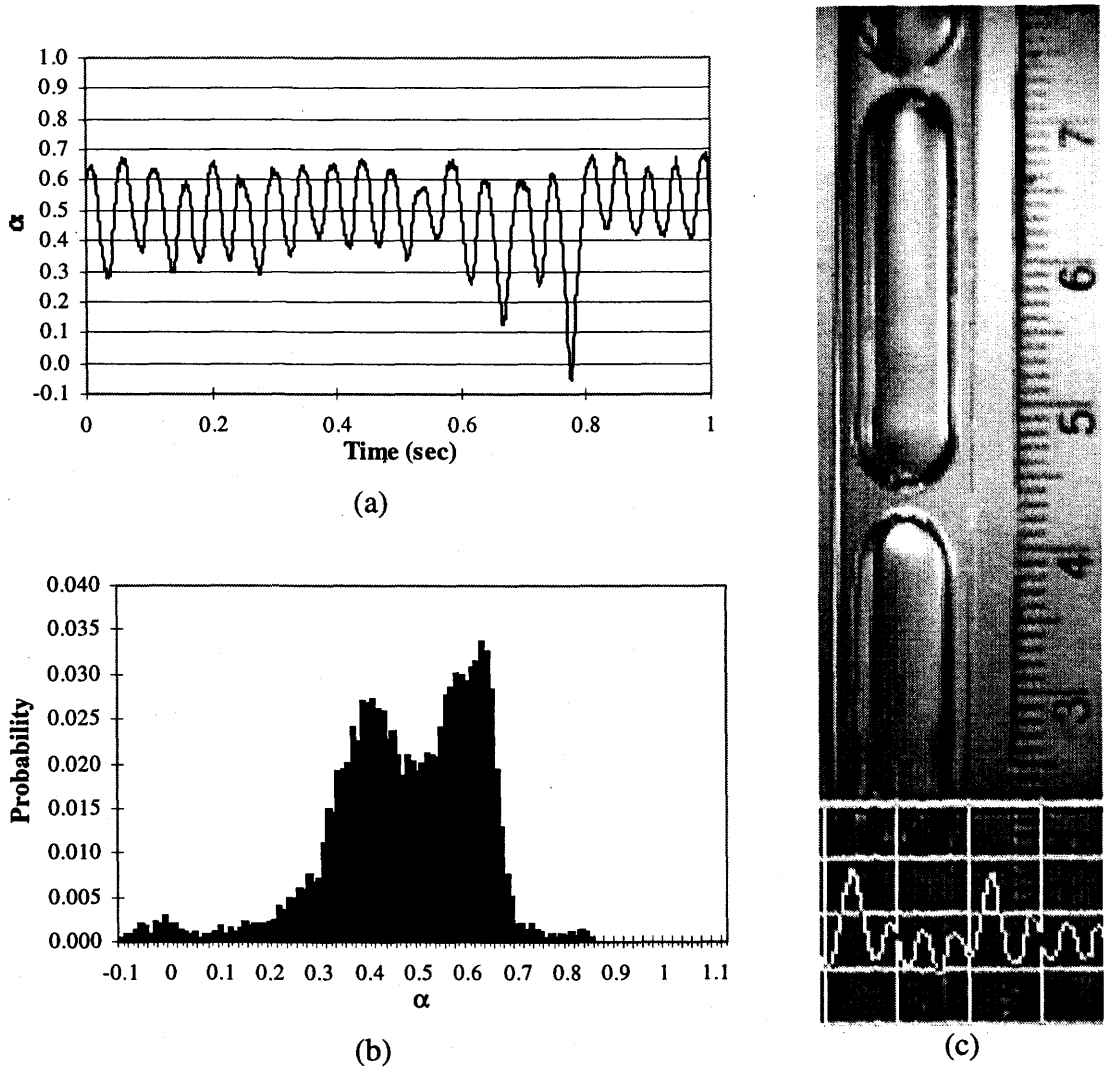

Figure 5.3 - Slug Flow run 96F4P49 with V_{SL} = 0.22 m/s and V_{SG} = 0.29 m/s, showing; (a) Time trace, (b) PDF, and (c) Flow image.

5.1.3 Transitional Flow

The transitional flow regime is typically characterized by the void fraction time trace and PDF shown in Figure 5.4. Also shown in Figure 5.4 is a typical image of the unstable, chaotic slug region which characterizes frothy slug-annular flow. The void fraction time trace of a transitional flow tends to stay at a high void fraction, with random dips into lower void fractions. Typically, these lower void fraction dips are very short lived, indicating the unstable nature of the slug. The PDF for this flow regime shows a single broad peak, with the maximum typically between a void fraction of 0.7 to

0.9, with a long tail extending down to void fractions as low as 0. The single peak in the PDF reflects the annular nature of the flow, and the long tail represents the passing of short, unstable slugs. While the void fraction time trace, PDF, and flow image presented in Figure 5.4 are for a frothy slug-annular flow, distorted slug flow shows similar characteristics in the PDF and time trace.

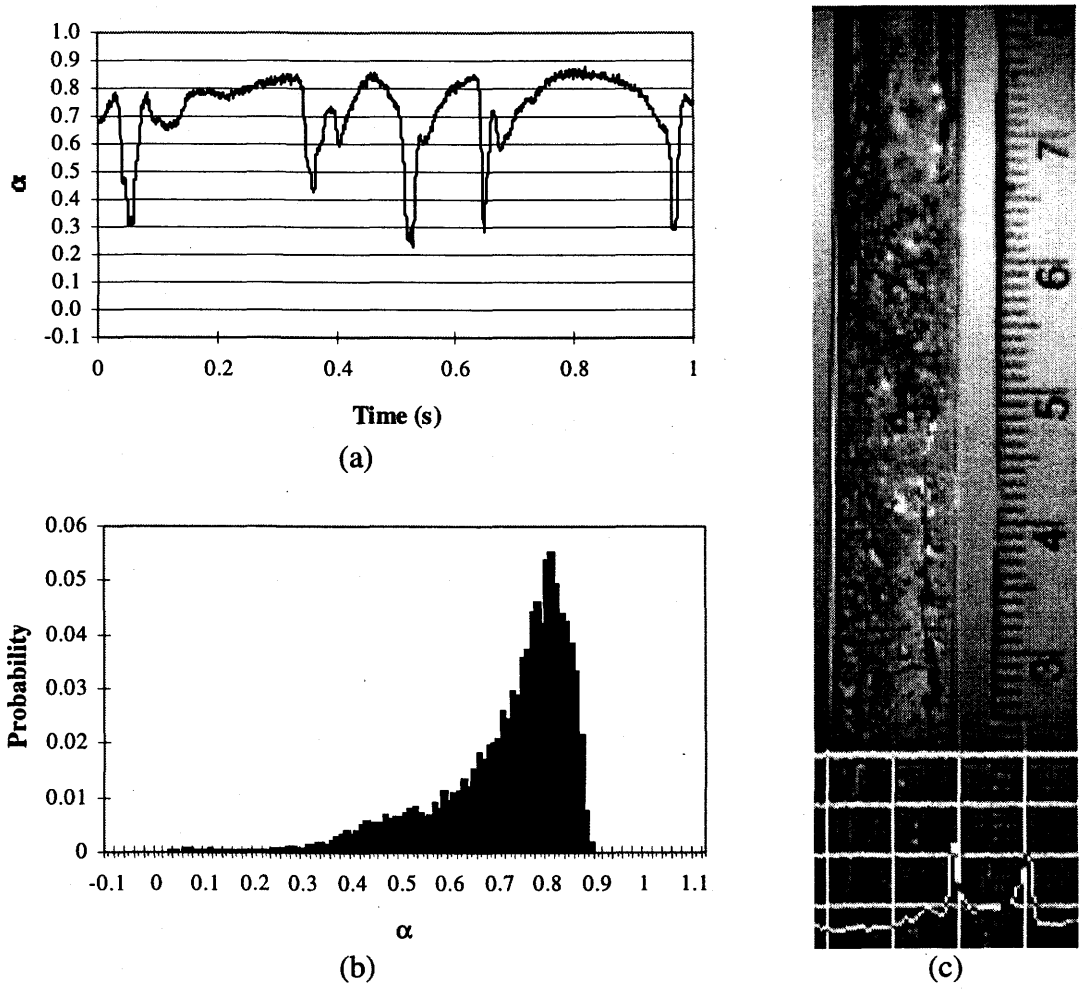

Figure 5.4 - Transitional Flow run 96F4P27 with V_{SL} = 0.25 m/s and V_{SG} = 2.98 m/s, showing; (a) Time trace, (b) PDF, and (c) Flow image.

5.1.4 Annular Flow

Annular flow is typically represented by the void fraction time trace and PDF shown in Figure 5.5. The void fraction time trace for annular flow remains constant at a void fraction typically between 0.80 and 0.90 as a smooth annular film passes through the

sensor. The smooth film is occasionally interrupted by the passing of waves, shown in the time trace as small dips into lower void fractions. Figure 5.5(c) is a typical flow image of annular flow, which shows the smooth annular film at the top and bottom, and the passing of a wave at the 5 cm mark. A typical PDF for annular flow has a very narrow peak at a void fraction between 0.80 and 0.90, with a short tail extending into lower void fractions. The narrow peak in the PDF indicates that the film maintains a nearly constant thickness between the passing of waves.

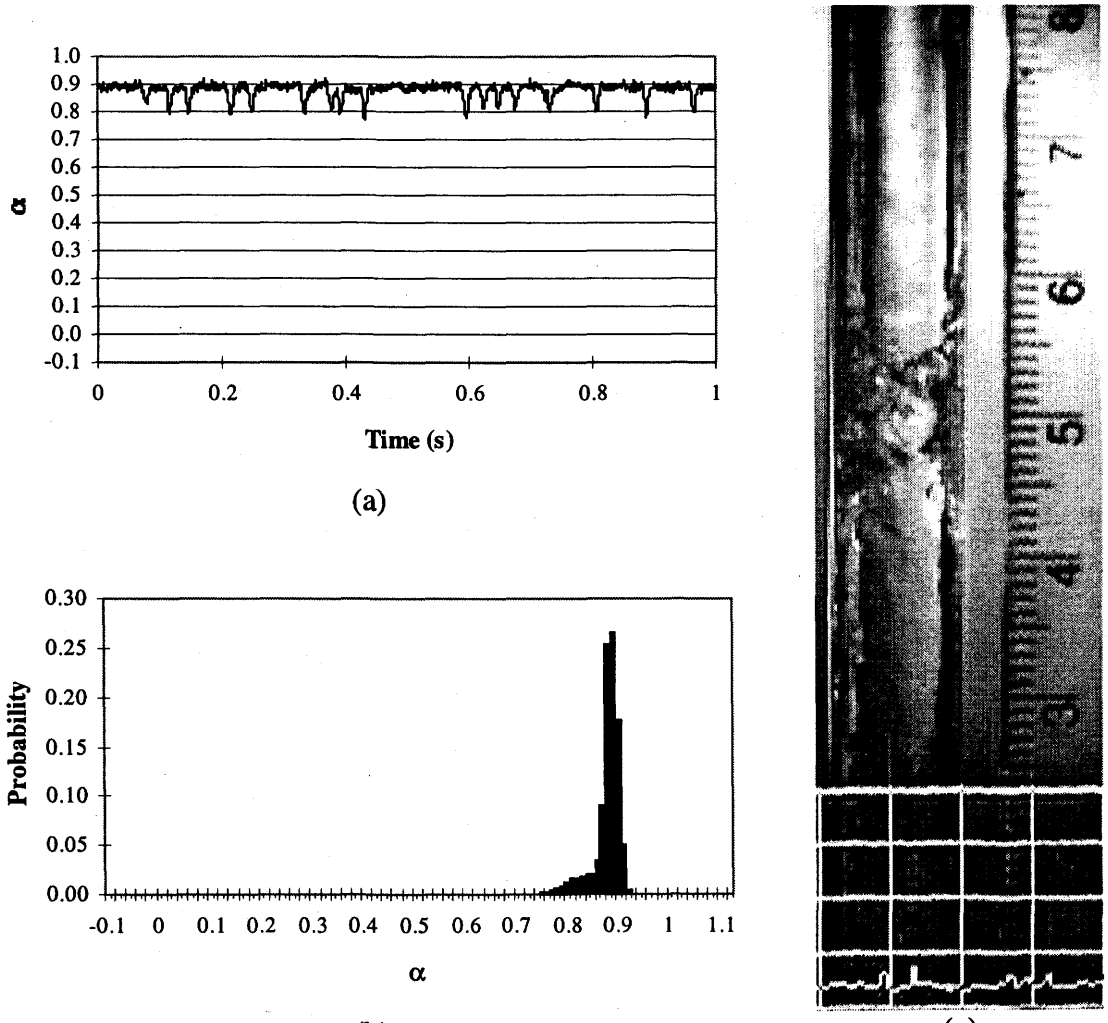

Figure 5.5 - Annular Flow run 96F2P48 with V_{SL} = 0.07 m/s and V_{SG} = 20.94 m/s, showing; (a) Time trace, (b) PDF, and (c) Flow image.

5.2 Transitions

The PDF plots presented in the previous sections show clear differences between each flow regime. However, as the flow approaches a transition region between two distinct flow regimes, the differences between the PDF plots become more subtle. Regardless, it was found that the PDF showed definable differences between the flow regimes, even very close to the transitions. This is illustrated in the following three sections. Since the transitions between flow regimes take place over a range of flow settings, flows which displayed characteristics of two neighboring flow regimes were labeled as a transitional flow. Therefore, in the following three sections, a PDF and video image is presented for the flow just before the transition, during the transition, and after the transition.

5.2.1 Bubbly-to-Slug

The bubbly-to-slug transition takes place when small (typically less than 1 D) discrete bubbles begin to pack together and flow in clusters. This leads to coalescence and the formation of the Taylor bubbles which characterize slug flow. While both bubbly and slug flows are usually easy to identify from the video images, the subjectivity of the observer can often bias where the transition between the two regimes actually occurs.

Figure 5.6 shows how the void fraction PDF changes as the flow transitions from bubbly to slug flow. Also shown in Figure 5.6 are flow images corresponding to each flow setting. Figure 5.6(a) is a bubbly flow, as can be clearly seen in the flow image. The PDF in Figure 5.6(a) is that of a typical bubbly flow with a single peak at a void fraction of approximately 0.16.

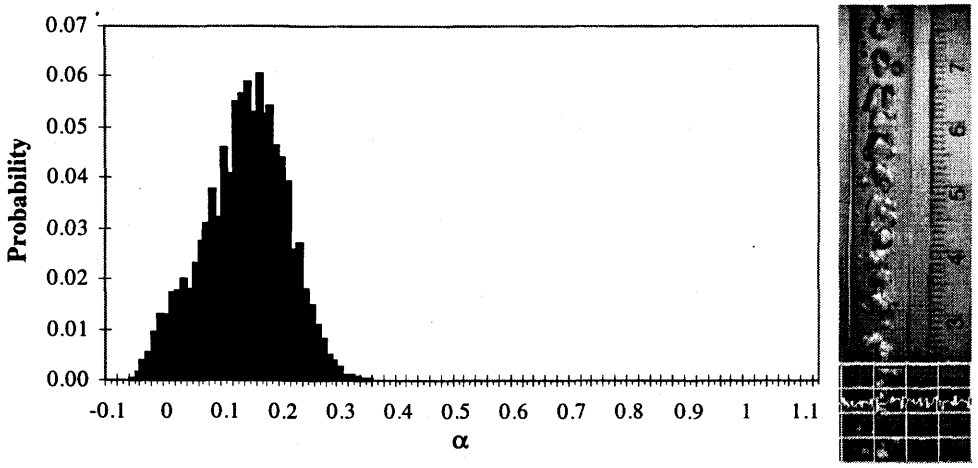

(a) V_{SL} = 2.51 m/s, V_{SG} = 0.59 m/s

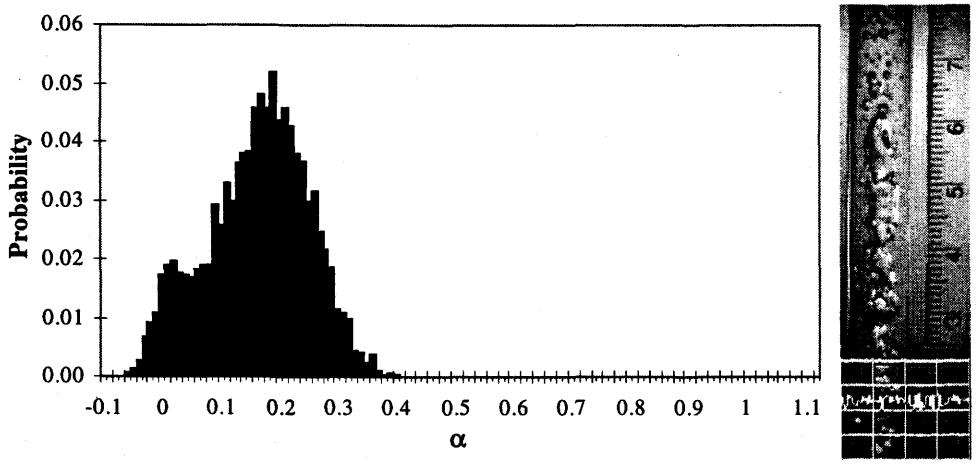

(b) V_{SL} = 2.51 m/s, V_{SG} = 0.79 m/s

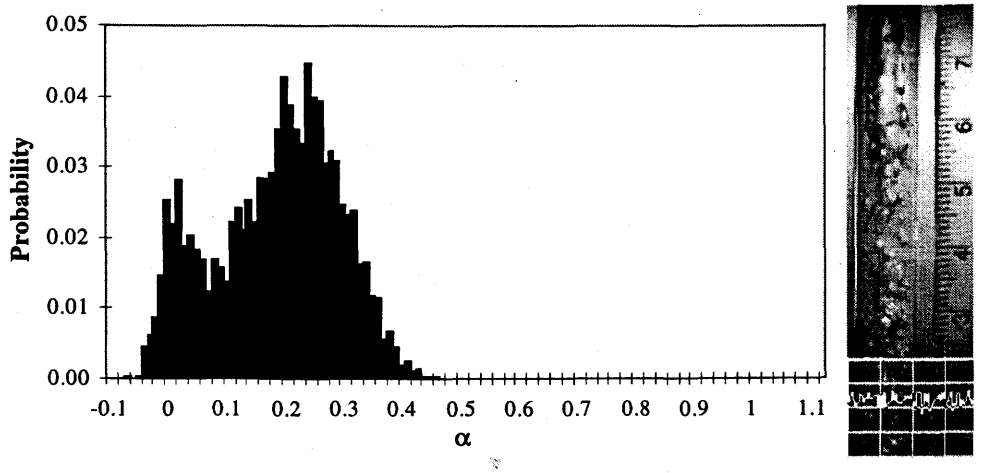

(c) V_{SL} = 2.50 m/s, V_{SG} = 0.99 m/s

Figure 5.6 - Bubbly-to-slug transition void fraction PDF plots and flow images; (a) F3P38 – Bubbly, (b) F3P39 – Bubbly/Slug, and (c) F3P40 – Slug.

In Figure 5.6(b), the gas flow rate has been increased, and the flow is in a transition from bubbly to slug flow. The video image of this flow setting shows the formation of bubbles which are approaching 1 D in length, and the bubbles are beginning to flow in clusters, separated by slugs of water with fewer bubbles. The PDF for this flow setting is much like that of a bubbly flow, with a second peak just beginning to form at a void fraction of near zero. The start of the second peak indicates that the bubbles are beginning to flow in clusters separated by slugs of liquid with little or no bubbles. Note also that the main peak is now at a void fraction of about 0.2, indicating larger and more closely packed bubbles.

A further increase in gas flow rate results in the PDF and flow image shown in Figure 5.6(c). At this flow setting the flow has transitioned into slug flow, and the video image clearly depicts a Taylor bubble near the top of the viewing section. The PDF has now taken on the two definite peaks characteristic of slug flow, one at a void fraction of about 0.02, and one at approximately 0.25.

5.2.2 Slug-to-Transitional Flow

The transition from slug to transitional flow is often very difficult to determine from flow images alone; hence visual identifications are quite subjective. The transition occurs when the gas phase, flowing in the Taylor bubbles of slug flow, begins to reach high enough inertia to temporarily break through some of the liquid slugs separating the Taylor bubbles. The liquid phase quickly recovers to form another slug, which is then broken again by the incoming, high speed gas phase. As the gas flow rate is increased, more and more slugs become unstable until there are no stable slugs and transitional flow exists. Recall that in Chapter 1, transitional flow was divided into two sub-regimes; namely distorted slug and frothy slug-annular flow. The PDF analysis is presented for both cases to show its validity over the entire transitional flow range.

5.2.2.1 Slug-to-Distorted Slug

Figure 5.7 shows how the void fraction PDF changes as the flow transitions from slug to distorted slug flow. Slug flow is clearly depicted in Figure 5.7(a). The video image shows a clear, stable slug between two well defined Taylor bubbles. The PDF for this flow setting clearly shows the double peaks which characterize slug flow. The fact that the peak at the high void fraction is very narrow and reaches a relatively high probability indicates that the Taylor bubbles are very long and smooth, as can be verified by examining the video images. The small peak at the low void fraction of about 0.02 indicates that the slugs are short with few bubbles.

Figure 5.7(b) is a flow which shows characteristics of both slug and distorted slug flow. The video image shows a distorted slug about to be destroyed by the bubble behind it. However, there are just as many cases in the video where, what appears to be a stable slug, passes through the viewing section. The PDF for this flow shows characteristics of both flow regimes. It has a broad peak at a high void fraction, with a long tail into low void fractions, which is characteristic of transitional flow. However, there is still a small peak at a void fraction of 0.03 indicating that there are still some stable slugs passing through the sensor, as usually found in slug flow.

Figure 5.7(c) shows the result of increasing the gas flow rate slightly, causing a definite transition to distorted slug flow. The video image shows a bubble about to burst through an unstable slug, while the PDF is that of a typical transitional flow. The PDF has a single peak at a void fraction of about 0.84, with a long tail extending into void fractions as low as zero. The peak at the low void fraction evident in Figures 5.7(a & b) is not seen anymore, leaving the long flat tail that is typical of transitional flows.

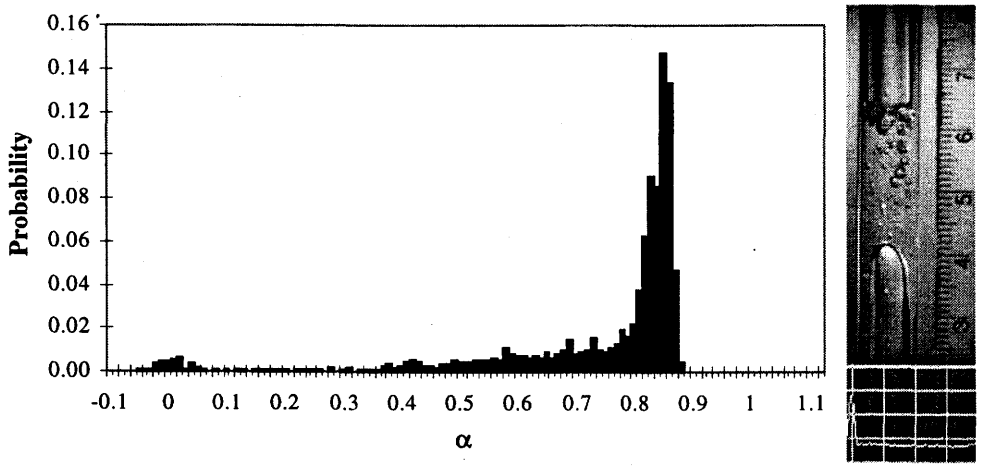

(a) V_{SL} = 0.10 m/s, V_{SL} = 1.09 m/s

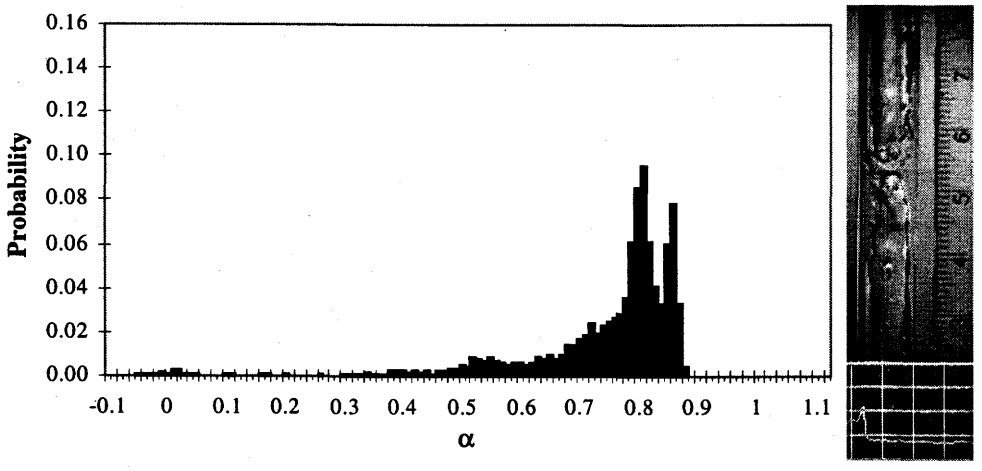

(b) V_{SL} = 0.10 m/s, V_{SG} = 1.29 m/s

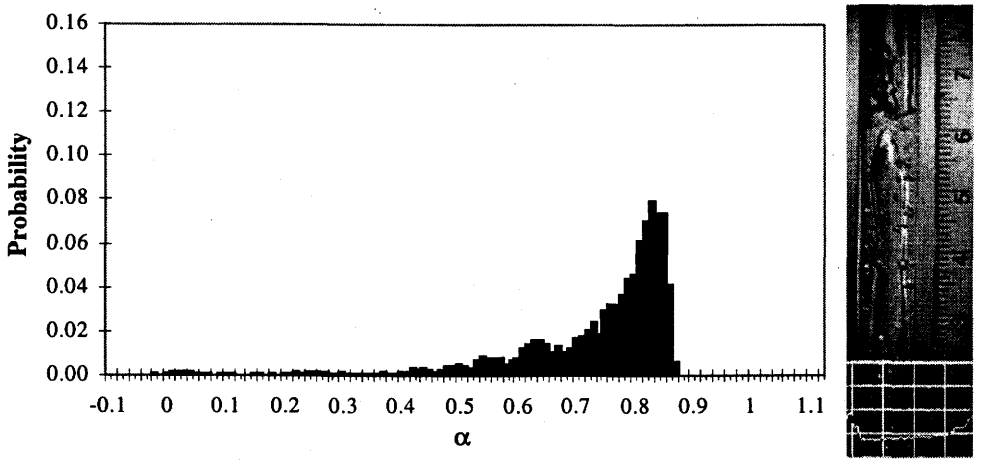

(c) V_{SL} = 0.11 m/s, V_{SG} = 1.59 m/s

Figure 5.7 - Slug-to-distorted slug transition void fraction PDF plots and video images; (a) 96F4P3 – Slug, (b) 96F4P4 – Slug/Distorted Slug, and (c) 96F4P5 – Distorted Slug.

5.2.2.2 Slug-to-Frothy Slug-Annular

Figure 5.8 shows the PDF plots and video images for a slug-to-frothy slug-annular transition. The slug flow video, shown in Figure 5.8(a), depicts a stable slug followed by the nose of a Taylor bubble. At such high liquid flow rates, the air-water interface of the Taylor bubbles appears more irregular, and there are more bubbles trapped in the liquid slugs. The PDF for this flow setting shows two clear peaks at void fractions of about 0.05 and 0.82. The peak at the high void fraction reaches a considerably smaller probability and is of much wider spread than that of Figure 5.7(a). This is largely due to the irregular and dynamic interfaces. While a smooth, regular interface results in a constant void fraction as the bubble passes, and thus a high probability of that void fraction occurring, an irregular and dynamic film results in a void fraction which fluctuates over a small range (typically about 0.15), thus spreading the probability density function. The low void fraction peak in this case is at a slightly higher void fraction than in Figure 5.7(a) due to the increase in the number of bubbles found in the liquid slugs.

Figure 5.8(b) shows the PDF and video image for a flow which is in transition between slug and frothy slug-annular flow. The video image shows a frothy slug region where the gas is in the process of breaking through the liquid slug, resulting in a chaotic, bubbly mixture. The PDF has a broad peak at a void fraction of approximately 0.78, with a long tail extending down to void fractions as low as zero. This is very similar to the typical PDF of transitional flow, as shown in Figure 5.4. However, as in Figure 5.7(b), there is still a small peak at a void fraction of about 0.06, indicating the passage of some stable, though bubbly, slugs.

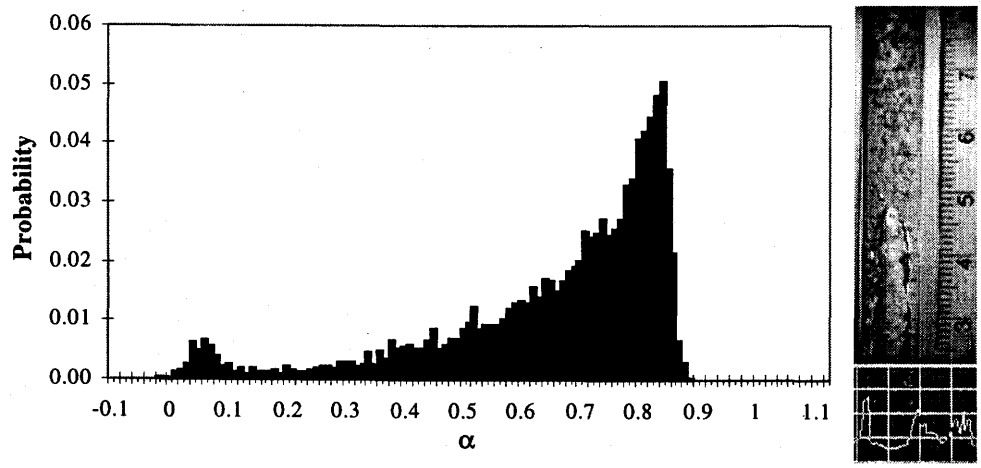

(a) V_{SL} = 0.43 m/s, V_{SG} = 1.98 m/s

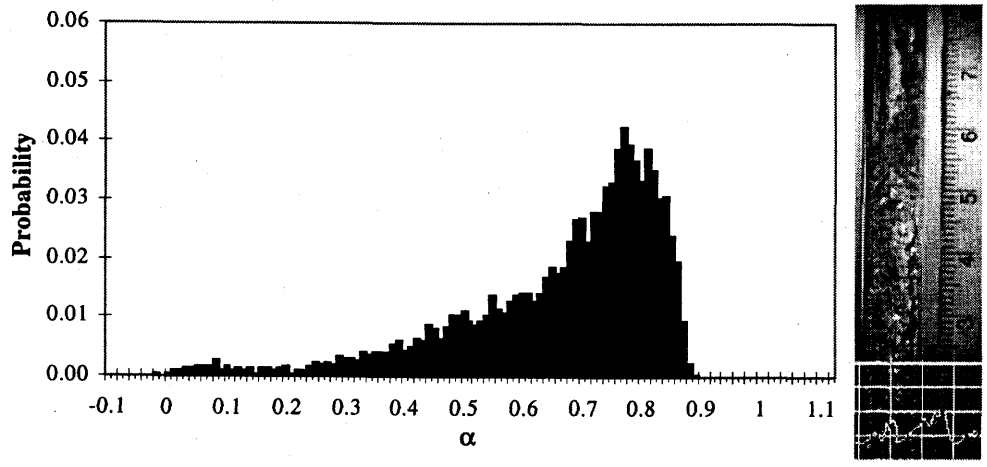

(b) V_{SL} = 0.40 m/s, V_{SG} = 2.48 m/s

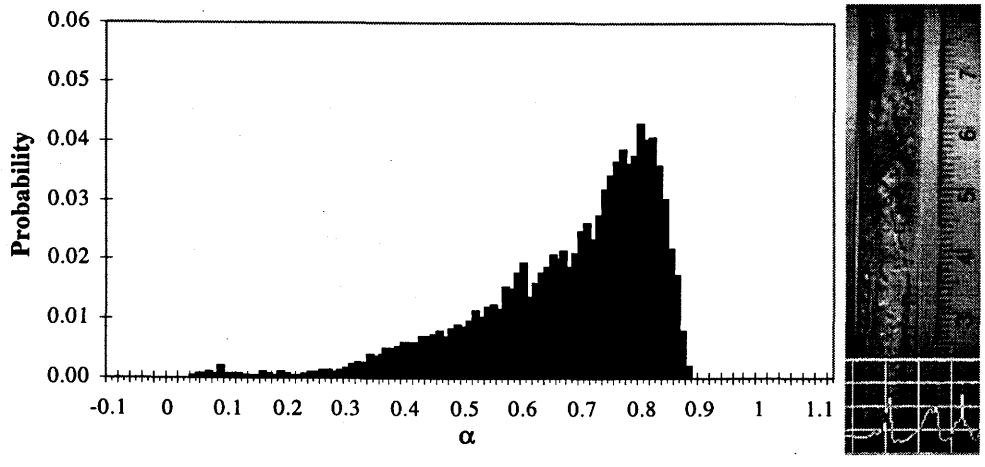

(c) V_{SL} = 0.40 m/s, V_{SG} = 2.98 m/s

Figure 5.8 - Slug-to-frothy slug-annular transition void fraction PDF plots and video images; (a) 96F4P30 – Slug, (b) 96F4P32 – Slug /Frothy Slug-Annular, and (c) 96F4P33 – Frothy Slug-Annular.

The PDF and video image in Figure 5.8(c) indicate a frothy slug-annular flow. The video image shows the passage of a chaotic, highly aerated, unstable slug region which is typical of frothy slug-annular flows. The PDF is that of a typical transitional flow, with the broad peak at a high void fraction and the long tail extending into low void fractions. The single rectangle protruding above the rest at a void fraction of about 0.07 possibly indicates that the transition to fully frothy slug-annular flow is not quite complete and a stable slug or two may have been present.

5.2.3 Transitional-to-Annular

The transitional-to-annular flow transition is recognized when the unstable slugs of transitional flow no longer bridge the tube and become instead more of a disturbance wave on the annular film. The flow then becomes annular flow, occasionally interrupted by large amplitude waves that do not completely bridge the tube. This transition is the most difficult to identify from video images, especially at high liquid flow rates. The unstable slugs and disturbance waves are often very frothy and the inner features of the flow cannot be easily observed. As for the transition from slug to transitional flow, this transition exhibits slight differences between high and low liquid velocity flows. Again, the PDF analysis are presented for both cases (e.g. a transition from distorted slug to annular flow, and from frothy slug-annular to annular flow) to verify its applicability over the entire range of transitional flow.

5.2.3.1 Distorted Slug-to-Annular

Figure 5.9 shows the void fraction PDF plots and the video images for a transition from distorted slug to annular flow. The video image in Figure 5.9(a) shows the passage of an unstable slug, and there appears to be bridging. The corresponding PDF shows a sharp peak at a high void fraction due to the mainly annular nature of the flow, with a tail which extends down to a void fraction of 0.45. The significance of where the tail of the PDF stops will be discussed later in this section.

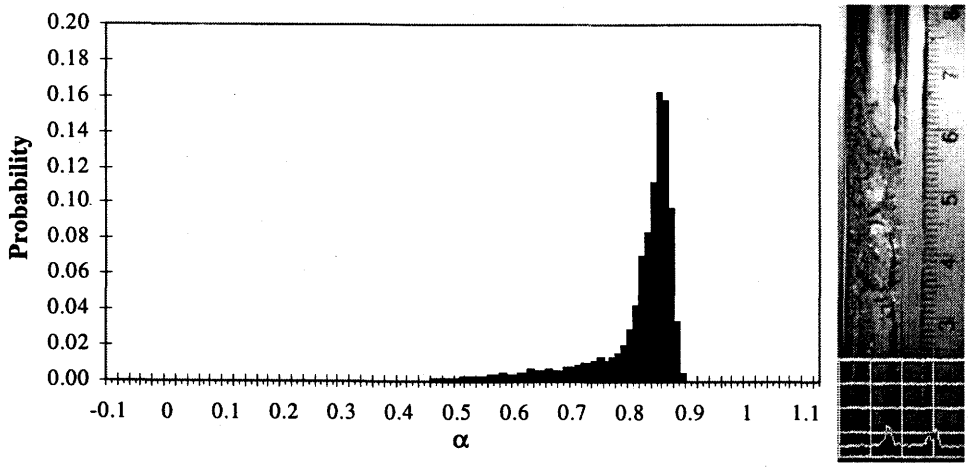

(a) V_{SL} = 0.06 m/s, V_{SG} = 4.97 m/s

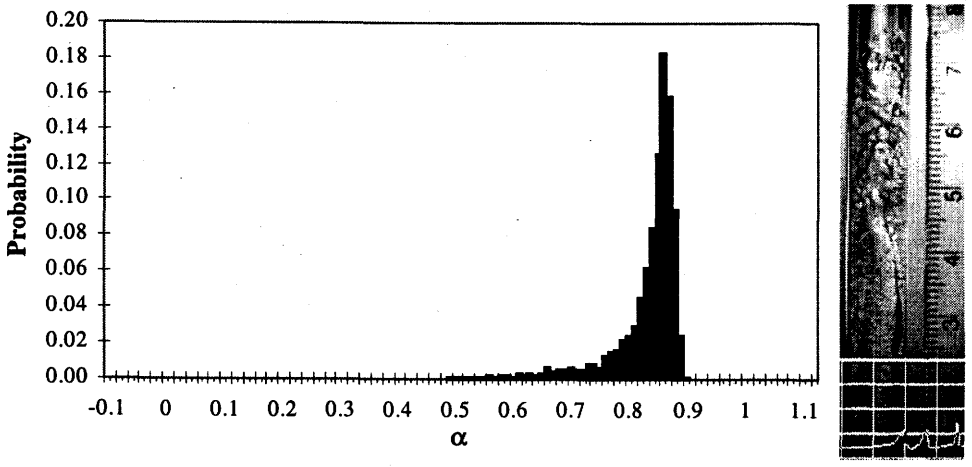

(b) V_{SL} = 0.06 m/s, V_{SG} = 6.92 m/s

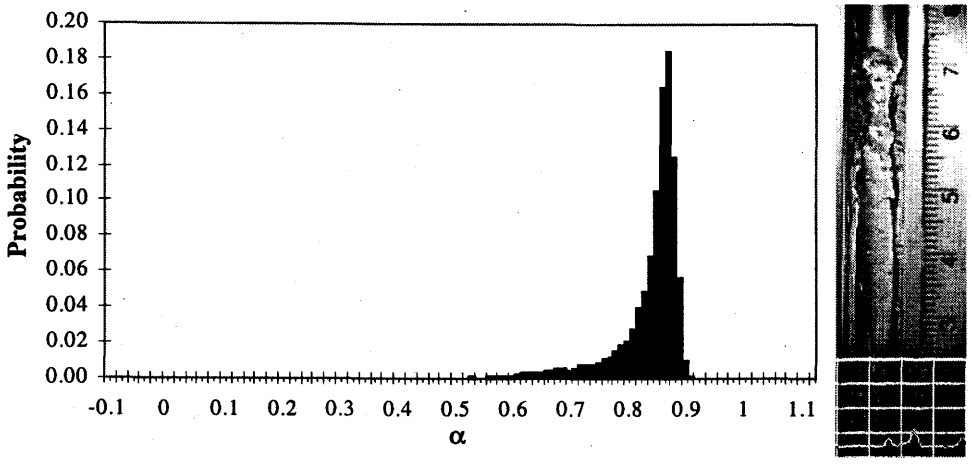

(c) V_{SL} = 0.06 m/s, V_{SG} = 8.92 m/s

Figure 5.9 - Distorted slug-to-annular transition void fraction PDF plots and video images; (a) 96F2P50 – Distorted Slug, (b) 96F2P51 –Distorted Slug/Annular, and (c) 96F2P52 – Annular.

Figure 5.9(b) is from a flow setting that falls in the transition region between distorted slug and annular flow. Thus, it contains many of the features of both flows. The video image shows the passage of what appears to be an unstable slug, but it is difficult to determine if the bridging is complete. However, examination of the video tape for this flow setting reveals several instances where bridging is likely not complete, as well as several other images where bridging occurs. Again, the waves/unstable slugs obscure the inside features, making it almost impossible to state whether or not bridging has occurred. The PDF for this flow setting shows a slightly higher peak at the high void fraction, indicating the more annular nature of this flow than the previous one, with a tail extending down to a void fraction of about 0.49.

Figure 5.9(c) shows the result of increasing the gas flow rate further, causing a transition to annular flow. The video image clearly shows the passing of a wave on the annular film, and in this case it is clear that the wave does not bridge the tube. The PDF for this flow setting is similar to the previous two, with a slightly higher peak and a tail extending down to a void fraction of about 0.53.

5.2.3.2 Frothy Slug-Annular to Annular

An example of how the void fraction PDF and the video images change as the flow transitions from frothy slug-annular to annular flow is shown in Figure 5.10. The video image of frothy slug-annular flow near the transition, shown in Figure 5.10(a), shows the passage of a typical unstable, frothy slug region. The presence of bubbles in the slug region makes it difficult to determine whether liquid bridging is complete. Images such as the one shown are found consistently in the video recording of the flow. The PDF for this flow has a single peak at a high void fraction, with a tail extending down to a void fraction of about 0.43. The peak in this PDF is not nearly as high as the ones previously shown in Figure 5.9. In this case the annular film is more irregular and dynamic than at lower liquid flow rates, and disturbances are much more common, thus there is a lower probability of any single void fraction being consistently reached, and therefore the PDF peak is smaller.

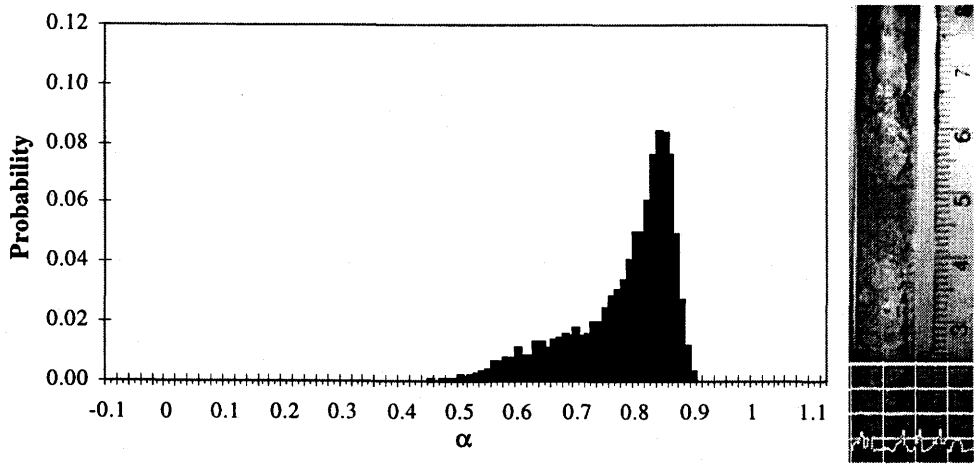

(a) V_{SL} = 0.32 m/s, V_{SG} = 9.91 m/s

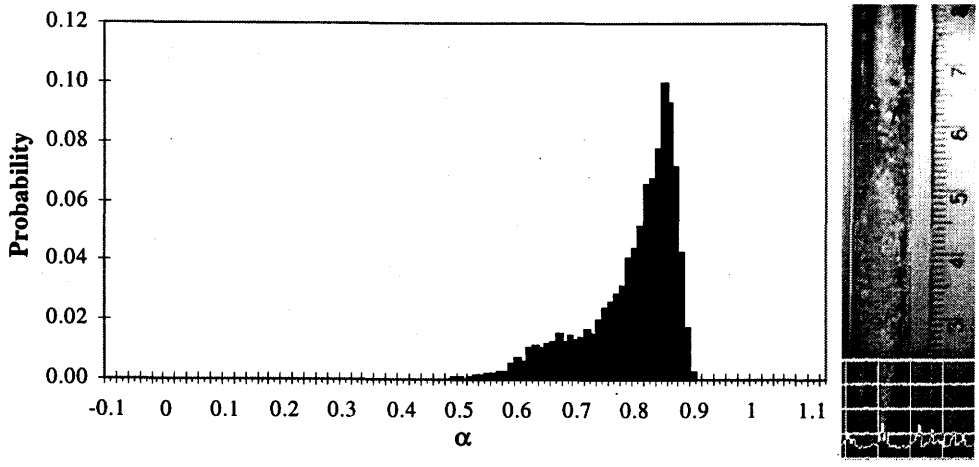

(b) V_{SL} = 0.31 m/s, V_{SG} = 11.92 m/s

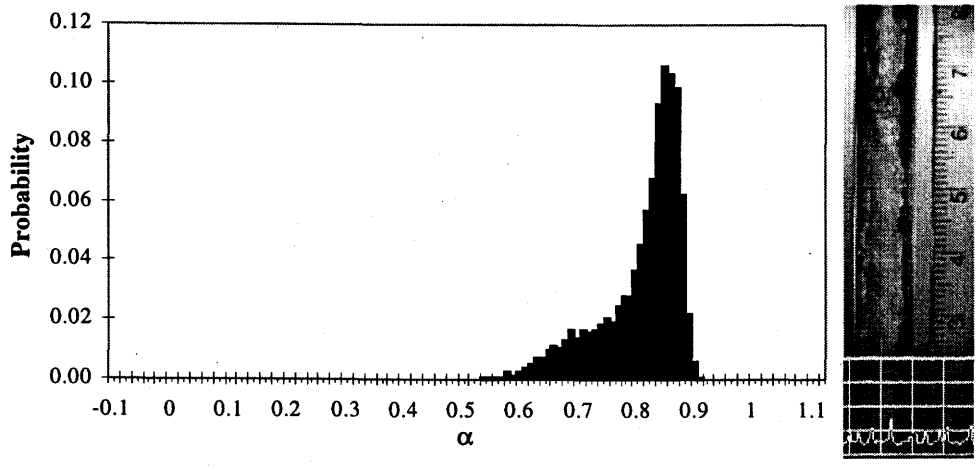

(c) V_{SL} = 0.31 m/s, V_{SG} = 13.91 m/s

Figure 5.10 - Frothy slug-annular-to-annular transition void fraction PDF plots and video images; (a) 96F2P26 – Frothy Slug-Annular, (b) 96F2P27 – Frothy Slug-Annular/Annular, and (c) 96F2P28 – Annular.

Figure 5.10(b) is the void fraction PDF and video image for a flow which is in transition from frothy slug-annular to annular flow. The video image shows the passage of a disturbance which appears to be a non-bridging wave. However, it is very difficult to say for certain if the area around the 5.5 cm mark on the scale is a bridging event, or if it is obscured because it is the region where the peak of the disturbance wave is passing. The video recording of this flow setting shows approximately the same number of disturbances that appear to bridge the tube as those that appear not to. Again the PDF has a single peak, slightly greater than that of Figure 5.10(a), with a tail extending down to a void fraction of about 0.49.

The transition to annular flow seems to be complete in Figure 5.10(c). The video image shows the passage of a disturbance wave which does not seem to bridge the tube. The video recordings of this flow setting show that while most of the disturbance waves appear not to bridge the tube, there is the odd occasion where the film is too obscured to tell if bridging actually has not occurred. The PDF for this flow setting again shows the single peak at a high void fraction, with a tail extending down to a void fraction of about 0.54.

After examining the PDF plots of Figure 5.9 and Figure 5.10, it is clear that they more or less resemble each other. However, there is one feature that does offer a method of determining the flow regime without the aid of the video. In both cases, as the transition took place, the tail of the PDF stopped at higher values. Where the tail ends indicates the lowest void fraction in the flow, which will correspond to the disturbances, be they waves on the annular film or unstable slugs/bridging events. Thus, it is the tail of the PDF which gives some clue as to which flow regime is present. One simply has to determine the void fraction at which an unstable liquid slug can no longer bridge the tube and becomes a disturbance wave. This of course is not expected to be a single value of void fraction, but instead a small range over which the transition takes place.

On studying Figures 5.9 and 5.10, they show that when the PDF tail reaches a void fraction below 0.45, transitional flow exists, and when the tail does not extend past 0.50, annular flow exists. The transition between transitional flow and annular flow takes place when the PDF tail stops somewhere between 0.45 and 0.50. Examination of PDF plots and video recordings of the flow settings not presented here also seem to suggest the same thing (see Appendix C).

To try to shed some light on why the transition would occur when the void fraction in the slugs is between 0.45 and 0.50, consider the case of a liquid slug containing many small bubbles. In an effort to determine where the transition from bubbly to slug flow exists, Dukler *et al.* (1988) pointed out that the maximum void fraction that small spherical bubbles arranged in a cubic array can achieve is 0.52. For larger bubbles of non-spherical shape, the maximum void fraction drops to approximately 0.40. Dukler *et al.* (1988) speculated that the transition from bubble to slug flow, where bubbles agglomerate and coalesce, takes place at a void fraction of about 0.45. Thus, for a disturbance passing the void fraction sensor to be a bridging event (i.e. a short slug), it must have a void fraction less than 0.52 if it contains small bubbles. If the bridging event contains larger bubbles, then the void fraction must be below 0.4. If the void fraction PDF plot does not show values below 0.52, then a complete bridging must not have occurred, and annular flow thus exists. One can then conclude that a transitional flow, containing many bridging events, could only occur when the tail of the PDF plot extends below 0.45, and that annular flow would occur when the lowest α value on a PDF plot remains above 0.50.

Since the void fraction sensor measures a volumetric void fraction over a tube length of 2 D, it is possible that disturbances shorter than 2 D will not be properly represented in the PDF. To check this possibility, two things were done. First, the film was reviewed to determine the typical length of a disturbance in the transitional and annular flow regimes. It was found that the majority of the disturbances were typically about 2 D in length. This can be clearly seen from the video images in Figures 5.9 and 5.10. The

second way of checking if short slugs were being missed by the void fraction sensor, was to examine PDF plots of the film thickness measurement. Since the film thickness was a local measurement, it would pick up even the shortest slug or bridging event.

Figures 5.11 and 5.12 are the film thickness PDF plots corresponding to the flow settings shown in Figures 5.9 and 5.10, respectively. It is clear that none of these PDF plots show a tail that extends all the way to 4.76 mm, which is half the tube diameter; thus indicating a complete liquid bridging. The probes are, however, sensitive to bubbles that are trapped in the liquid film, and thus will indicate a thinner film thickness than what is actually there (if bubbles are present in the film). Therefore, some compensation for the void fraction in the disturbance waves must be made. This compensation is as follows:

$$\delta_{meas.} = \delta_{actual}(1-\alpha), \tag{5.1}$$

where δ_{actual} is the actual film thickness including bubbles, $\delta_{meas.}$ is the measured film thickness, and α is the void fraction between the probes.

If we make the assumption that a disturbance covering half the tube diameter (δ_{actual} = 4.76 mm) has the maximum void fraction for small closely packed bubbles (α = 0.52, Dukler *et al.*, 1988), then Equation (5.1) would give the measured film thickness to be 2.28 mm. This assumption gives the minimum value the film thickness probes can read for bridging not to occur. Disturbances with a void fraction less than 0.52 will have a film thickness between 2.28 mm and 4.76 mm, and may or may not bridge the tube, depending on the void fraction. However, if the film thickness is less than 2.28 mm, then the bridging can not be complete, even if the wave contains many bubbles. As a further clarification, Figure 5.13 depicts the passage of several waves with various combinations of void fraction and film thickness.

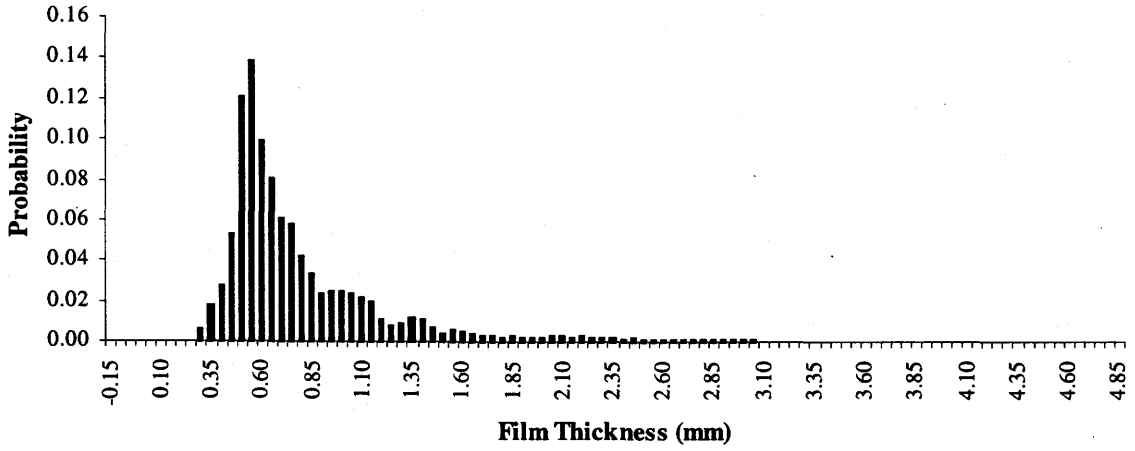

(a) V_{SL} = 0.06 m/s, V_{SG} = 4.97 m/s

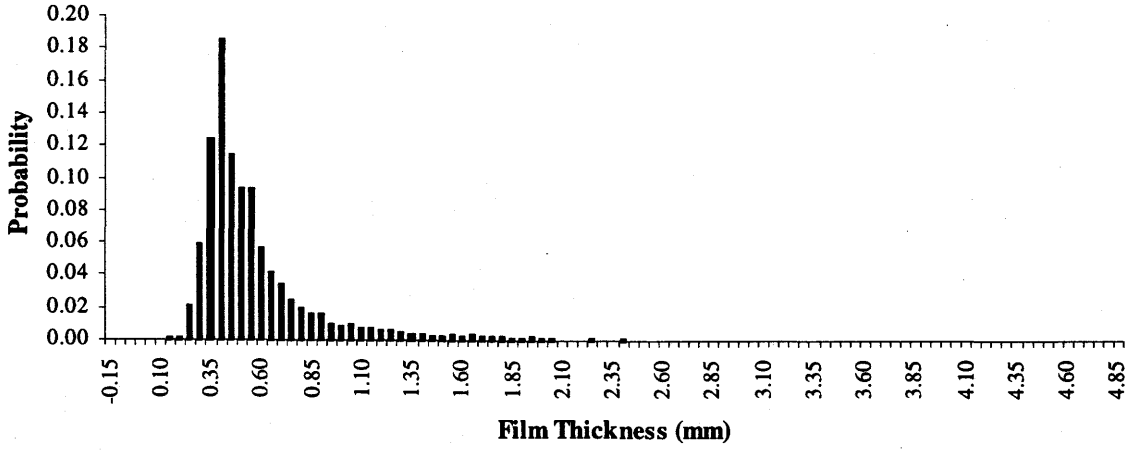

(b) V_{SL} = 0.06 m/s, V_{SG} = 6.92 m/s

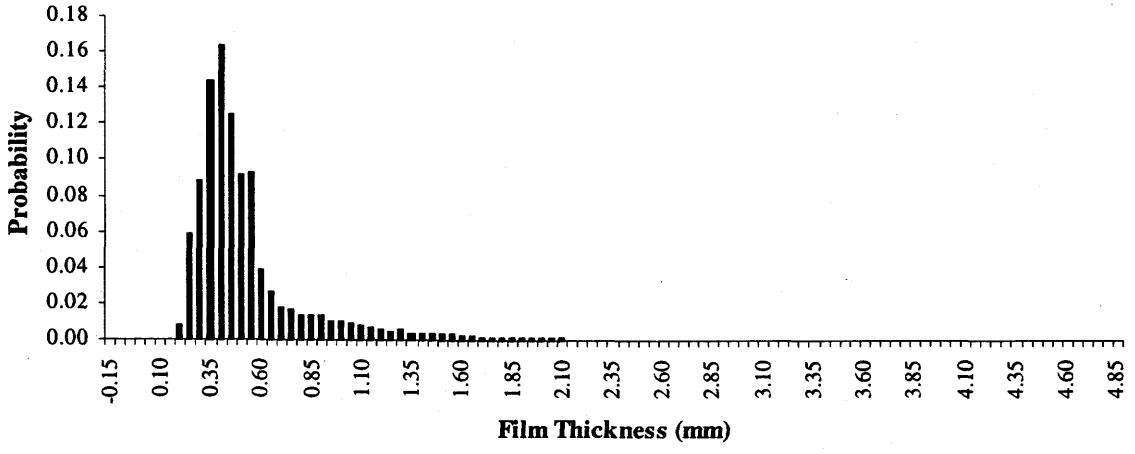

(c) V_{SL} = 0.06 m/s, V_{SG} = 8.92 m/s

Figure 5.11 - Distorted slug-to-annular transition film thickness PDF plots; (a) 96F2P50 – Distorted Slug, (b) 96F2P51 – Distorted Slug/Annular, and (c) 96F2P52 – Annular.

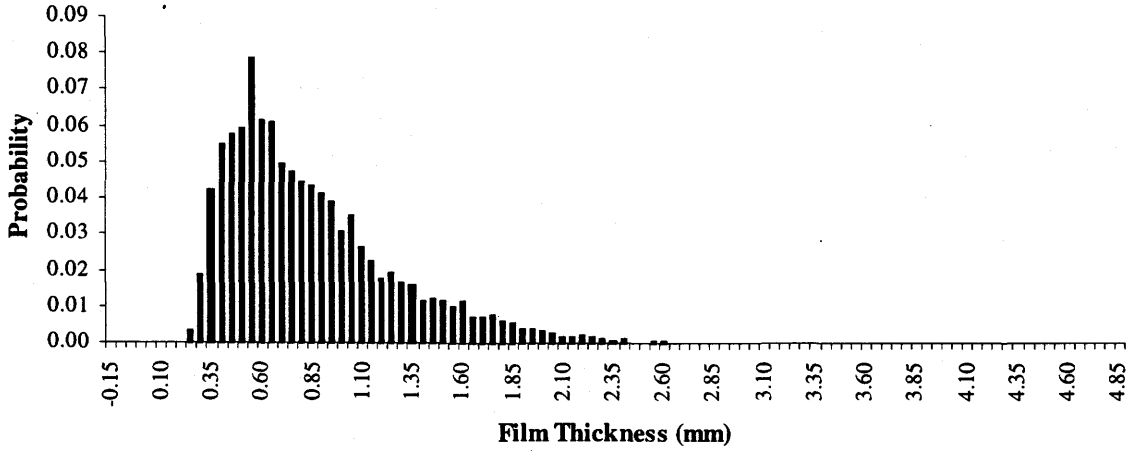

(a) V_{SL} = 0.32 m/s, V_{SG} = 9.91 m/s

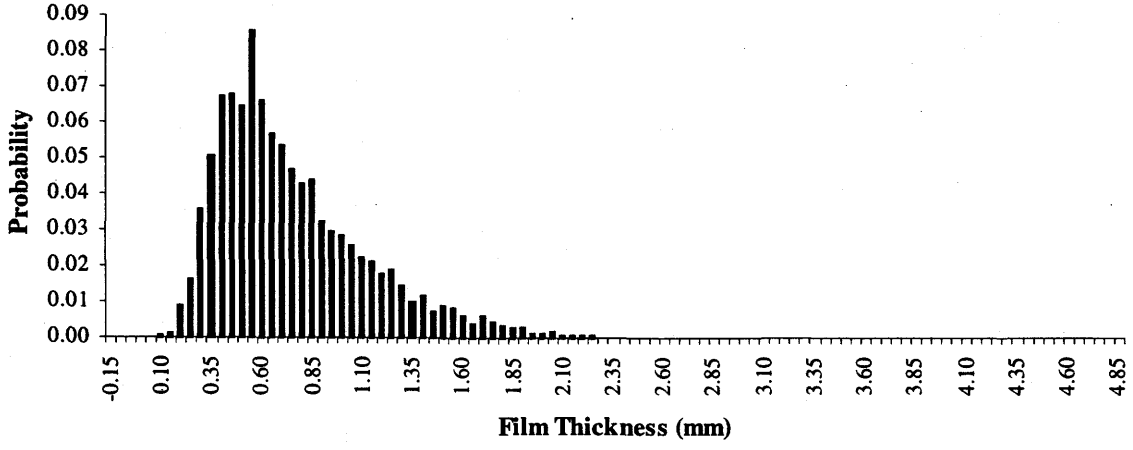

(b) V_{SL} = 0.31 m/s, V_{SG} = 11.92 m/s

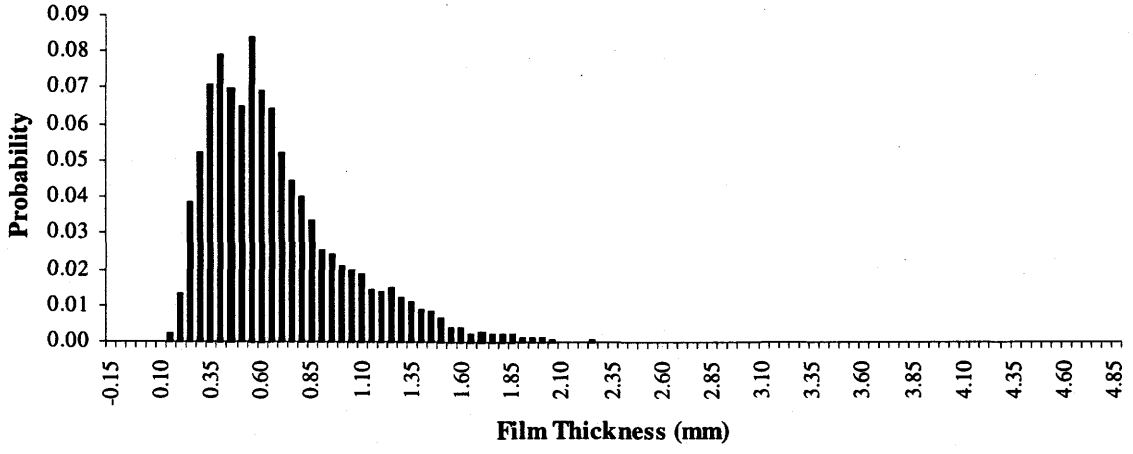

(c) V_{SL} = 0.31 m/s, V_{SG} = 13.91 m/s

Figure 5.12 - Frothy slug-annular-to-annular transition film thickness PDF plots; (a) 96F2P26 – Frothy Slug-Annular, (b) 96F2P27 – Frothy Slug-Annular/Annular, and (c) 96F2P28 – Annular.

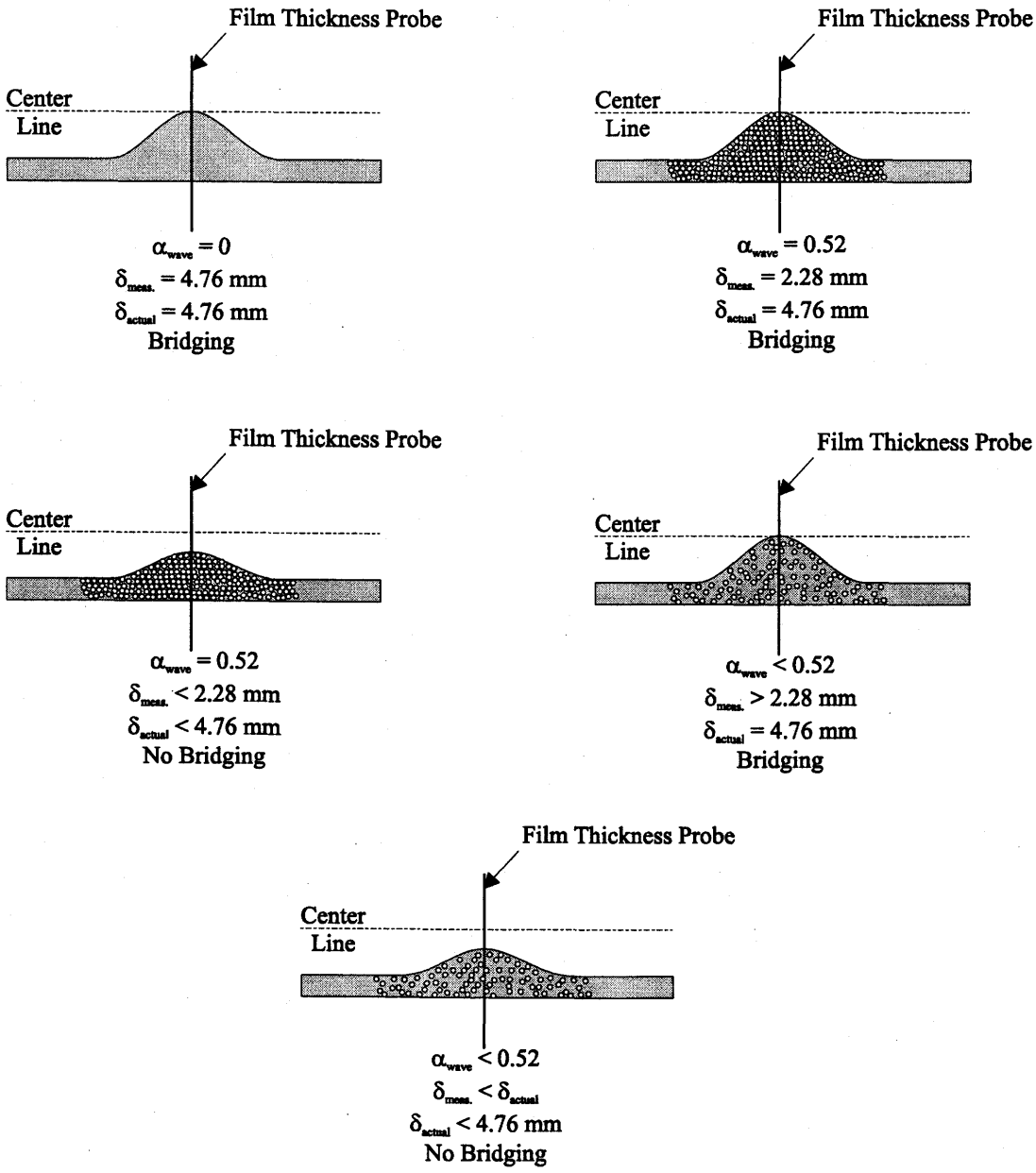

Figure 5.13 - Illustration of the effects of the presence of bubbles in the liquid film on film thickness measurements.

If we now re-examine Figures 5.11 and 5.12 again, and consider a film thickness of 2.28 mm as a bridging event, we can see that the transitional flows of Figure 5.11(a) and Figure 5.12(a) both have a tail that extends well past 2.28 mm. This indicates that if the disturbances are frothy and contain packed small bubbles (as the video images show, especially at high liquid flow rates), bridging occurs. The transitional flows of Figure

5.11(b) and Figure 5.12(b) show a tail that extends to a film thickness at or slightly past 2.28 mm, indicating that the events are bridging if the disturbances are very frothy. When the annular flows of Figure 5.11(c) and Figure 5.12(c) are examined, we see that the tail of the PDF remains below 2.28 mm, indicating that bridging is not complete, even if the disturbances are at the maximum void fraction of 0.52.

Thus, it has been verified that transitional flow exists when the tail of the void fraction PDF extends below a void fraction of 0.45. Annular flow will exist when the void fraction PDF is completely contained at void fractions above 0.50. The transition between these two flow regimes happens when the tail of the void fraction PDF extends into the 0.45 to 0.50 range of void fraction.

5.3 Flow Identification Summary

In summary, the four flow regimes can be identified from the void fraction PDF plots with the following criteria:

Bubbly Flow – A single peak in the void fraction PDF at a low void fraction, typically less than 0.20.

Slug Flow – A double peaked PDF with one peak at a high void fraction and one at a low void fraction. Some slug flows at low liquid velocities may show two peaks very close together.

Transitional Flow – A single peak in the PDF at a high void fraction, with a tail extending down to void fractions less than 0.45.

Annular Flow – A single sharp peak in the PDF at a high void fraction, typically between 0.80 to 0.90, with a short tail extending to void fractions no less than 0.50.

The transitions between the flow regimes are characterized by the following criteria:

Bubbly-to-Slug – Characterized by the onset of a second peak in the bubbly flow PDF, but two distinct peaks can not be clearly identified.

Slug-to-Transitional – Characterized by the near disappearance of the lower peak in the slug flow PDF.

Transitional-to-Annular – Characterized by the tail of the single peak in the PDF ending at a void fraction between 0.45 and 0.50.

With these criteria, the main flow regimes and the transitions between them can be easily, and for the most part, objectively identified from the void fraction PDF alone without the aid of flow images.

6. FLOW REGIME TRANSITION MODELS

Over the past ten years several efforts have been made to determine an accurate transition model for the bubbly-to-slug, and the slug-to-annular transitions. This study not only provides void fraction measurements (a parameter often used in the transition models), it also gives a more objective method of flow regime identification than what is possible using video images. Thus, an accurate evaluation of the transition models in the literature is possible.

Three predominant transition models exist in the literature for microgravity two-phase flow. A model which attempts to predict the bubbly-to-slug transition is known as the drift-flux model, and was originally derived by Zuber and Findlay (1965) for normal gravity vertical two-phase flow. Zhao and Rezkallah (1993) used a Weber number based model to predict the transition from slug to transitional flow and from transitional to annular flow. Bousman (1995) proposed a void matching technique to predict the transition from slug to annular flow (transitional flow was not considered a flow regime in that study).

The methodology or theory behind each of the above mentioned models, followed by an evaluation using the present data set, is presented in this chapter.

6.1 Drift-Flux Model

6.1.1 Methodology

As previously mentioned, the drift-flux model was originally developed by Zuber and Findlay (1965) for normal gravity, vertical upward flows. This model takes into account the non-uniform velocity and void fraction distributions across the tube, as well as the drift velocity between the two phases.

One important aspect of the drift-flux model, is that it was derived in terms of cross-sectional average values of the liquid and gas velocities, and the void fraction. Since these parameters are most often measured as cross-sectional averages, which is the case in this study, it is important that these parameters are used directly in the model. The cross-section average value of a parameter F is defined as:

$$\langle F \rangle = \frac{1}{A}\int_A F dA, \tag{6.1}$$

where A is the cross-sectional area of the tube.

The superficial velocities are then essentially measured average quantities, and the following relations apply:

$$V_{SG} = \langle V_G \rangle \langle \alpha \rangle, \text{ and} \tag{6.2}$$

$$V_{SL} = \langle V_L \rangle (1 - \langle \alpha \rangle), \tag{6.3}$$

where V_G and V_L are the actual gas and liquid velocities, respectively. Two other important parameters in the drift-flux model are the average total volumetric flux $\langle j \rangle$; defined as:

$$\langle j \rangle = V_{SG} + V_{SL}, \tag{6.4}$$

and the gas drift velocity V_{Gj}; is defined as:

$$V_{Gj} = V_G - j. \tag{6.5}$$

The j without the brackets indicates the local total volumetric flux.

From Equations (6.2) through (6.5), Zuber and Findlay (1965) developed the following equation for the gas velocity V_G:

$$V_G = C_0 \langle j \rangle + \frac{\langle \alpha V_{Gj} \rangle}{\langle \alpha \rangle \langle j \rangle}, \tag{6.6}$$

where C_0 is the distribution coefficient defined as:

$$C_0 = \frac{\langle \alpha j \rangle}{\langle \alpha \rangle \langle j \rangle}. \tag{6.7}$$

The distribution coefficient accounts for the non-uniform distribution of void fraction and velocity across the tube cross-section. A C_0 greater than 1 indicates a void and velocity profile which is maximum at the center and minimum near the tube walls, while a C_0 less than one indicates velocity and void profiles which are "saddle" type with a maximum near the walls. A C_0 of unity indicates a uniform void and velocity profile.

The second term on the right hand side of Equation (6.6) accounts for the local relative velocity. Equation (6.6) was developed with no assumptions on the type of flow regime, and is therefore valid over all the flow regimes.

For bubbly and slug flow under microgravity conditions, the drift term of Equation (6.6) is very small, since the drift velocity V_{Gj} is generally much smaller than the total volumetric flux j. Thus, Equation (6.6) can be written as:

$$V_G = \frac{V_{SG}}{\langle \alpha \rangle} = C_0 \langle j \rangle \tag{6.8}$$

for microgravity bubbly and slug flows.

Equation (6.8) suggests that if C_0 is known, then α can be predicted, and vice versa. Several researchers have used void fraction data to determine C_0 and have reported a range of values typically between 1.2 and 1.3. Such an analysis will also be performed with the current data set in the following section.

Bousman *et al.* (1996) describe a method of using the drift flux model to determine a bubbly-to-slug flow regime transition model. Combining Equations (6.4), (6.8), and (6.3), and solving for V_{SL} results in an expression relating V_{SL} and V_{SG} such that:

$$V_{SL} = \frac{\left(1 - C_0 \langle \alpha \rangle\right)}{C_0 \langle \alpha \rangle} V_{SG} \,. \tag{6.9}$$

To determine the transition boundary, the value of C_0 is determined from the void fraction data and Equation (6.8), and a transition, or critical value of $\langle \alpha \rangle$ is then selected. Previous research has shown that the critical void fraction is dependant on tube diameter. Bousman *et al.* (1996) chose transition void fractions of 0.4 for a 12.7 mm

tube and 0.23 for a 25.4 mm tube. Colin and Fabre (1995) found critical void fractions of 0.45 for 6, 10, and 19 mm tubes and 0.2 for a 40 mm tube. The critical void fractions determined by Colin and Fabre (1995) were determined for use with a simpler model, obtained by setting $C_0 = 1$ in Equation (6.9). While undoubtedly the tube diameter has a significant effect on the transition, the results from previous studies lack consistency and repeatability.

The following section presents the results of applying the drift flux model to the present data set.

6.1.2 Results

Before the drift flux transition model can be used, a suitable value of C_0 must first be determined. Equation (6.8) suggests that the slope of a plot of $\frac{V_{SG}}{\langle\alpha\rangle}$ versus $\langle j \rangle$ will give C_0, as shown in Figure 6.1. In this case the data gives a C_0 of 1.28, with a coefficient of determination (R^2) of 0.9779. This compares well with the results of Elkow and Rezkallah (1997), who obtained a C_0 of 1.25 with a similar apparatus and the same tube diameter (the current data set was taken on the same apparatus, but several changes had been made to the pumping system and test section). This C_0 also compares quite well with Bousman (1995) who determined a C_0 of 1.27 for a 12.7 mm tube when it was calculated in a similar manner. Bousman *et al.* (1996) also report a C_0 of 1.21 for a 12.7 mm tube, when V_G was measured by cross-correlation between two wire probes. A similar C_0 of 1.20 was also reported by Colin and Fabre (1995) for 6, 10, 19, and 40 mm tubes. Thus, the C_0 determined here is at the upper end of the range of values reported by other researchers, but it is still in reasonably good agreement.

It should be pointed out that the line labeled homogeneous flow in Figure 6.1 represents a flow which has a uniform void and velocity profile, and a slip velocity (gas drift velocity V_{Gj}) of zero. Points which are above this line have a positive slip velocity,

while points below this line have a negative slip velocity. In microgravity bubbly and slug flows, one expects all of the points to lie on or above the homogeneous flow line, with the net difference between the liquid and gas velocities due only to the C_0 value greater than one. However, in Figure 6.1 there are a few bubbly flow points (indicated by open symbols) which fall below the homogeneous flow line, indicating a negative slip.

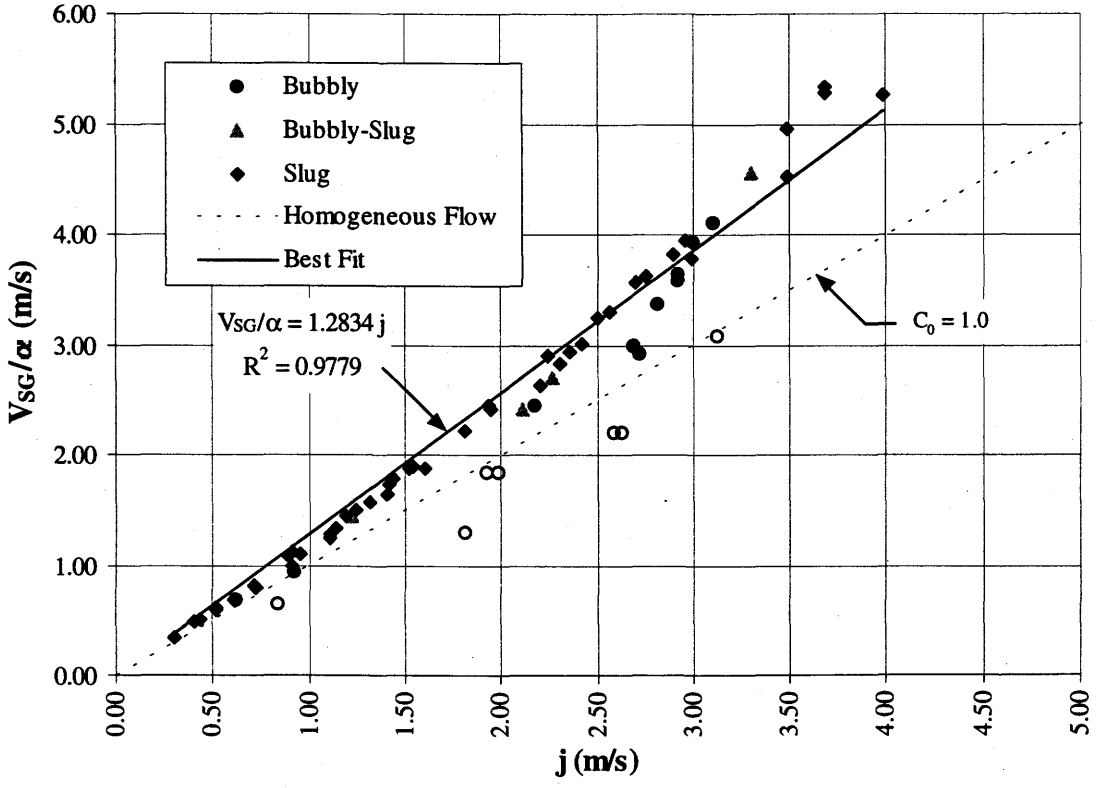

Figure 6.1 - Gas velocity as a function of total volumetric flux to determine C_0.

One possible explanation for these points to be below the homogeneous flow line is that the gas bubbles had not yet reached their terminal velocity (i.e., the velocity of the surrounding liquid) when the void fraction measurement was taken. For this reason, these points were not included in the calculation of C_0. If these points are included, the value of C_0 drops slightly to 1.24, which is still in good agreement with the values reported in the literature. In order to test this entry length hypothesis, a single bubble injected into an infinite flowing stream is investigated in Section 6.1.3.

The next step in the flow regime transition model is to select a transition void fraction for use with Equation (6.9). Bousman (1995) chose the midpoint of the bubbly-slug transition void fractions as the transition void fraction. The four bubbly-slug transition flows identified in this study have void fractions of 0.184, 0.174, 0.164, and 0.174. Thus, the midpoint of the transition would be 0.174.

Figure 6.2 is the flow pattern map for the transition from bubbly to slug flow. The solid line in Figure 6.2 is the transition line predicted by Equation (6.9) using a C_0 of 1.28 and a transition void fraction of 0.174. This line separates the bubbly and slug flows reasonably well, with only one bubbly flow point in the slug region. Also plotted in Figure 6.2 is the transition line determined by Bousman (1995) for a 12.7 mm tube, and the one determined by using the transition void fraction determined by Colin and Fabre (1995) for 6, 10, and 19 mm tubes with the drift flux model. Clearly there is a great deal of discrepancy between these lines. The new data shows a transition region which agrees better with the transition void fraction of 0.23 determined by Bousman (1995) for a 25.4 mm tube, and the transition void fraction of 0.20 found by Colin *et al.* (1991) for a 40 mm tube. The transition line also compares very well with the transition identified by Elkow (1995) who determined the transition void fraction to be 0.20 with a similar apparatus and the same mixer as the present study. Zhao and Rezkallah (1993) also report a transition void fraction of 0.18 for a 9.525 mm tube.

There are a few possible reasons for the discrepancy between this data and that reported by Bousman (1995) and Colin and Fabre (1995) for similar size tubes. One possibility is that differences in the mixer designs could result in different bubble sizes at the same flow rates. The fact that transition void fractions of Elkow (1995) and Zhao and Rezkallah (1993) compare so well with the present data, all of which used the same mixer, suggests that the mixer or initial bubble size may play an important role in determining where the transition takes place.

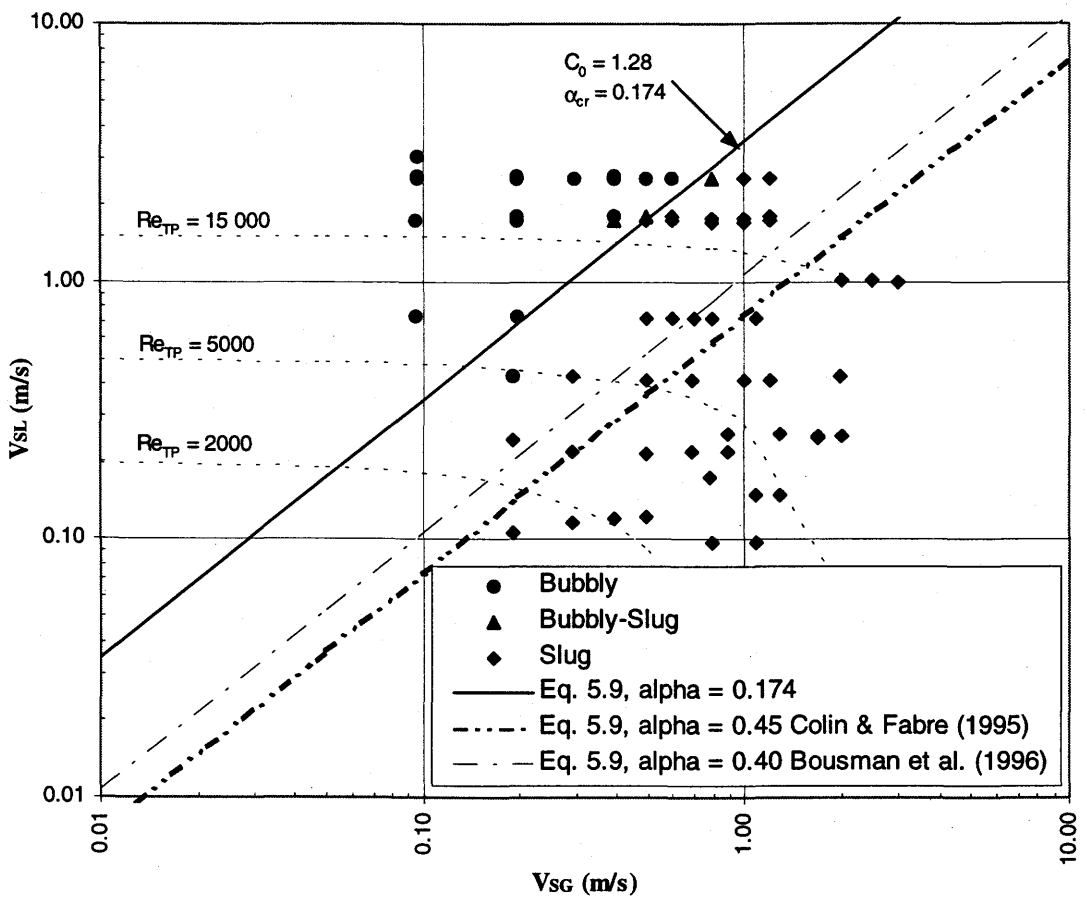

Figure 6.2 - Bubbly-to-slug transition flow pattern map.

Another possibility for the differences in transition void fraction is that different research groups may have slightly different criteria for identifying the transition to slug flow, resulting in a shift in the transition line. A more objective method of flow regime identification, such as the one described in Chapter 5 would serve to make transition identifications more comparable.

A third possible reason for the discrepancies are the different flow rates at which the data were taken. The transition data for this study and that of Elkow (1995) and Zhao and Rezkallah (1993) were taken at much higher liquid flow rates than Bousman (1995) and Colin and Fabre (1995). Bousman (1995) restricted his 12.7 mm tube study to liquid superficial velocities less than 1.0 m/s, while the 6, 10, and 19 mm tube study of Colin and Fabre (1995) extended only to V_{SL} equal to about 1.5 m/s. The current data

and that of Elkow (1995) and Zhao and Rezkallah (1993) extend to V_{SL} = 2.5 m/s (Zhao and Rezkallah, 1993, include V_{SL} greater than 3.0 m/s), with the majority of the bubbly flow data occurring at V_{SL} greater than 1.5 m/s.

The significance of the difference in V_{SL} settings is that at higher liquid velocities, the turbulence in the flow increases, causing the bubbles to deform and giving them a larger effective diameter. Thus, smaller bubbles are more likely to collide and coalesce to form larger bubbles and therefore the transition takes place at a lower void fraction. To illustrate this, the loci of the two-phase Reynolds number Re_{TP} equal to 2000, 5000, and 15000 was plotted in Figure 6.2. The two-phase Reynolds number is calculated, as suggested by Bousman (1995) as:

$$Re_{TP} = \frac{D\rho_M j}{\mu_L}, \tag{6.10}$$

where μ_L is the liquid viscosity and ρ_M is the mixture density defined as:

$$\rho_M = \langle\alpha\rangle\rho_G + (1-\langle\alpha\rangle)\rho_L. \tag{6.11}$$

In Equation (6.11), ρ_L is the liquid density, ρ_G is the gas density, and $<\alpha>$ is calculated from Equation (6.8). The Re_{TP} lines plotted in Figure 6.2 experience a sharp curve as V_{SG} is increased because the mixture density as calculated by Equation (6.11) becomes less valid as the flow transitions into slug flow.

Bousman (1995) suggests that Re_{TP} greater than 2000 is a turbulent flow. Figure 6.2 clearly shows that all of the bubbly and transitional points are in the fully turbulent flow area with the majority above Re_{TP} = 15 000. The bubbly flow images from Bousman (1995) also seem to show small closely packed spherical bubbles, while the flow images for the present set show larger and more deformed bubbles, except at the lowest V_{SL}

settings. Thus, it is possible that the increased turbulence at the high V_{SL} settings promote a transition to slug flow at a lower void fraction.

6.1.3 Entry Effects

To further explore why a few bubbly flow points fall below the homogeneous flow line in Figure 6.1, a single bubble injected into a flowing stream is briefly studied. In microgravity, where buoyancy effects are negligible, a bubble is accelerated by the fluid until it reaches the velocity of the fluid. The only force accelerating the bubble is the drag on the bubble created by the fluid flowing around the bubble.

To determine the distance required to accelerate the bubble to the velocity of the fluid, we start by performing the following force balance:

$$D = ma = m\frac{dV_b}{dt}, \tag{6.12}$$

where D is the drag on the bubble, m is the mass of the bubble, a is the acceleration of the bubble, V_b is the velocity of the bubble, and t is time. The true mass of the bubble is used rather than the virtual mass because the bubble is not pushing through the liquid, but is instead being pushed by the liquid.

We can also write:

$$\frac{dV_b}{dt} = \frac{dx}{dt}\cdot\frac{dV_b}{dx} = V_b\frac{dV_b}{dx}, \tag{6.13}$$

where x is the position of the bubble. The mass of the bubble is given by:

$$m = \rho_g \frac{4}{3}\pi r^3, \tag{6.14}$$

where ρ_g is the density of the gas in the bubble and r is the radius of the bubble.

The drag on the bubble is a function of the velocity difference between the bubble and the fluid V_{lb} and the bubble diameter d_b, and is given by:

$$D = \frac{1}{2} C_D \rho_l \frac{\pi}{4} d_b^2 V_{lb}^2. \tag{6.15}$$

In Equation (6.15), ρ_l is the fluid density and C_D is the drag coefficient for a bubble. Clift *et al.* (1978) suggest that $C_D = 16/Re_D$ for Re_D (Reynolds number based on the bubble diameter) less than about 2 and that C_D is generally slightly less than that of solid spheres for Re_D greater than 2. The C_D for a solid sphere is about 0.5 for Re_D greater than about 100. To cover the transition region ($2 < Re_D < 100$), the drag coefficient of the bubble is approximated as $16/Re_D$ for Re_D less than 40, and as 0.5 for Re_D greater than 40, as shown in Figure 6.3. The Reynolds number based on the bubble diameter is calculated as:

$$Re_D = \frac{\rho_l V_{lb} d_b}{\mu_l}, \tag{6.16}$$

where μ_l is the liquid viscosity.

Substituting Equations (6.13), (6.14) and (6.15) into Equation (6.12) and simplifying gives an expression for the bubble velocity as a function of position:

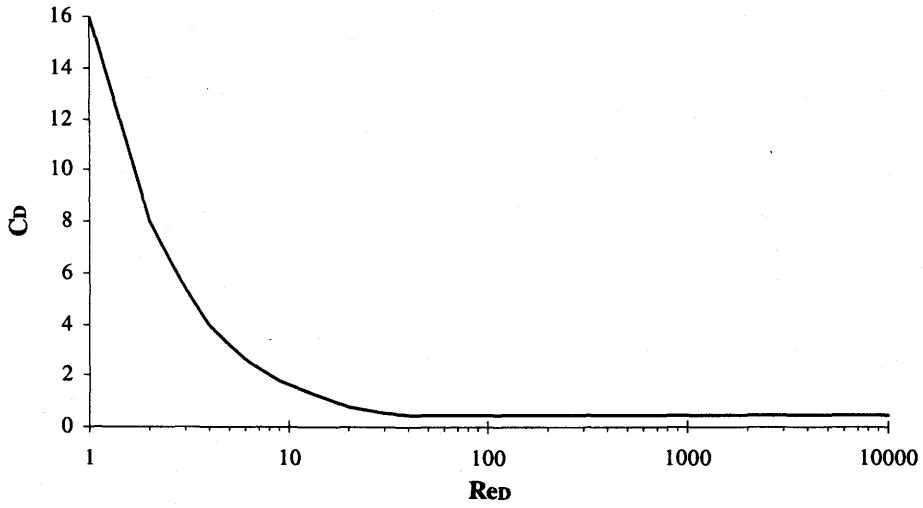

Figure 6.3 - Estimated drag coefficient for bubbles as a function of Reynolds number.

$$\frac{V_b}{V_{lb}^2}\frac{dV_b}{dx} = \frac{3}{4d_b}\frac{\rho_l}{\rho_g}C_D. \qquad (6.16)$$

A finite difference method was then used to calculate V_b as a function of position for various bubble sizes and fluid velocities. It was found that for bubble sizes less than 10 mm, the velocity development was not affected by bubble size. However, the velocity of the fluid had a significant effect on the velocity development. The velocity development profiles for a 5 mm air bubble in water flowing at velocities of 0.75, 1.75, and 2.5 m/s are shown in Figure 6.4. The points that fall below the homogeneous flow line in Figure 6.1 correspond to small bubbles in liquid flow rates of V_{SL} = 0.73, 1.75, 2.50, and 3.03 m/s (the points with the lowest j correspond to the lowest V_{SL} setting and increase with V_{SL}).

Figure 6.4 shows that at each liquid flow rate there is still at least some small difference between the liquid and gas velocities at the void fraction sensor location, indicating some negative slip velocity. Thus, it is possible that the bubble velocity is not fully developed at the void fraction sensor, resulting in the measured negative slip velocity for a few of the bubbly flows. As the bubbles become larger and approach the tube

diameter, this model becomes invalid due to wall effects. The larger bubble sizes and the small liquid path around them create more drag and the bubbles approach the liquid velocity more quickly. It is likely for this reason that the other bubbly and slug flows appear to be fully developed.

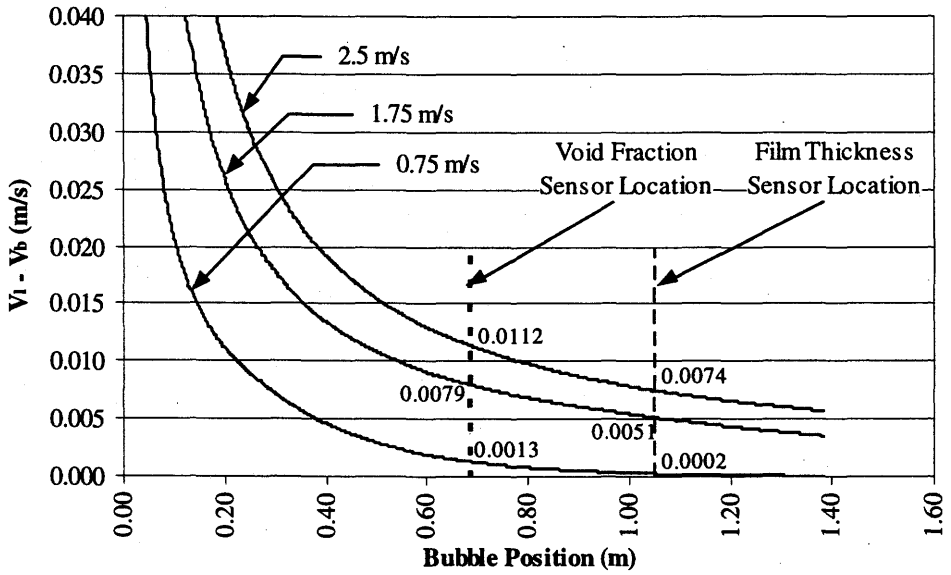

Figure 6.4 - Estimated bubble velocity development (numbers indicate velocity at indicated bubble position).

As a further verification of this entry length hypothesis, bubble velocities were also calculated by cross-correlating the readings from the two film thickness probes. The results of these calculation are also presented in Figure 6.5 (labeled Vg from FT probes). The error bars on these points are a result of the discretization error in the time delay for the 1024 Hz sampling rate. Figure 6.5 shows that none of the velocities calculated from the film thickness probe fall below the homogeneous flow line, indicating that the bubble velocities must be more fully developed at the location of the film thickness sensor (approximately 110 D downstream of the mixer). Figure 6.4 supports this statement, as in each case the difference between the bubble and fluid velocity has been somewhat reduced when the bubble reaches the film thickness probes.

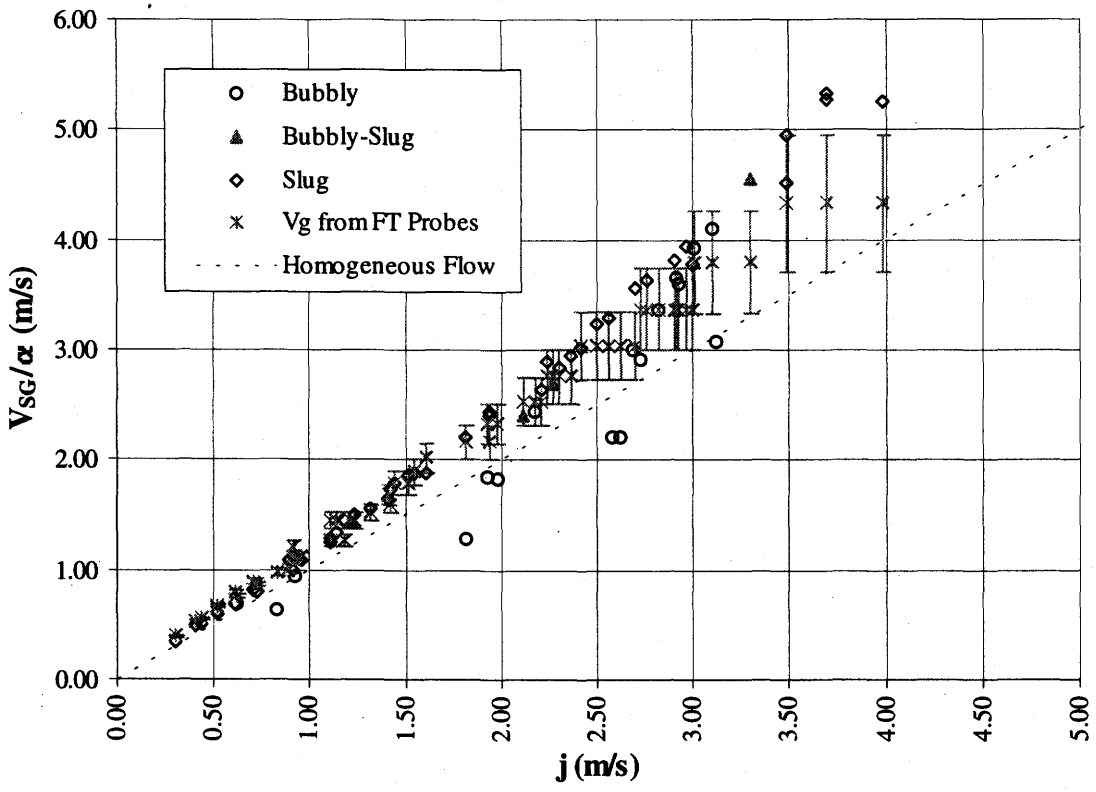

Figure 6.5 - Gas velocity calculated from void fraction and film thickness sensors.

6.2 Weber Number Transition Model

6.2.1 Methodology

The Weber number transition model was suggested by Zhao and Rezkallah (1993) to provide a flow regime map which nicely separated the annular, transitional, and slug flows. Zhao and Rezkallah (1993) argued that the dominant forces in microgravity two-phase flows are inertia and surface tension. The Weber number, defined as:

$$We = \frac{V^2 D\rho}{\sigma} = \frac{\text{inertial force}}{\text{surface tension}}, \tag{6.17}$$

represents the ratio between the two dominant forces. Thus, the logical coordinates for a microgravity flow regime map are the liquid and gas Weber numbers. Since the Weber

number includes the phase velocity term, and in the absence of actual phase velocity measurements, the liquid and gas Weber number are calculated in terms of the superficial velocities, as follows:

$$We_{SL} = \frac{V_{SL}^2 D\rho_L}{\sigma_L} \tag{6.18}$$

and

$$We_{SG} = \frac{V_{SG}^2 D\rho_G}{\sigma_L}. \tag{6.19}$$

In Equations (6.18) and (6.19), σ_L is the liquid-air surface tension.

Zhao and Rezkallah (1993) suggest that bubbly and slug flows are surface tension dominated flows, and will thus occur at low We_{SG}. Annular flow is inertia dominated so it will occur at large values of We_{SG}. In transitional flow, inertia and surface tension forces are comparable, and hence it occupies the region between annular and slug flow. Zhao and Rezkallah (1993) suggested that the transitional flow regime begins at a value of We_{SG} equal to about 1, and the onset to annular flow occurs at a We_{SG} equal to approximately 20. Later studies by Rezkallah and Zhao (1995) and Rezkallah (1996) revised this map and gave each transition line an upwards slope of approximately 1:4. The results of the present study are discussed next.

6.2.2 Results

The Weber number based flow pattern map for the data collected in this study is presented in Figure 6.6. Also shown in Figure 6.6 are the transition lines proposed by Rezkallah (1996). The line separating slug and transitional flow fits the new data very well, while the line separating transitional and annular flow seems to over-predict the

transition. This line, however has what appears to be the correct slope. This over-prediction is likely due to the difficult and highly subjective video flow regime identification method used to determine the flow regimes upon which the transition line was based. It is the author's experience that determining whether a flow is fully annular or transitional using only video observation is a very difficult task. This study presents a mainly objective method of determining flow regimes, and hence less reliance on the subjectivity of 2-D video observations.

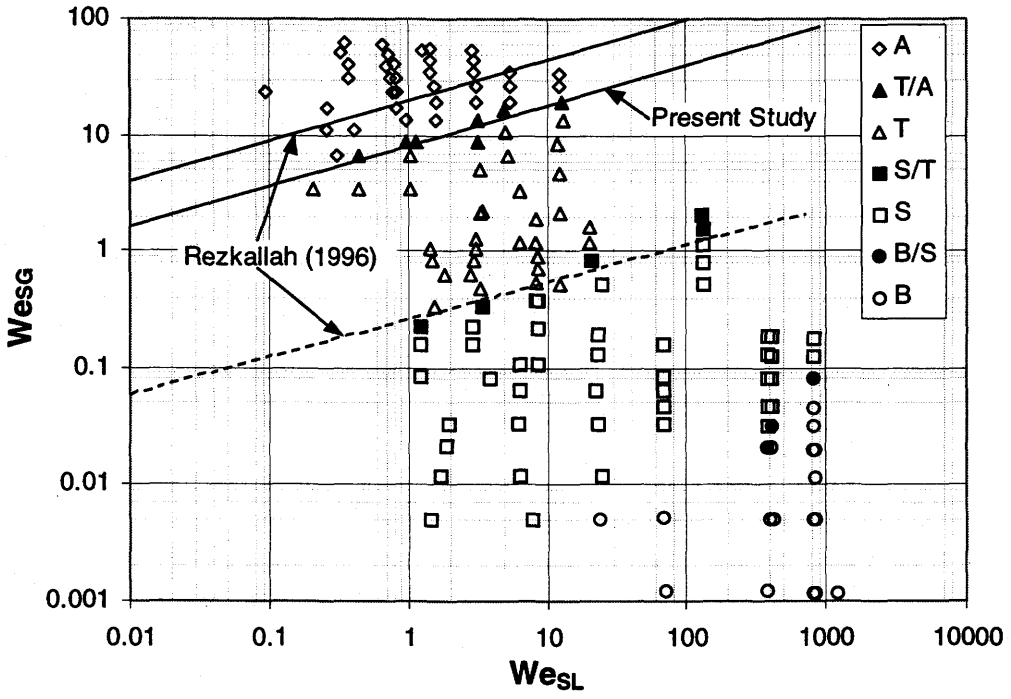

Figure 6.6 - Weber number based flow pattern map; A = Annular Flow, T/A = Transitional/Annular Flow, T = Transitional Flow, S/T = Slug/Transitional Flow, S = Slug Flow, B/S = Bubbly/Slug Flow, B = Bubbly Flow.

6.3 Void Matching Slug-to-Annular Transition Model

6.3.1 Methodology

Bousman (1995) suggested a slug-to-annular flow transition model which was based on a void fraction model for annular flow developed from a force balance. The transition

was then defined as the point at which the void fraction for slug flow, determined from Equation (6.8), equaled the void fraction predicted from the annular flow model.

To derive the annular flow void fraction model, Bousman (1995) started with a force balance across the tube and on the liquid film; to get:

$$\tau_i = \tau_w \alpha^{1/2}, \tag{6.20}$$

where τ_i is the interfacial shear stress and τ_w is the shear stress at the tube wall. Expressing the shear stresses in terms of the interfacial and wall friction factors, f_i and f_w then gives:

$$\tau_i = \frac{f_i \rho_G \langle V_G \rangle^2}{2} = \frac{f_i \rho_G \langle V_{SG} \rangle^2}{2\langle \alpha \rangle^2}, \tag{6.21}$$

and

$$\tau_i = \frac{f_w \rho_L \langle V_L \rangle^2}{2} = \frac{f_w \rho_L \langle V_{SL} \rangle^2}{2(1-\langle \alpha \rangle)^2}. \tag{6.22}$$

Substitution of Equations (6.21) and (6.22) into Equation (6.20) yields:

$$\frac{\langle \alpha \rangle^{5/2}}{(1-\langle \alpha \rangle)^2} = \frac{f_i}{f_w} \frac{\rho_G}{\rho_L} \left[\frac{V_{SG}}{V_{SL}} \right]^2. \tag{6.23}$$

Bousman (1995) then assumes that the interfacial friction factor can be expressed as the single phase gas friction factor f_G multiplied by an enhancement factor, which is a function only of void fraction. Thus, the interfacial friction factor is expressed as:

$$f_i = \phi(\langle\alpha\rangle) f_G, \tag{6.24}$$

where $\phi(<\alpha>)$ is the enhancement function. The gas friction factor is calculated for gas flowing alone in a tube of diameter $D - 2\bar{h}$, where $\bar{h}$ is the average film thickness.

The friction factors are then determined from the Blasius relation, given by:

$$f = \frac{C}{Re^n}, \tag{6.25}$$

where C = 0.046, n = 0.2 for turbulent flow and C = 16, n = 1 for laminar flow. Bousman (1995) evaluates Equation (6.25) with the following Reynolds numbers:

$$Re_G = \frac{DV_{SG}\rho_G}{\mu_G \langle\alpha\rangle^{1/2}} \tag{6.26}$$

and

$$Re_L = \frac{DV_{SL}\rho_L}{\mu_L}. \tag{6.27}$$

Substitution, with the appropriate Blasius constants, of Equations (6.26), (6.27), and (6.24) into Equation (6.23) leads to two void fraction models for annular flow, one for turbulent gas and turbulent liquid, and one for turbulent gas and laminar liquid. These relations are:

turbulent-turbulent, $$V_{SL} = V_{SG}\left[\frac{(1-\langle\alpha\rangle)^2 \phi(\langle\alpha\rangle)}{\langle\alpha\rangle^{2.4} B}\right]^{1/1.8} \tag{6.28}$$

and

$$\text{turbulent-laminar,} \quad V_{SL} = \frac{0.00288 D^{0.8} \nu_G^{0.2} \rho_G V_{SG}^{1.8} \phi(\langle\alpha\rangle)(1-\langle\alpha\rangle)^2}{\mu_L \langle\alpha\rangle^{2.4}}, \tag{6.29}$$

$$\text{where} \quad B = \left[\frac{\nu_L}{\nu_G}\right]^{0.2}\left[\frac{\rho_L}{\rho_G}\right]. \tag{6.30}$$

In Equations (6.29) and (6.30) ν_L and ν_G are the kinematic viscosity of the liquid and gas, respectively. Bousman (1995) used the Wallis relation to determine the single phase enhancement function:

$$\phi(\langle\alpha\rangle) = 1 + 150(1-\alpha^{1/2}). \tag{6.31}$$

The transition between slug and annular flow is where the void fraction predicted from Equation (6.28) or (6.29) (depending on whether the liquid is laminar or turbulent) is equal to that predicted by the Drift-Flux relation for slug flow, Equation (6.8). Thus, the transition line for turbulent gas, laminar liquid, is found by equating Equation (6.8) to Equation (6.28), and upon rearrangement we get:

$$\langle\alpha\rangle = \frac{1}{C_0} - \langle\alpha\rangle\left[\frac{\left(1-\langle\alpha\rangle^2 \phi(\langle\alpha\rangle)\right)}{\langle\alpha\rangle^{2.4} B}\right]^{5/9}. \tag{6.32}$$

This equation predicts that the transition line will be a line of constant void fraction if C_0 is constant, and $\phi<\alpha>$ is a function of α only.

The turbulent gas, laminar liquid, transition line is found by equating Equation (6.8) to Equation (6.29), which upon rearrangement gives:

$$U_{GS}\left[\frac{1-C_0\langle\alpha\rangle}{C_0\langle\alpha\rangle}\right]=\frac{0.00288\,D^{0.8}\,\nu_G^{0.2}\,\rho_G\,U_{GS}^{1.8}\,\phi(\langle\alpha\rangle)(1-\langle\alpha\rangle)^2}{\mu_L\langle\alpha\rangle^{2.4}}. \qquad (6.33)$$

Note that Equation (6.33) is undefined at $<\alpha> = 1/C_0$, and that the transition line predicted by Equation (6.33) will cross that predicted by Equation (6.32) when the void fractions determined from each equation are equal. Thus, Equation (6.33) is valid only in the narrow range between the $1/C_0$ and the turbulent transition void fraction.

6.3.2 Results

To obtain the turbulent transition line for the current data set, Equation (6.32) was solved numerically to determine the transition void fraction, then Equation (6.8) was used to plot the loci of points at which that void fraction occurred on the flow map. The laminar transition line was then determined by varying $<\alpha>$ in Equation (6.33) from the turbulent solution to $1/C_0$ and then solving for V_{SG}. Equation (6.8) is then used to determine V_{SL} for each $<\alpha>$ and V_{SG} combination.

The transition line, calculated using the $C_0 = 1.28$, determined previously for this data set, is shown on the flow regime map of Figure 6.7. Also shown in Figure 6.7 is the transition line determined with $C_0 = 1.21$, as suggested by Bousman (1995). Clearly, both lines fall within the transitional flow region, mainly because transitional flow covers such a wide range of flow rates. Note that the value of C_0 has a significant effect on the location of the transition line. The $C_0 = 1.28$ line is closer to separating slug and transitional flow, while the $C_0 = 1.21$ line is closer to separating transitional flow from annular flow.

6.4 Summary

In this Chapter, three flow regime transition models were examined. The drift-flux model for the transition from bubbly to slug flow separated the two flow regimes quite

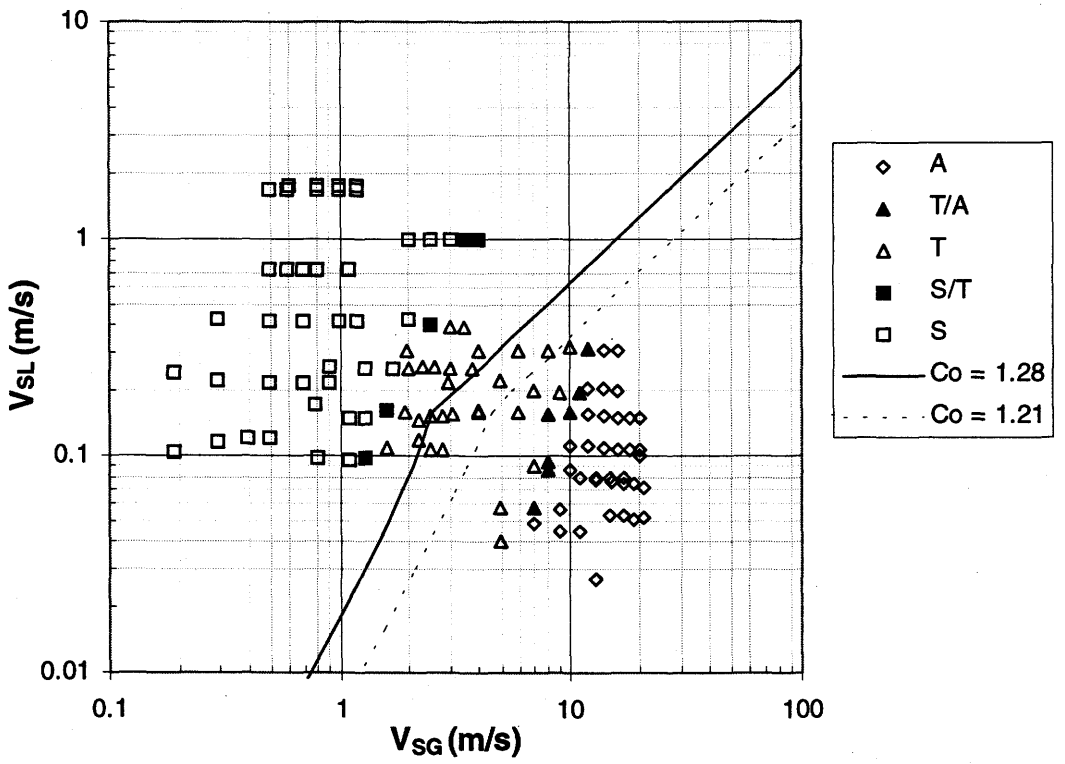

Figure 6.7 - Slug-to-annular transition flow pattern map; A = Annular Flow, T/A = Transitional/Annular Flow, T = Transitional Flow, S/T = Slug/Transitional Flow, S = Slug Flow.

well, but was dependant on the selected transition void fraction. The transition void fraction seems to be dependant on several variables, with the most apparent being the tube diameter and the method of mixing the two phases at the test section inlet. More work needs to be done to determine how these and other variables affect the transition.

The Weber number based flow regime map provided a simple, intuitive method of separating the slug, transitional, and annular flow regimes. The transition boundary previously determined by Rezkallah (1996) for slug-to-transitional flow separated the new data nicely. The transitional flow to annular flow boundary for the new data is at a slightly lower We_{SG} than determined by Rezkallah (1996), perhaps due to the refinement in the flow regime identification process.

The void matching slug-to-annular transition model proposed by Bousman (1995) resulted in a line that fell in the transitional flow regime. However, the usefulness of this model is in question, as it does not predict the boundaries of the transitional flow regime. It would seem that a designer would be much better served using the Weber number based flow pattern map, as it is quite successful in separating the slug, transitional, and annular flow regimes.

7. CONCLUSIONS AND RECOMMENDATIONS

7.1 Conclusions

This report covered the development and the use of a capacitance void fraction sensor. The design of the sensor was first presented in detail, followed by the calibration and testing of the sensor. The void fractions measured by the sensor on a recent microgravity flight campaign were then used in the form of probability density functions to determine a more objective method for identifying the main flow regimes and their transitions than what is possible using video images. Once the flow regimes were identified, the data was used to test three flow regime transition models. These models were the drift flux model, originally proposed by Zuber and Findlay (1965) and later modified by Bousman (1995) for microgravity bubbly-to-slug transition, the void matching transition model developed by Bousman (1995) for the slug-to-annular transition, and the Weber number based model developed by Zhao and Rezkallah (1993) for the transition from slug to transitional flow and transitional to annular flow.

The following is a summary of the main conclusions from this study:

1. A capacitance type void fraction sensor with a sensing length of 2 D was developed which could precisely and reliably measure void fraction. The calibration shows a coefficient of determination of 0.9983, a standard error of 0.011, and a precision error of 0.022 over the calibration range of $0.05 \leq \alpha \leq 0.88$.

2. The microgravity void fraction data was compared with that of Elkow (1995) and Bousman (1995) and was found to be in excellent agreement.

3. Using the probability density functions of the void fraction measurements a mainly objective method of flow regime identification was developed. With this method the flow regimes can be identified as follows:

   Bubbly Flow – A single peak in the void fraction PDF at a low void fraction, typically less than 0.20.

   Slug Flow – A double peaked PDF with one peak at a high void fraction and one at a low void fraction. Some slug flows at low liquid velocities may show two peaks very close together.

   Transitional Flow – A single peak in the PDF at a high void fraction, with a tail extending down to void fractions less than 0.45.

   Annular Flow – A single sharp peak in the PDF at a high void fraction, typically between 0.80 to 0.90, with a short tail extending to void fractions no less than 0.50.

   The following characteristics relate to flow transitions at microgravity:

   Bubbly-to-Slug – Characterized by the onset of a second peak in the bubbly flow PDF, typically at or near zero α, but two distinct peaks can not be clearly identified.

   Slug-to-Transitional – Characterized by the near disappearance of the lower peak in the slug flow PDF.

   Transitional-to-Annular – Characterized by the tail of the single peak in the PDF ending at a void fraction between 0.45 and 0.50.

4. The drift-flux model for the transition from bubbly to slug flow separated the two flow regimes quite well. The drawback of this model is that it is dependant on the

selected value for the transition void fraction. The transition void fraction seems to be dependant on several variables, with the most apparent being the tube diameter and the method of mixing the two phases at the test section inlet. A transition void fraction of 0.17 seemed to separate the present data set, and a distribution coefficient of $C_0 = 1.28$ was determined for this data set.

5. The Weber number based flow regime map provided a simple, intuitive method of separating the slug, transitional, and annular flow regimes. The line previously determined by Rezkallah (1996) for the slug-to-transitional flow boundary separated the new data well. The transitional-to-annular flow boundary for the new data is at a slightly lower We_{SG} than determined by Rezkallah (1996), perhaps due to the refinement in the flow regime identification process.

6. The void matching slug-to-annular transition model proposed by Bousman (1995) resulted in a single line in the transitional flow regime. However, since transitional flow in microgravity covers a wide range of gas and liquid velocities, the usefulness of this model is in question, as it does not predict the boundaries of the transitional flow regime. It would seem that a designer would be much better served using the Weber number based flow pattern map, as it is quite successful in separating the slug, transitional, and annular flow regimes.

7. Velocities measured with the void fraction sensor, when compared to the velocities determined from the cross-correlation of the film thickness gave an RMS percent difference of 19%. While this is an acceptable difference, due to the sensing length of the void fraction sensor, the method is limited to flows which contain well defined, well separated Taylor bubbles.

7.2 Recommendations for Future Work

This study has laid the ground work for the development an objective method of determining flow regimes in two-phase, gas-liquid microgravity flows. With this work as a background, the author recommends that the following work be undertaken:

1. While this study had sufficient data for each transition, additional data along each transition would serve to better define the flow regime transitions. Additional data spanning the entire flow map would also serve to substantiate the flow regime identification method presented in this study.

2. An important factor in two-phase flow is the tube diameter. The method of flow regime determination presented in this study should be tested on a variety of tube diameters, with void fraction sensors scaled appropriately. Once this method is proven for a variety of tube diameters, it could be implemented throughout the microgravity two-phase flow community. This would provide greater consistency in the location of flow regime boundaries found by different research groups than what can be achieved by video identifications.

3. Further work should be done to describe the PDF plots for each flow regime in terms of a set statistical parameters that are consistent across the whole flow regime. This would create a set of rules which were completely objective and would not rely at all on human judgement.

4. It was shown in this study that the location of the void fraction sensor may be too close to the mixer for some bubbly flows. To correct this potential problem, the sensor should be moved farther along the test section.

5. With the development of a completely objective method of flow regime determination, the next step would be to create and refine flow regime transition models which better delineate the data.

REFERENCES

Bendat, J.S. & Piersol, A.G., Engineering Applications of Correlation and Spectral Analysis (John Wiley & Sons, Inc., New York, 1980)

Bendat, J.S. & Piersol, A.G., Random Data: Analysis and Measurement Procedures (John Wiley & Sons, Inc., New York, 1971)

Bousman, Scott, Studies of Two-Phase Gas-Liquid Flow in Microgravity. NASA Contractor Report 19534, 1995

Bousman, W.S. & Dukler, A.E., "Ground Based Studies of Gas-Liquid Flows in Microgravity Using Learjet Trajectories," 32nd Aerospace Sciences Meeting & Exhibit, Reno, NV, AIAA, 1994

Bousman, W.S., McQuillen, J.B. & Witte, L.C., "Gas-Liquid Flow Patterns in Microgravity: Effects of Tube Diameter, Liquid Viscosity and Surface Tension," Int. J. of Multiphase Flow, Vol. 22, No. 6, 1996

Clift, R., Grace, J.R. & Weber, M.E., Bubbles, Drops, and Particles (Academic Press, New York, 1978)

Colin, C. & Fabre, J., "Bubble and Slug Flow at Microgravity Conditions: State of Knowledge and Open Questions," Chem. Eng. Comm., Vols 141-142, 1996

Colin, C. & Fabre, J., "Gas-Liquid Pipe Flow Under Microgravity Conditions: Influence of Tube Diameter on Flow Patterns and Pressure Drops," Adv. Space Res., Vol. 16, No. 7, 1995

Colin, C., Fabre, J., & Dukler, A.E., "Gas-Liquid Flow at Microgravity Conditions – I. Dispersed Bubble and Slug Flow," Int. J. of Multiphase Flow, Vol. 17, No. 4, 1991

Costigan, G. & Whalley, P.B., "Slug Flow Regime Identification From Dynamic Void Fraction Measurements In Vertical Air-Water Flows," Int. J. of Multiphase Flow, Vol. 23, No. 2, 1997

Dounan , J., Zhengjie, W., Zhenwan, Y. & Dongming, Q., "Experimental Study of void Fraction in Vertically Upward and Downward Liquid-Gas Two-Phase at Low Velocity," Two-Phase Flow and Heat Transfer: China-U.S. Progress (Hemisphere Publishing Corporation, Washington, DC., 1985)

Dukler, A.E., Fabre, J.A., McQuillen, J.B., & Vernon, R., "Gas-Liquid Flow at Microgravity Conditions: Flow Patterns and Their Transitions," Int. J. of Multiphase Flow, Vol. 14, No. 4, 1988

Elkow, Kenneth J. Void Fraction Measurement and Analysis at Normal Gravity and Microgravity Conditions, M.Sc. Thesis University of Saskatchewan Saskatoon, Saskatchewan, 1995

Elkow, K.J. and Rezkallah, K.S., "Statistical Analysis of Void Fluctuations in Gas-Liquid Flows Under 1-g and μ-g Conditions Using a Capacitance Sensor," Int. J. of Multiphase Flow, Vol. 23, No. 5, 1997

Elkow, K.J. and Rezkallah, K.S., "Void Fraction Measurements In Gas-Liquid Flows Under 1-g and μ-g Conditions Using Capacitance Sensors," Int. J. of Multiphase Flow, Vol. 23, No. 5, 1997

Elkow, K.J., Rezkallah, K.S., "Void Fraction Measurements In Gas-Liquid Flows Using Capacitance Sensors," Meas. Sci. Technol., Vol. 7, 1996

Huang, S.M., Stott, A.L., Green, R.G. & Beck, M.S., "Electronic Transducers for Industrial Measurement of Low Value Capacitances," J. Phys. E: Sci. Instrum., Vol. 21, 1988

Huckerby, Scott C., Two-Phase Liquid-Gas Flow Pattern Observations Under Microgravity Conditions, M.Sc. Thesis (University of Saskatchewan, Saskatoon, 1992)

Jones, O.C. & Zuber, N., "The Interrelation Between Void Fraction Fluctuations and Flow Patterns In Two-Phase Flow," Int. J. of Multiphase Flow, Vol. 2, 1975

Lide, D.R., CRC Handbook of Chemistry and Physics, 73rd Ed. (CRC Press, Boca Raton, 1992-1993)

OMEGA Engineering Inc., Ultra-Low Flow Sensor, Operators Manual (Stamford, CT., 1993)

Rezkallah, K.S., "Weber Number Based Flow-Pattern Maps for Liquid-Gas Flows at Microgravity," Int. J. of Multiphase Flow, Vol. 22, No. 6, 1996

Rezkallah, K.S. & Zhao, L., "Flow Pattern Map For Two-Phase Liquid-Gas Flows Under Reduced Gravity Conditions," J. of Advances in Space Research, Vol. 16, No. 7, 1995

Rite, Raymond W., Heat Transfer in Gas-Liquid Flows Through a Vertical Circular Tube Under Microgravity Conditions, Ph.D. Thesis (University of Saskatchewan, Saskatoon, 1995)

Siemens, Gregory, "Design, Construction and Testing of a Capacitive Void Fraction Sensor for Use in Two Component, Two-Phase Flow," (Saskatoon, University of Saskatchewan, Not published)

Song, C.H., No, H.C., & Chung, M.K., "Investigation of Bubble Flow Developments And Its Transition Based On The Instability of Void Fraction Waves," Int. J. of Multiphase Flow, Vol. 21, No. 3, 1995

Zhao, L. & Rezkallah, K.S., "Gas-Liquid Flow Patterns at Microgravity Conditions," Int. J. of Multiphase Flow, Vol. 19, No. 5, 1993

Zhao, L. & Rezkallah, K.S., "Experimental Study of the Characteristics of Slug Flow at Microgravity," ASME National Heat Transfer Conference, Portland, Aug. 1995

APPENDIX A - INSTRUMENTATION

This appendix gives specifications and calibration information on instrumentation used in this study. Information is included for the liquid flow meters, the gas mass flow controllers, the absolute pressure transducer, and the film thickness probes.

A.1 Liquid Flow Meters

The specifications for the OMEGA® (1993) turbine flow meters used in this study are listed in Table A.1. These flow meters generate a square wave signal from an infrared electro-optical transmitter, which is then converted to a voltage through an OMEGA FLSC-28 Signal Conditioner. Each flow meter was calibrated by measuring the mass flow through the meter over a given period of time to obtain the mass flow rate. The mass flow rate is converted to a superficial velocity, which is compared against the voltage output from the meter to obtain the calibration relation. The calibration results are shown in Table A.2. In Table A.2 VDC is the direct current voltage output from the flow meter.

Table A.1 - Specifications of liquid turbine flow meters from OMEGA® (1995)

Accuracy	±1 % of reading
Repeatability	±0.1 % of reading
Linearity	±1 % of reading
Viscosity Range	1-15 centistokes
Working Pressure	150 psig at 175 °F
Ambient Temperature	-40 °F to +185 °F
Wetted Material	PVDF
Power Supply	5-18 VDC, 6-33 mA
Flow Range:	
FTB601	0.1-2 LPM
FTB602	0.3-9 LPM
FTB603	0.5-15 LPM
Max. Pressure Drop:	
FTB601	7 psid
FTB602	24 psid
FTB603	24 psid

Table A.2 - Calibration relations for liquid flow meters.

Flow Meter	Calibration Relation	Coefficient of Determination (R^2)
FTB601	V_{SL} = 0.062283*VDC+.0008	0.9995
FTB602	V_{SL} = 0.281034*VDC+.0056	0.9999
FTB603	V_{SL} = 0.689472*VDC+.0263	0.9982

A.2 Gas Mass Flow Controllers

The gas mass flow controllers used in this study were the MKS 10 SLM, 20 SLM, and 100 SLM mass flow controllers, the specifications of which are given in Table A.3. The mass flow controllers are factory calibrated for nitrogen at standard conditions, however, the same calibration can be used for air. The perfect gas law is used to convert the measured flow rate Q_m to the actual flow rate Q_g. This relation is given by:

$$Q_g = \frac{P_o Q_m T_g}{P_g T_o}, \qquad (A.1)$$

where P_o and T_o are the standard pressure and temperature, and P_g and T_g are the inlet pressure and temperature of the gas. To check the calibration of each mass flow controller, the output was compared against benchmark flow controllers which had been recently factory calibrated, and against the flow rate calculated from the pressure drop across an orifice plate with a known discharge coefficient. The calibration relation for each mass flow controller is shown in Table A.4.

Table A.3 - Specifications for the MKS 10 SLM, 20 SLM, and 100 SLM mass flow controllers.

Full Scale Nitrogen Equivalent Ranges	10, 20, and 100 SLM
Control Range	1.0 – 100 % of F.S.
Accuracy (including non-linearity)	±1.0 % of F.S.
Resolution (measurement)	0.1 % of F.S.
Temperature Coefficients	
Zero	< 0.05 % of F.S./°C (500 ppm)
Span	< 0.10 % of Reading/°C (1000 ppm)
Operating Temperature Range	15 – 40 °C
Maximum Inlet Pressure	150 psig
Pressure Coefficient	0.005 % of Reading/psi
Minimum Pressure Drop	11 Torr at atmosphere (0.2 psi)

Table A.4 - Calibration relations for the MKS 10 SLM, 20 SLM, and 100 SLM mass flow controllers.

Mass Flow Controller	Calibration Relation
100 SLM	$Q_g = 20.039*VDC + 0.1171$
20 SLM	$Q_g = 4.0278*VDC - 0.0764$
10 SLM	$Q_g = 2.0319*VDC - 0.1789$

A.3 Absolute Pressure Transducer

The Validyne P305A absolute pressure transducer used in this study has the specifications listed in Table A.5. The pressure transducer consists of a magnetically permeable diaphragm which separates two inductance coils. As the pressure deflects the diaphragm, the inductance in one coil increases, while it decreases in the other. The polarity and magnitude of the pressure can then be converted to a DC voltage through an AC bridge circuit. The calibration of the absolute pressure transducer gave the following relation:

$$psia = 11.965*VDC + 1.7831.$$

Table A.5 - Specifications for the Validyne P305A absolute pressure transducer.

Range	0 – 60 psia
Accuracy	± 0.5 % F.S. including linearity, hysteresis, and repeatability
Overpressure	20 psia, or 200 % F.S. whichever is greater, with < 0.5 % zero shift
Pressure Media	Fluids compatible with Type 410 Stainless Steel and Inconel
Excitation	10.8 to 32 VDC @ 8.0 mA nominal
Signal Output	0 – 5 VDC F.S. @ 0.5 mA
Zero Balance	< 0.1 VDC, Adjustable ±1 VDC
Operating Temperature	-65 °F to +250 °F
Temperature Error	< 2 % F.S./100 °F
Frequency Response	0 – 200 Hz flat ±1 db for electronics
Output Noise	≤ 5 mV RMS

A.4 Film Thickness Probes

The film thickness probes consisted of two 0.05 mm stainless steel wires separated by 2 mm, stretched across the tube, as shown in Figure A.1. Half of each wire was electrically insulated from the flow while the other half was in contact with the two phases. A conductance measuring circuit operating at 3 kHz measured the conductance

between the two wires. Since water and air have much different conductivity, the total conductivity measured by the probes will be a function of the relative amounts of air and water between the probes. Thus, the film thickness probes work similar to the void fraction sensor, except that they measure conductance rather than capacitance. The measured conductance was found to vary linearly with the film thickness.

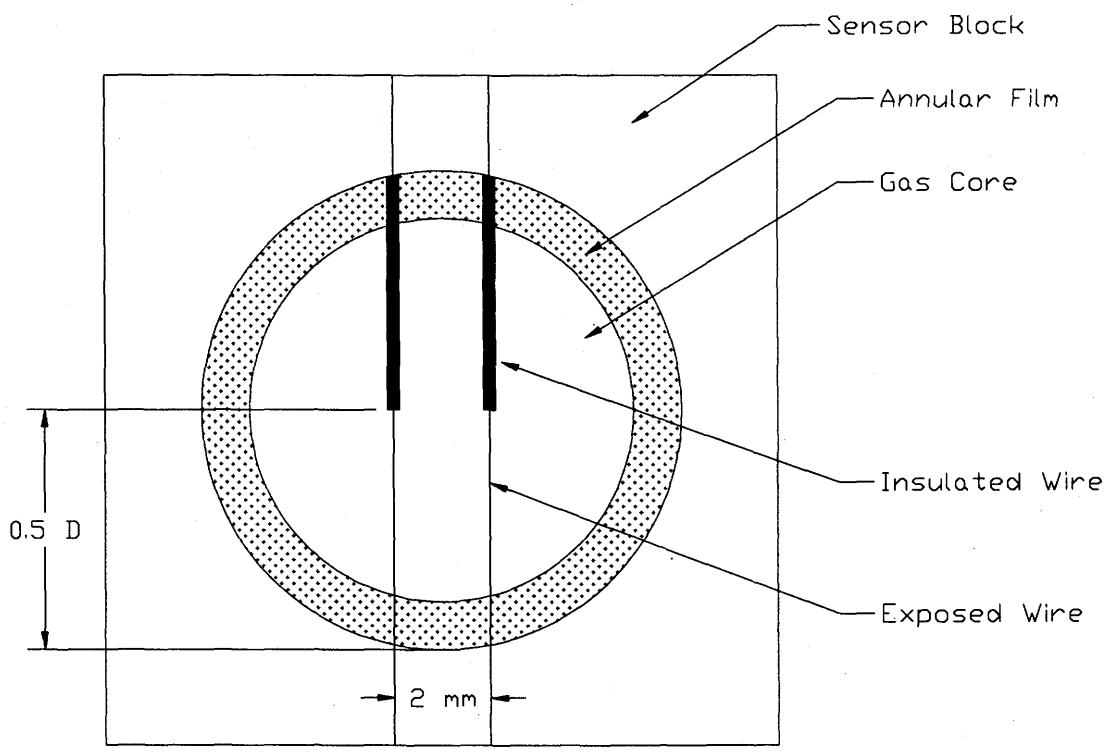

Figure A.1 - Simplified diagram of film thickness probe.

APPENDIX B - DATA

This appendix contains the tabulated data used in this study. The data is presented in four tables, one table for each the four microgravity flights during which the data was collected. Each set point is represented by a code such as 96F3P28, which gives the year the data was taken (1996), the flight number (F3), followed by the parabola number (P28). The data is presented in this way for easy cross-referencing to the probability density functions presented in Appendixes C and D. Also presented in this appendix is the bubble velocity data used in Chapters 4 and 6, also organized according to flight day. In each of the tables the flow regime is identified according to the following code:

B = bubbly flow,
B-S = bubbly-to-slug,
S = slug flow,
S-T = slug-to-transitional,
T = transitional flow,
T-A = transitional-to-annular, and
A = annular flow.

Table B.1 - Microgravity data for flight one.

	Flow Regime	P_{abs} (kPa)	Temp. (°C)	V_{SL} (m/s)	V_{SG} (m/s)	α_{ave}
96F1P2	T	91.91	23.18	0.04	4.92	0.829
96F1P3	A	91.88	22.67	0.05	6.92	0.855
96F1P4	A	91.86	22.19	0.04	8.91	0.864
96F1P5	A	91.83	22.16	0.04	10.91	0.873
96F1P6	A	91.84	21.77	0.03	12.91	0.885
96F1P7	A	91.78	21.42	0.05	14.92	0.882
96F1P8	A	91.70	21.23	0.05	16.95	0.885
96F1P9	A	91.69	20.90	0.05	18.95	0.888
96F1P10	A	91.66	20.57	0.05	20.94	0.889
96F1P15	A	91.45	21.68	0.08	10.96	0.858
96F1P16	A	91.46	21.65	0.08	12.91	0.860
96F1P17	A	91.45	21.31	0.08	14.92	0.860
96F1P18	A	91.42	21.17	0.08	16.90	0.869
96F1P24	T-A	91.39	21.95	0.09	7.94	0.826
96F1P29	A	91.07	21.04	0.11	17.91	0.869
96F1P30	A	91.05	20.81	0.11	19.91	0.859
96F1P32	T	91.07	21.80	0.16	3.95	0.755
96F1P33	T	91.04	21.69	0.16	5.96	0.790
96F1P34	T-A	91.04	21.50	0.16	7.96	0.807

Table B.2 - Microgravity data for flight two.

	Flow Regime	P_{abs} (kPa)	Temp. (°C)	V_{SL} (m/s)	V_{SG} (m/s)	α_{ave}
96F2P2	T	89.00	21.95	0.16	3.96	0.764
96F2P5	T-A	89.03	21.69	0.16	9.94	0.815
96F2P6	A	89.10	21.51	0.15	11.96	0.829
96F2P7	A	89.07	21.41	0.15	13.96	0.838
96F2P8	A	89.11	21.35	0.15	15.96	0.846
96F2P10	A	89.22	21.30	0.15	17.91	0.855
96F2P11	A	89.20	21.12	0.15	19.90	0.862
96F2P12	A	89.26	21.63	0.20	11.96	0.816
96F2P13	A	89.24	21.50	0.21	13.95	0.828
96F2P14	A	89.22	21.45	0.20	15.95	0.838
96F2P15	T	89.21	21.91	0.22	2.96	0.720
96F2P16	T	89.27	21.85	0.22	4.95	0.761
96F2P18	T	89.29	21.79	0.20	6.92	0.781
96F2P19	T	89.32	21.69	0.20	8.93	0.798
96F2P20	T-A	89.36	21.51	0.20	10.92	0.811
96F2P21	T	89.41	21.90	0.31	1.95	0.679
96F2P22	T	89.48	21.87	0.31	3.96	0.720
96F2P23	T	89.55	21.80	0.31	5.92	0.738
96F2P24	T	89.46	21.78	0.30	7.95	0.765
96F2P26	T	89.56	21.70	0.32	9.91	0.781
96F2P27	T-A	89.65	21.59	0.31	11.92	0.796
96F2P28	A	89.59	21.48	0.31	13.92	0.809
96F2P29	A	89.67	21.40	0.31	15.92	0.818
96F2P32	T-A	89.62	21.36	0.09	7.91	0.823
96F2P34	A	89.62	21.35	0.11	9.92	0.830
96F2P35	A	89.62	21.19	0.11	11.91	0.845
96F2P36	A	89.65	20.98	0.11	13.96	0.853
96F2P37	A	89.66	20.85	0.11	15.91	0.860
96F2P39	A	89.68	20.96	0.10	19.89	0.874
96F2P40	T	89.69	21.30	0.09	4.92	0.799
96F2P42	T	89.73	21.40	0.09	6.93	0.815
96F2P43	A	89.74	21.11	0.09	9.96	0.840
96F2P44	A	89.76	20.80	0.08	12.95	0.857
96F2P45	A	89.75	20.68	0.08	14.96	0.865
96F2P46	A	89.71	20.54	0.07	16.95	0.871
96F2P47	A	89.74	20.31	0.07	18.95	0.875
96F2P48	A	89.77	20.20	0.07	20.94	0.879
96F2P50	T	89.81	21.40	0.06	4.97	0.814
96F2P51	T-A	89.80	21.20	0.06	6.92	0.831
96F2P52	A	89.82	21.04	0.06	8.92	0.838

Table B.3 - Microgravity data for flight three.

	Flow Regime	P_{abs} (kPa)	Temp. (°C)	V_{SL} (m/s)	V_{SG} (m/s)	α_{ave}
96F3P2	B	88.44	22.48	1.72	0.10	0.074
96F3P3	B	88.48	22.50	1.79	0.20	0.107
96F3P5	B	88.43	22.57	1.78	0.40	0.161
96F3P6	B-S	88.44	22.63	1.78	0.50	0.184
96F3P7	S	88.63	22.68	1.77	0.59	0.202
96F3P8	S	88.43	22.68	1.77	0.79	0.241
96F3P10	S	88.09	22.69	1.77	0.99	0.273
96F3P11	S	88.16	22.69	1.77	1.19	0.303
96F3P12	B	88.71	22.73	2.53	0.10	0.044
96F3P13	B	88.76	22.80	2.53	0.20	0.067
96F3P15	B	88.77	22.87	2.53	0.39	0.110
96F3P16	B	88.80	22.89	2.51	0.49	0.126
96F3P18	B	88.81	22.92	2.51	0.59	0.145
96F3P19	B-S	88.80	22.96	2.51	0.79	0.174
96F3P21	S	88.91	23.03	2.50	1.19	0.225
96F3P22	B	88.43	23.17	3.03	0.10	0.031
96F3P23	B	88.83	23.05	1.73	0.20	0.106
96F3P26	B-S	88.89	23.07	1.72	0.40	0.164
96F3P27	S	89.01	23.06	1.71	0.49	0.188
96F3P28	S	88.90	23.09	1.71	0.59	0.209
96F3P29	S	88.79	23.06	1.71	0.79	0.245
96F3P30	S	88.70	23.03	1.70	0.99	0.279
96F3P31	S	88.87	23.02	1.71	1.19	0.311
96F3P32	B	88.99	23.16	2.49	0.10	0.043
96F3P34	B	89.00	23.20	2.49	0.20	0.065
96F3P35	B	88.99	23.22	2.52	0.30	0.088
96F3P36	B	89.04	23.26	2.52	0.40	0.109
96F3P38	B	89.04	23.29	2.51	0.59	0.145
96F3P39	B-S	88.99	23.30	2.51	0.79	0.174
96F3P40	S	88.44	23.33	2.50	0.99	0.200
96F3P42	S	88.50	23.36	2.50	1.19	0.224
96F3P43	B	89.08	23.20	0.74	0.09	0.148
96F3P44	B	89.06	23.19	0.73	0.20	0.209
96F3P46	S	89.04	23.19	0.72	0.49	0.342
96F3P47	S	89.07	23.18	0.72	0.59	0.381
96F3P48	S	89.02	23.18	0.72	0.69	0.402
96F3P50	S	88.83	23.09	0.73	0.79	0.424
96F3P51	S	88.61	23.06	0.72	1.09	0.494

Table B.4 - Microgravity data for flight four.

	Flow Regime	P_{abs} (kPa)	Temp. (°C)	V_{SL} (m/s)	V_{SG} (m/s)	α_{ave}
96F4P2	S	87.02	20.19	0.10	0.79	0.733
96F4P3	S	86.41	20.18	0.10	1.09	0.756
96F4P4	S-T	86.41	20.19	0.10	1.29	0.743
96F4P5	T	86.42	20.19	0.11	1.59	0.724
96F4P7	T	86.51	20.30	0.12	2.18	0.750
96F4P8	T	86.51	20.30	0.11	2.48	0.754
96F4P9	T	86.50	20.29	0.11	2.78	0.761
96F4P10	S	86.54	20.35	0.17	0.78	0.717
96F4P12	S	86.57	20.33	0.15	1.09	0.726
96F4P13	S	86.60	20.32	0.15	1.29	0.720
96F4P14	S-T	86.63	20.31	0.16	1.59	0.716
96F4P15	T	86.64	20.31	0.16	1.89	0.740
96F4P16	T	86.70	20.39	0.15	2.18	0.744
96F4P17	T	86.67	20.34	0.15	2.48	0.743
96F4P18	T	86.73	20.32	0.15	2.78	0.736
96F4P19	T	86.74	20.30	0.15	3.08	0.755
96F4P20	S	86.87	20.40	0.26	0.89	0.666
96F4P22	S	86.82	20.53	0.26	1.29	0.684
96F4P23	S	86.83	20.51	0.25	1.69	0.700
96F4P24	S	86.87	20.52	0.25	1.99	0.686
96F4P25	T	87.00	20.59	0.26	2.28	0.709
96F4P26	T	87.06	20.59	0.26	2.58	0.699
96F4P27	T	87.09	20.59	0.25	2.98	0.716
96F4P28	T	87.09	20.58	0.25	3.78	0.736
96F4P29	S	87.10	20.69	0.25	1.68	0.689
96F4P30	S	87.14	20.64	0.43	1.98	0.659
96F4P32	S-T	87.35	20.78	0.40	2.48	0.665
96F4P33	T	87.26	20.64	0.40	2.98	0.676
96F4P34	T	87.34	20.62	0.40	3.48	0.689
96F4P36	S	87.42	20.79	1.01	1.99	0.525
96F4P37	S	87.49	20.76	1.01	2.48	0.549
96F4P38	S	87.52	20.80	1.00	2.98	0.567
96F4P39	S	87.54	20.71	1.00	3.48	0.590
96F4P40	S	87.53	20.80	1.00	3.98	0.596
96F4P42	B	88.06	21.19	0.43	0.19	0.278
96F4P43	S	88.09	21.29	0.43	0.29	0.373
96F4P44	S	88.12	21.25	0.42	0.49	0.495

Table B.1 (continued) – Microgravity data for flight four.

	Flow Regime	P_{abs} (kPa)	Temp. (°C)	V_{SL} (m/s)	V_{SG} (m/s)	α_{ave}
96F4P45	S	88.13	21.21	0.42	0.69	0.541
96F4P46	S	87.82	21.19	0.42	0.99	0.605
96F4P47	S	87.72	21.19	0.42	1.19	0.633
96F4P48	S	88.21	21.38	0.24	0.19	0.383
96F4P49	S	88.21	21.40	0.22	0.29	0.480
96F4P50	S	88.16	21.39	0.22	0.49	0.605
96F4P52	S	88.04	21.39	0.22	0.69	0.620
96F4P53	S	87.74	21.32	0.22	0.89	0.719
96F4P54	S	88.23	21.51	0.11	0.19	0.565
96F4P55	S	88.24	21.52	0.12	0.29	0.607
96F4P56	S	88.24	21.52	0.12	0.40	0.658
96F4P57	S	88.12	21.50	0.12	0.49	0.713

Table B.5 - Gas velocity data for flight three.

	Flow Regime	V_{SG} (m/s)	V_{SL} (m/s)	α_{ave}	j (m/s)	V_{SG}/α (m/s)	V_G CC† (m/s)	δV_G CC† (m/s)	V_G αTT‡ (m/s)	δV_G αTT‡ (m/s)
96F3P2	B	0.10	1.72	0.074	1.81	1.29	2.17	0.15	-	-
96F3P3	B	0.20	1.79	0.107	1.98	1.83	2.33	0.18	-	-
96F3P5	B	0.40	1.78	0.161	2.17	2.45	2.53	0.21	-	-
96F3P6	B-S	0.50	1.78	0.184	2.27	2.70	2.76	0.25	-	-
96F3P7	S	0.59	1.77	0.202	2.37	2.94	2.76	0.25	-	-
96F3P8	S	0.79	1.77	0.241	2.56	3.29	3.03	0.30	-	-
96F3P10	S	0.99	1.77	0.273	2.76	3.63	3.37	0.37	-	-
96F3P11	S	1.19	1.77	0.303	2.96	3.94	3.37	0.37	-	-
96F3P12	B	0.10	2.53	0.044	2.63	2.20	3.03	0.30	-	-
96F3P13	B	0.20	2.53	0.067	2.73	2.92	3.37	0.37	-	-
96F3P15	B	0.39	2.53	0.110	2.92	3.59	3.37	0.37	-	-
96F3P16	B	0.49	2.51	0.126	3.00	3.92	3.79	0.47	-	-
96F3P18	B	0.59	2.51	0.145	3.11	4.11	3.79	0.47	-	-
96F3P19	B-S	0.79	2.51	0.174	3.30	4.56	3.79	0.47	-	-
96F3P21	S	1.19	2.50	0.225	3.69	5.28	4.33	0.62	-	-
96F3P22	B	0.10	3.03	0.031	3.12	3.08	-	-	-	-
96F3P23	B	0.20	1.73	0.106	1.92	1.85	2.33	0.18	-	-
96F3P26	B-S	0.40	1.72	0.164	2.11	2.41	2.53	0.21	-	-
96F3P27	S	0.49	1.71	0.188	2.21	2.64	2.53	0.21	-	-
96F3P28	S	0.59	1.71	0.209	2.30	2.83	2.76	0.25	-	-
96F3P29	S	0.79	1.71	0.245	2.50	3.24	3.03	0.30	-	-
96F3P30	S	0.99	1.70	0.279	2.70	3.57	3.03	0.30	-	-
96F3P31	S	1.19	1.71	0.311	2.90	3.82	3.37	0.37	-	-
96F3P32	B	0.10	2.49	0.043	2.59	2.20	-	-	-	-
96F3P34	B	0.20	2.49	0.065	2.69	3.00	-	-	-	-
96F3P35	B	0.30	2.52	0.088	2.82	3.37	3.37	0.37	-	-
96F3P36	B	0.40	2.52	0.109	2.91	3.64	3.37	0.37	-	-
96F3P38	B	0.59	2.51	0.145	3.10	4.10	3.79	0.47	-	-
96F3P39	B-S	0.79	2.51	0.174	3.30	4.56	3.79	0.47	-	-
96F3P40	S	0.99	2.50	0.200	3.49	4.96	4.33	0.62	-	-
96F3P42	S	1.19	2.50	0.224	3.69	5.33	4.33	0.62	-	-
96F3P43	B	0.09	0.74	0.148	0.83	0.64	0.98	0.03	-	-
96F3P44	B	0.20	0.73	0.209	0.92	0.93	1.08	0.04	-	-
96F3P46	S	0.49	0.72	0.342	1.22	1.45	1.44	0.07	-	-
96F3P47	S	0.59	0.72	0.381	1.32	1.56	1.52	0.08	-	-
96F3P48	S	0.69	0.72	0.402	1.42	1.73	1.60	0.08	-	-
96F3P50	S	0.79	0.73	0.424	1.52	1.87	1.78	0.11	-	-
96F3P51	S	1.09	0.72	0.494	1.82	2.21	2.17	0.15	-	-

† - indicates gas velocity calculated from cross-correlation of film thickness probes.
‡ - indicates gas velocity calculated from void fraction time trace.

Table B.6 - Gas velocity data for flight four.

	Flow Regime	V_{SG} (m/s)	V_{SL} (m/s)	α_{ave}	j (m/s)	V_{SG}/α (m/s)	V_G CC† (m/s)	δV_G CC† (m/s)	V_G αTT‡ (m/s)	δV_G αTT‡ (m/s)
96F4P2	S	0.79	0.10	0.733	0.89	1.08	1.01	0.03	1.08	0.06
96F4P3	S	1.09	0.10	0.756	1.19	1.44	1.26	0.05	1.46	0.11
96F4P10	S	0.78	0.17	0.717	0.96	1.09	1.12	0.04	1.23	0.08
96F4P12	S	1.09	0.15	0.726	1.24	1.50	1.44	0.07	1.10	0.06
96F4P13	S	1.29	0.15	0.720	1.44	1.79	1.78	0.11	1.63	0.14
96F4P20	S	0.89	0.26	0.666	1.14	1.33	1.44	0.07	1.52	0.12
96F4P22	S	1.29	0.26	0.684	1.54	1.88	1.90	0.12	0.73	0.03
96F4P23	S	1.69	0.25	0.700	1.94	2.41	2.17	0.15	1.79	0.16
96F4P24	S	1.99	0.25	0.686	2.24	2.90	2.76	0.25	1.90	0.19
96F4P29	S	1.68	0.25	0.689	1.94	2.45	2.17	0.15	-	-
96F4P30	S	1.98	0.43	0.659	2.42	3.01	3.03	0.30	2.68	0.37
96F4P36	S	1.99	1.01	0.525	3.00	3.78	3.37	0.37	2.59	0.34
96F4P37	S	2.48	1.01	0.549	3.49	4.52	4.33	0.62	2.81	0.40
96F4P38	S	2.98	1.00	0.567	3.98	5.26	4.33	0.62	3.42	0.60
96F4P42	B	0.19	0.43	0.278	0.62	0.69	0.76	0.02	3.71	0.70
96F4P43	S	0.29	0.43	0.373	0.73	0.79	0.87	0.02	-	-
96F4P44	S	0.49	0.42	0.495	0.91	1.00	1.12	0.04	1.44	0.11
96F4P45	S	0.69	0.42	0.541	1.11	1.28	1.26	0.05	-	-
96F4P46	S	0.99	0.42	0.605	1.41	1.64	1.68	0.09	1.82	0.17
96F4P47	S	1.19	0.42	0.633	1.61	1.88	2.02	0.13	1.77	0.16
96F4P48	S	0.19	0.24	0.383	0.43	0.50	0.55	0.01	-	-
96F4P49	S	0.29	0.22	0.480	0.51	0.61	0.67	0.01	-	-
96F4P50	S	0.49	0.22	0.605	0.71	0.81	0.89	0.03	-	-
96F4P52	S	0.69	0.22	0.620	0.91	1.12	1.21	0.05	-	-
96F4P53	S	0.89	0.22	0.719	1.11	1.24	1.44	0.07	1.23	0.08
96F4P54	S	0.19	0.11	0.565	0.30	0.34	0.39	0.00	-	-
96F4P55	S	0.29	0.12	0.607	0.41	0.48	0.53	0.01	-	-
96F4P56	S	0.40	0.12	0.658	0.52	0.60	0.66	0.01	0.74	0.03
96F4P57	S	0.49	0.12	0.713	0.61	0.69	0.80	0.02	0.81	0.03

† - indicates gas velocity calculated from cross-correlation of film thickness probes.
‡ - indicates gas velocity calculated from void fraction time trace.

APPENDIX C - VOID FRACTION PROBABILITY DENSITY FUNCTIONS AND FLOW IMAGES

This appendix presents the void fraction probability function for each flow setting acquired for this study. In addition, flow images are included with the PDF plots which depict a transition between flow regimes. Several images are also included for PDF plots which clearly depict one of the flow regimes. As in Appendix B, the plots are organized by the day and parabola on which the data was taken (i.e. 96F2P27 represents data taken during parabola 27 of flight day 2 during the 1996 flight campaign). As well, in each of the figures the flow regime is identified according to the following code:

B = bubbly flow,
B-S = bubbly-to-slug,
S = slug flow,
S-T = slug-to-transitional,
T = transitional flow,
T-A = transitional-to-annular, and
A = annular flow.

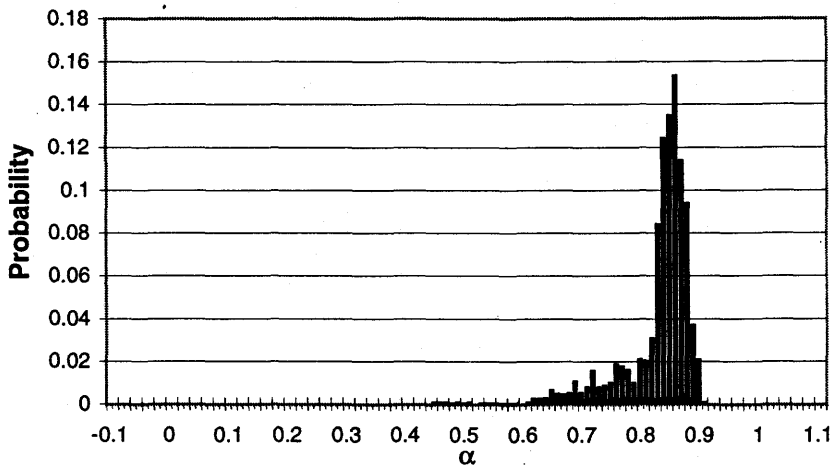

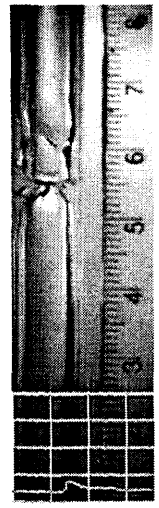

Figure C.1 - Void fraction PDF and flow image for 96F1P2 - T.

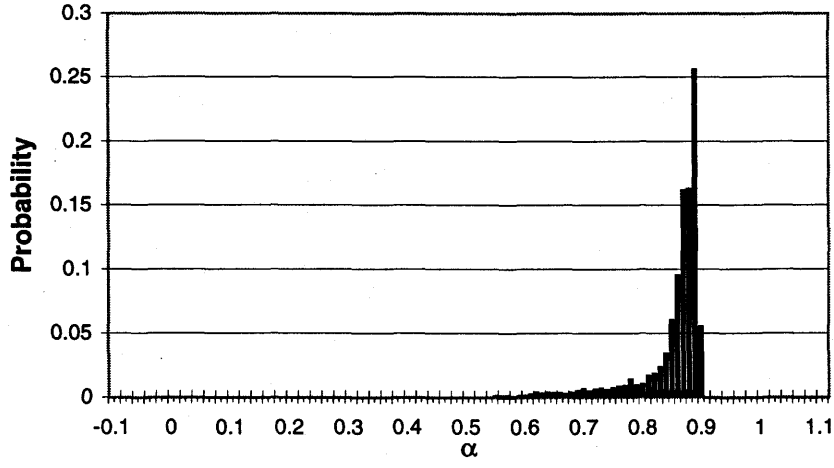

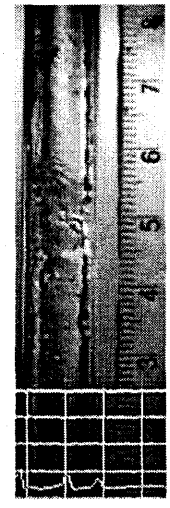

Figure C.2 - Void fraction PDF and flow image for 96F1P3 - A.

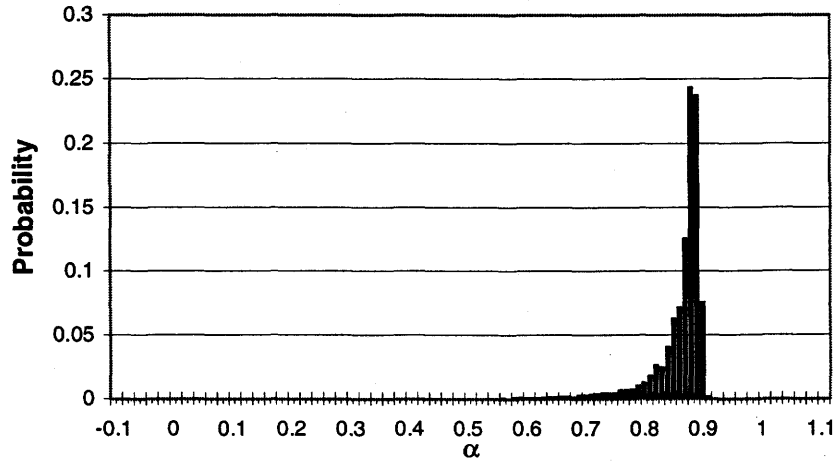

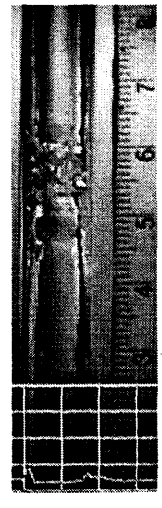

Figure C.3 - Void fraction PDF and flow image for 96F1P4 - A.

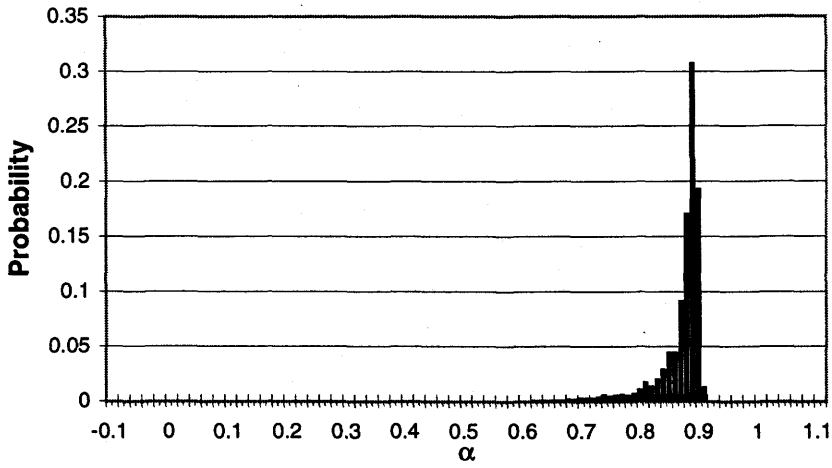

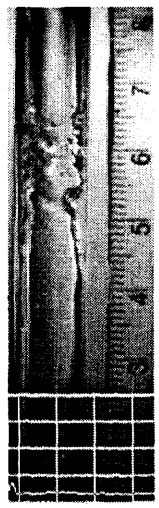

Figure C.4 - Void fraction PDF and flow image for 96F1P5 - A.

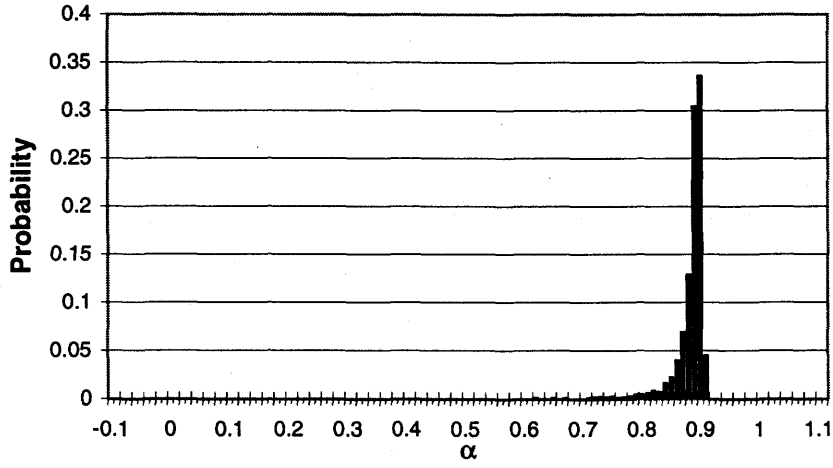

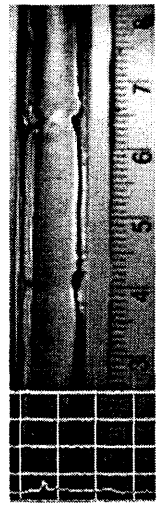

Figure C.5 - Void fraction PDF and flow image for 96F1P6 - A.

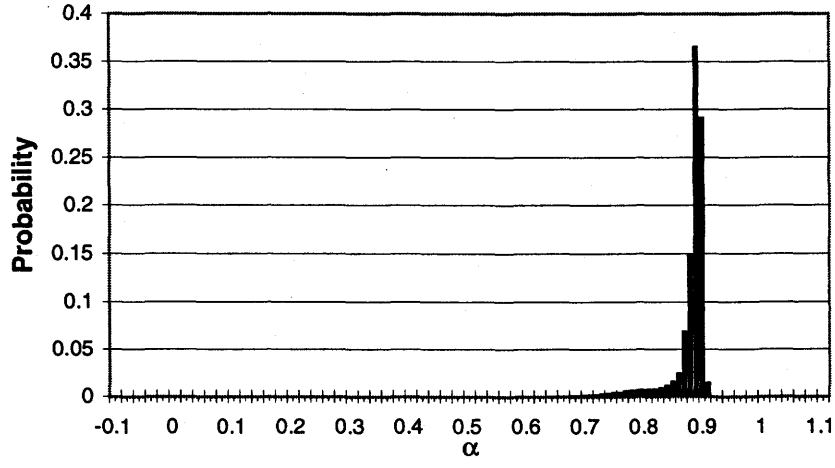

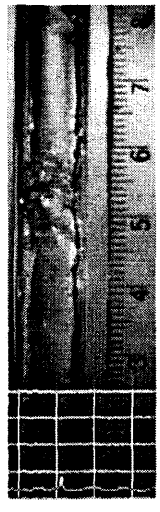

Figure C.6 - Void fraction PDF and flow image for 96F1P7 - A.

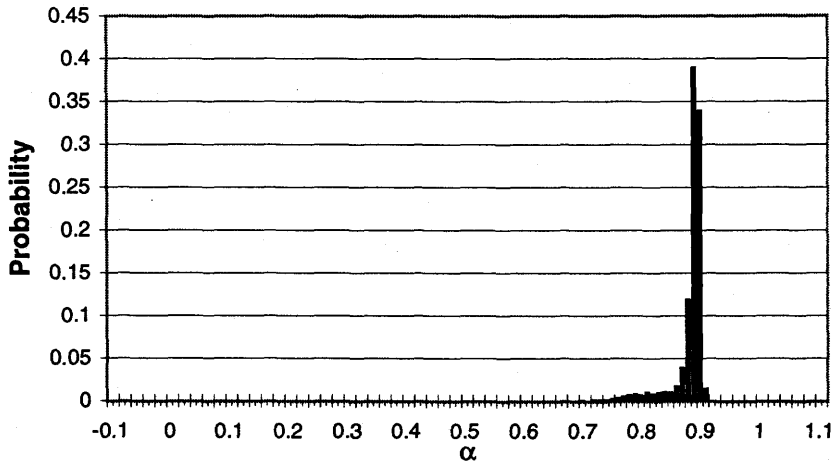

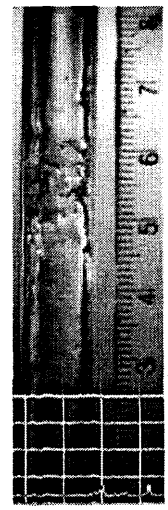

Figure C.7 - Void fraction PDF and flow image for 96F1P8 - A.

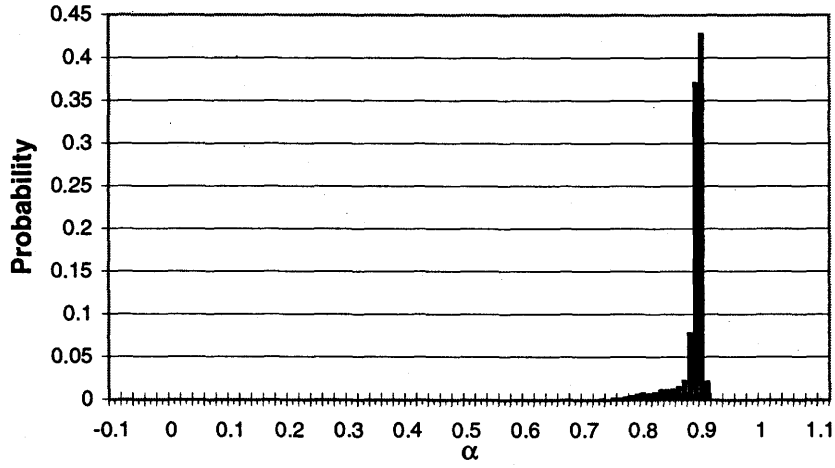

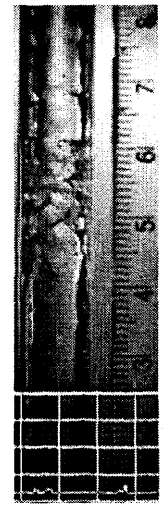

Figure C.8 - Void fraction PDF and flow image for 96F1P9 - A.

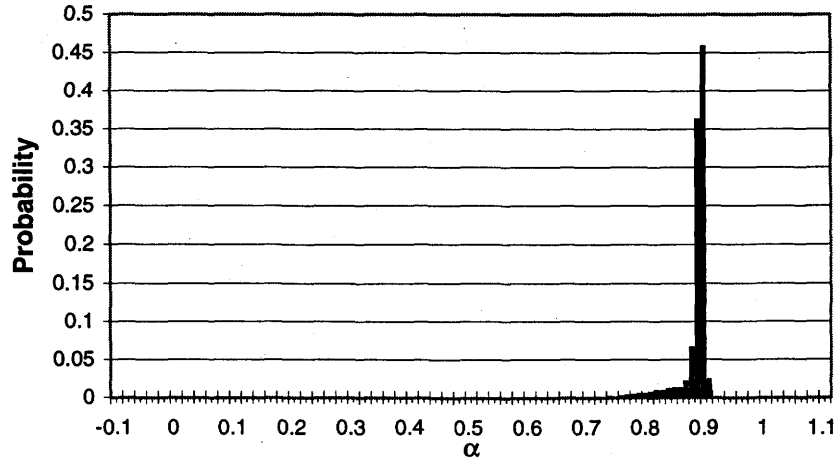

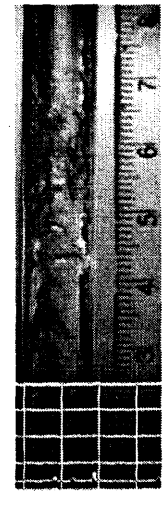

Figure C.9 - Void fraction PDF and flow image for 96F1P10 - A.

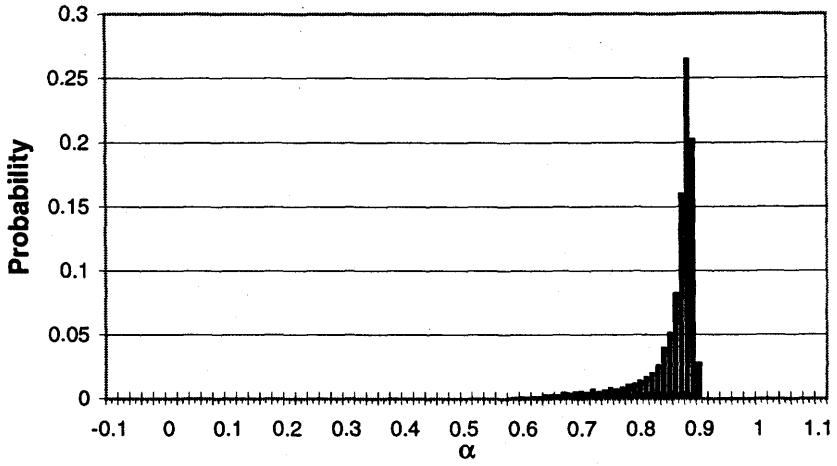

Figure C.10 - Void fraction PDF and flow image for 96F1P15 - A.

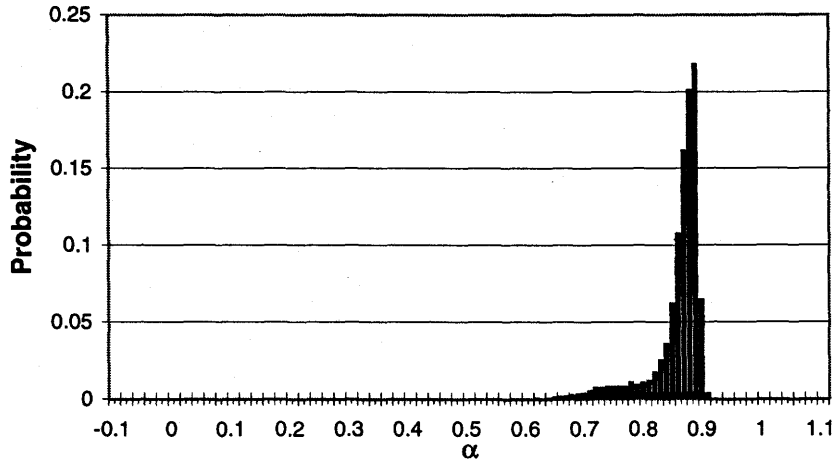

Figure C.11 - Void fraction PDF for 96F1P16 - A.

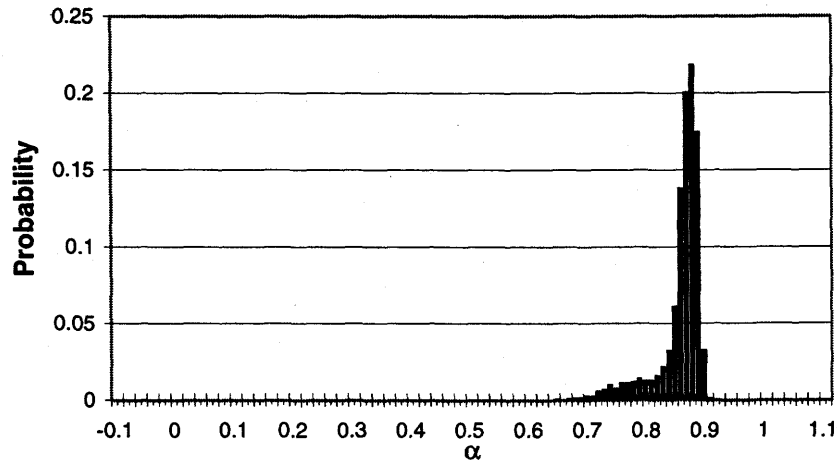

Figure C.12 - Void fraction PDF for 96F1P17 - A.

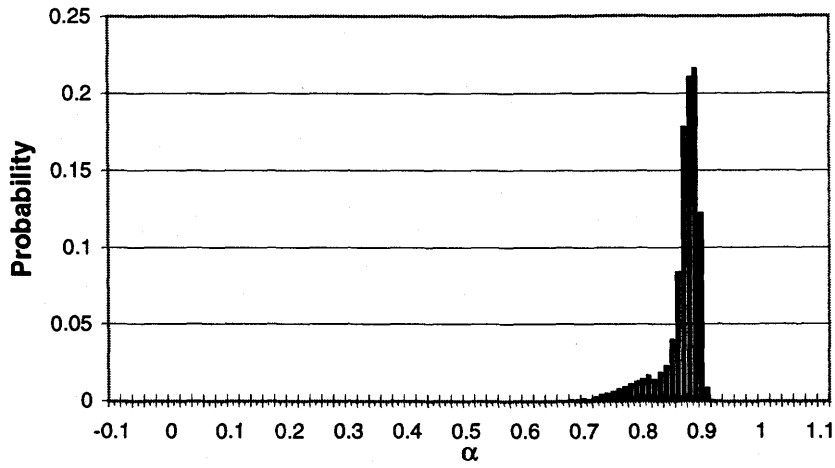

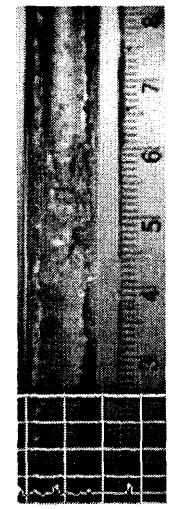

Figure C.13 - Void fraction PDF and flow image for 96F1P18 - A.

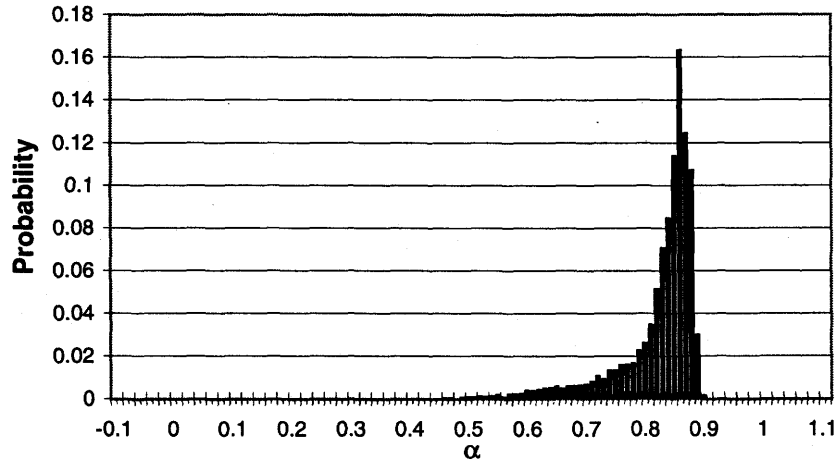

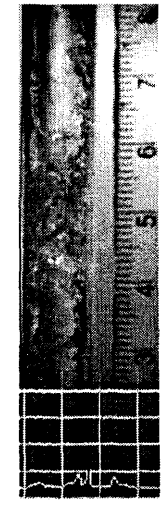

Figure C.14 - Void fraction PDF and flow image for 96F1P24 - T-A.

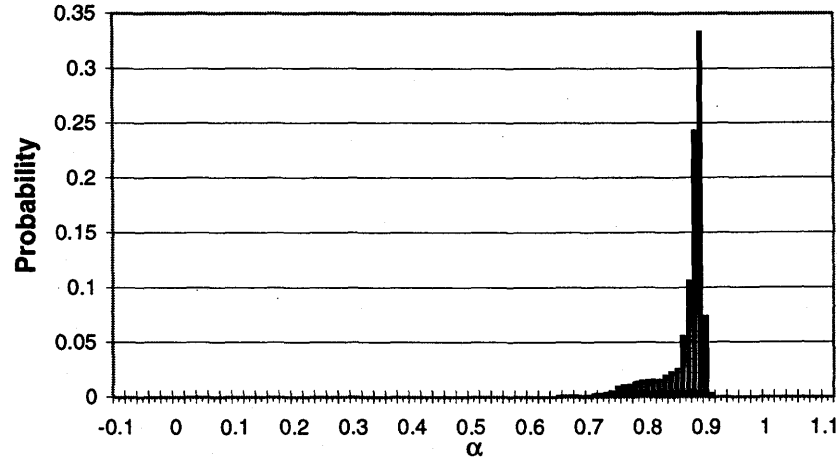

Figure C.15 - Void fraction PDF for 96F1P29 - A.

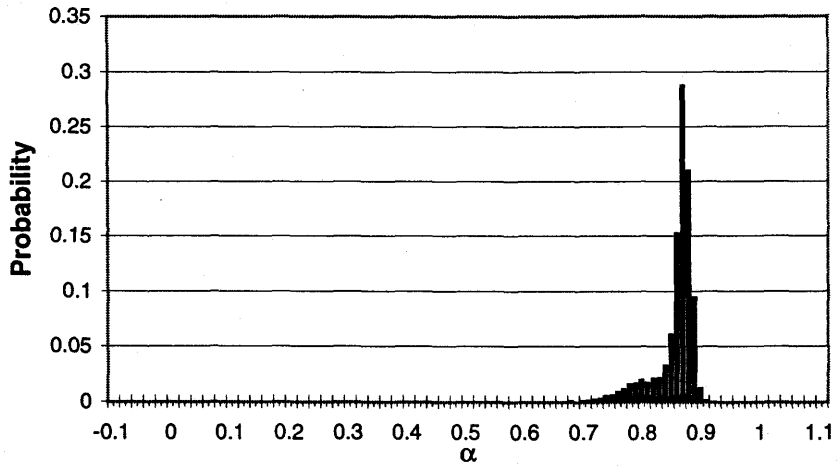

Figure C.16 - Void fraction PDF for 96F1P30 - A.

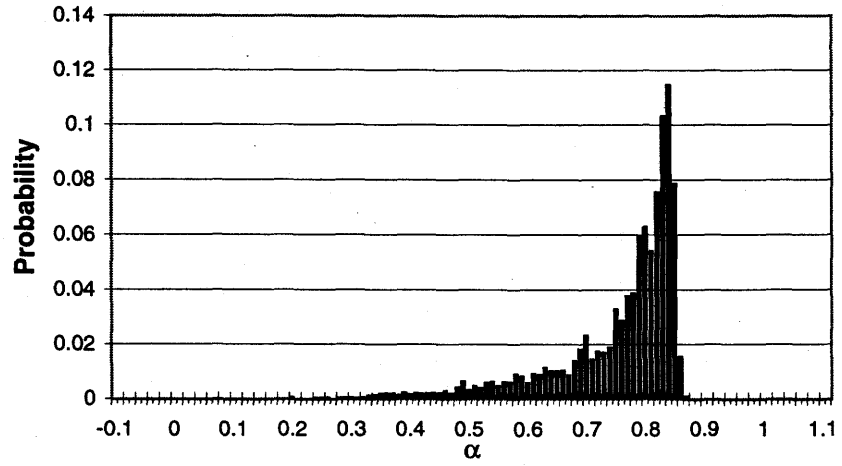

Figure C.17 - Void fraction PDF for 96F1P32 - T.

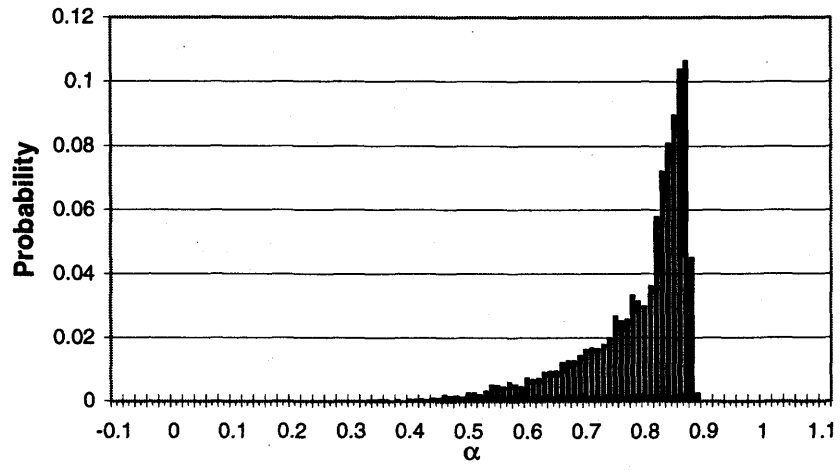

Figure C.18 - Void fraction PDF and video image for 96F1P33 - T.

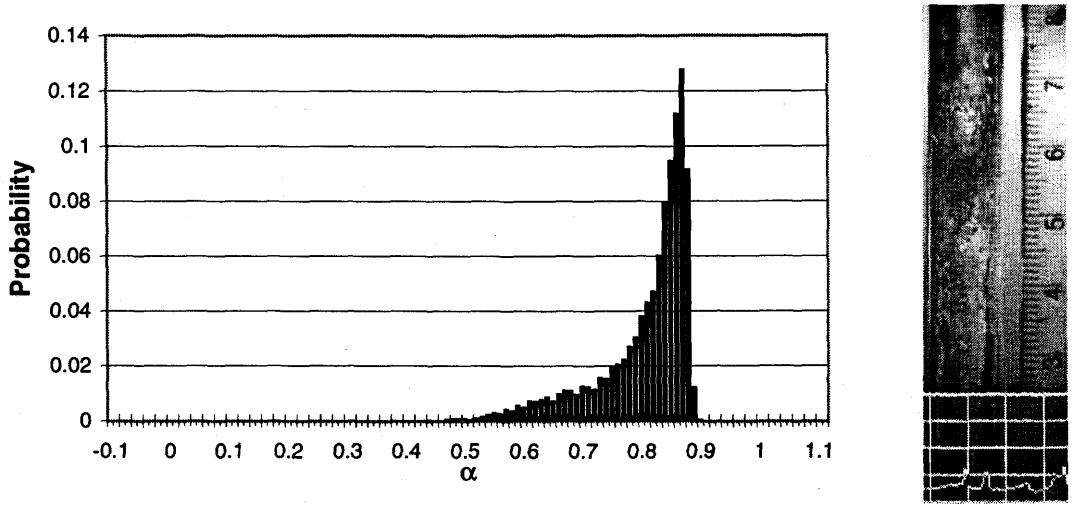

Figure C.19 - Void fraction PDF and flow image for 96F1P34 - T-A.

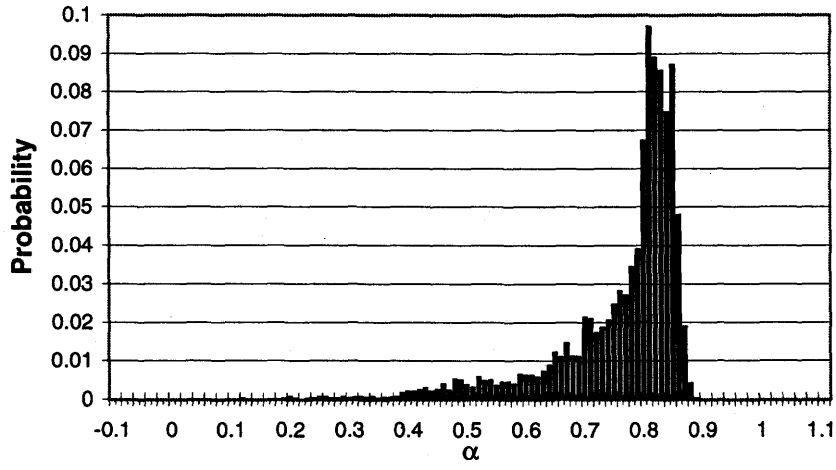

Figure C.20 - Void fraction PDF for 96F2P2 - T.

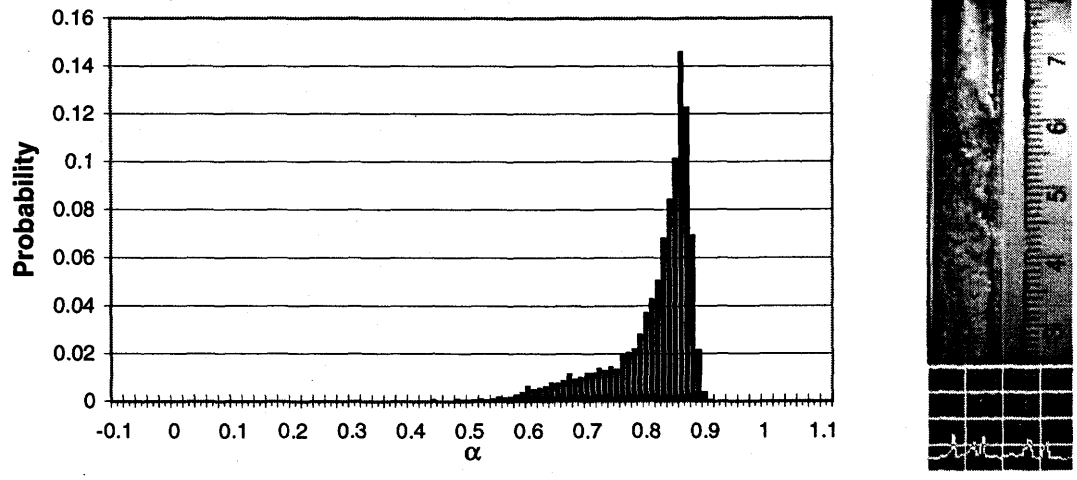

Figure C.21 - Void fraction PDF and video image for 96F2P5 - T-A.

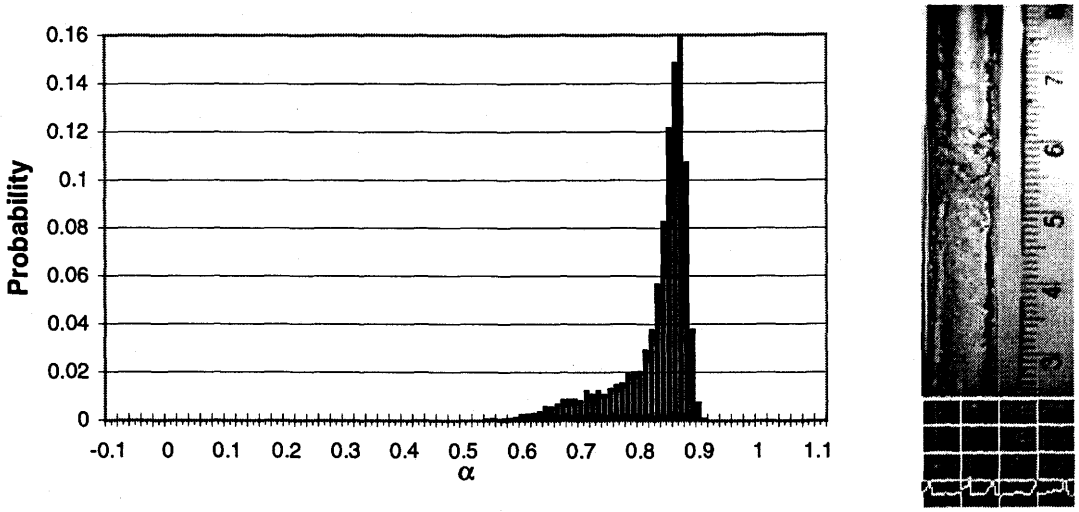

Figure C.22 - Void fraction PDF and video image for 96F2P6 - A.

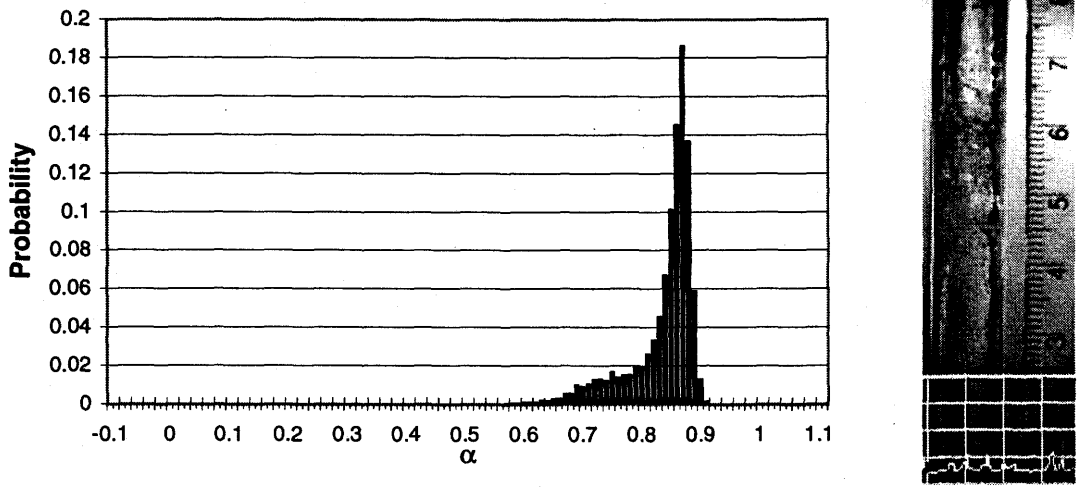

Figure C.23 - Void fraction PDF and video image for 96F2P7 - A.

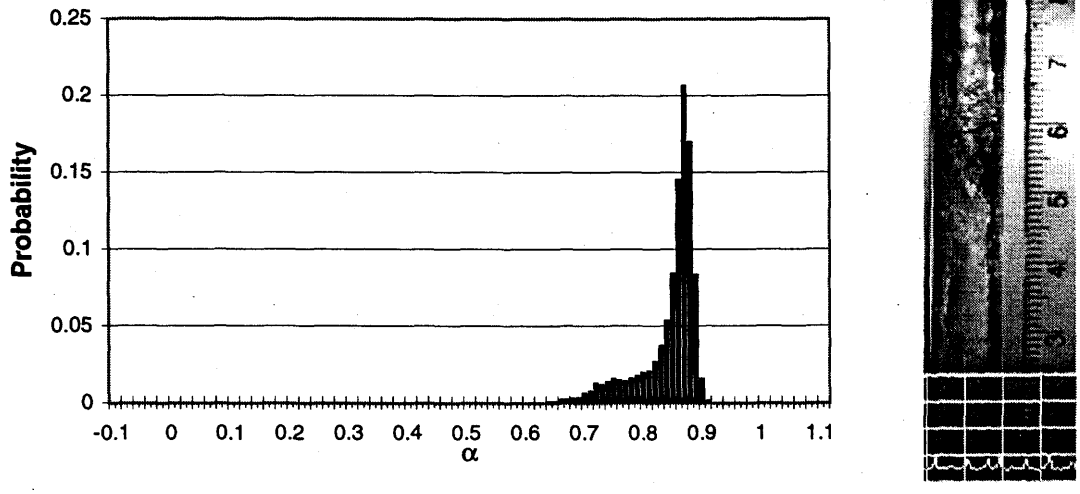

Figure C.24 - Void fraction PDF and video image for 96F2P8 - A.

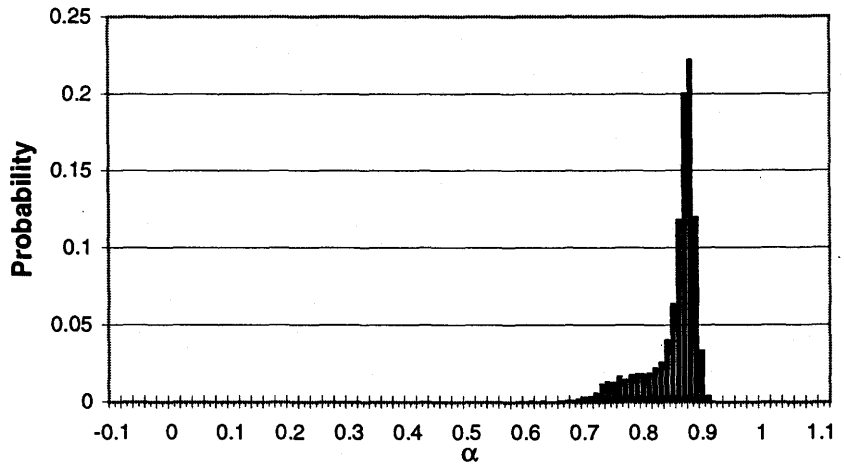

Figure C.25 - Void fraction PDF for 96F2P10 - A.

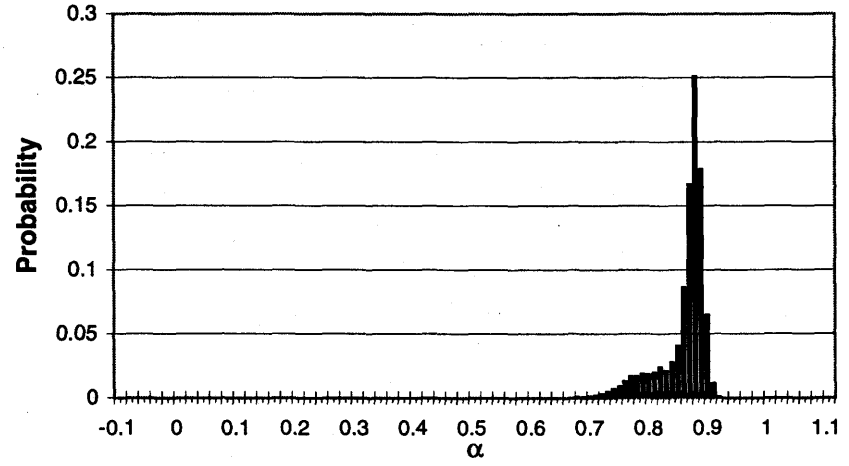

Figure C.26 - Void fraction PDF for 96F2P11 - A.

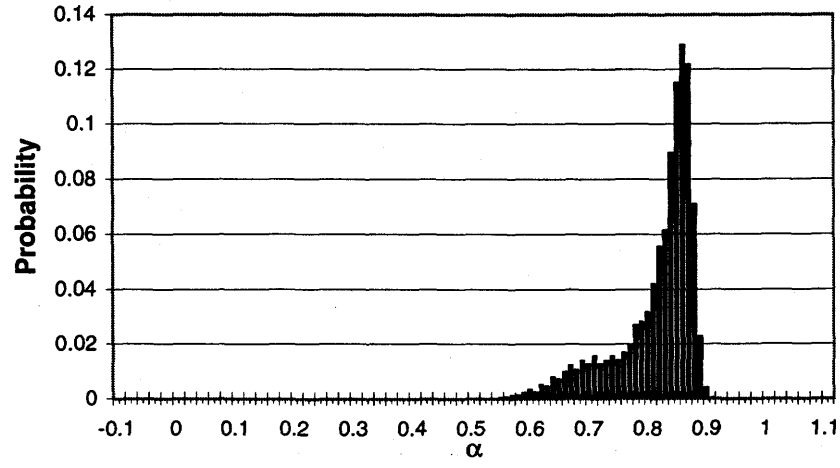

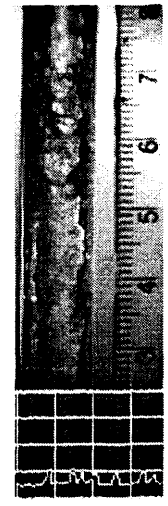

Figure C.27 - Void fraction PDF and video image for 96F2P12 - A.

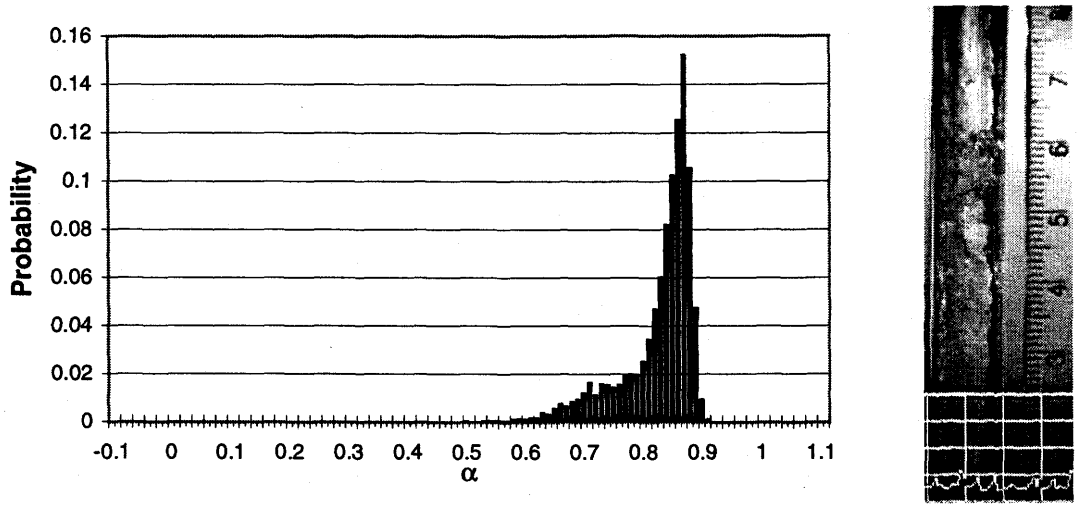

Figure C.28 - Void fraction PDF and video image for 96F2P13 - A.

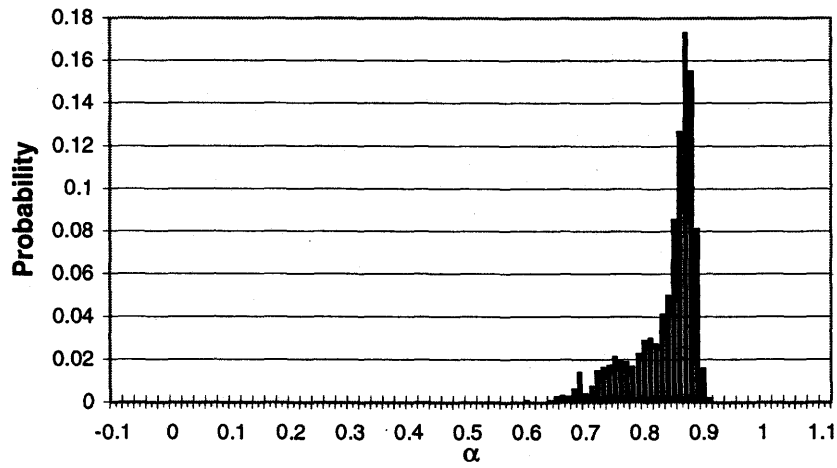

Figure C.29 - Void fraction PDF for 96F2P14 - A.

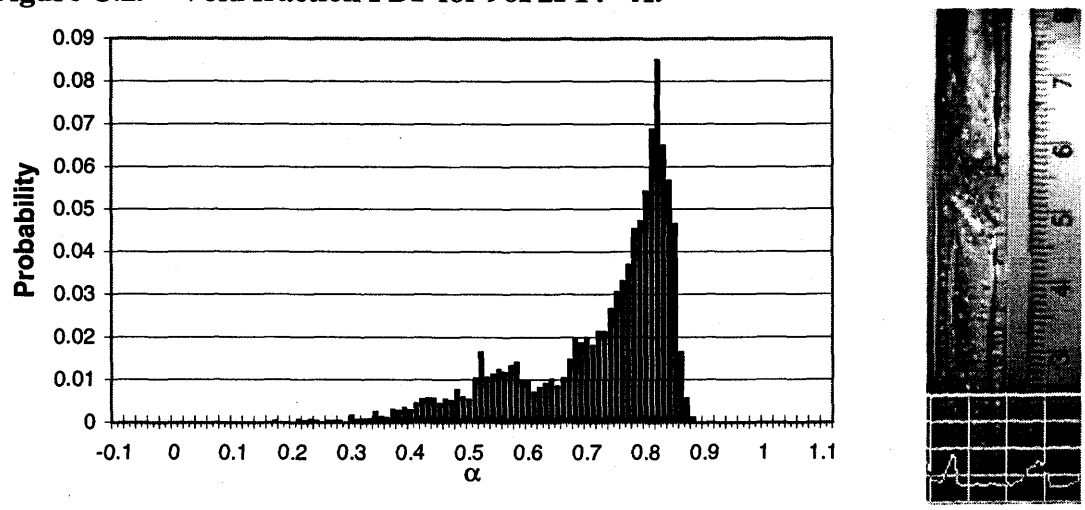

Figure C.30 - Void fraction PDF and video image for 96F2P15 - T.

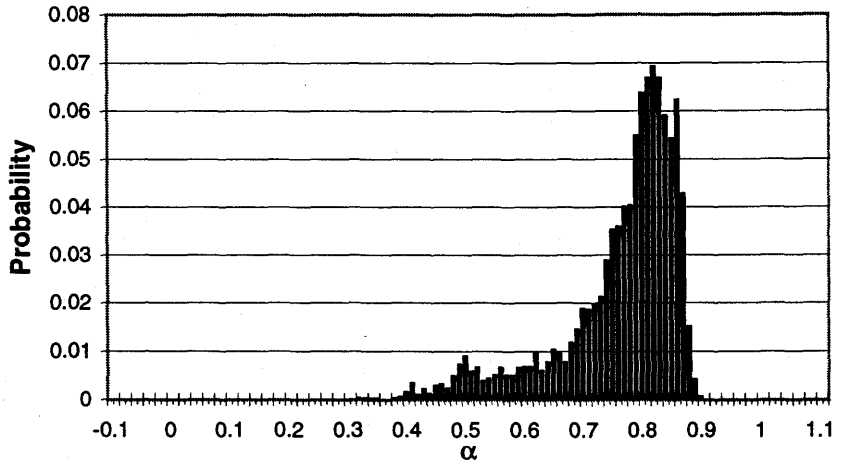

Figure C.31 - Void fraction PDF for 96F2P16 - T.

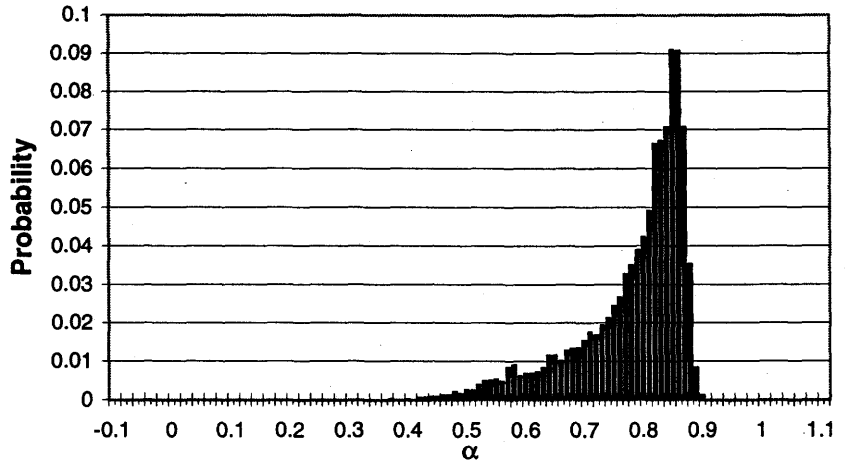

Figure C.32 - Void fraction PDF for 96F2P18 - T.

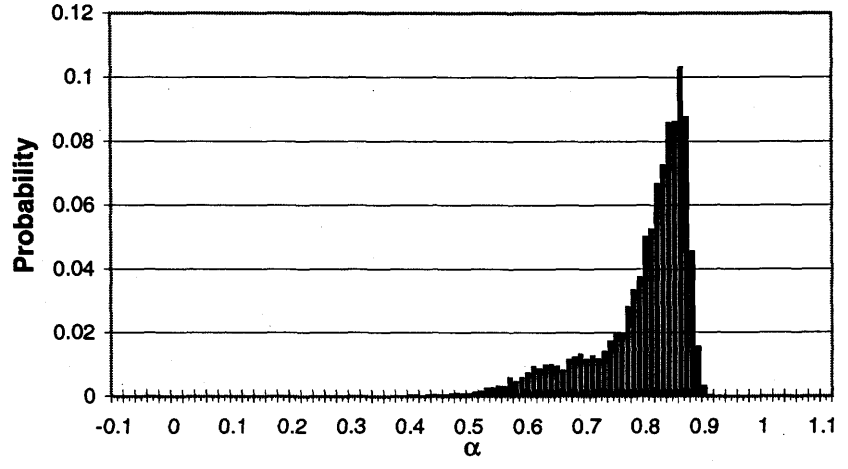

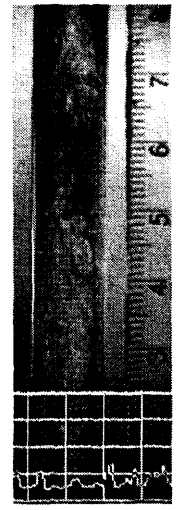

Figure C.33 - Void fraction PDF and video image for 96F2P19 - T.

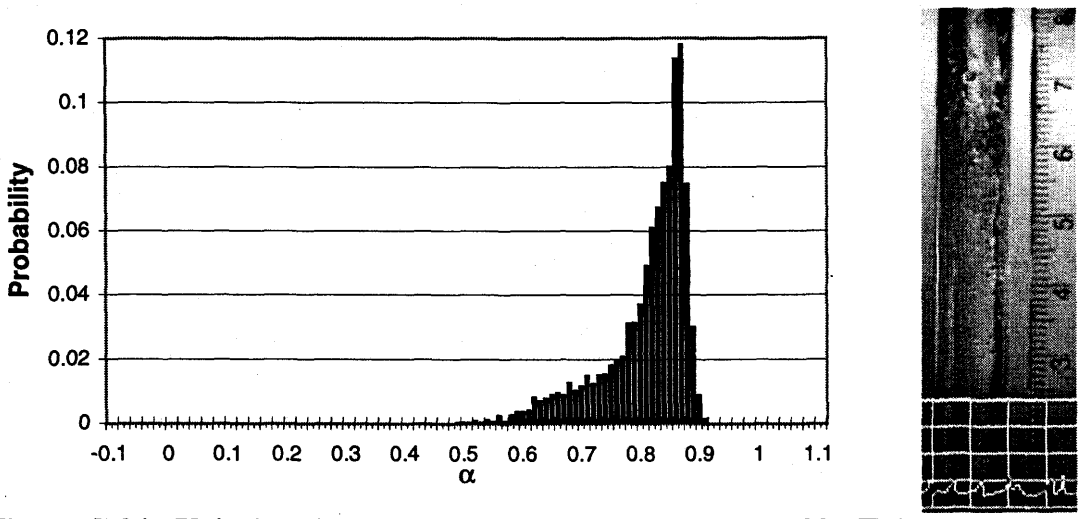

Figure C.34 - Void fraction PDF and video image for 96F2P20 - T-A.

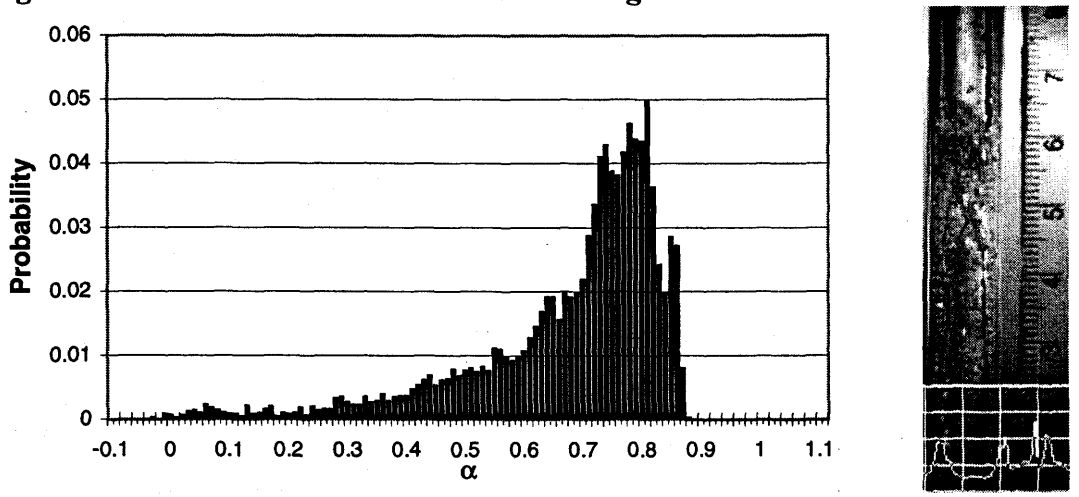

Figure C.35 - Void fraction PDF and video image for 96F2P21 - T.

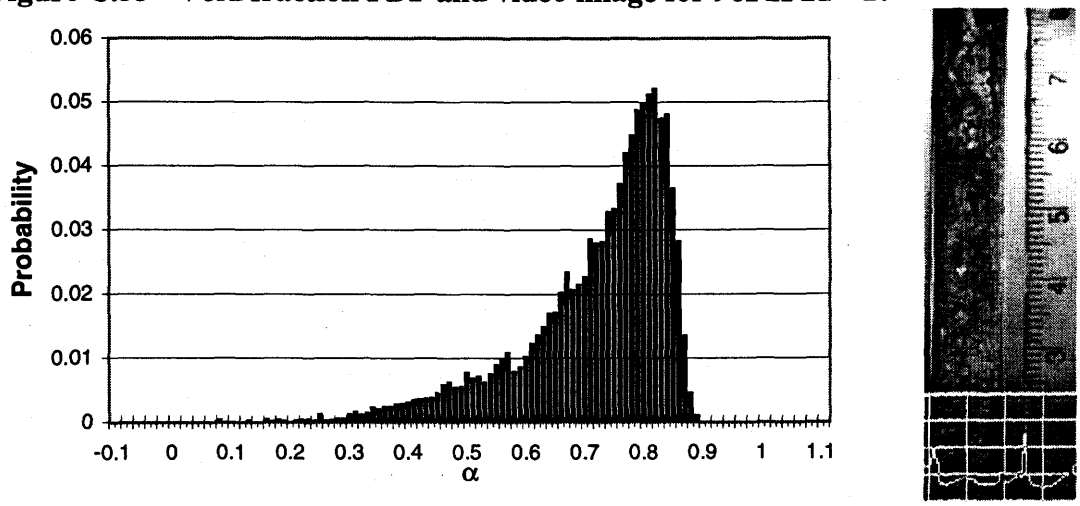

Figure C.36 - Void fraction PDF and video image for 96F2P22 - T.

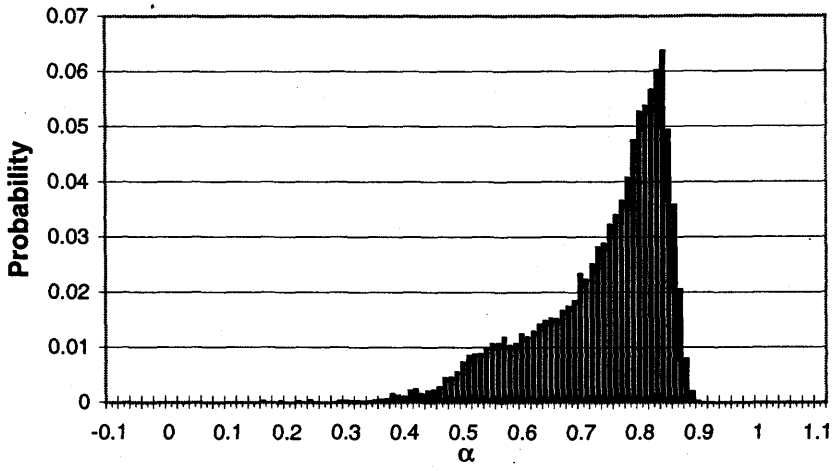

Figure C.37 - Void fraction PDF for 96F2P22 - T.

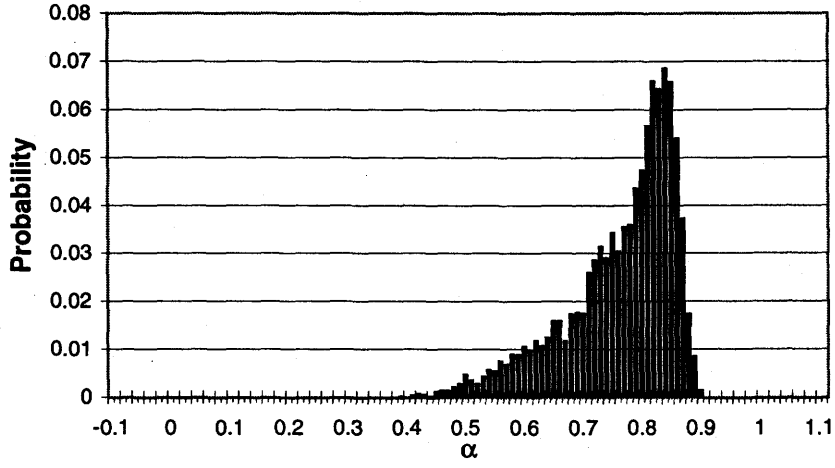

Figure C.38 - Void fraction PDF for 96F2P24 - T.

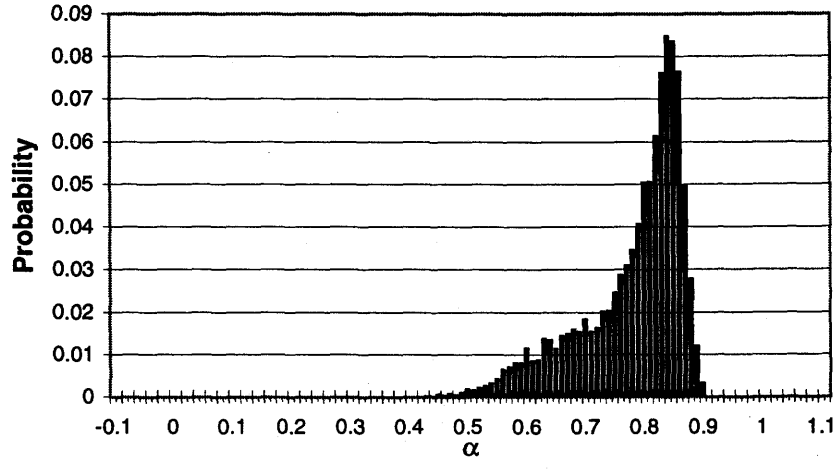

Figure C.39 - Void fraction PDF and video image for 96F2P26 - T.

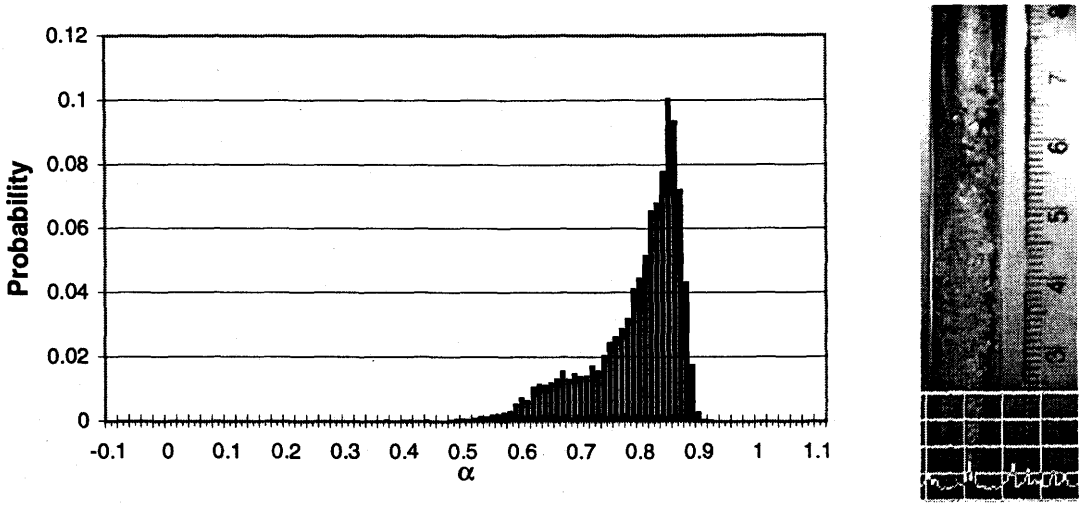

Figure C.40 - Void fraction PDF and video image for 96F2P27 - T-A.

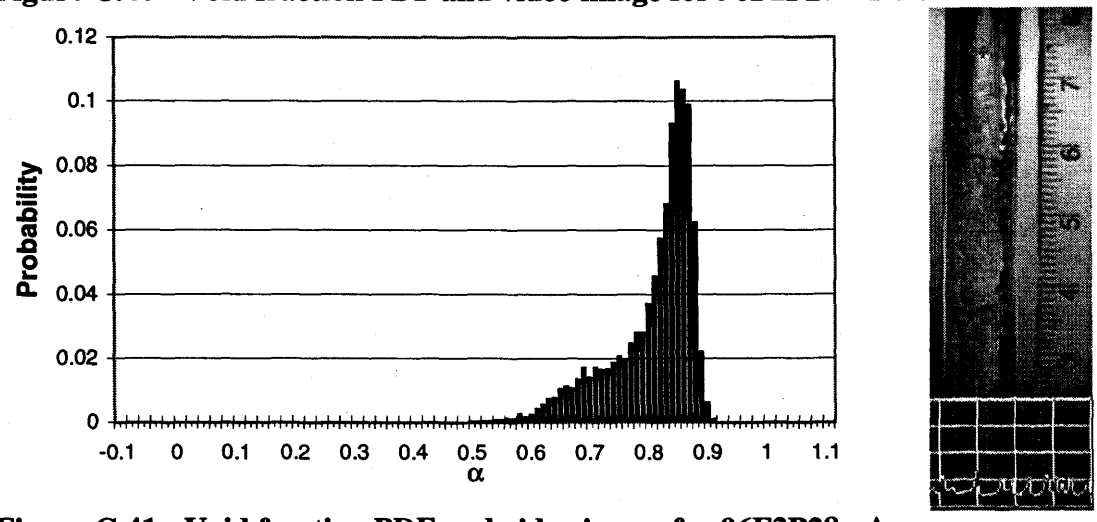

Figure C.41 - Void fraction PDF and video image for 96F2P28 - A.

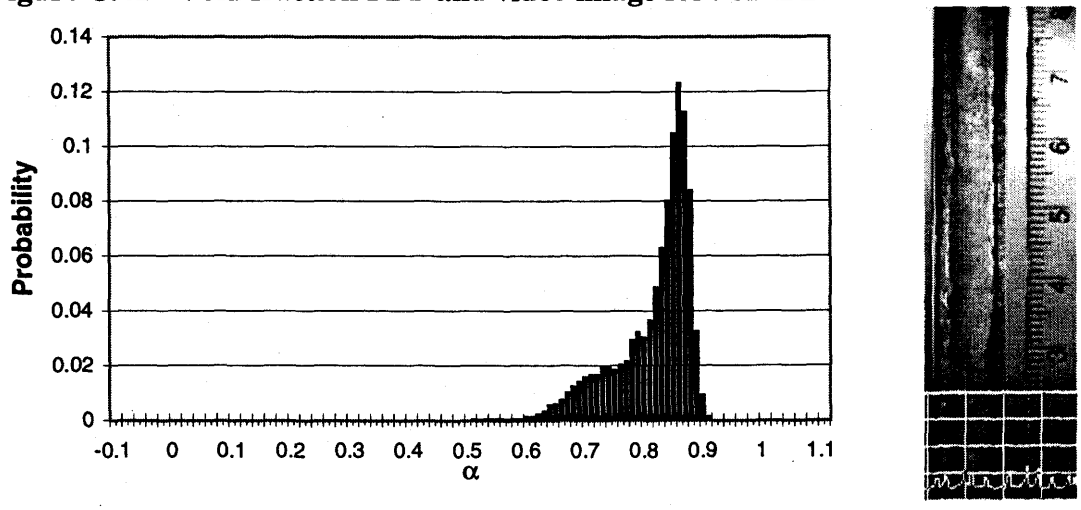

Figure C.42 - Void fraction PDF and video image for 96F2P29 - A.

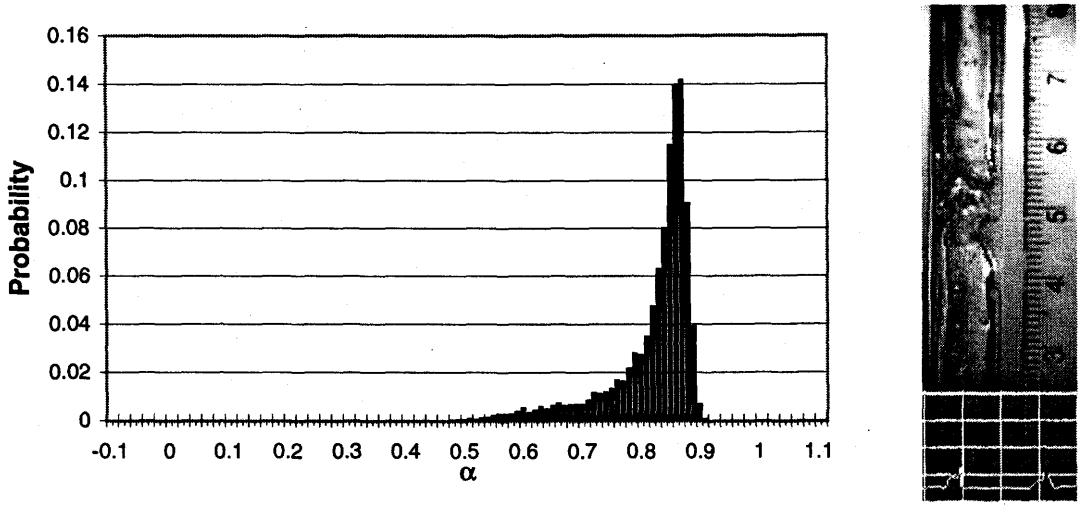

Figure C.43 - Void fraction PDF and video image for 96F2P32 - T-A.

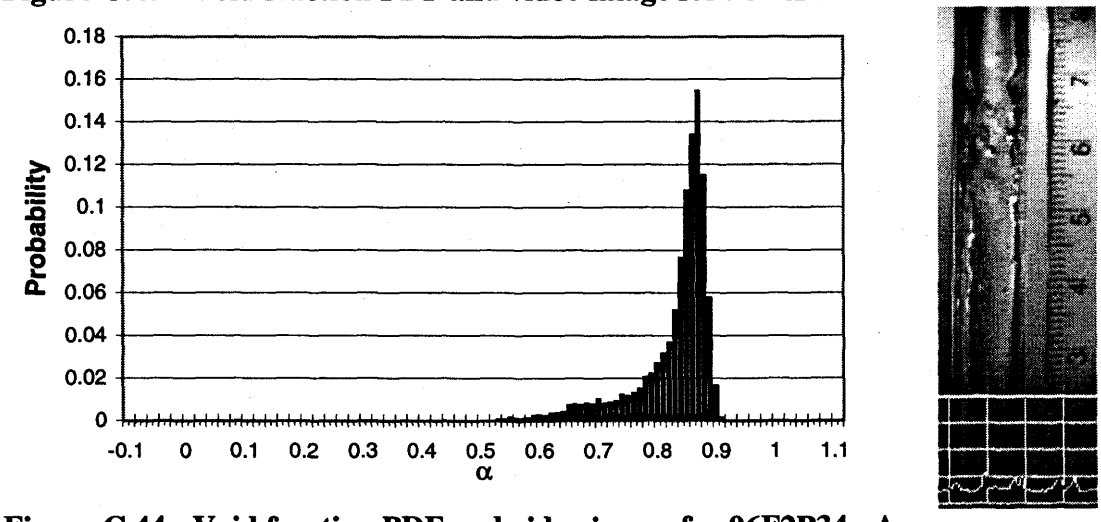

Figure C.44 - Void fraction PDF and video image for 96F2P34 - A.

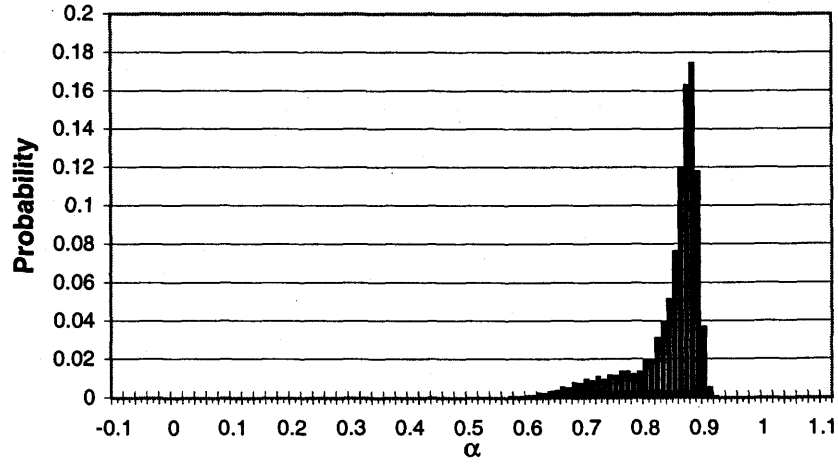

Figure C.45 - Void fraction PDF for 96F2P35 - A.

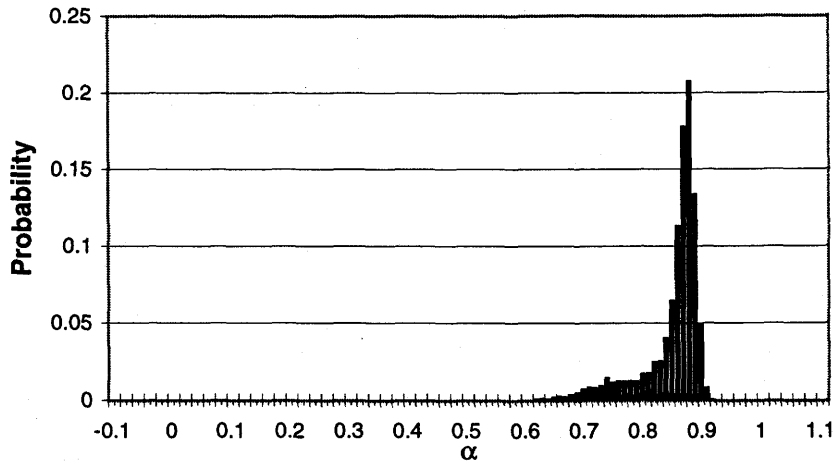

Figure C.46 - Void fraction PDF for 96F2P36 - A.

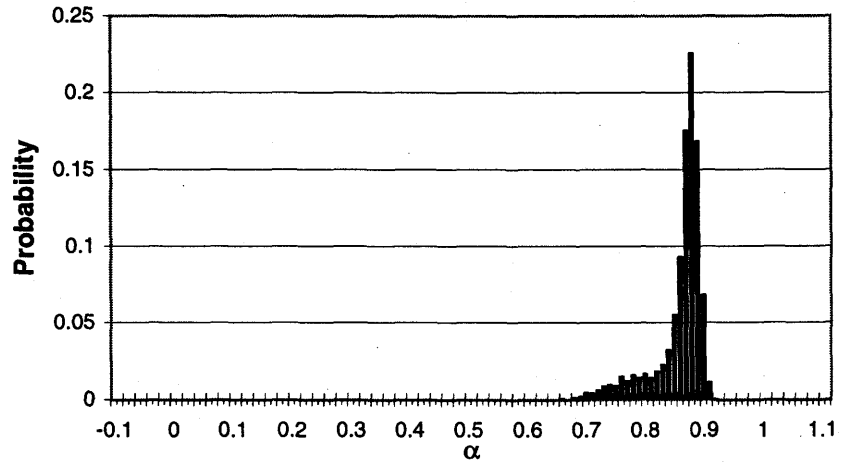

Figure C.47 - Void fraction PDF for 96F2P37 - A.

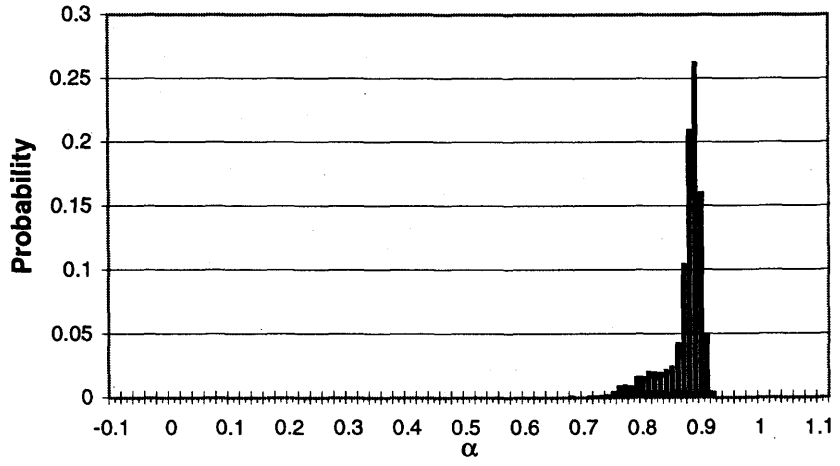

Figure C.48 - Void fraction PDF for 96F2P39 - A.

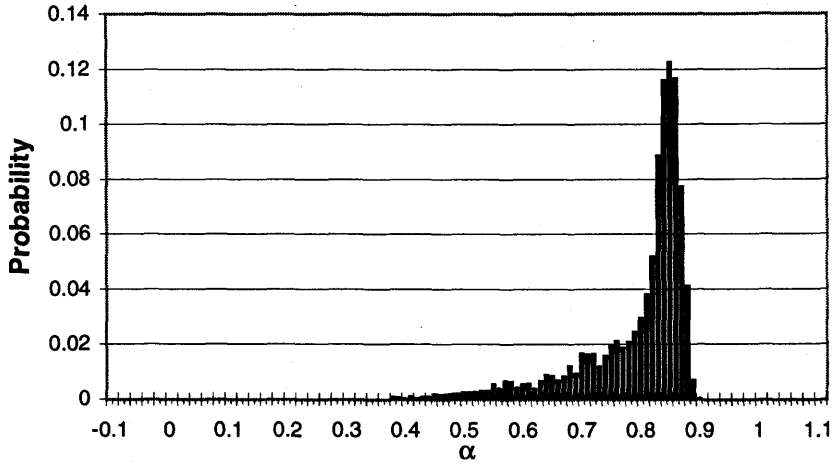

Figure C.49 - Void fraction PDF for 96F2P40 - T.

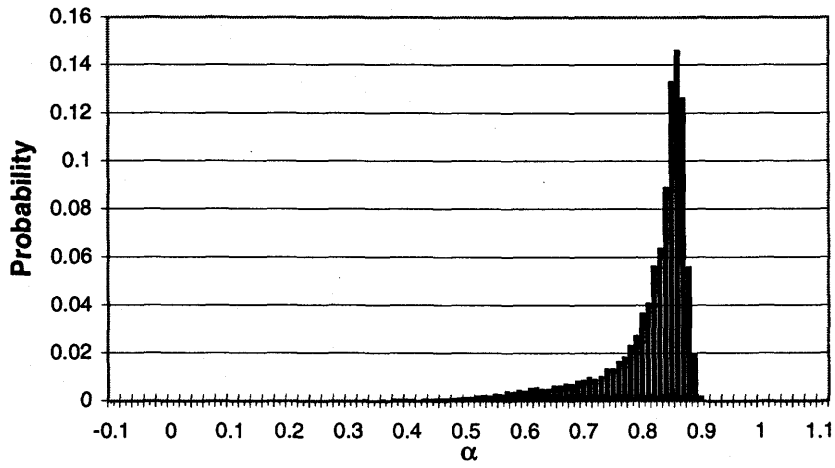

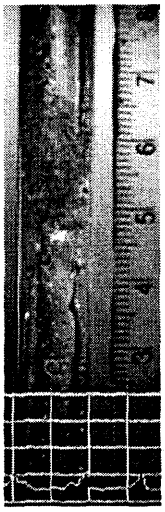

Figure C.50 - Void fraction PDF and video image for 96F2P42 - T.

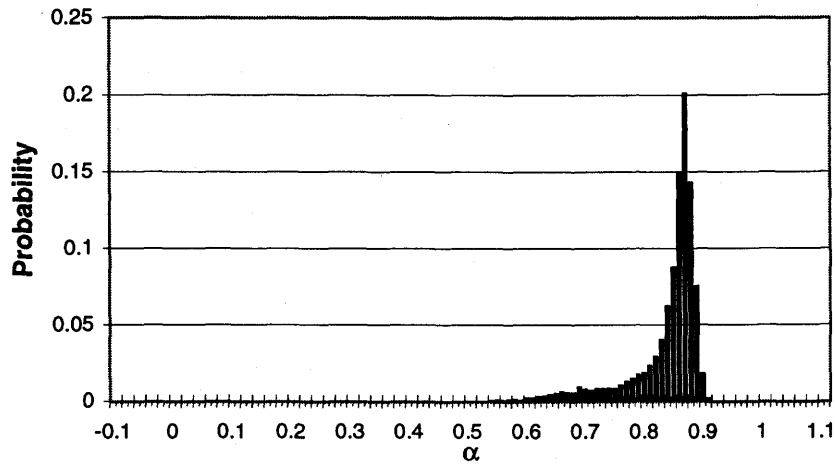

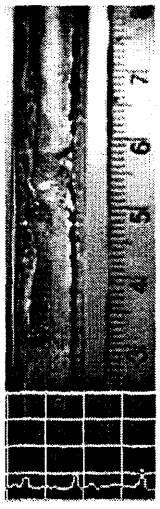

Figure C.51 - Void fraction PDF and video image for 96F2P42 - A.

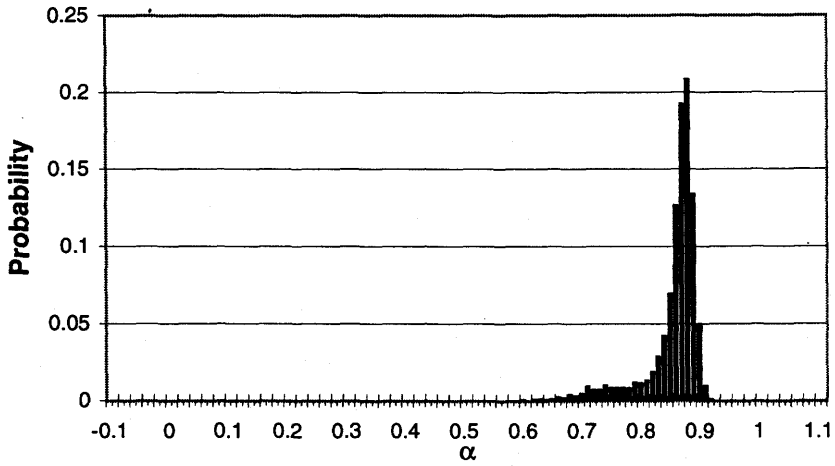

Figure C.52 - Void fraction PDF for 96F2P44 - A.

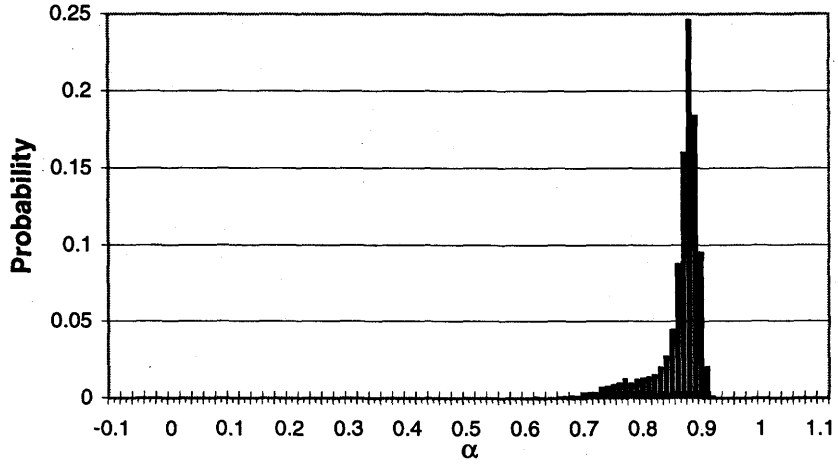

Figure C.53 - Void fraction PDF for 96F2P45 - A.

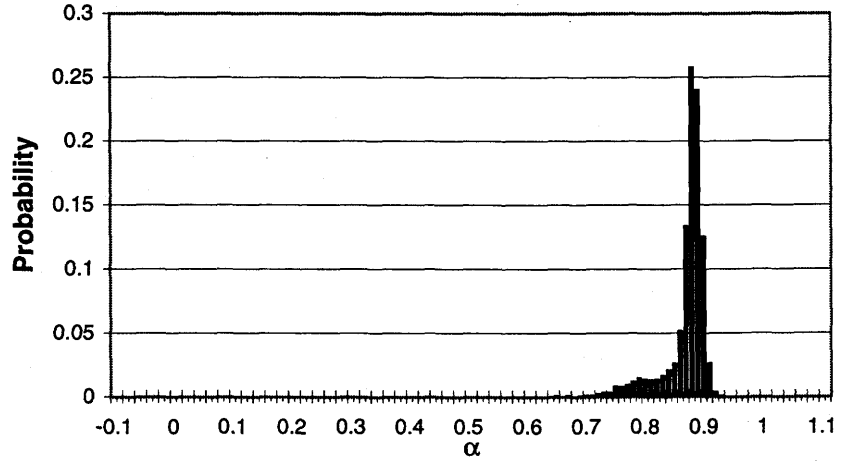

Figure C.54 - Void fraction PDF for 96F2P46 - A.

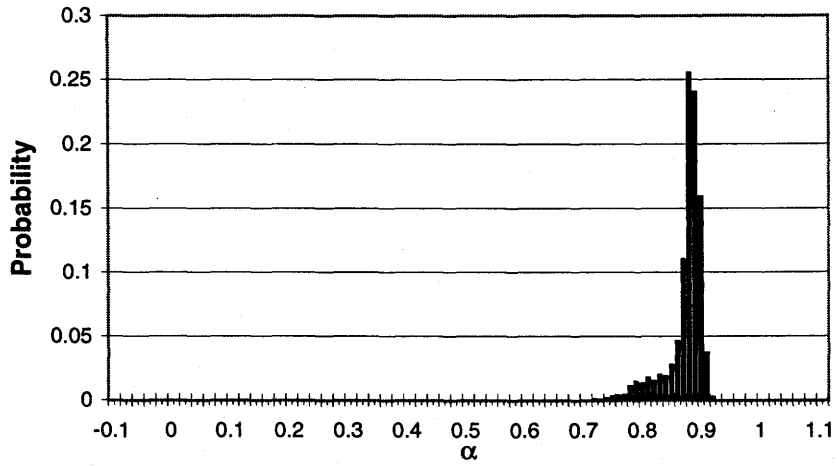

Figure C.55 - Void fraction PDF for 96F2P47 - A.

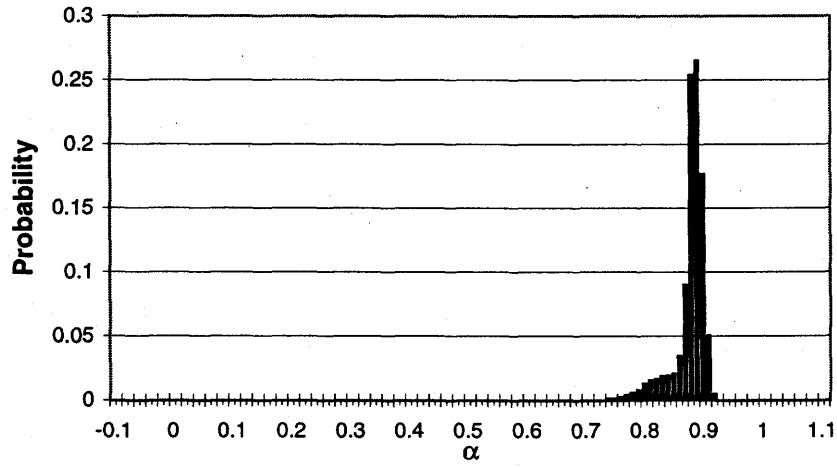

Figure C.56 - Void fraction PDF and video image for 96F2P48 - A.

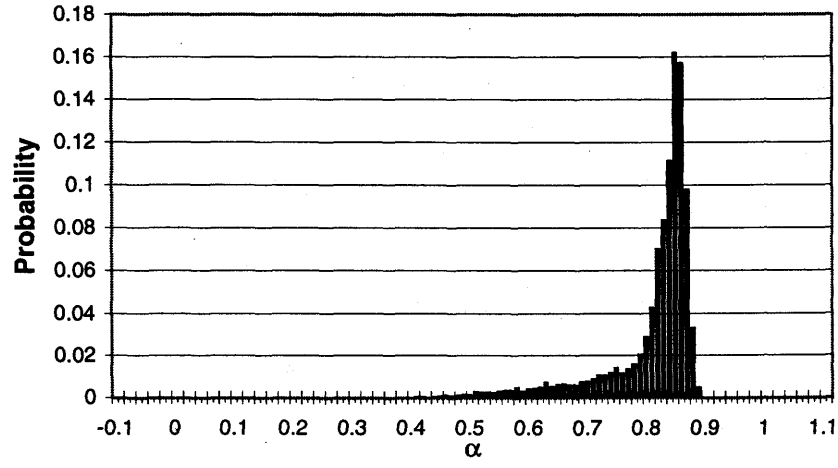

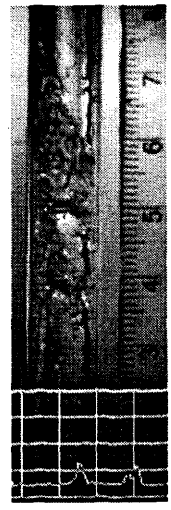

Figure C.57 - Void fraction PDF and video image for 96F2P50 - T.

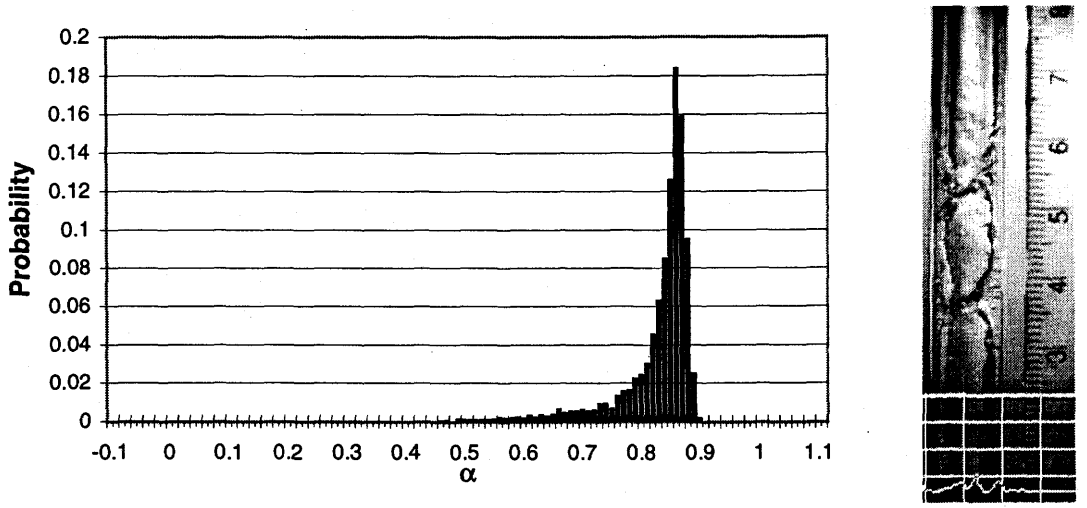

Figure C.58 - Void fraction PDF and video image for 96F2P51 - T-A.

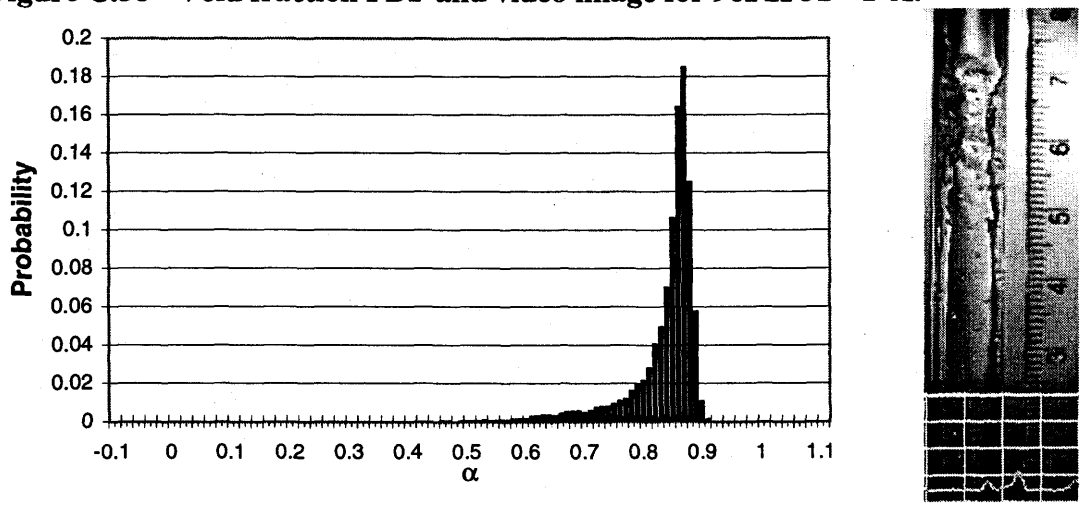

Figure C.59 - Void fraction PDF and video image for 96F2P52 - A.

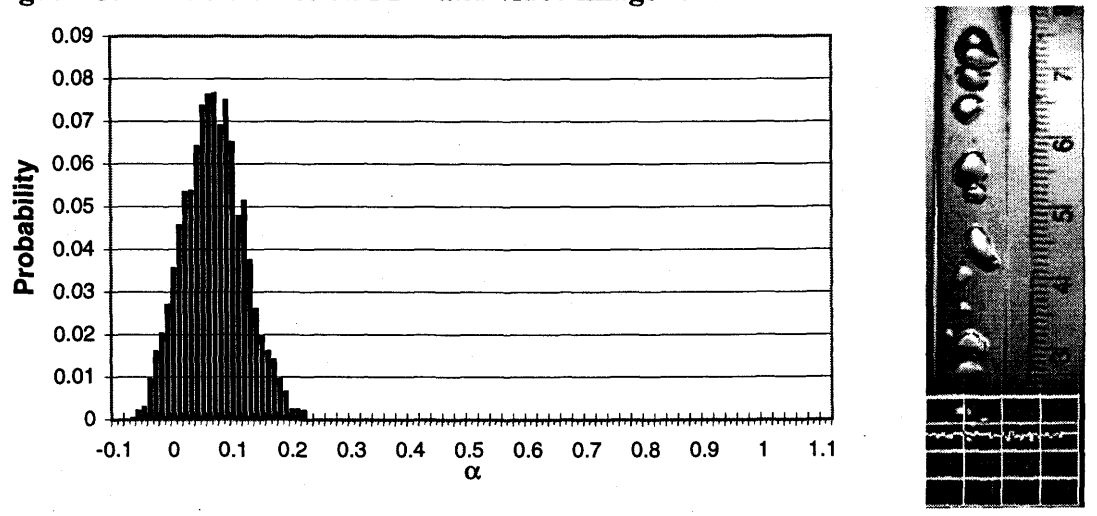

Figure C.60 - Void fraction PDF and video image for 96F3P2 - B.

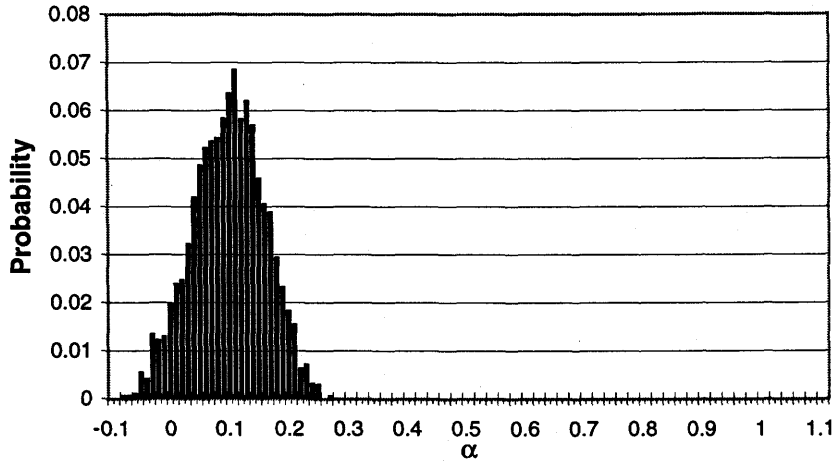

Figure C.61 - Void fraction PDF for 96F3P3 - B.

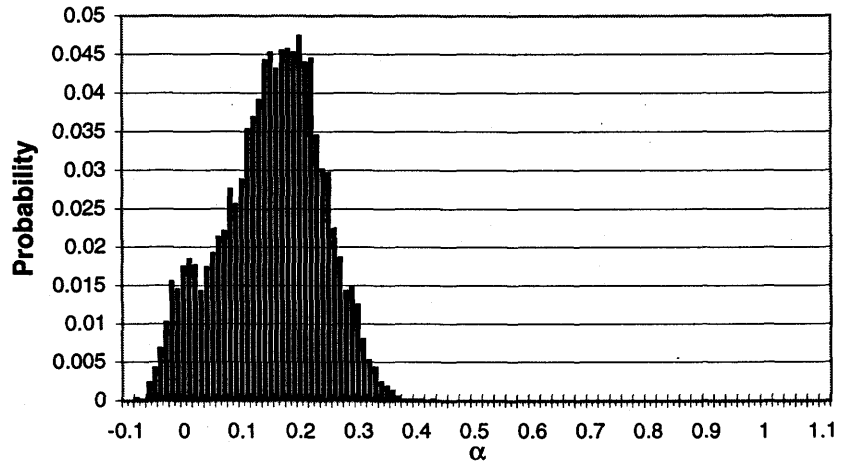

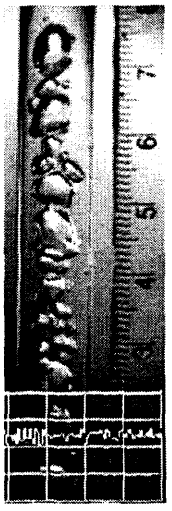

Figure C.62 - Void fraction PDF and video image for 96F3P5 - B.

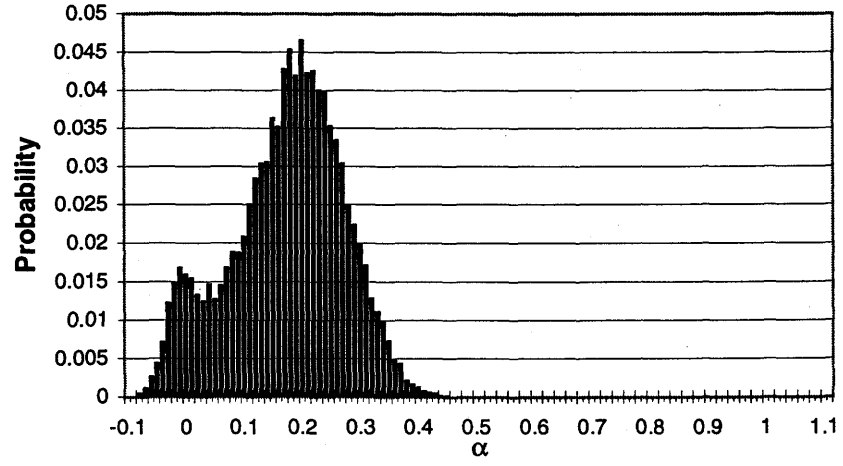

Figure C.63 - Void fraction PDF and video image for 96F3P6 - B-S.

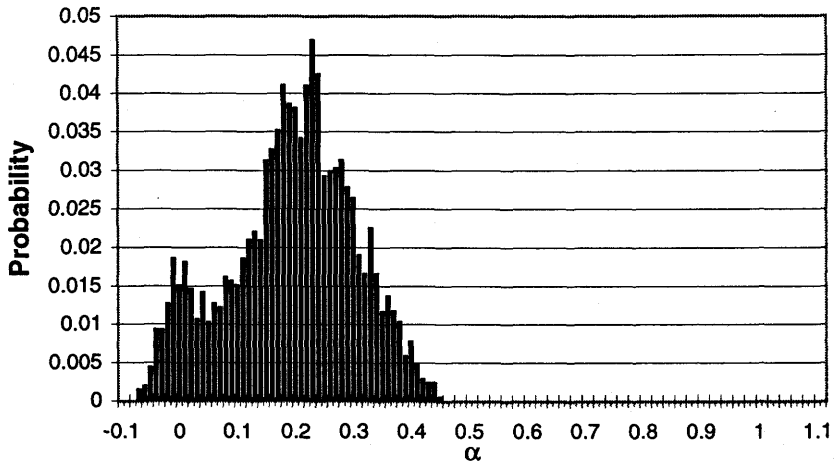

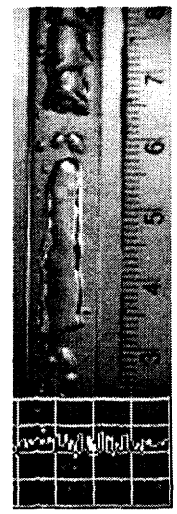

Figure C.64 - Void fraction PDF and video image for 96F3P7 - S.

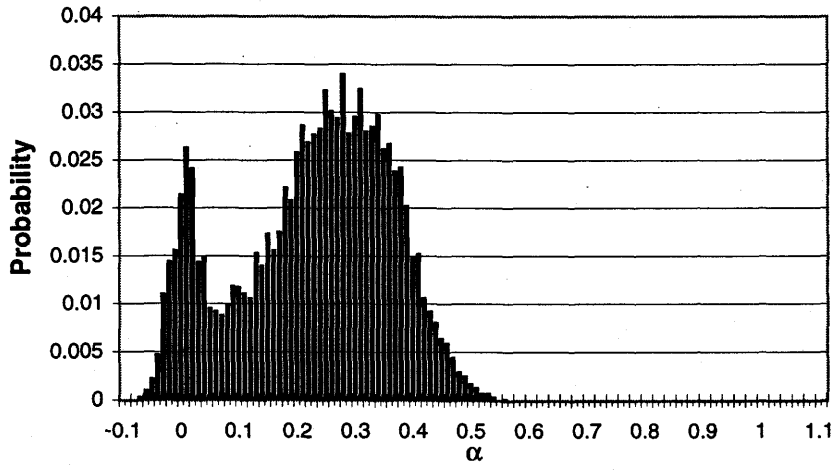

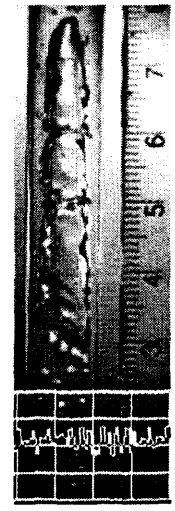

Figure C.65 - Void fraction PDF and video image for 96F3P8 - S.

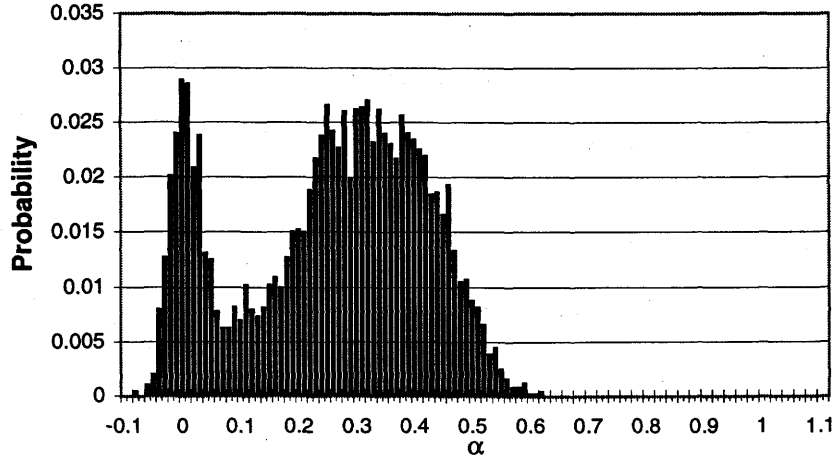

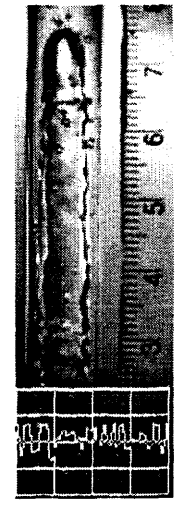

Figure C.66 - Void fraction PDF and video image for 96F3P10 - S.

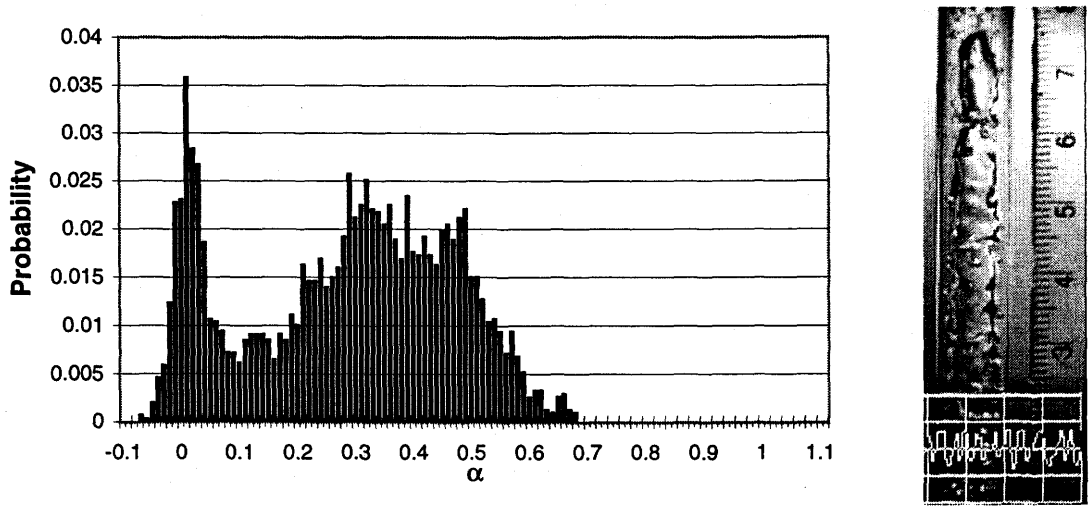

Figure C.67 - Void fraction PDF and video image for 96F3P11 - S.

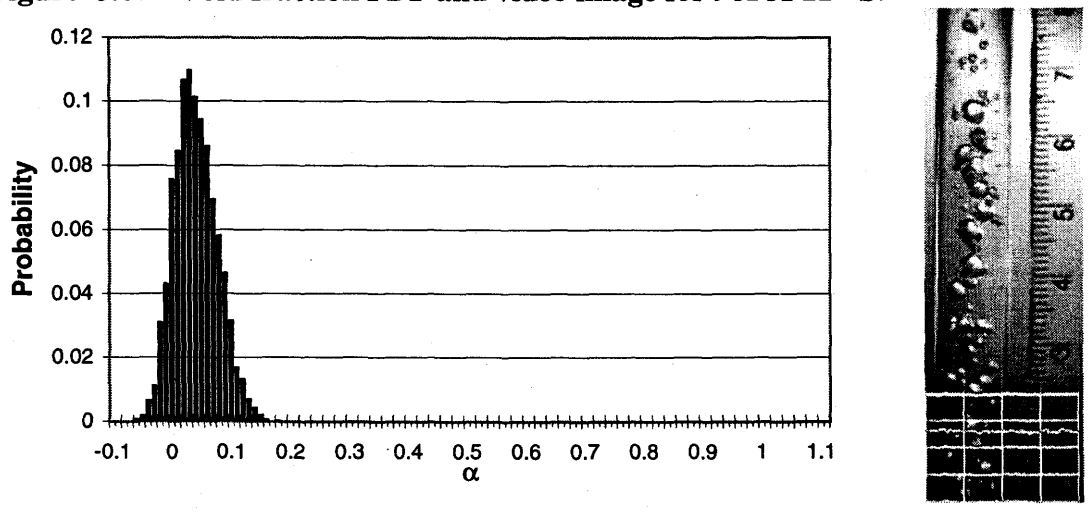

Figure C.68 - Void fraction PDF and video image for 96F3P12 - B.

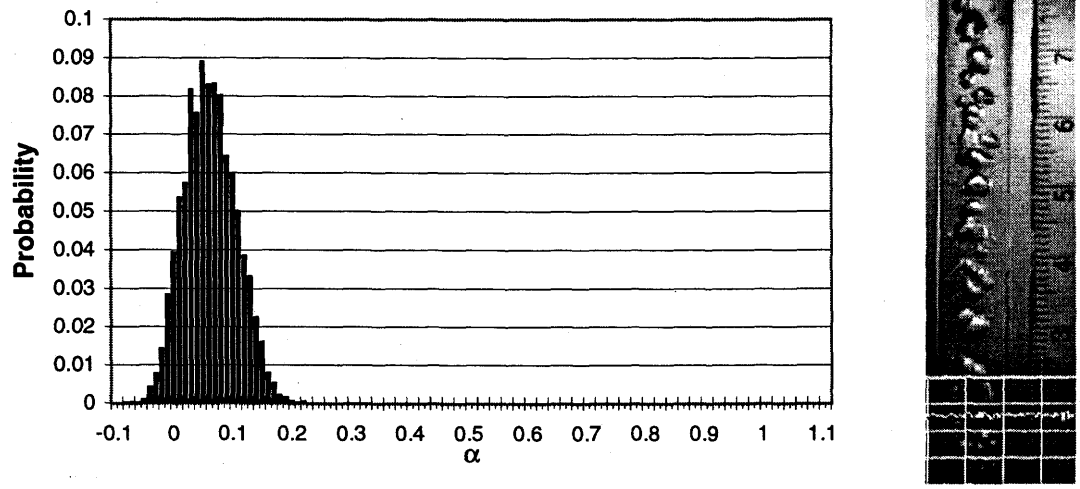

Figure C.69 - Void fraction PDF and video image for 96F3P13 - B.

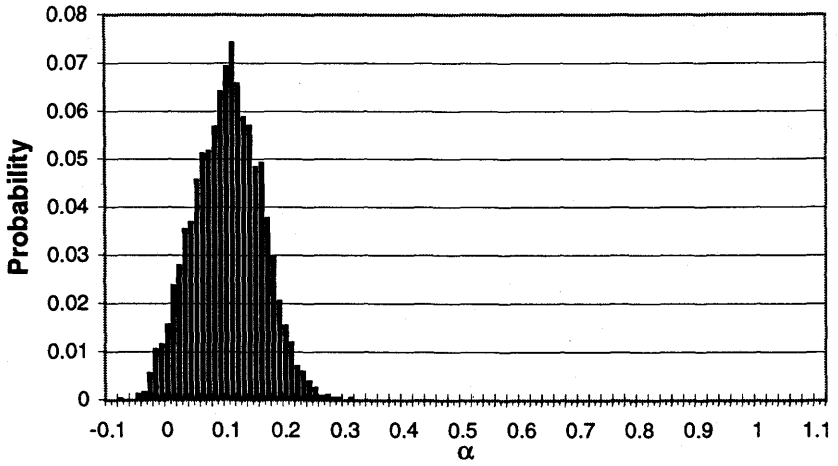

Figure C.70 - Void fraction PDF for 96F3P15 - B.

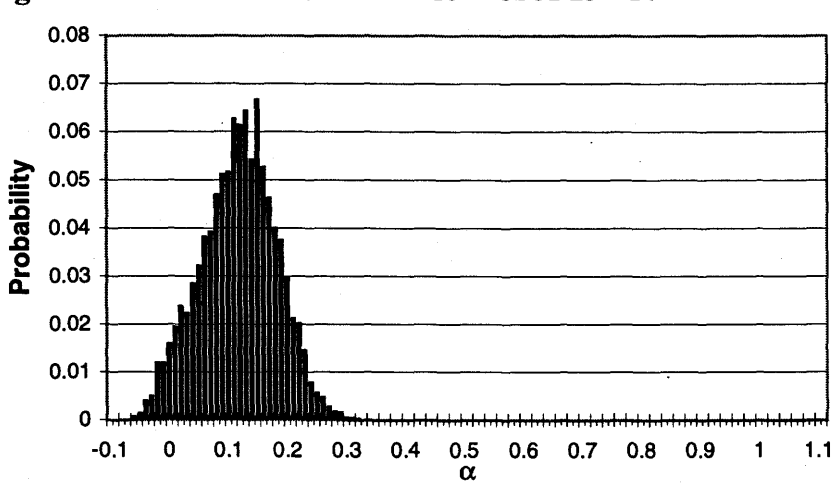

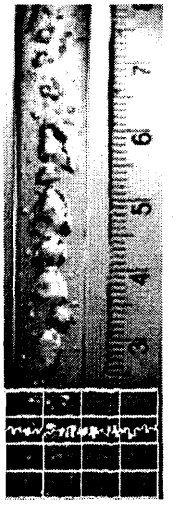

Figure C.71 - Void fraction PDF and video image for 96F3P16 - B.

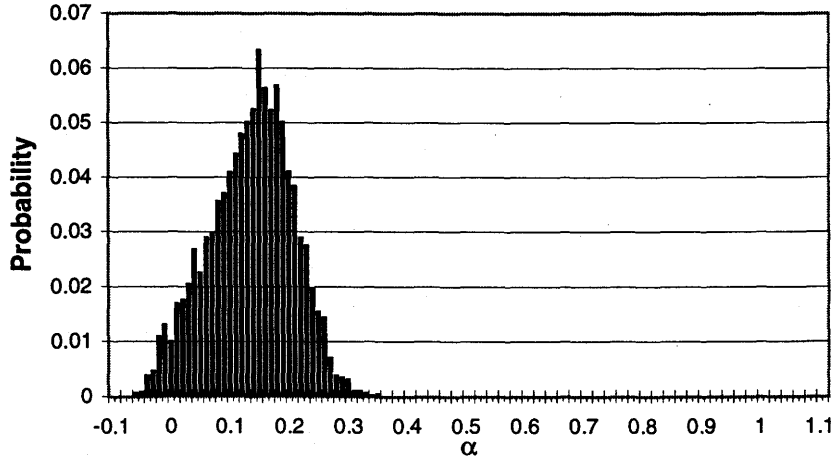

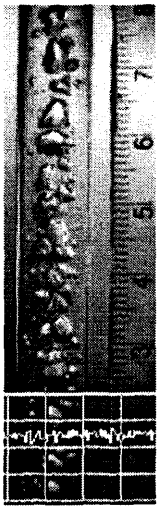

Figure C.72 - Void fraction PDF and video image for 96F3P18 - B.

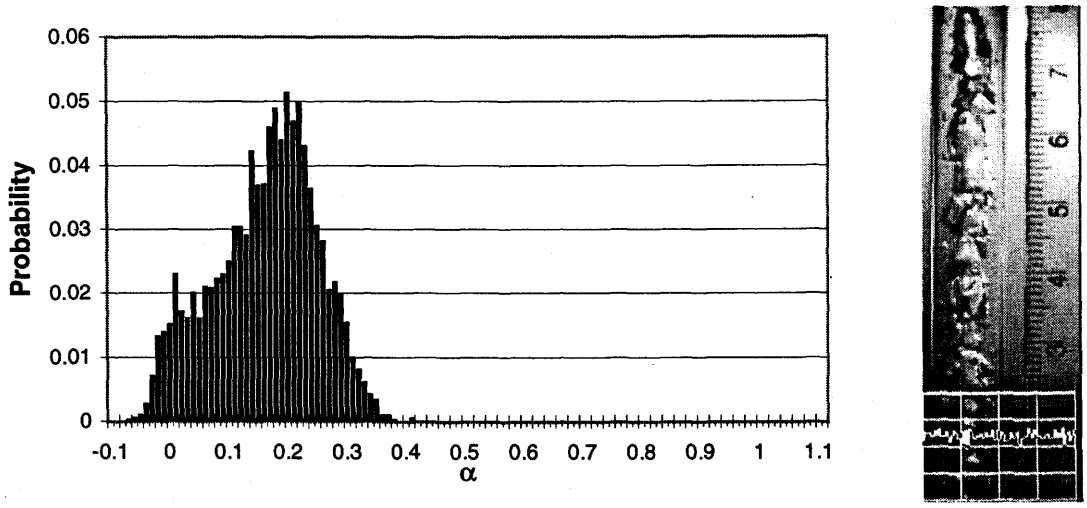

Figure C.73 - Void fraction PDF and video image for 96F3P19 - B-S.

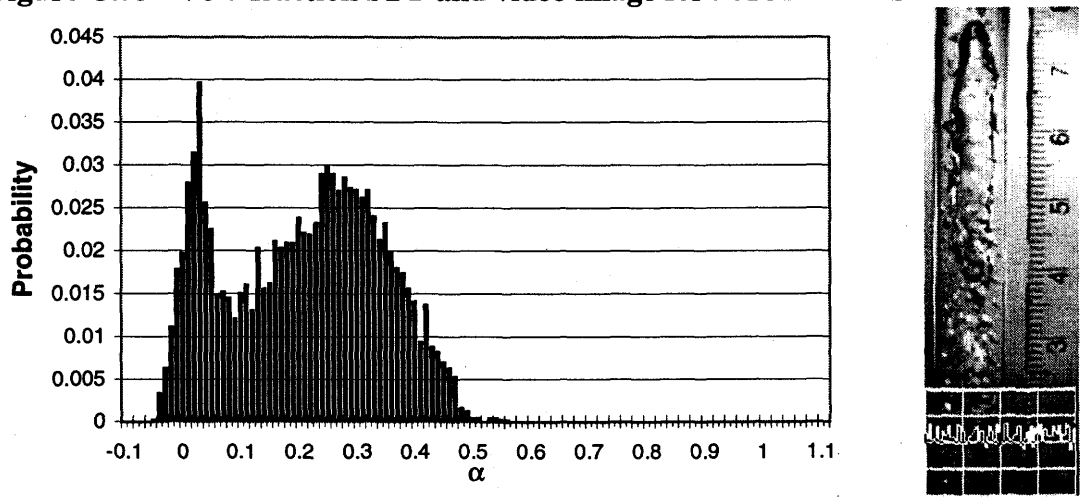

Figure C.74 - Void fraction PDF and video image for 96F3P21 - S.

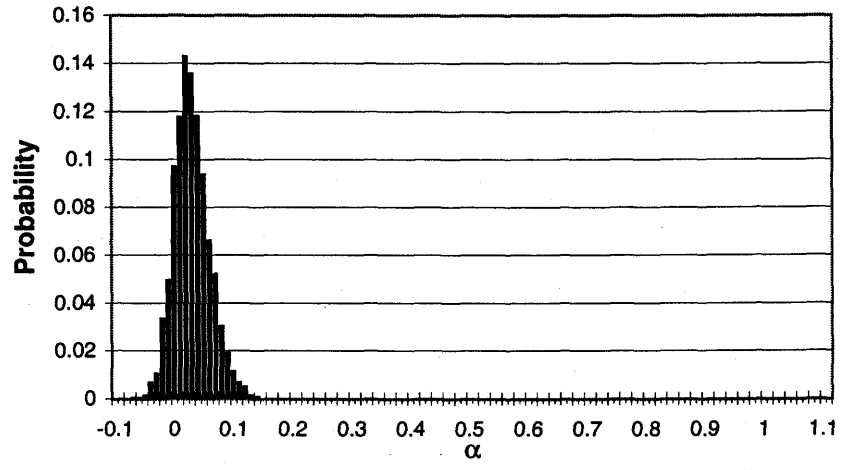

Figure C.75 - Void fraction PDF for 96F3P22 - B.

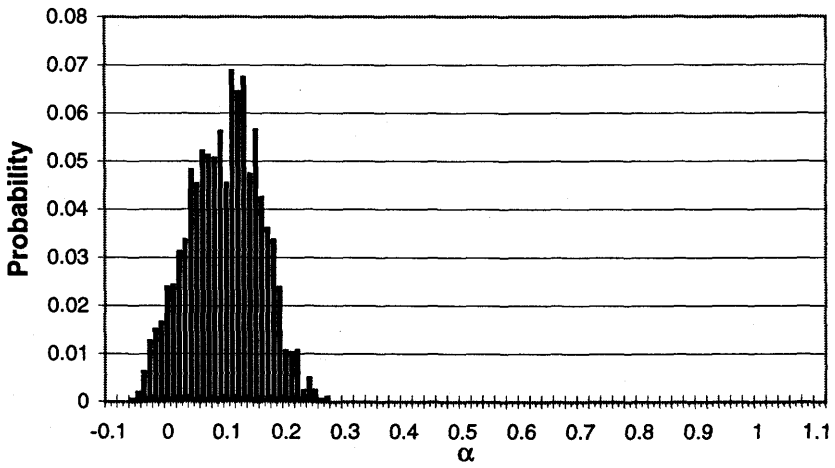

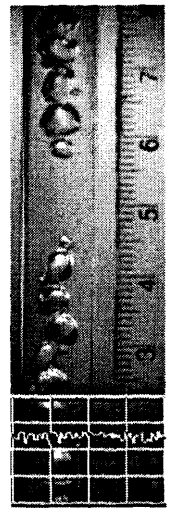

Figure C.76 - Void fraction PDF and video image for 96F3P23 - B.

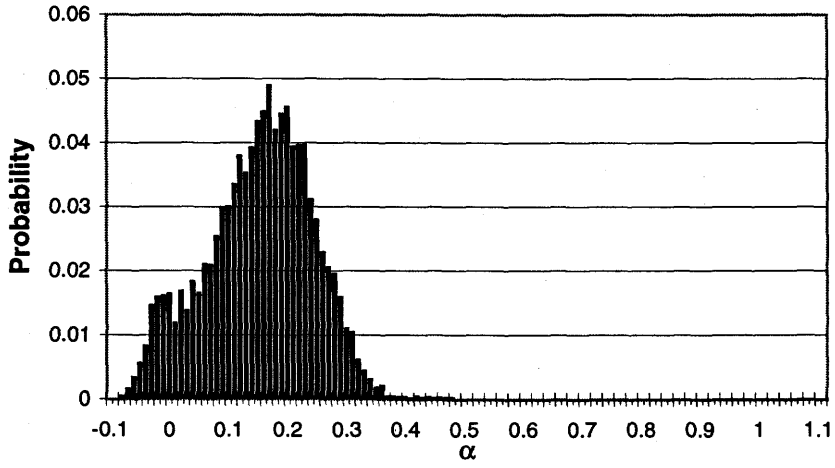

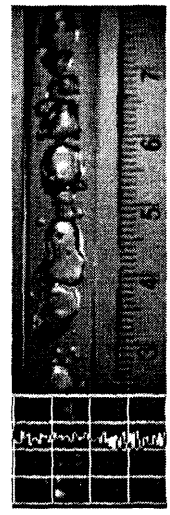

Figure C.77 - Void fraction PDF and video image for 96F3P26 - B-S.

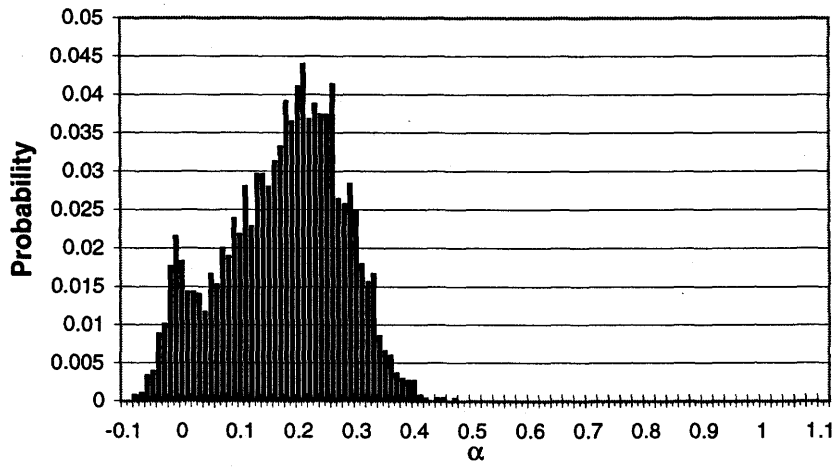

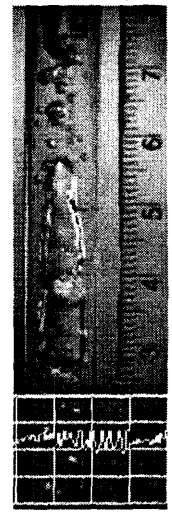

Figure C.78 - Void fraction PDF and video image for 96F3P27 - S.

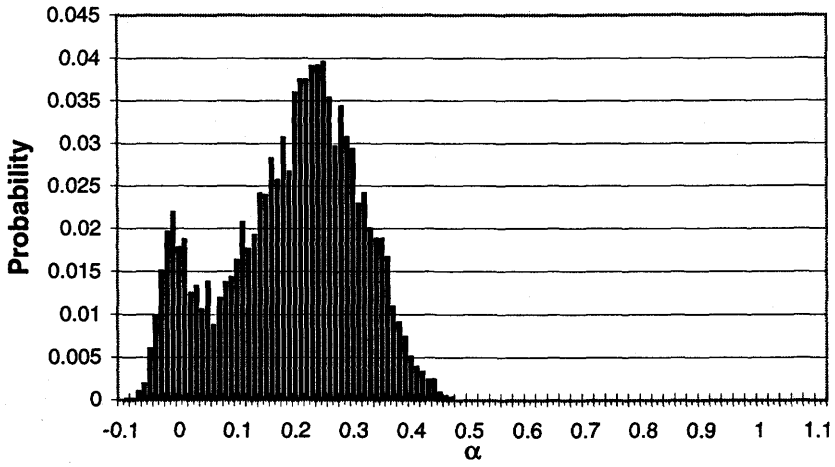

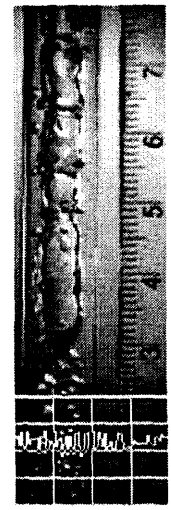

Figure C.79 - Void fraction PDF and video image for 96F3P28 - S.

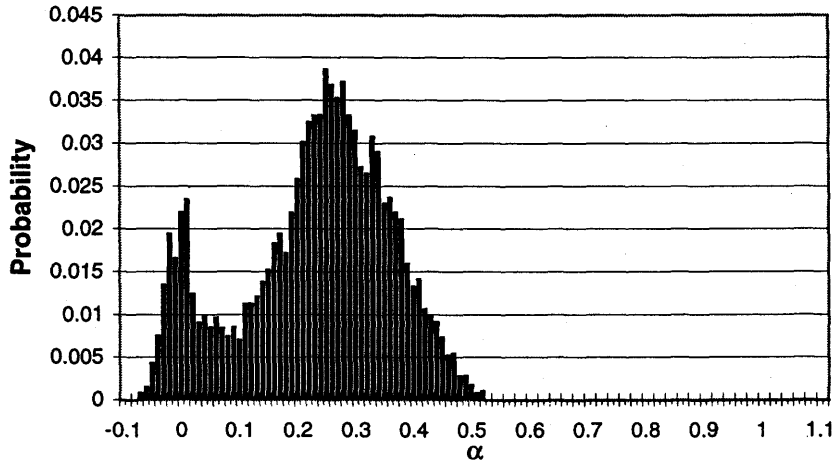

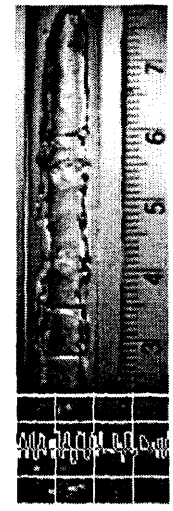

Figure C.80 - Void fraction PDF and video image for 96F3P29 - S.

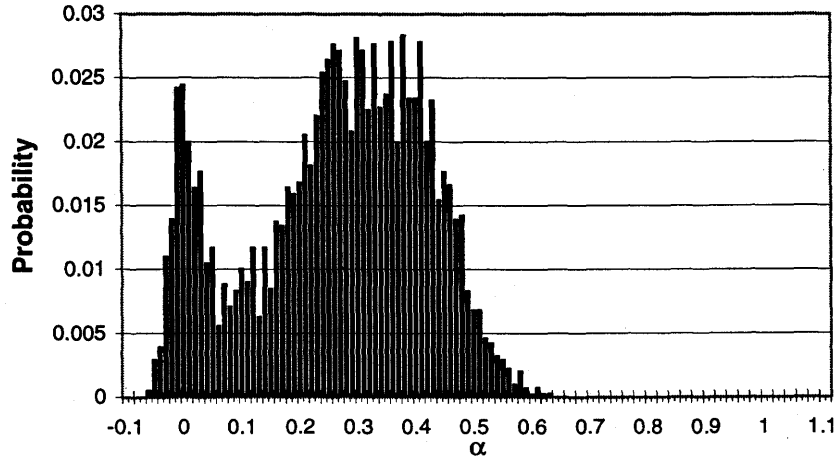

Figure C.81 - Void fraction PDF for 96F3P30 - S.

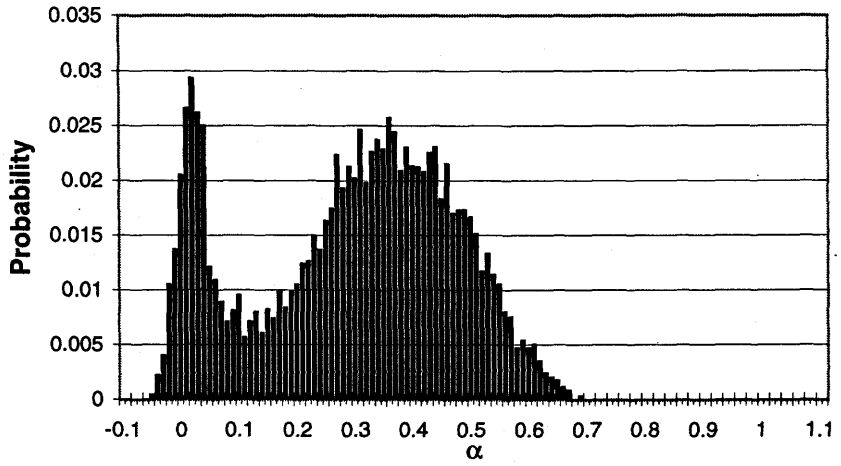

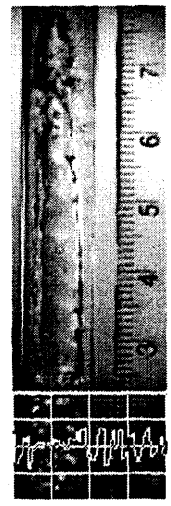

Figure C.82 - Void fraction PDF and video image for 96F3P31 - S.

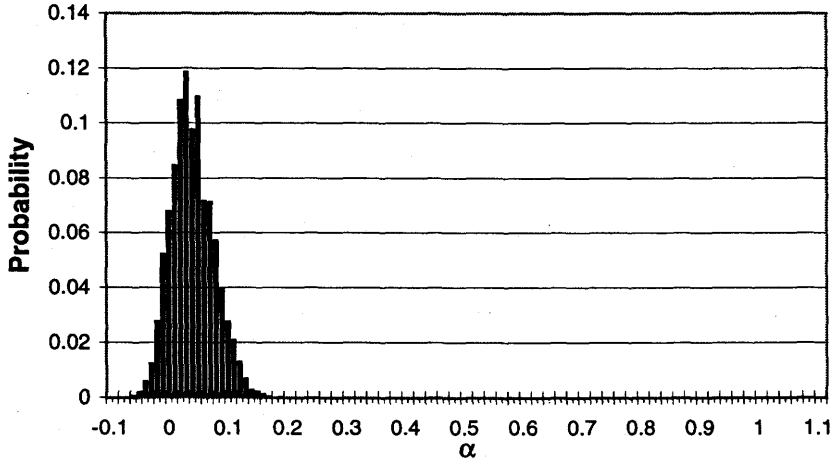

Figure C.83 - Void fraction PDF for 96F3P32 - B.

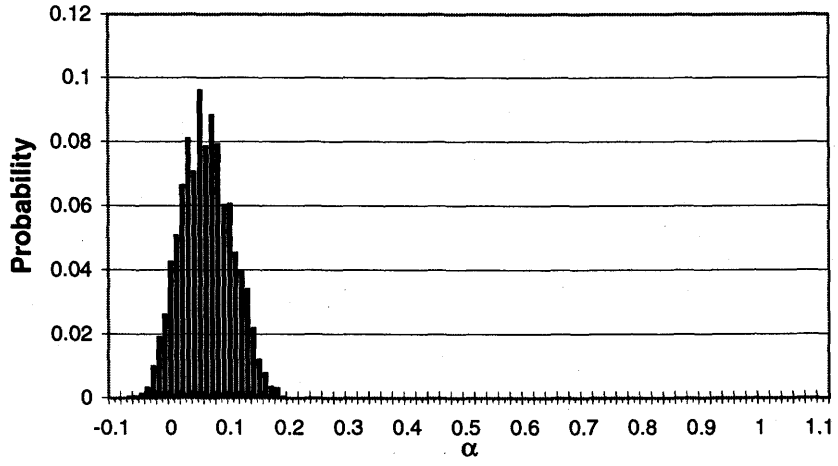

Figure C.84 - Void fraction PDF for 96F3P34 - B.

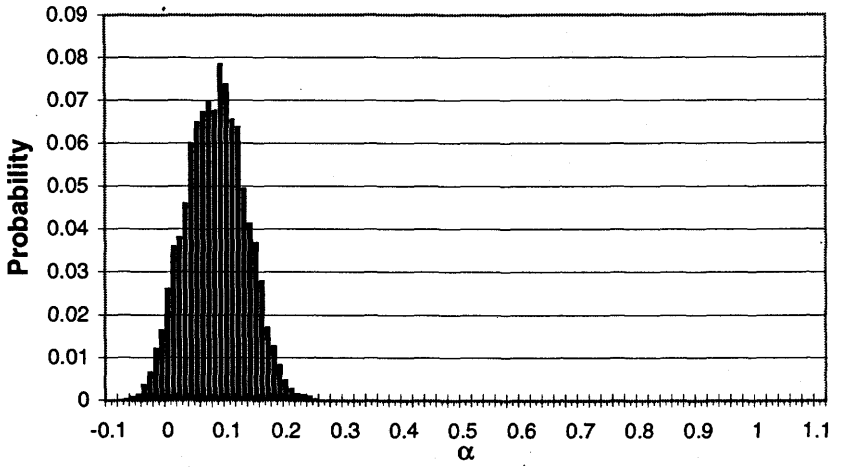

Figure C.85 - Void fraction PDF for 96F3P35 - B.

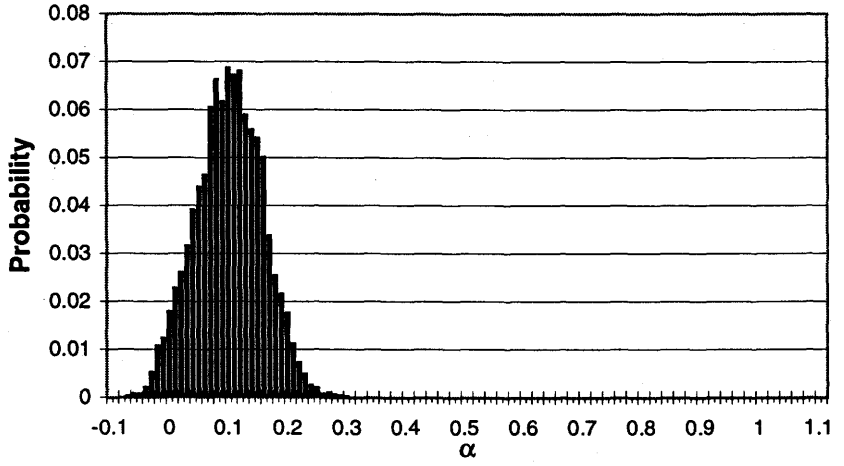

Figure C.86 - Void fraction PDF for 96F3P36 - B.

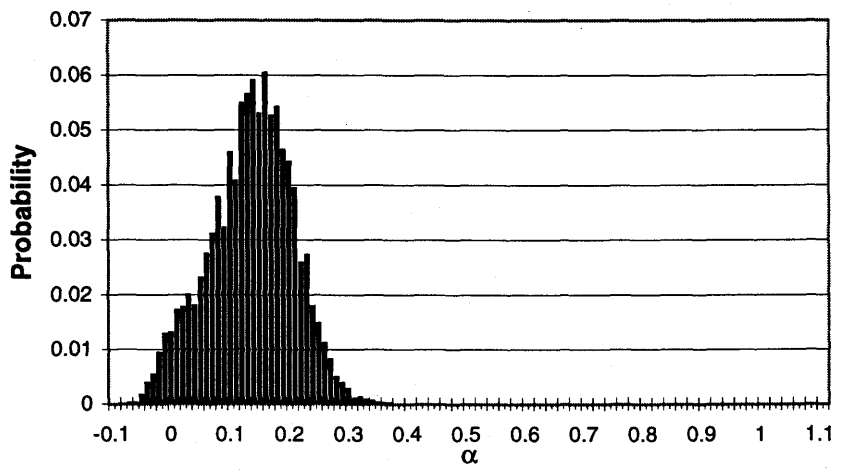

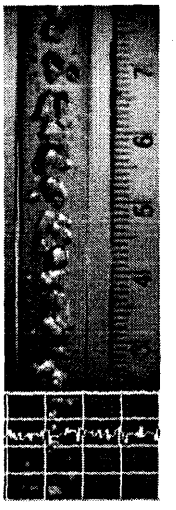

Figure C.87 - Void fraction PDF and video image for 96F3P38 - B.

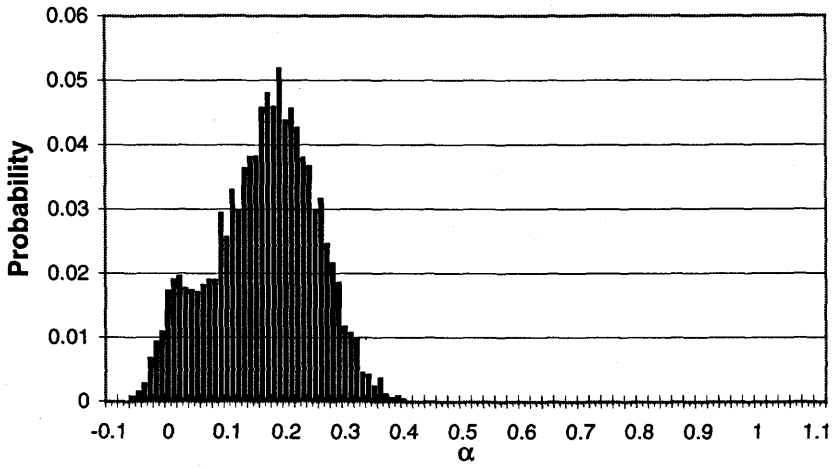

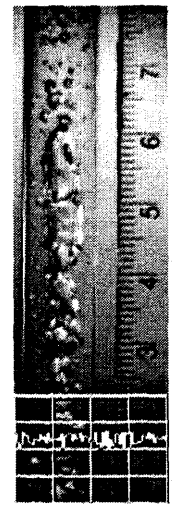

Figure C.88 - Void fraction PDF and video image for 96F3P39 - B-S.

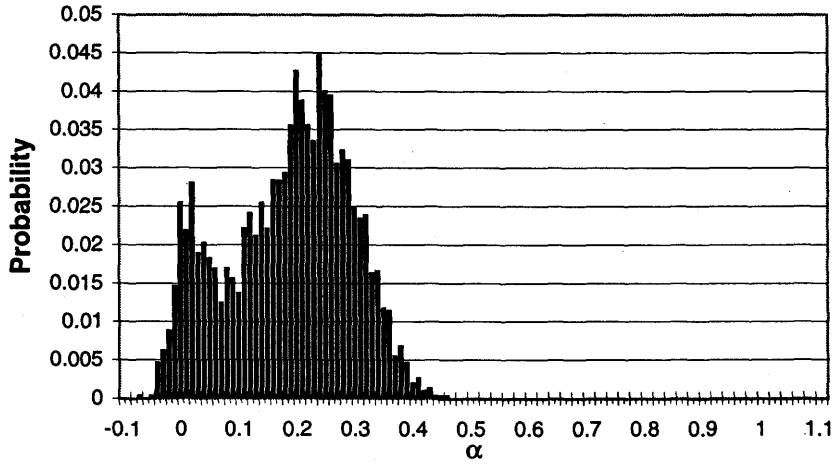

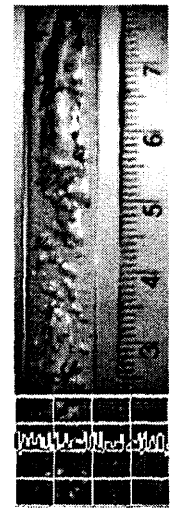

Figure C.89 - Void fraction PDF and video image for 96F3P40 - S.

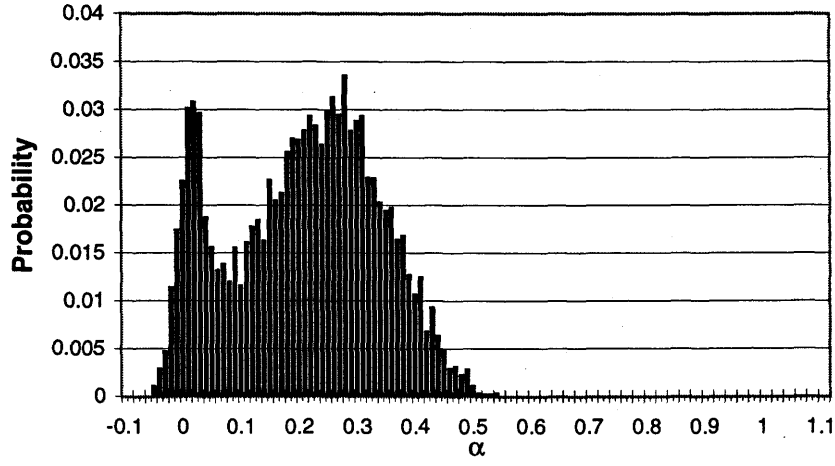

Figure C.90 - Void fraction PDF for 96F3P42 - S.

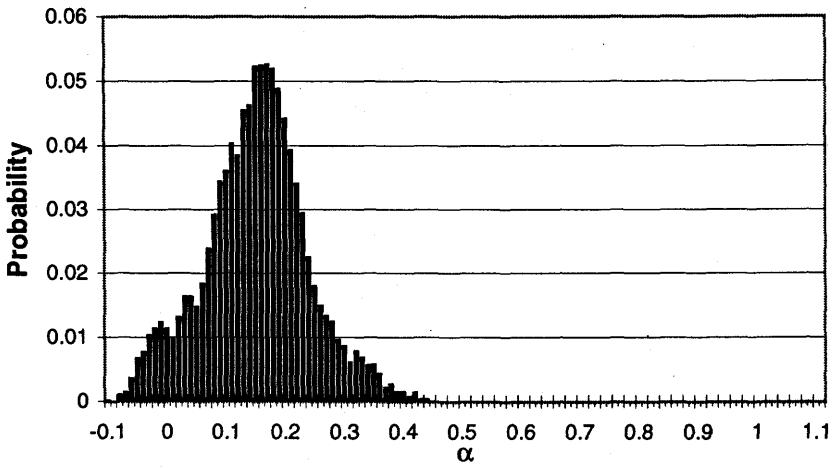

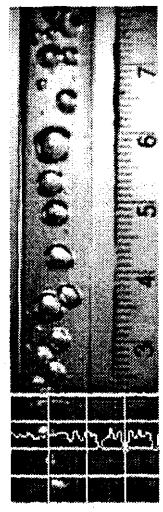

Figure C.91 - Void fraction PDF and video image for 96F3P43 - B.

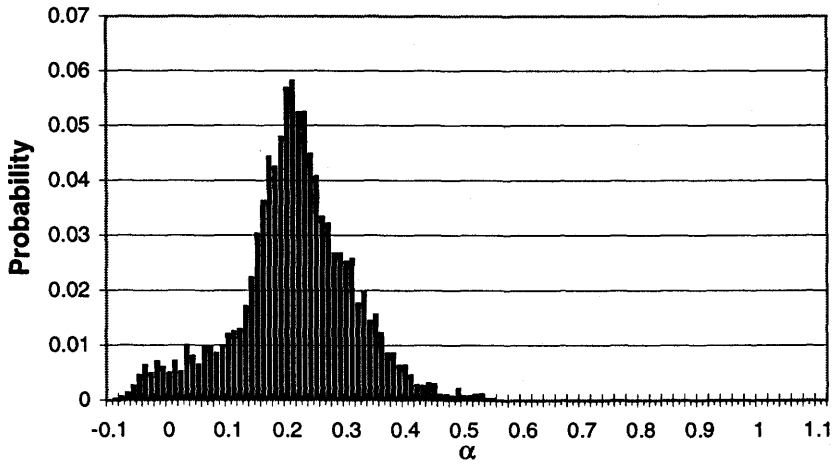

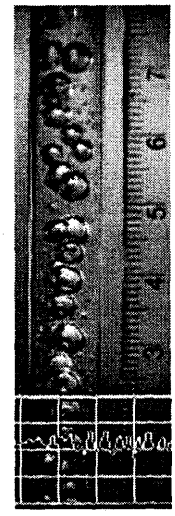

Figure C.92 - Void fraction PDF and video image for 96F3P44 - B.

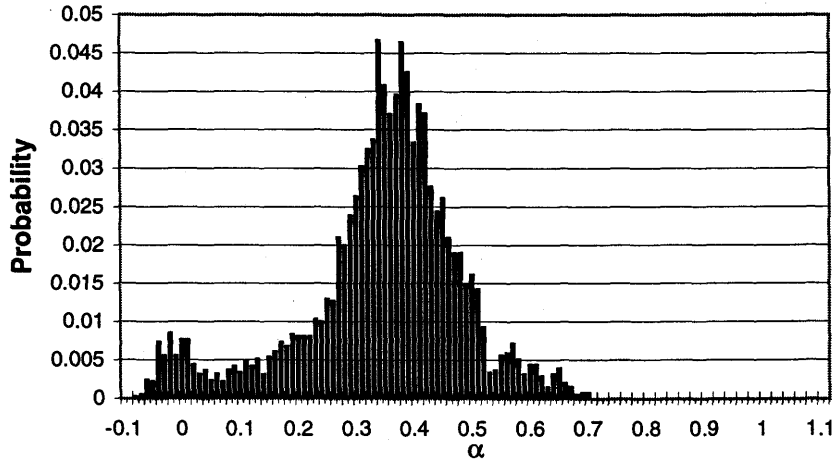

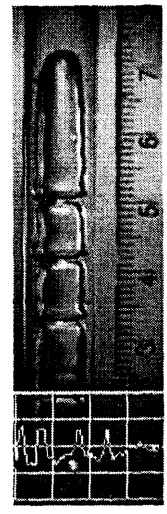

Figure C.93 - Void fraction PDF and video image for 96F3P46 - S.

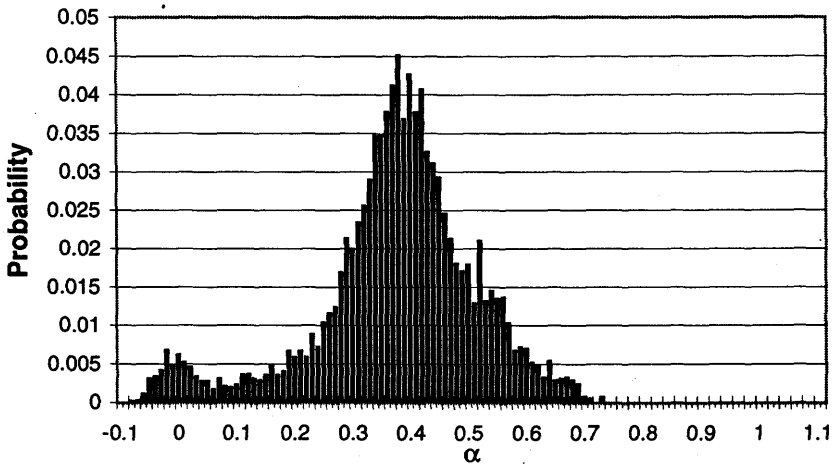

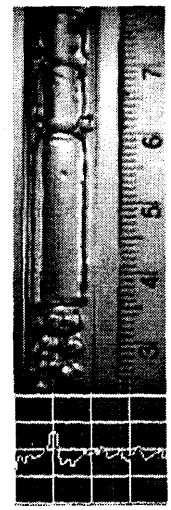

Figure C.94 - Void fraction PDF and video image for 96F3P47 - S.

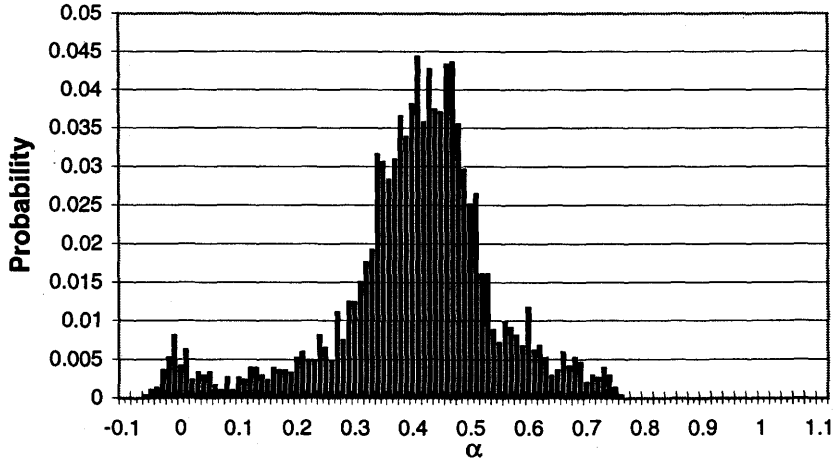

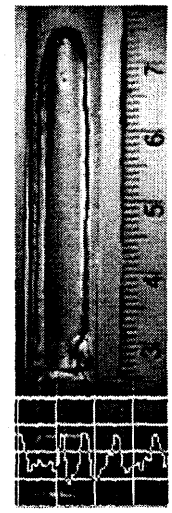

Figure C.95 - Void fraction PDF and video image for 96F3P48 - S.

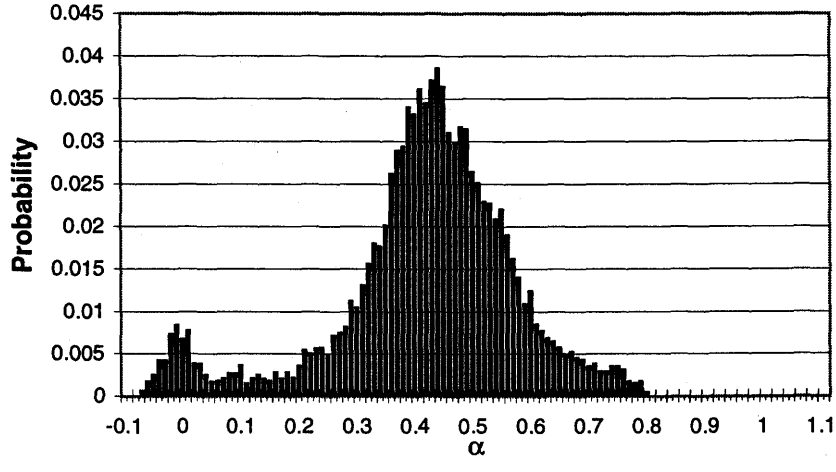

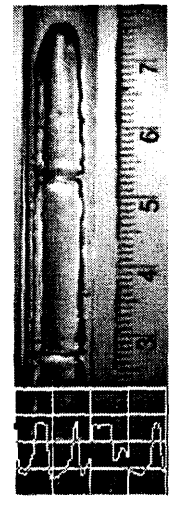

Figure C.96 - Void fraction PDF and video image for 96F3P50 - S.

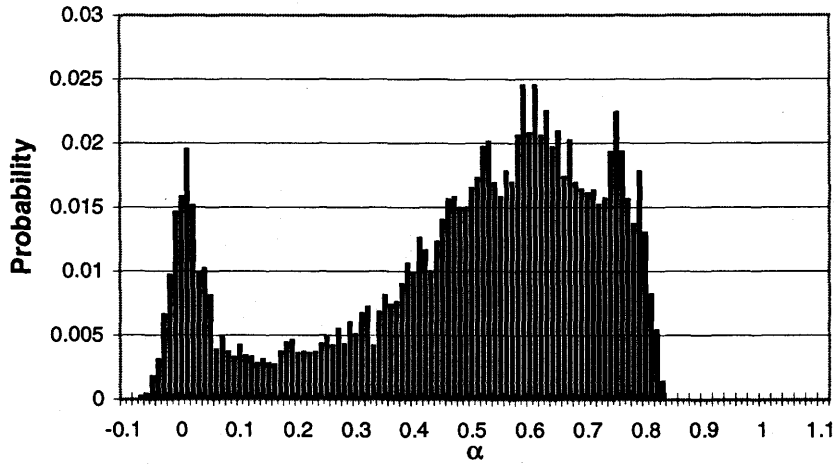

Figure C.97 - Void fraction PDF for 96F3P51 - S.

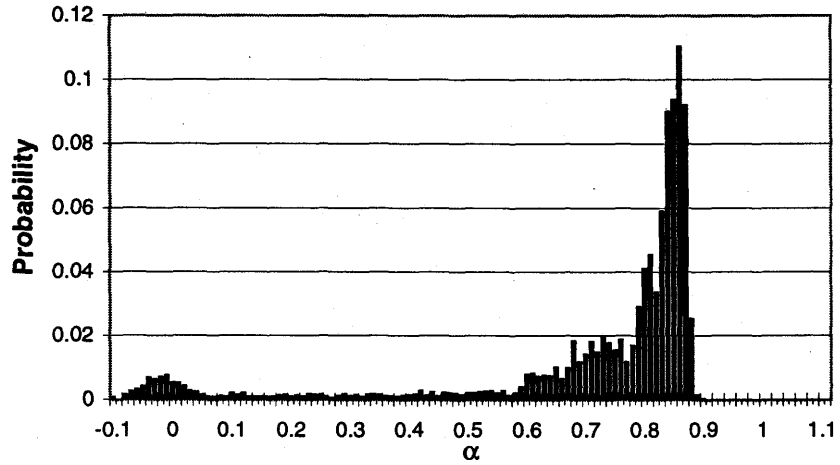

Figure C.98 - Void fraction PDF for 96F4P2 - S.

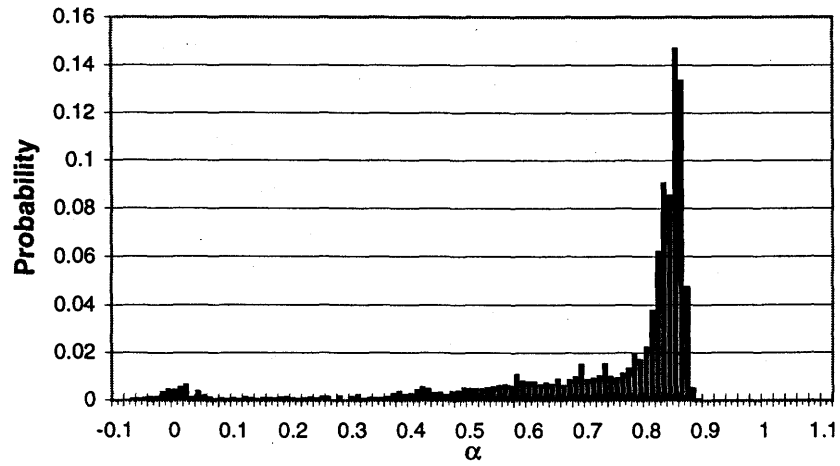

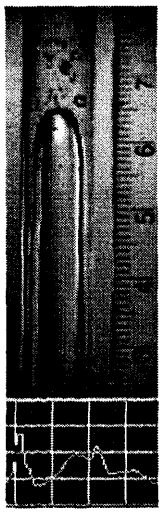

Figure C.99 - Void fraction PDF and video image for 96F4P3 - S.

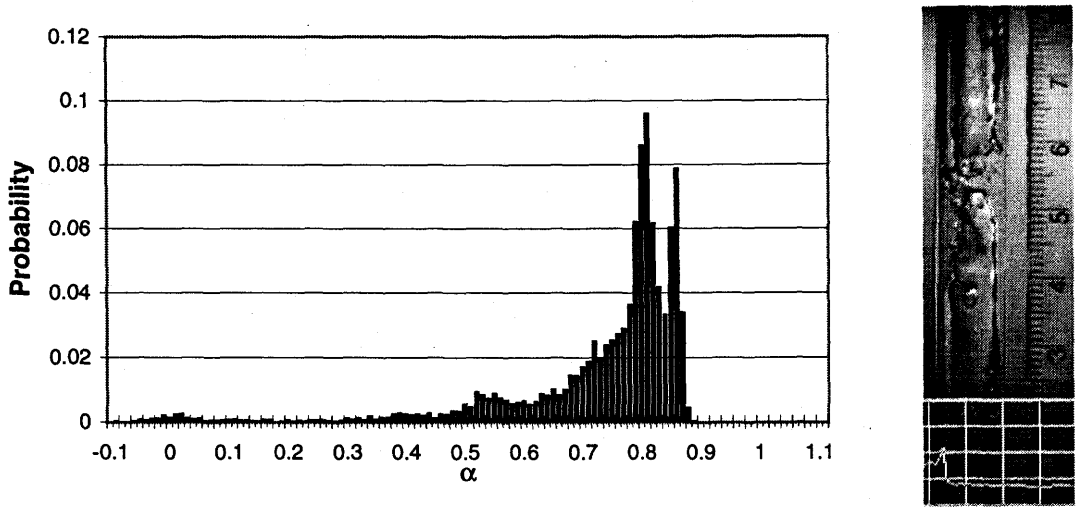

Figure C.100 - Void fraction PDF and video image for 96F4P4 - S-T.

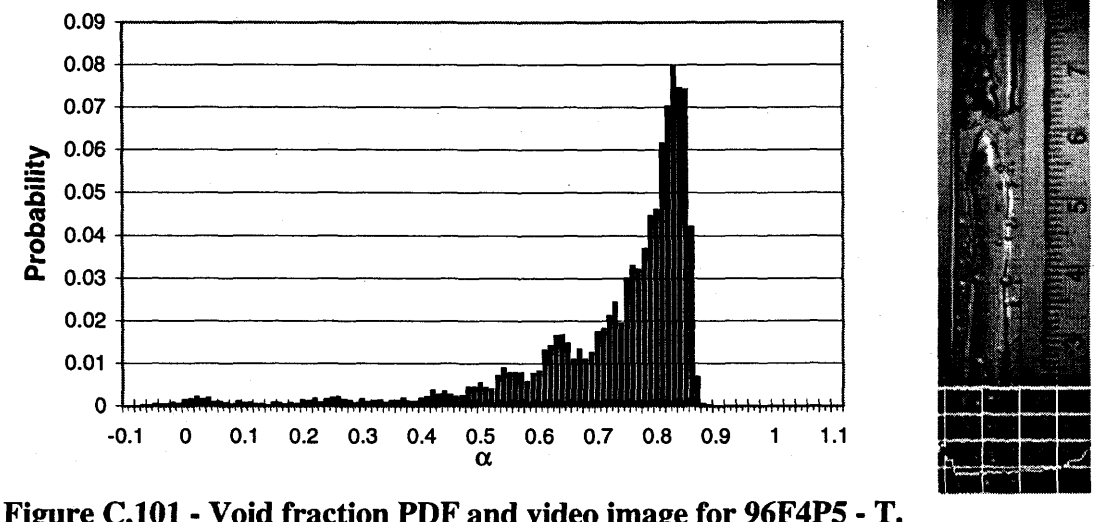

Figure C.101 - Void fraction PDF and video image for 96F4P5 - T.

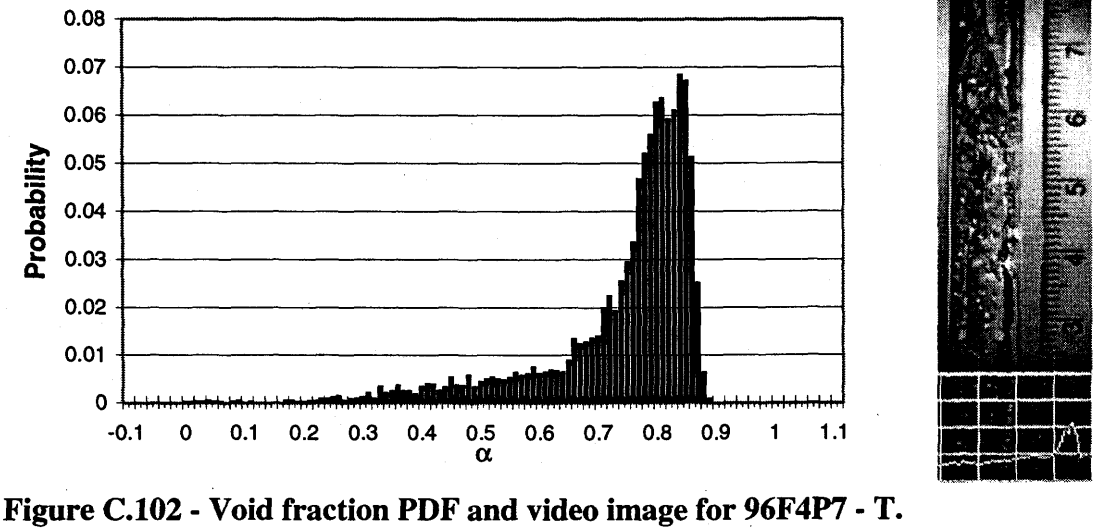

Figure C.102 - Void fraction PDF and video image for 96F4P7 - T.

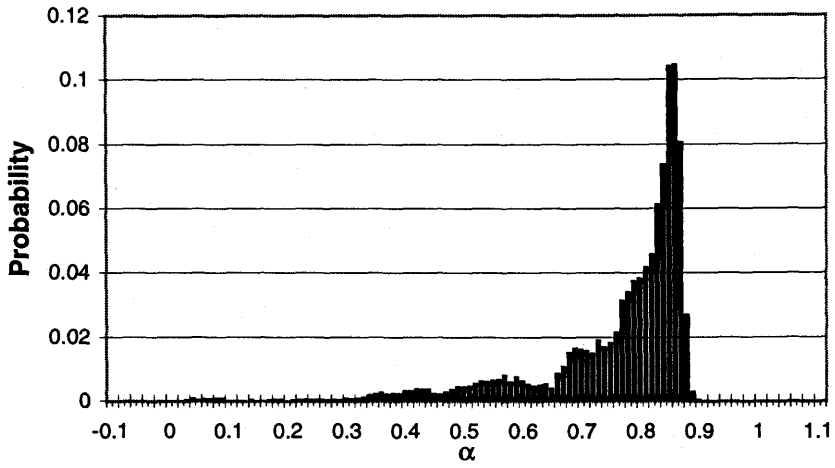

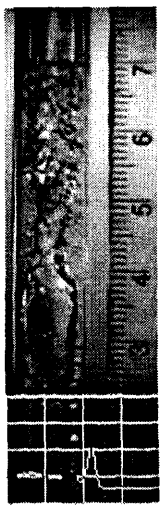

Figure C.103 - Void fraction PDF and video image for 96F4P8 - T.

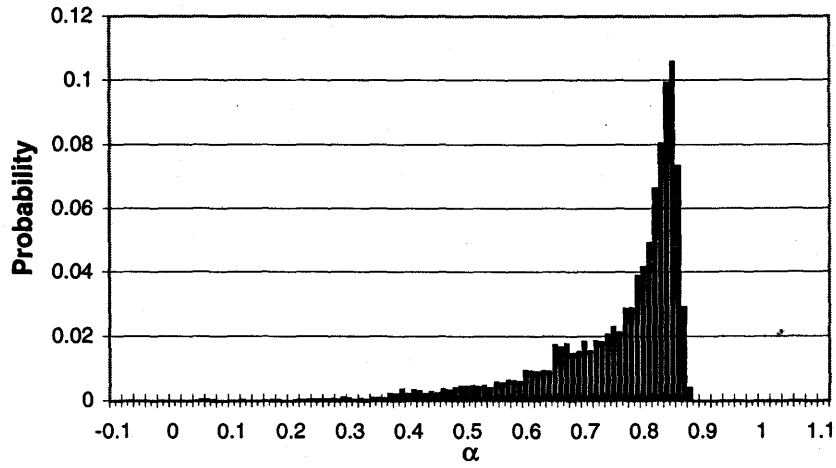

Figure C.104 - Void fraction PDF for 96F4P9 - T.

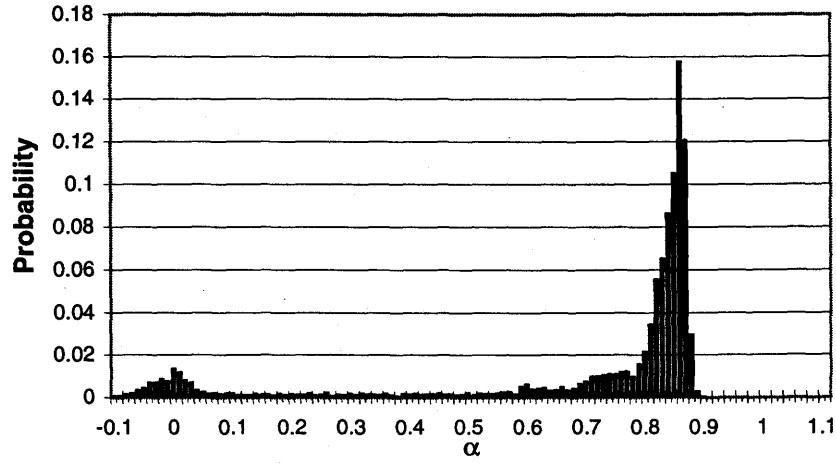

Figure C.105 - Void fraction PDF for 96F4P10 - S.

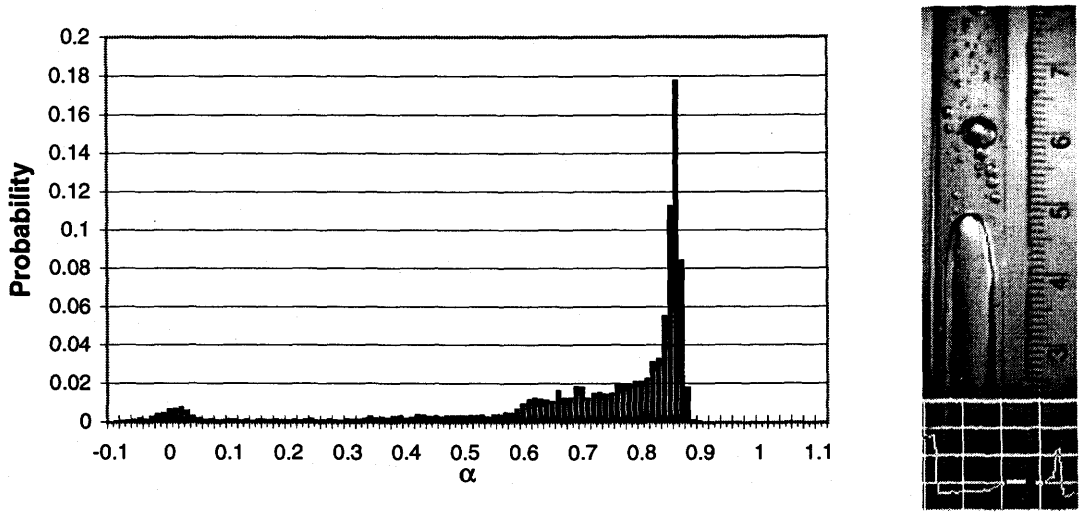

Figure C.106 - Void fraction PDF and video image for 96F4P12 - S.

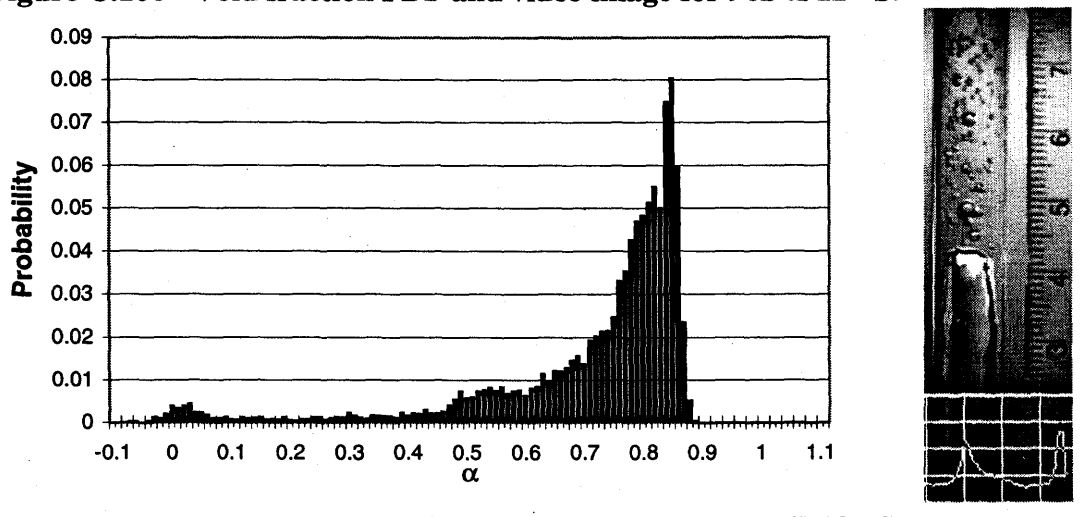

Figure C.107 - Void fraction PDF and video image for 96F4P13 - S.

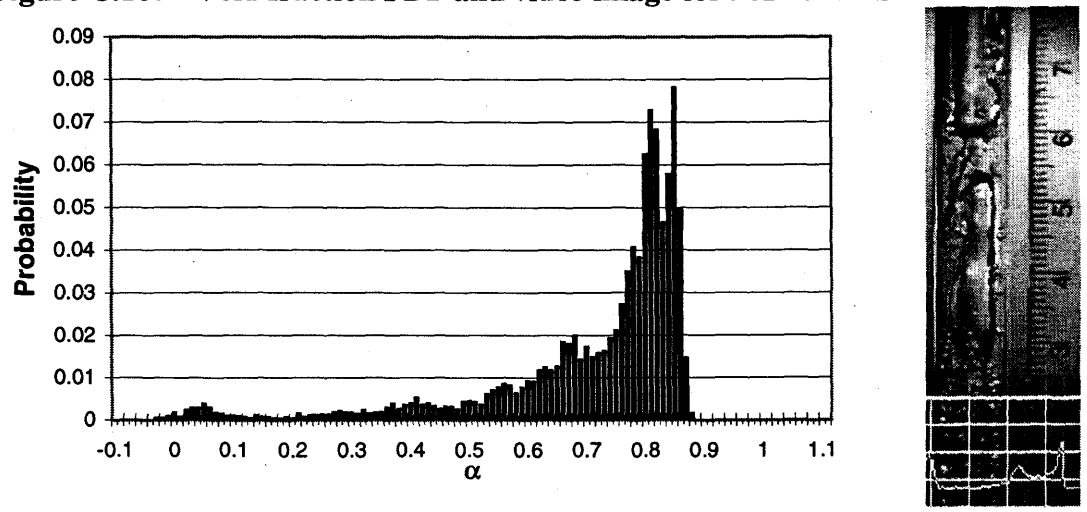

Figure C.108 - Void fraction PDF and video image for 96F4P14 - S-T.

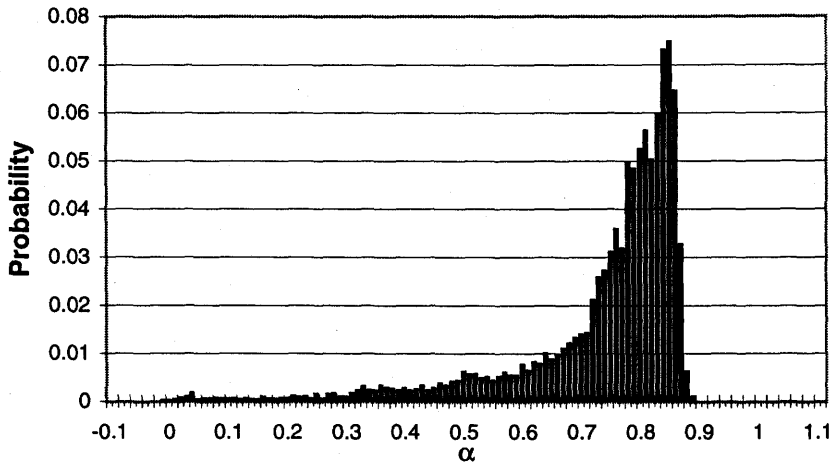

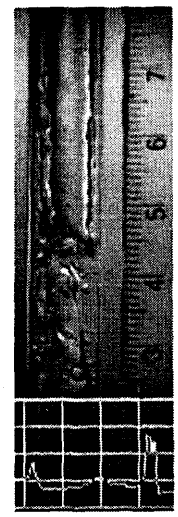

Figure C.109 - Void fraction PDF and video image for 96F4P15 - T.

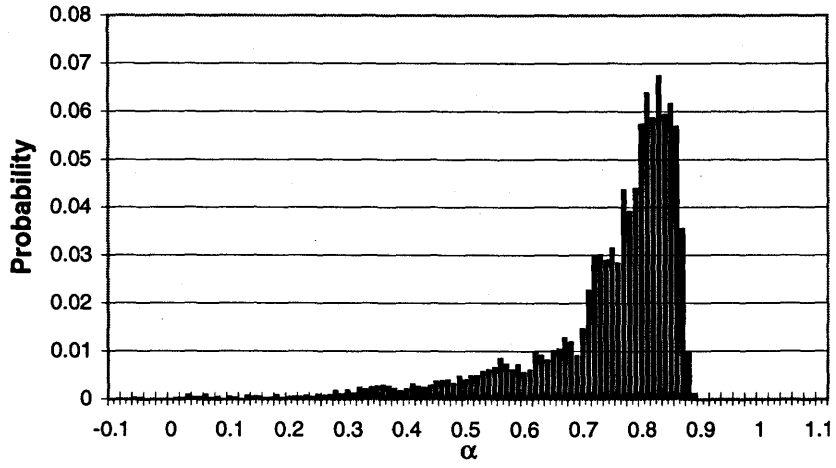

Figure C.110 - Void fraction PDF for 96F4P16 - T.

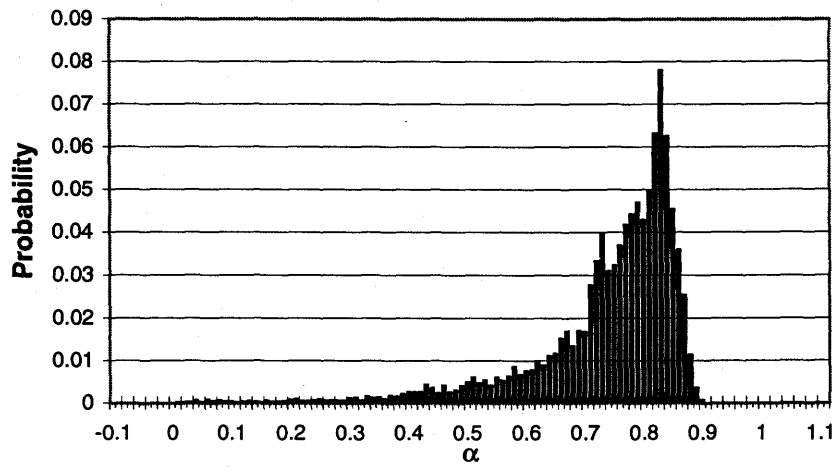

Figure C.111 - Void fraction PDF for 96F4P17 - T.

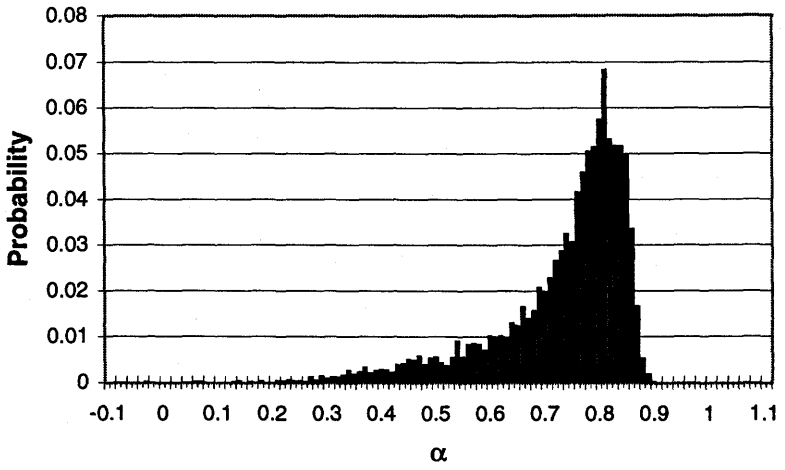

Figure C.112 - Void fraction PDF for 96F4P18 - T.

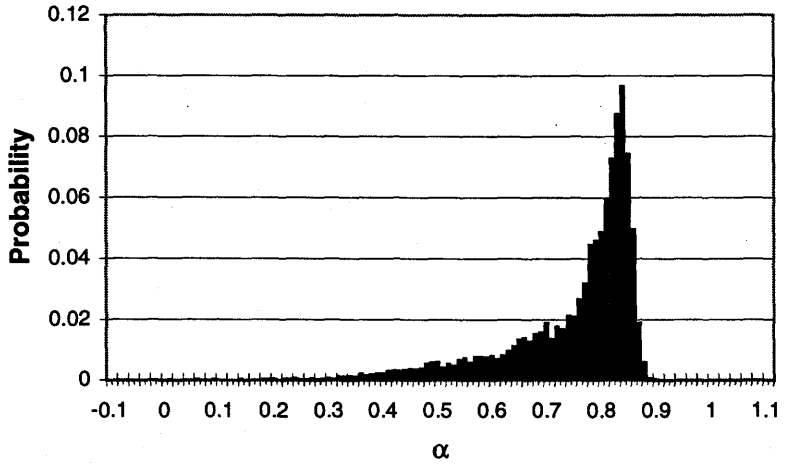

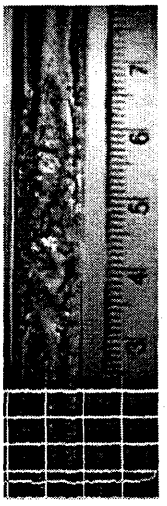

Figure C.113 - Void fraction PDF and video image for 96F4P19 - T.

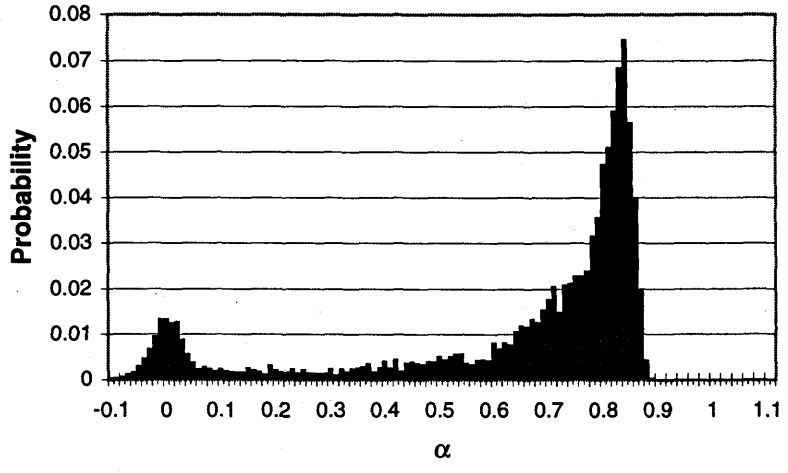

Figure C.114 - Void fraction PDF for 96F4P20 - S.

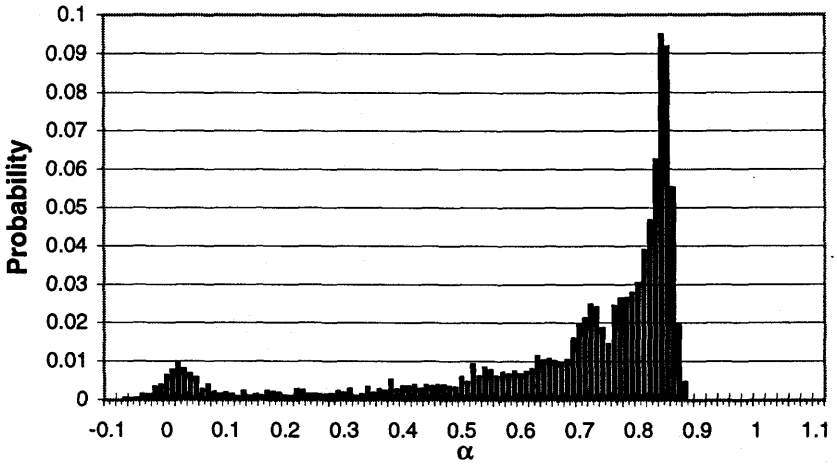

Figure C.115 - Void fraction PDF for 96F4P22 - S.

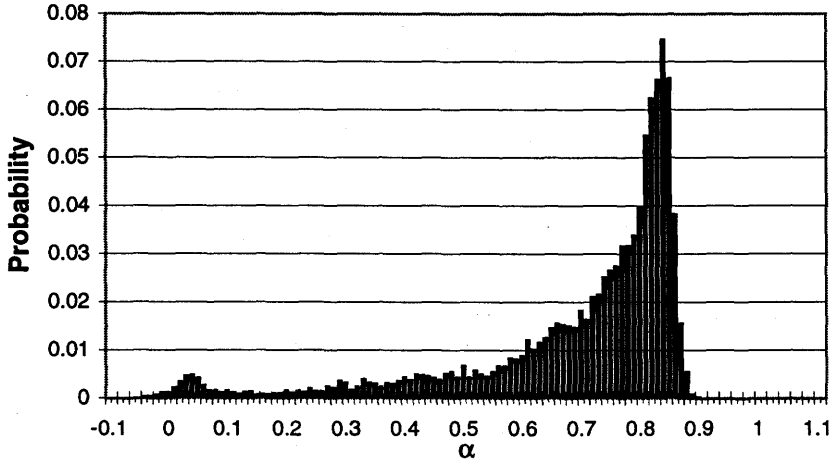

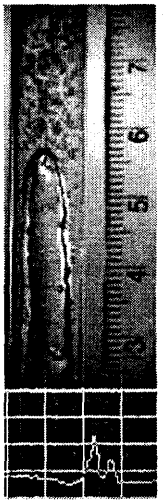

Figure C.116 - Void fraction PDF and video image for 96F4P23 - S.

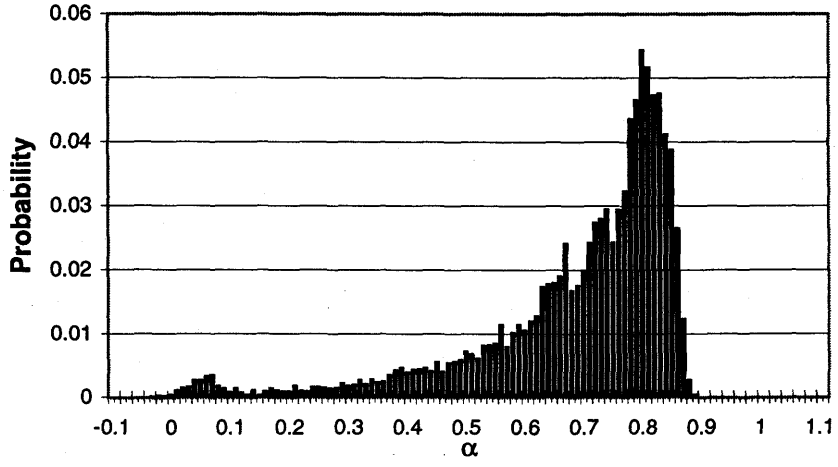

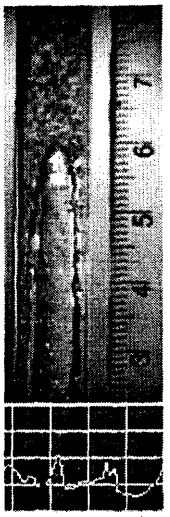

Figure C.117 - Void fraction PDF and video image for 96F4P24 - S.

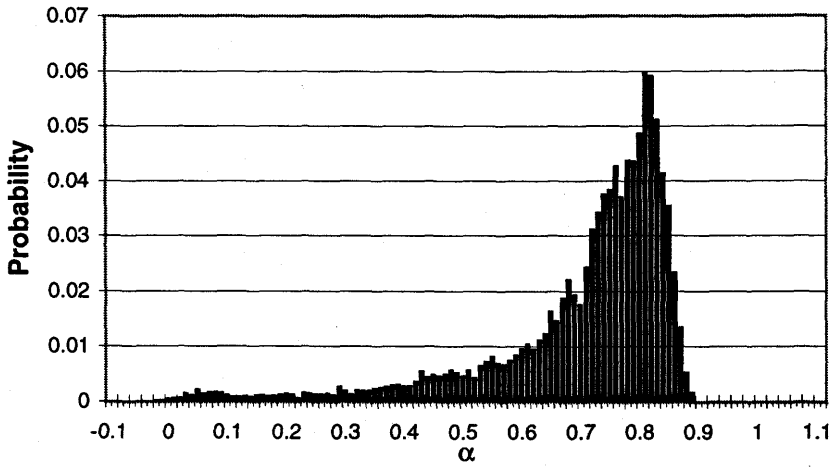

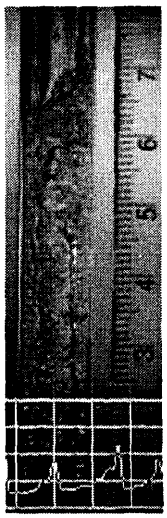

Figure C.118 - Void fraction PDF and video image for 96F4P25 - T.

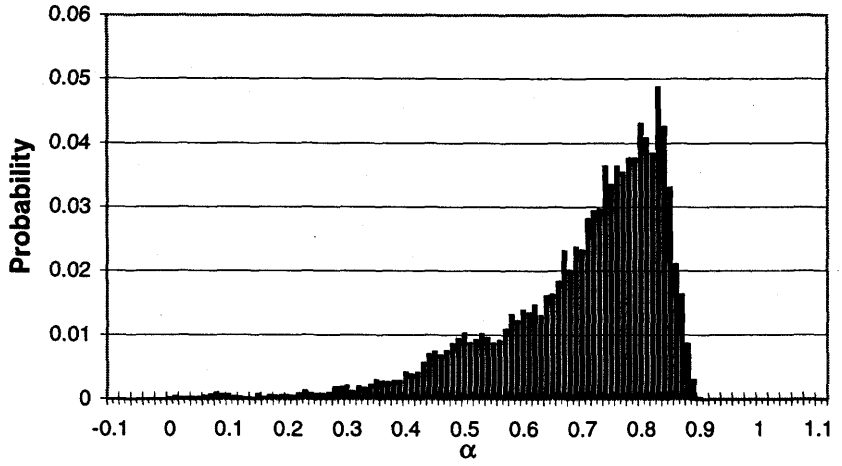

Figure C.119 - Void fraction PDF for 96F4P26 - T.

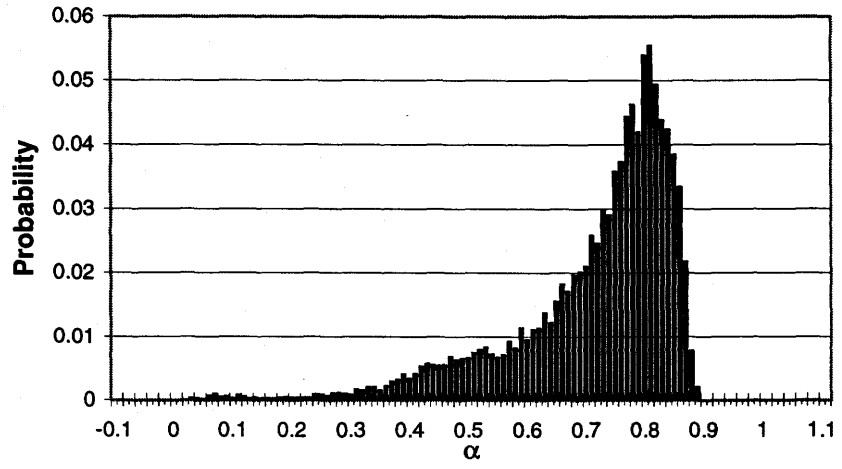

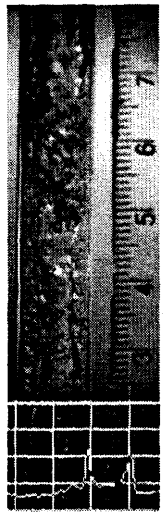

Figure C.120 - Void fraction PDF and video image for 96F4P27 - T.

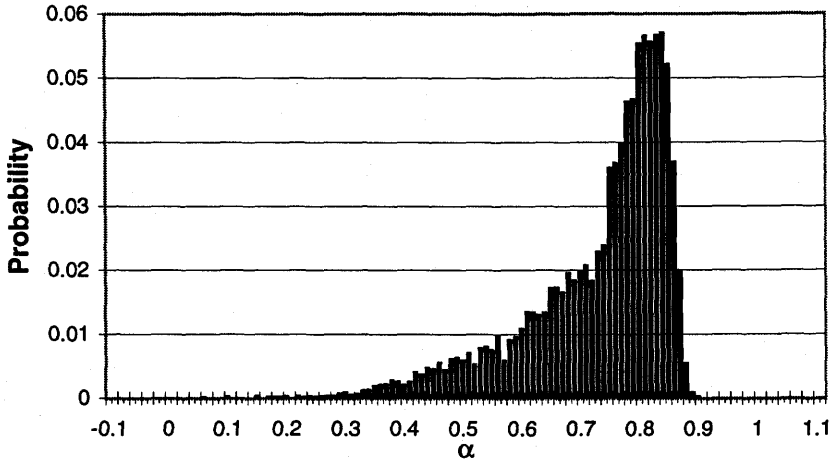

Figure C.121 - Void fraction PDF for 96F4P28 - T.

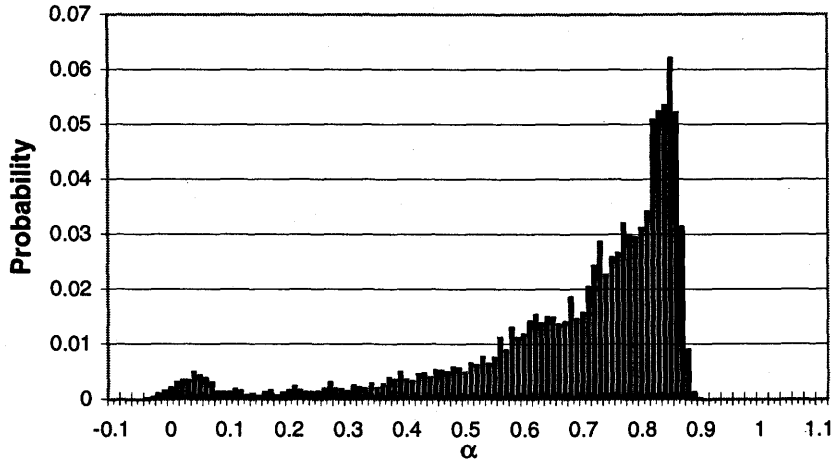

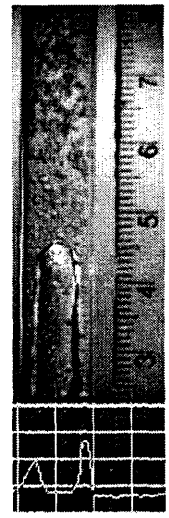

Figure C.122 - Void fraction PDF and video image for 96F4P29 - S.

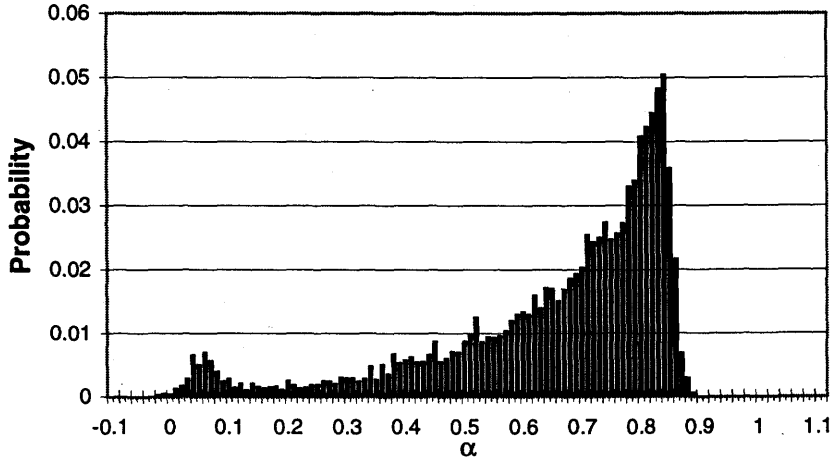

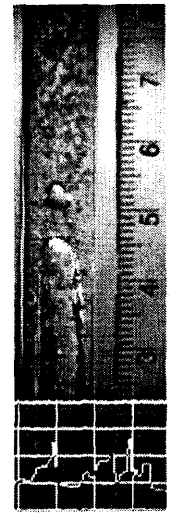

Figure C.123 - Void fraction PDF and video image for 96F4P30 - S.

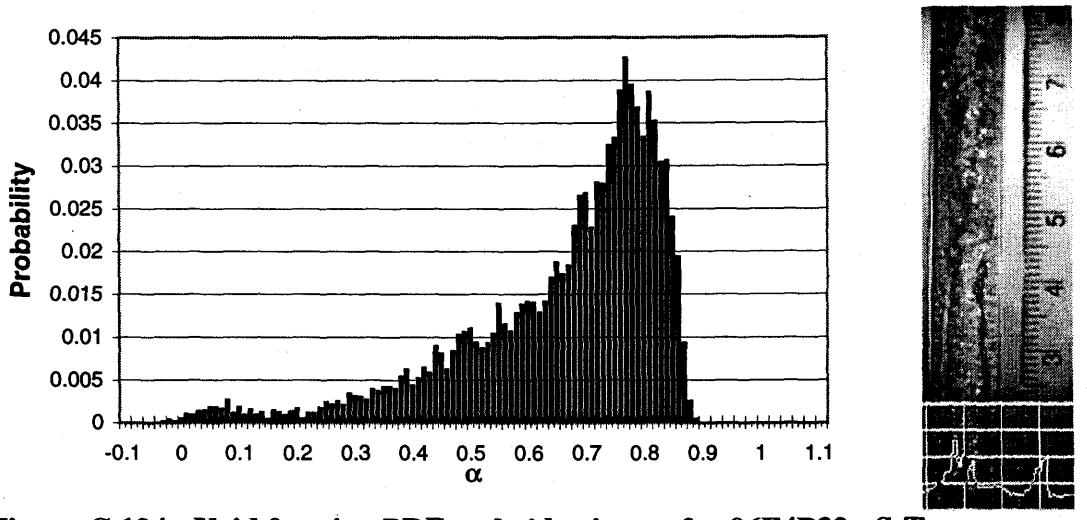

Figure C.124 - Void fraction PDF and video image for 96F4P32 - S-T.

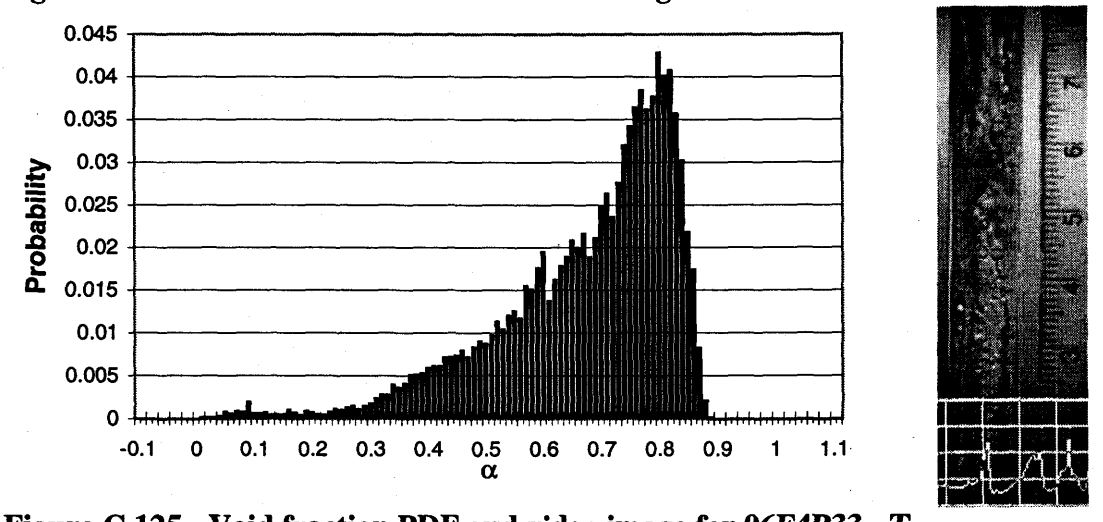

Figure C.125 - Void fraction PDF and video image for 96F4P33 - T.

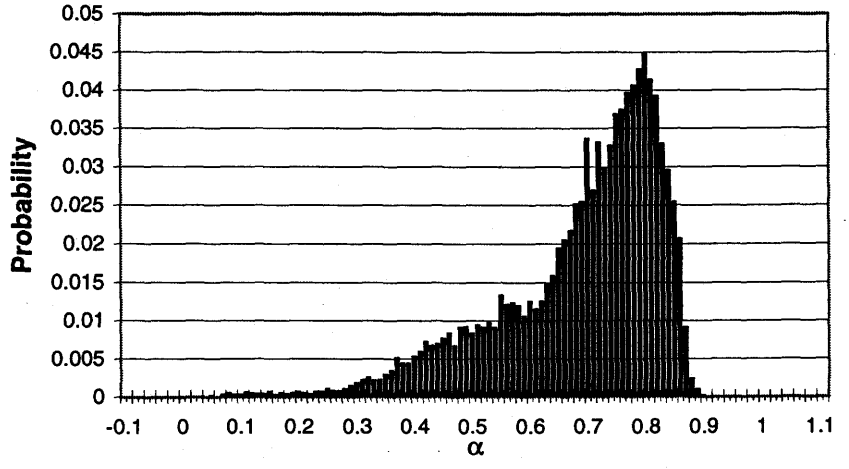

Figure C.126 - Void fraction PDF for 96F4P34 - T.

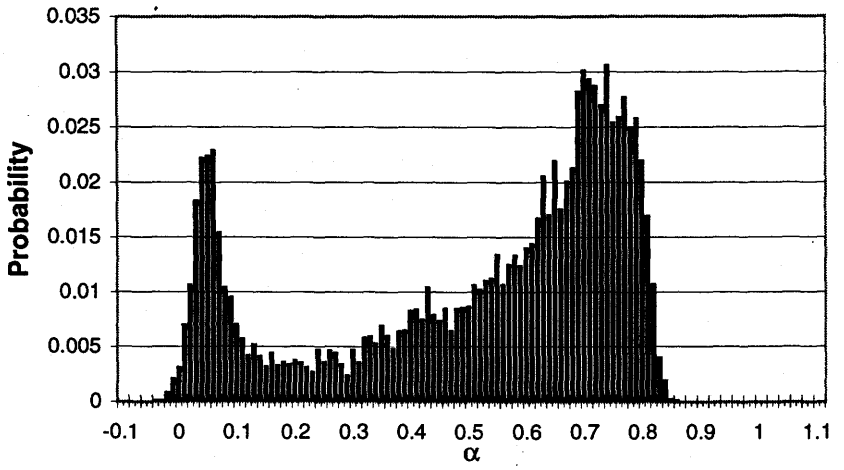

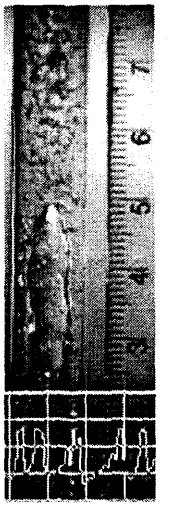

Figure C.127 - Void fraction PDF and video image for 96F4P36 - S.

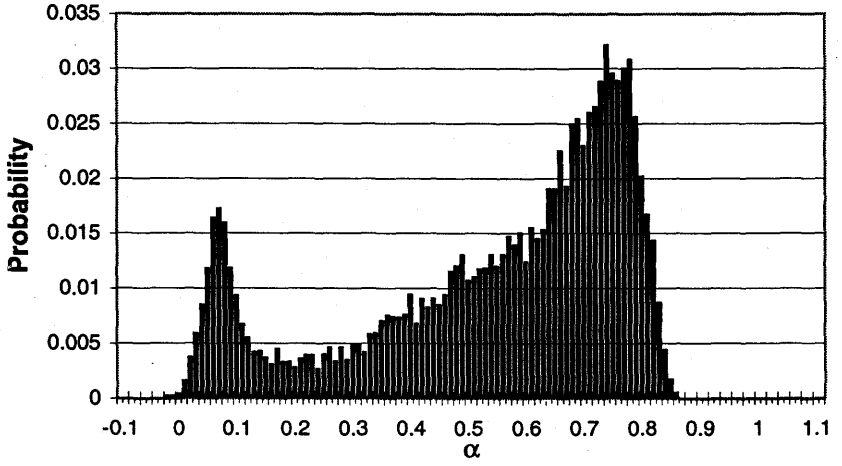

Figure C.128 - Void fraction PDF for 96F4P37 - S.

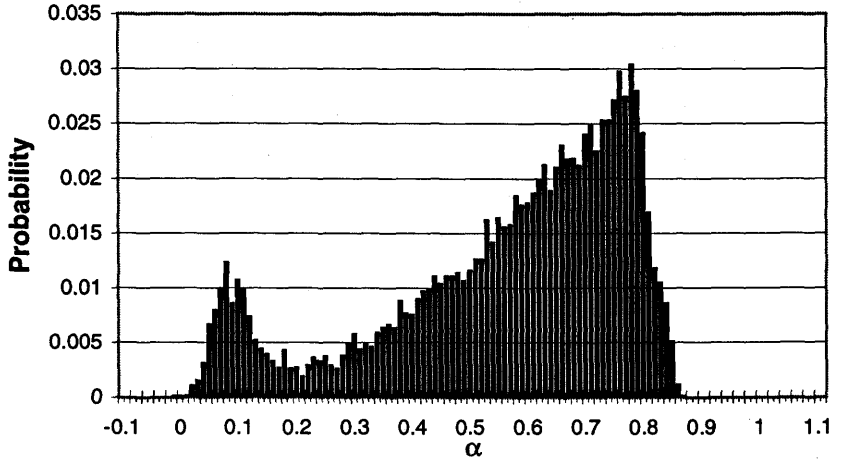

Figure C.129 - Void fraction PDF for 96F4P38 - S.

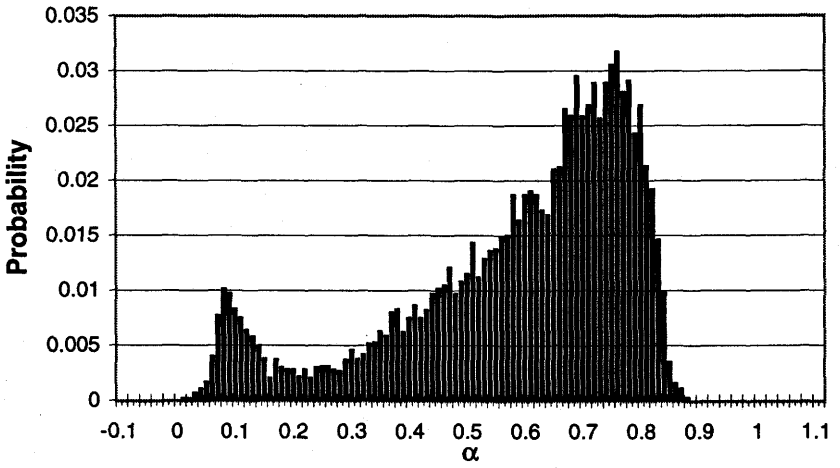

Figure C.130 - Void fraction PDF for 96F4P39 - S.

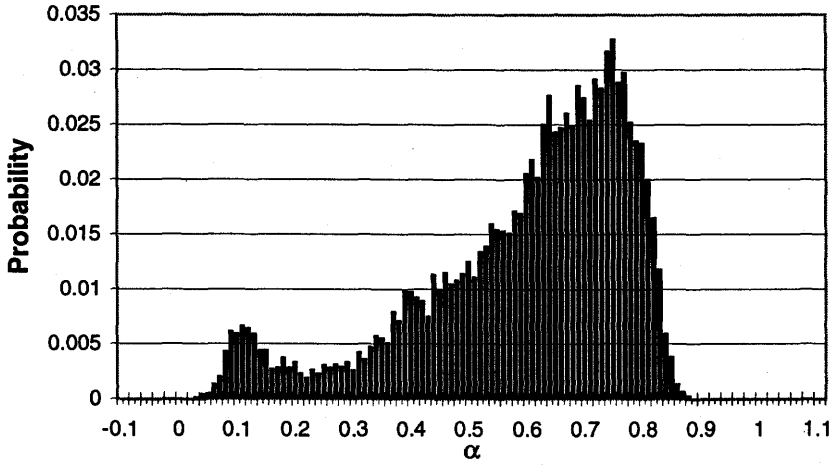

Figure C.131 - Void fraction PDF for 96F4P40 - S.

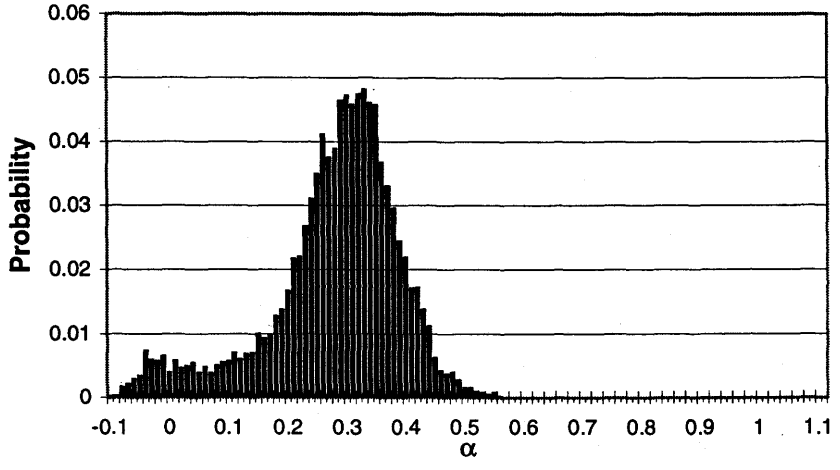

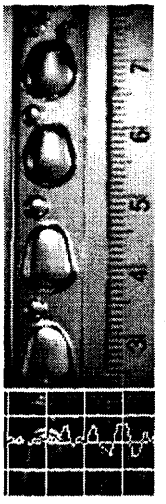

Figure C.132 - Void fraction PDF and video image for 96F4P42 - B.

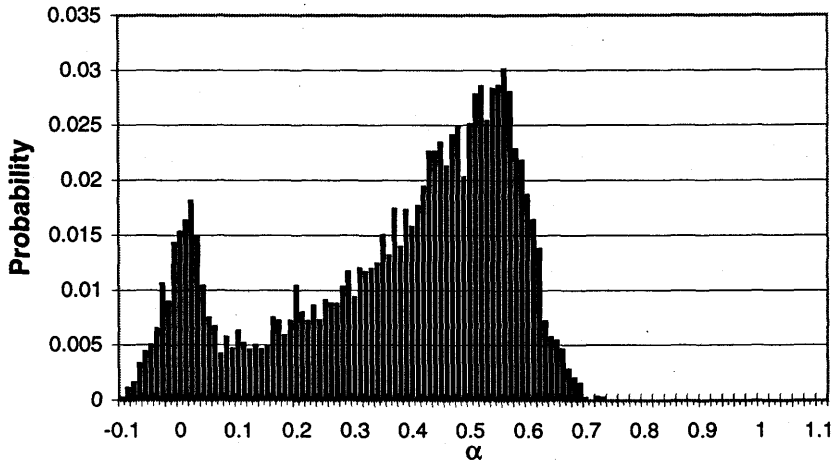

Figure C.133 - Void fraction PDF for 96F4P43 - S.

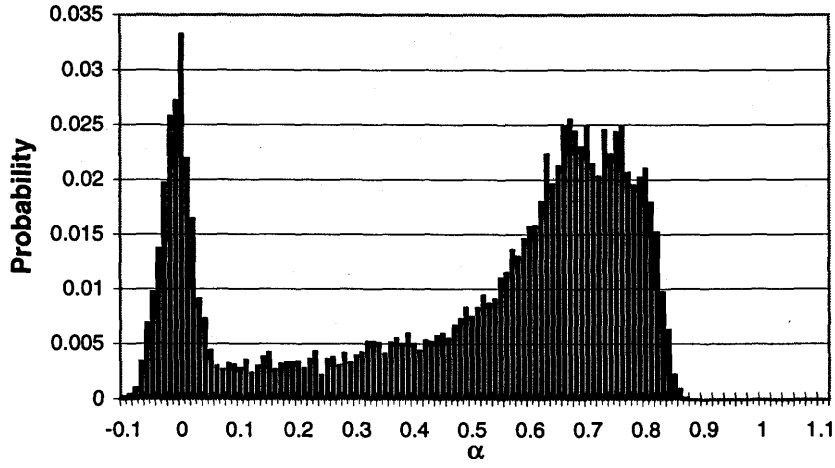

Figure C.134 - Void fraction PDF for 96F4P44 - S.

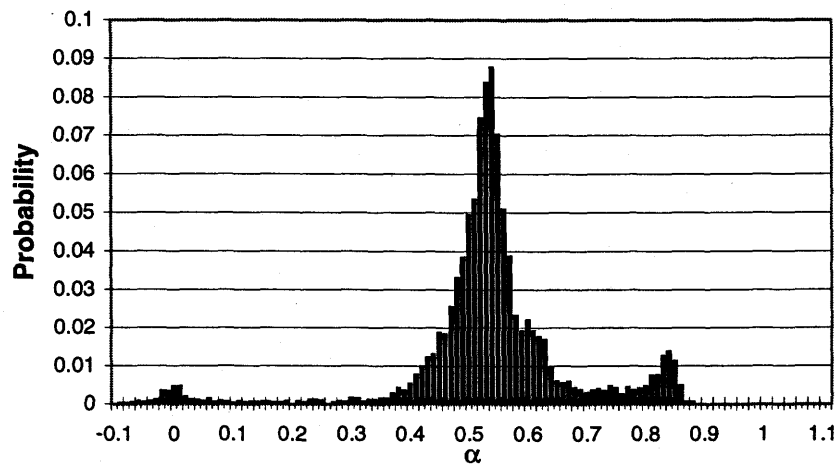

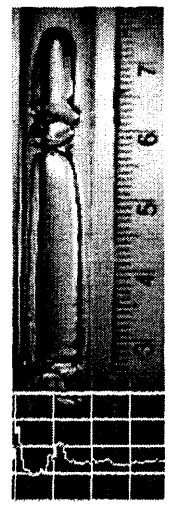

Figure C.135 - Void fraction PDF and video image for 96F4P45 - S.

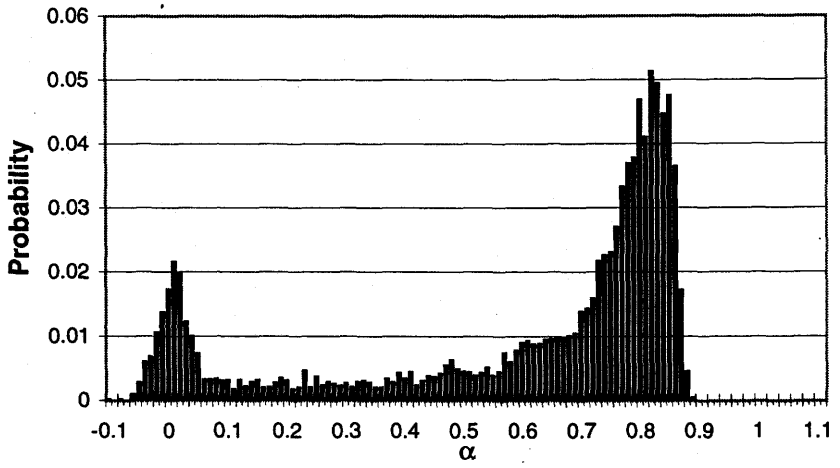

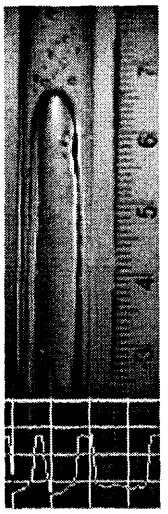

Figure C.136 - Void fraction PDF and video image for 96F4P46 - S.

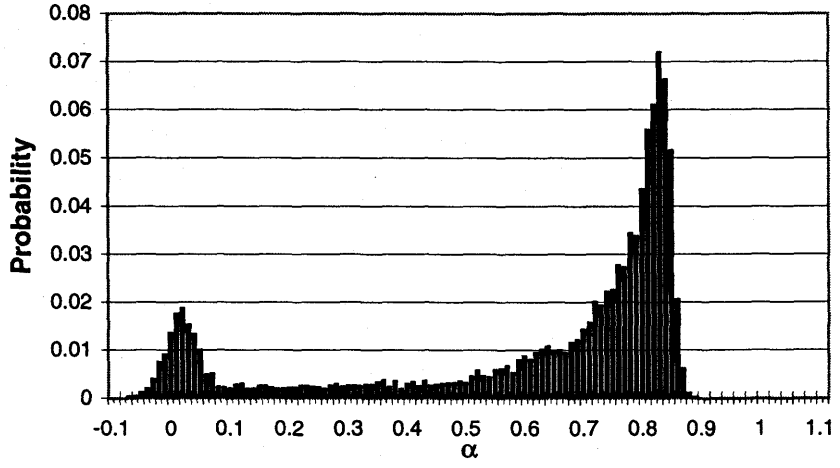

Figure C.137 - Void fraction PDF for 96F4P47 - S.

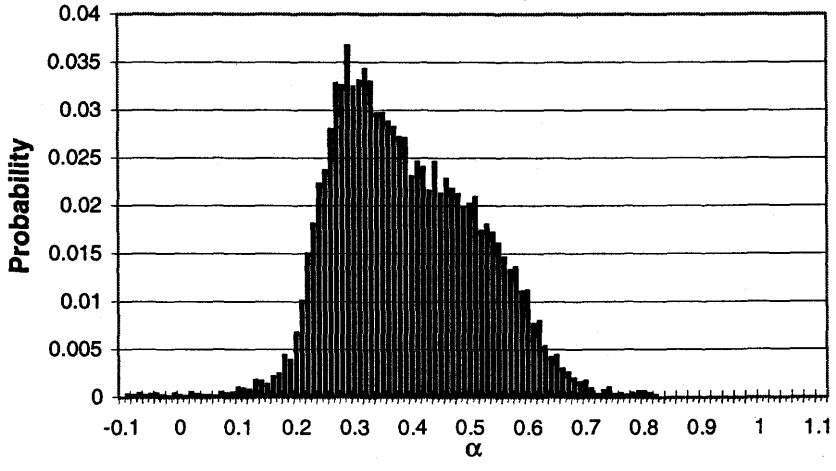

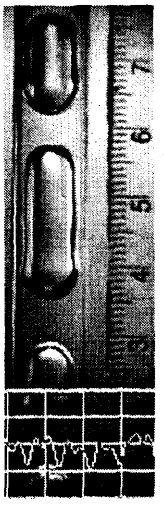

Figure C.138 - Void fraction PDF and video image for 96F4P48 - S.

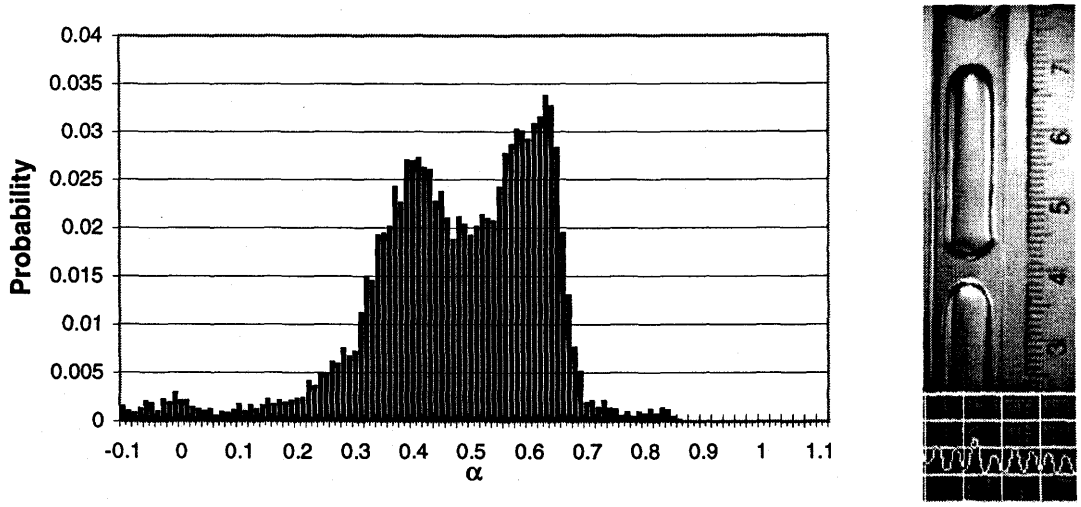

Figure C.139 - Void fraction PDF and video image for 96F4P49 - S.

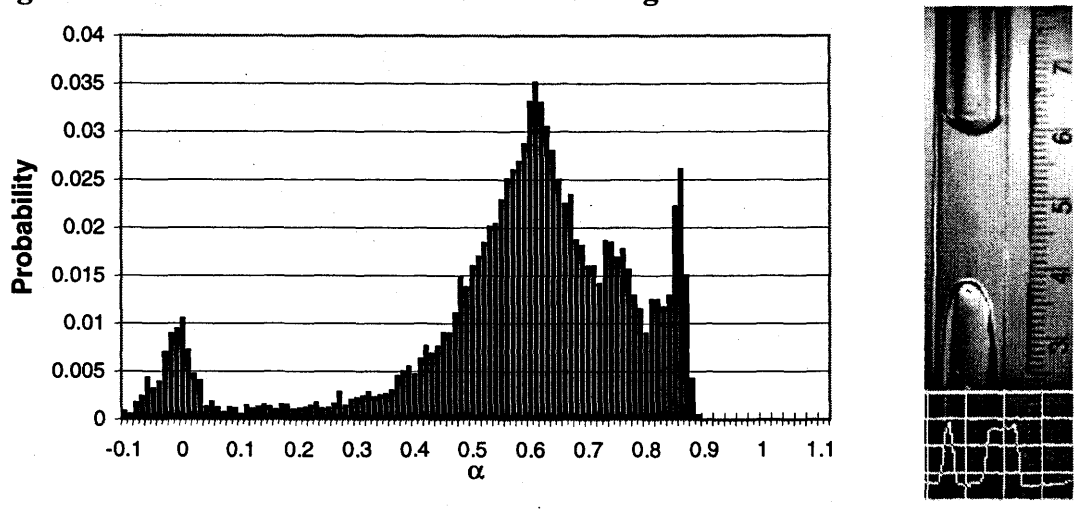

Figure C.140 - Void fraction PDF and video image for 96F4P50 - S.

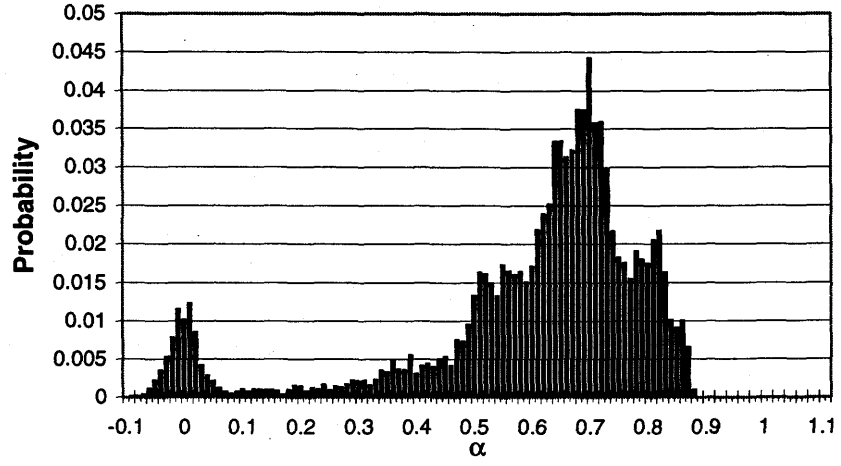

Figure C.141 - Void fraction PDF for 96F4P52 - S.

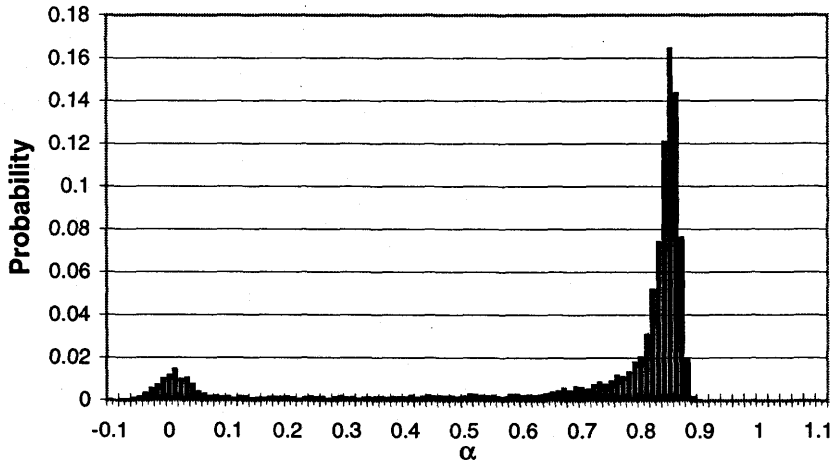

Figure C.142 - Void fraction PDF for 96F4P53 - S.

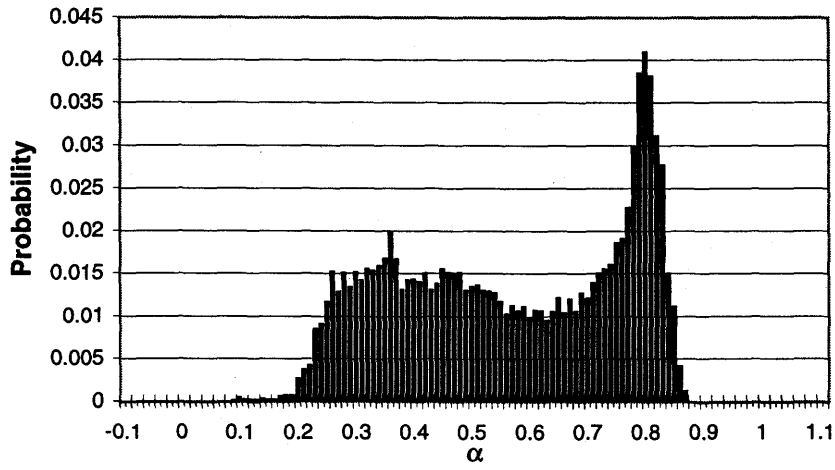

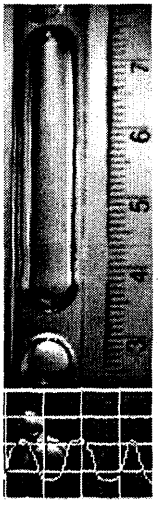

Figure C.143 - Void fraction PDF and video image for 96F4P54 - S.

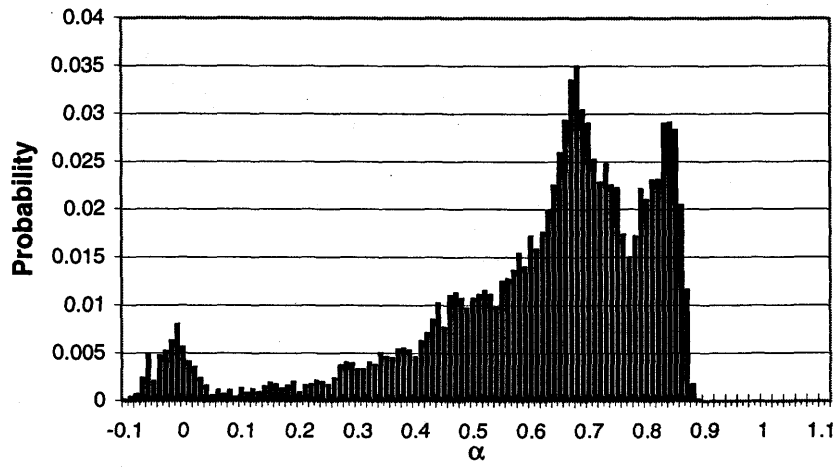

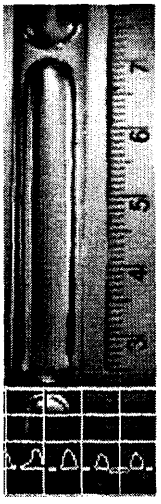

Figure C.144 - Void fraction PDF and video image for 96F4P55 - S.

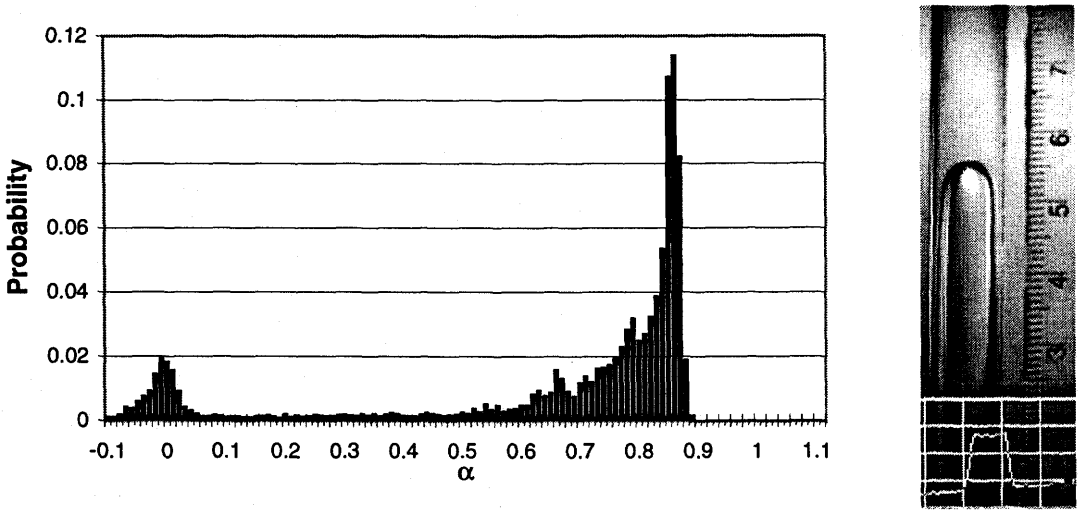

Figure C.145 - Void fraction PDF and video image for 96F4P56 - S.

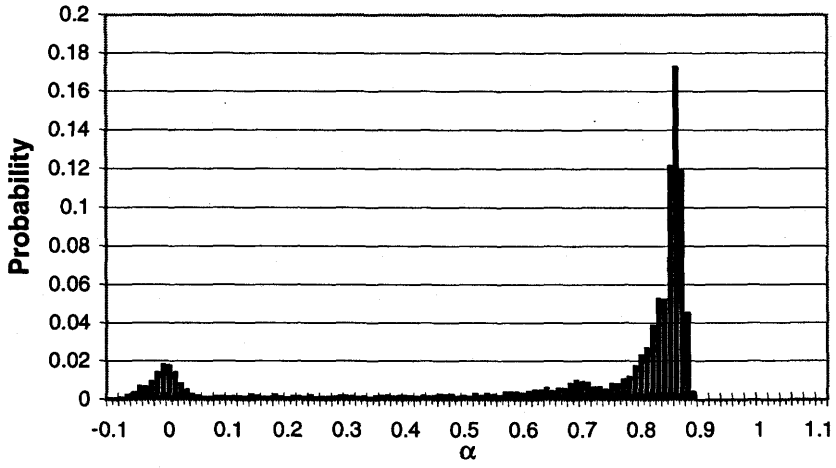

Figure C.146 - Void fraction PDF for 96F4P57 - S.

APPENDIX D - FILM THICKNESS PROBABILITY DENSITY FUNCTIONS

This appendix presents the film thickness probability functions for the flow settings which fall near the transitional-to-annular flow boundary. As in Appendix B, the plots are organized by the day and parabola on which the data was taken (i.e. 96F2P27 represents data taken during parabola 27 of flight day 2 during the 1996 flight campaign). As well, in each of the figures the flow regime is identified according to the following code:

T = transitional flow,
T-A = transitional-to-annular, and
A = annular flow.

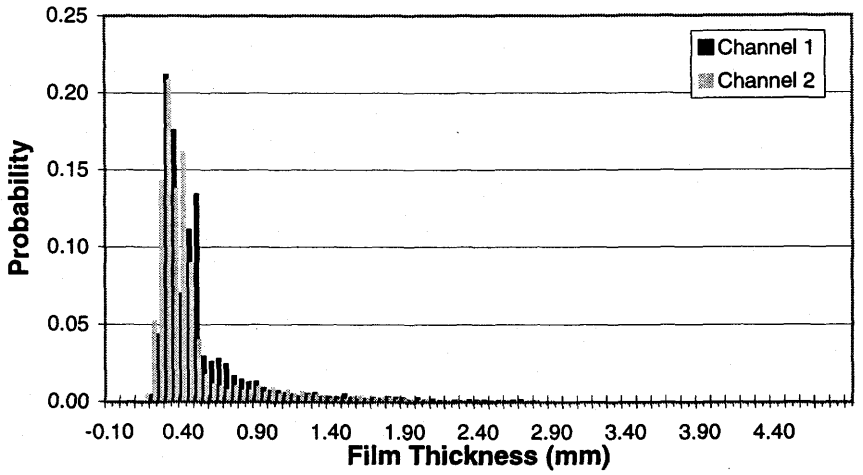

Figure D.1 - Film thickness PDF for 96F1P2 - T.

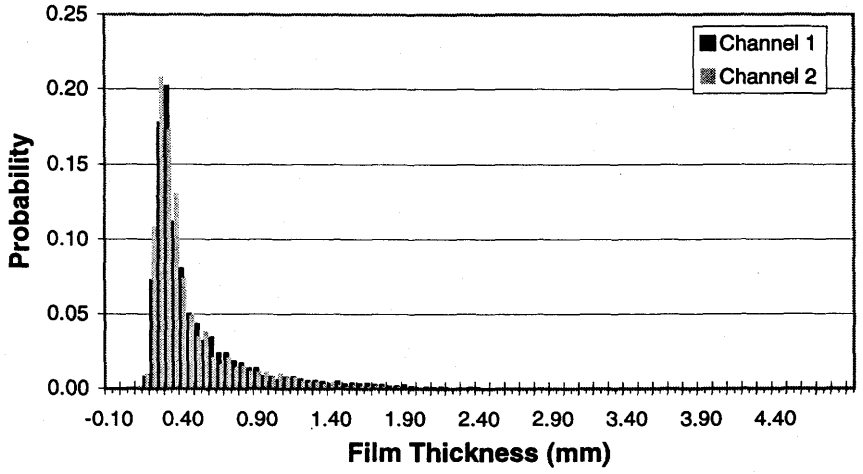

Figure D.2 - Film thickness PDF for 96F1P3 - A.

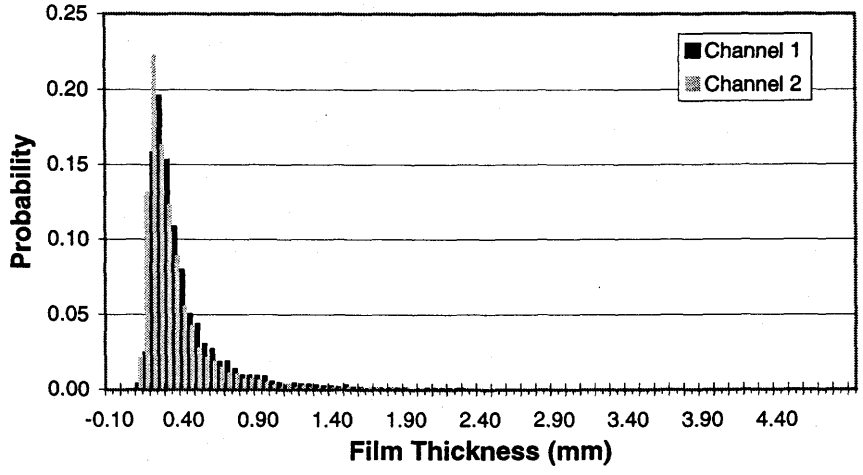

Figure D.3 - Film thickness PDF for 96F1P4 - A.

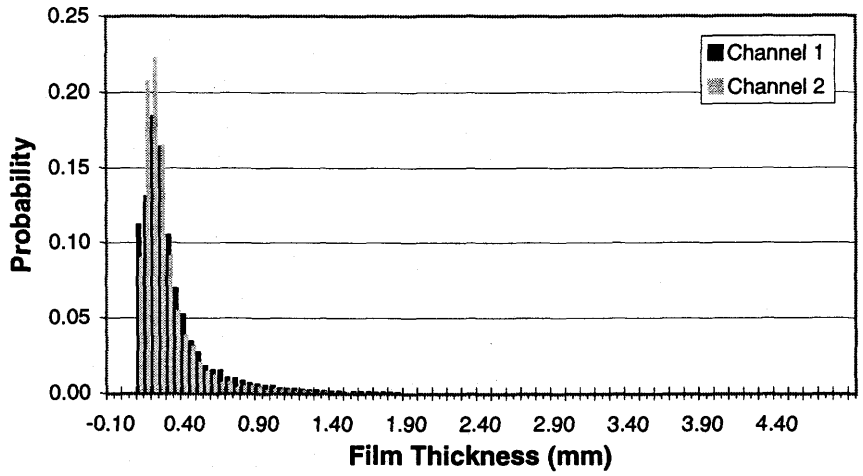

Figure D.4 - Film thickness PDF for 96F1P5 - A.

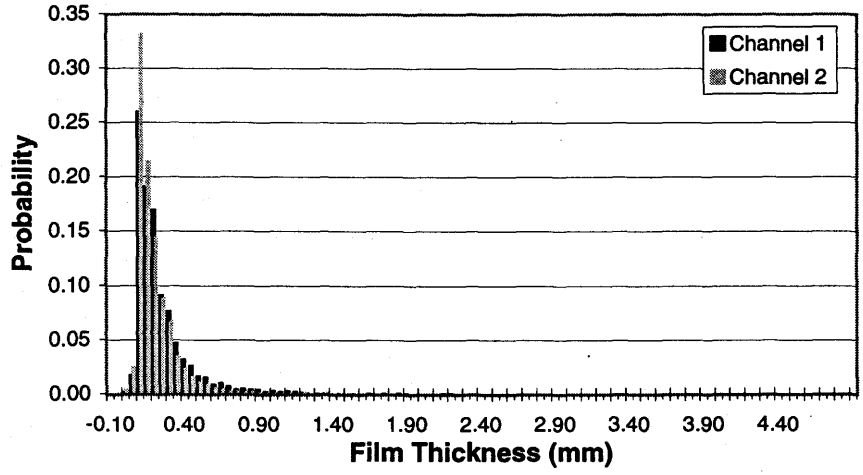

Figure D.5 - Film thickness PDF for 96F1P6 - A.

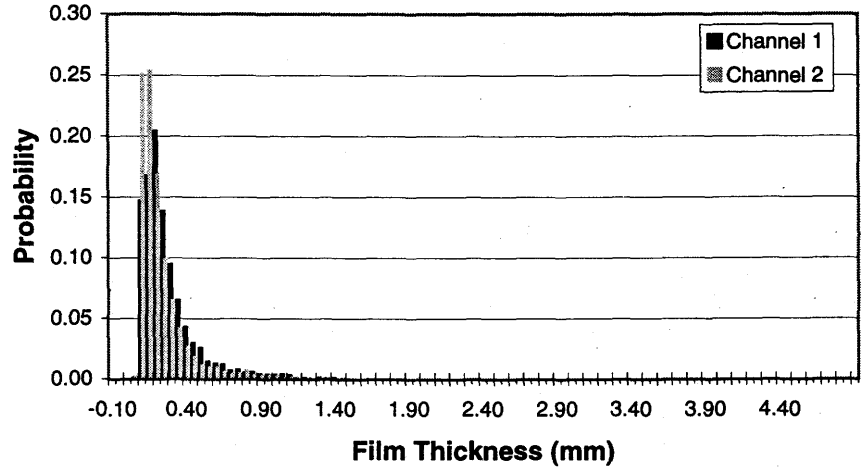

Figure D.6 - Film thickness PDF for 96F1P7 - A.

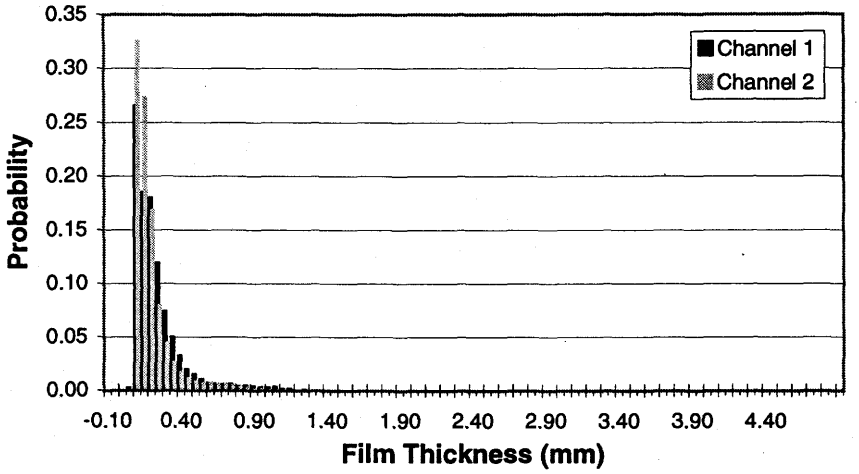

Figure D.7 - Film thickness PDF for 96F1P8 - A.

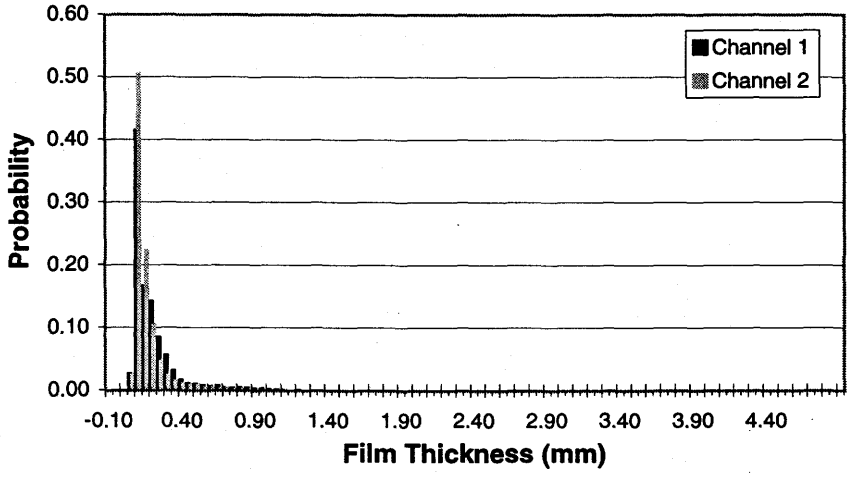

Figure D.8 - Film thickness PDF for 96F1P9 - A.

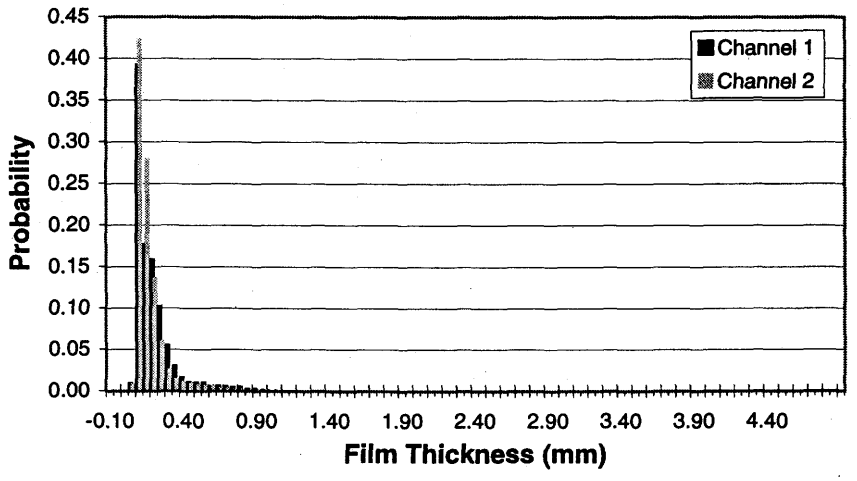

Figure D.9 - Film thickness PDF for 96F1P10 - A.

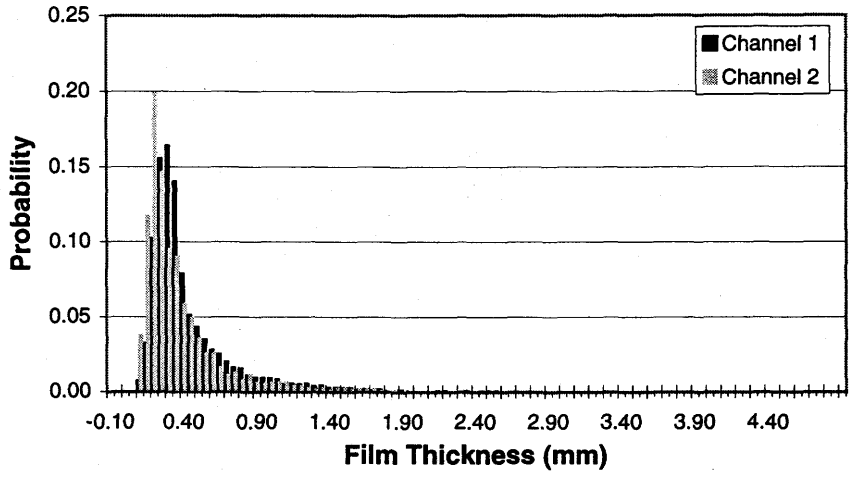

Figure D.10 - Film thickness PDF for 96F1P15 - A.

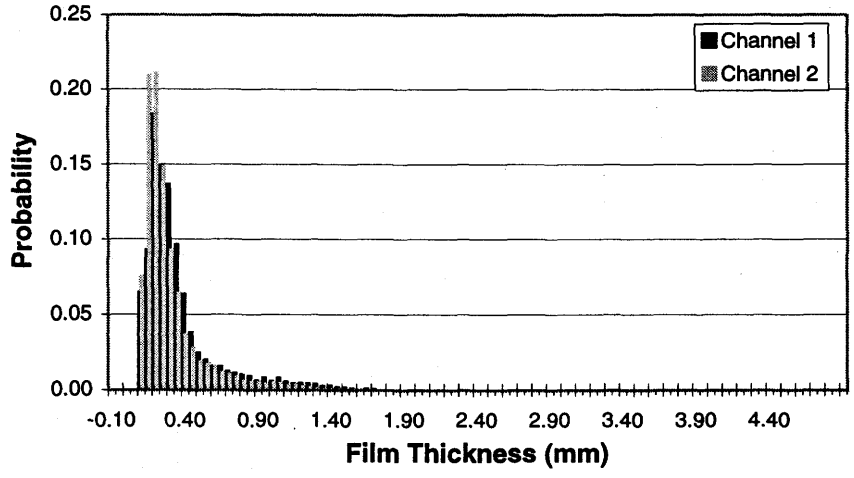

Figure D.11 - Film thickness PDF for 96F1P16 - A.

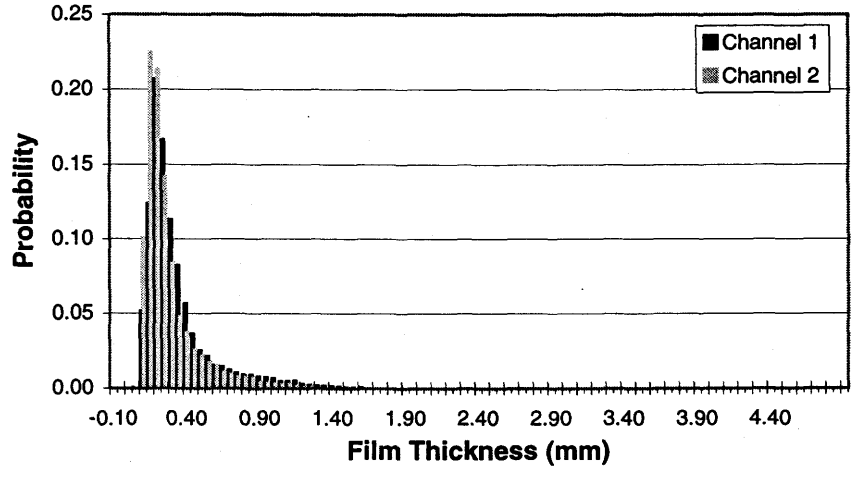

Figure D.12 - Film thickness PDF for 96F1P17 - A.

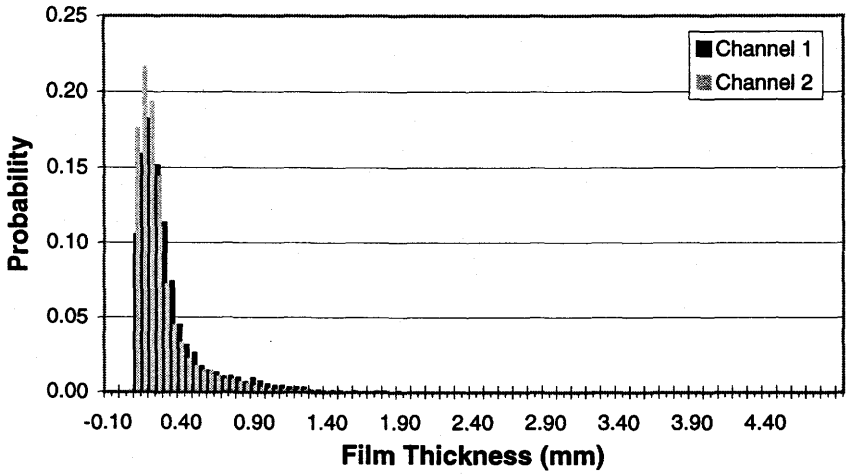

Figure D.13 - Film thickness PDF for 96F1P18 - A.

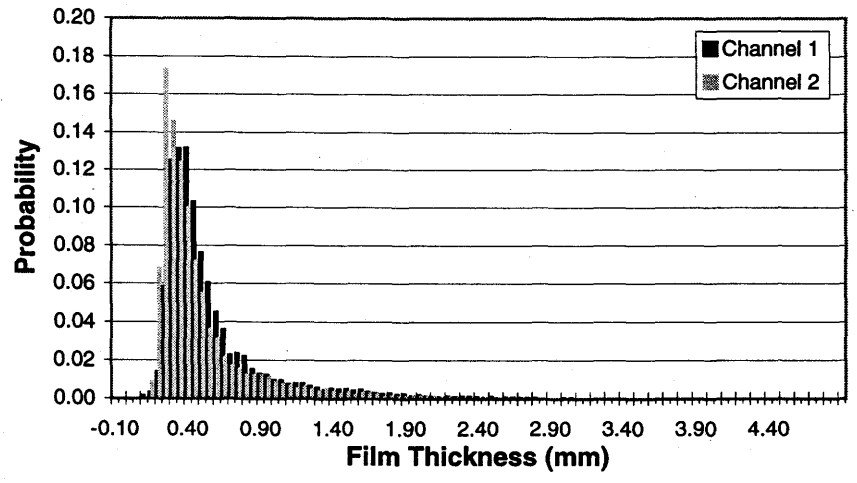

Figure D.14 - Film thickness PDF for 96F1P24 - T-A.

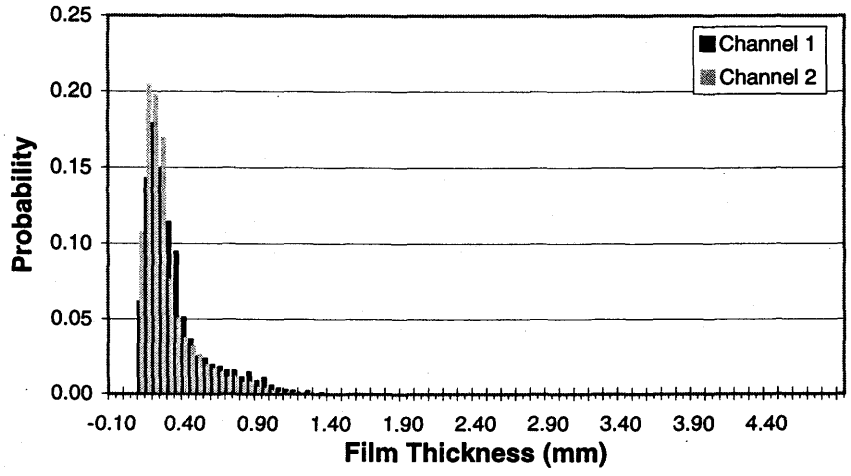

Figure D.15 - Film thickness PDF for 96F1P30 - A.

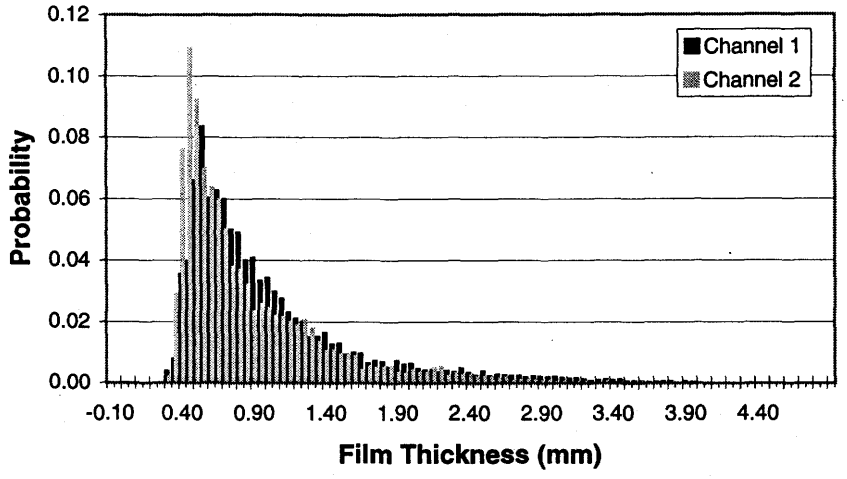

Figure D.16 - Film thickness PDF for 96F1P32 - T.

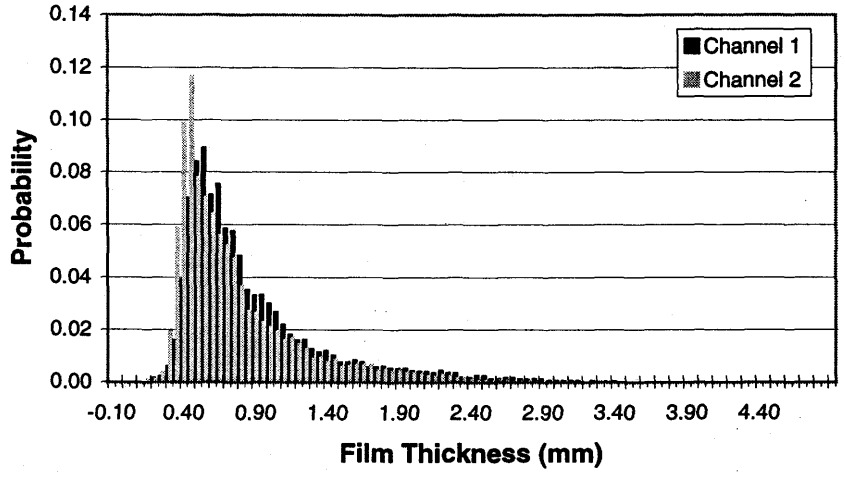

Figure D.17 - Film thickness PDF for 96F1P33 - T.

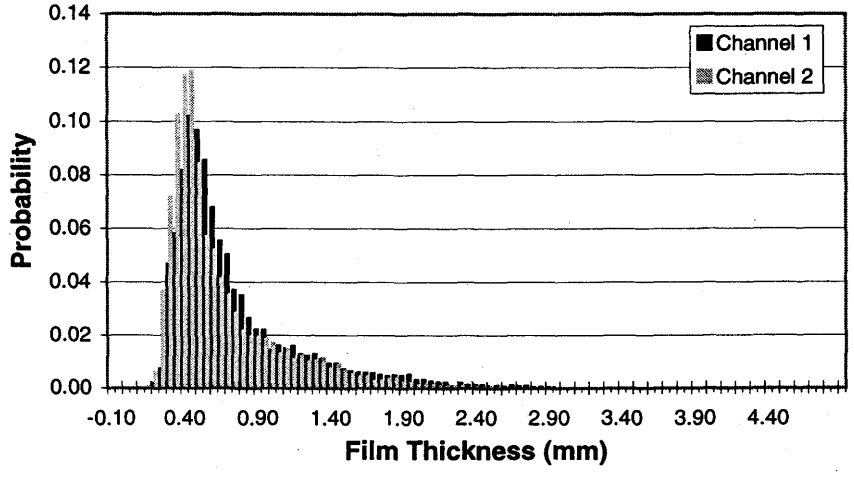

Figure D.18 - Film thickness PDF for 96F1P34 - T-A.

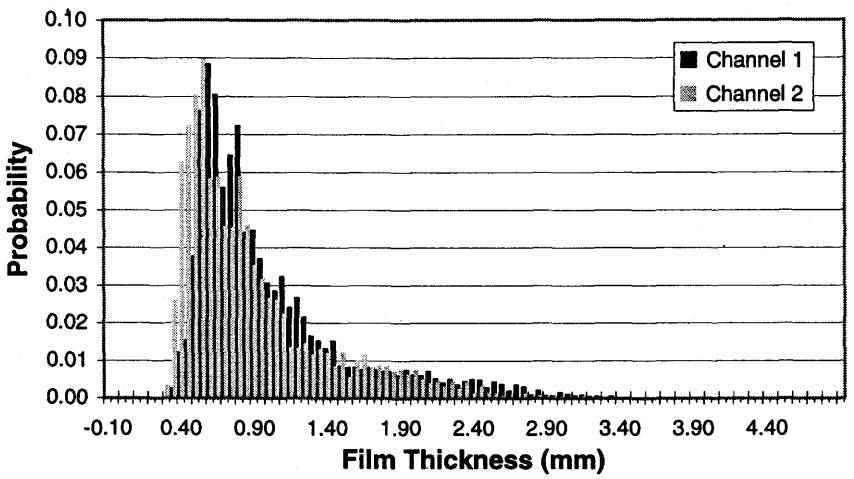

Figure D.19 - Film thickness PDF for 96F2P2 - T.

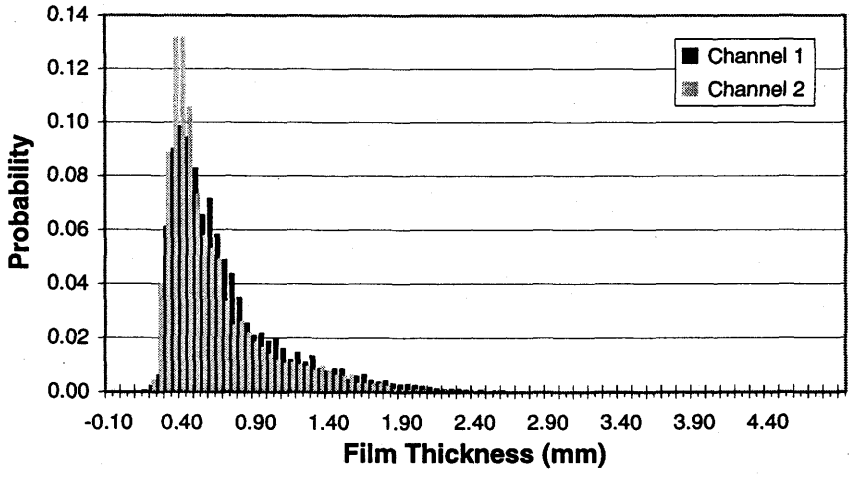

Figure D.20 - Film thickness PDF for 96F2P5 - T-A.

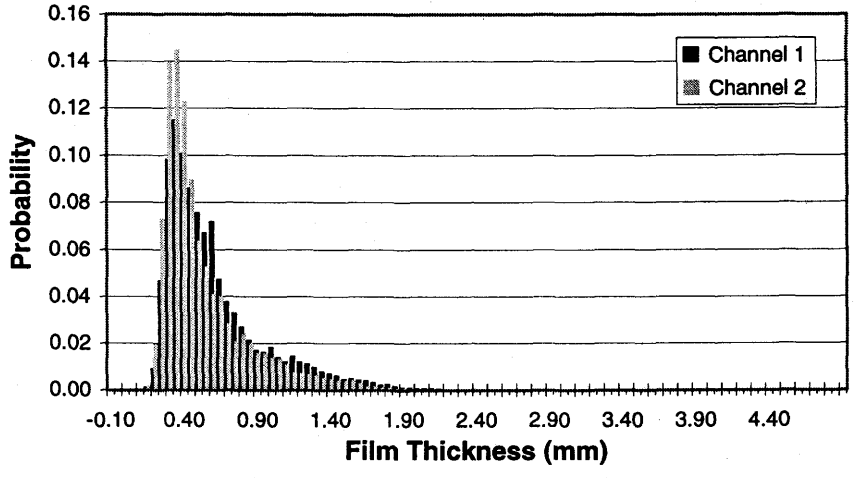

Figure D.21 - Film thickness PDF for 96F2P6 - A.

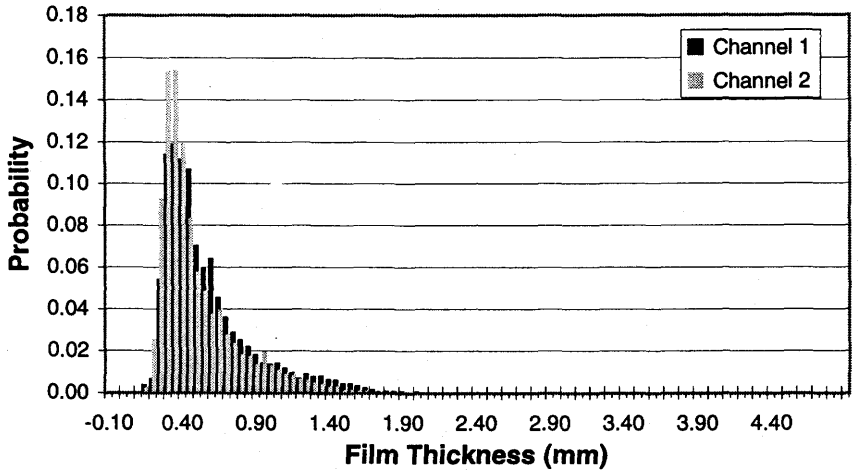

Figure D.22 - Film thickness PDF for 96F2P7 - A.

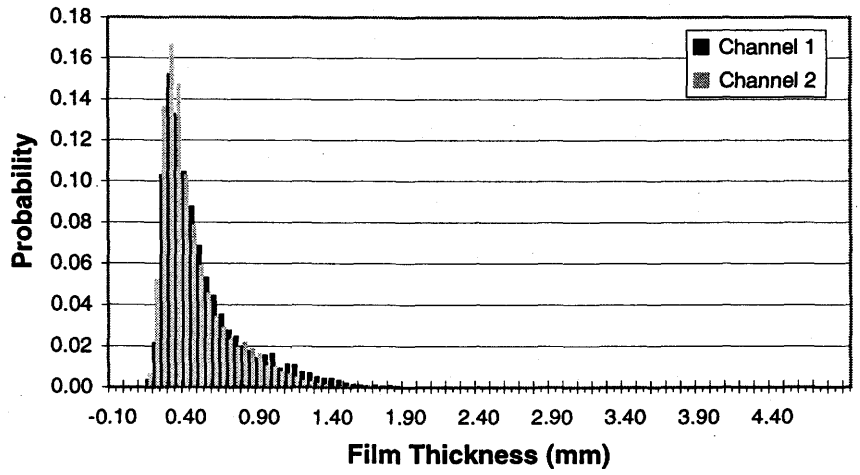

Figure D.23 - Film thickness PDF for 96F2P8 - A.

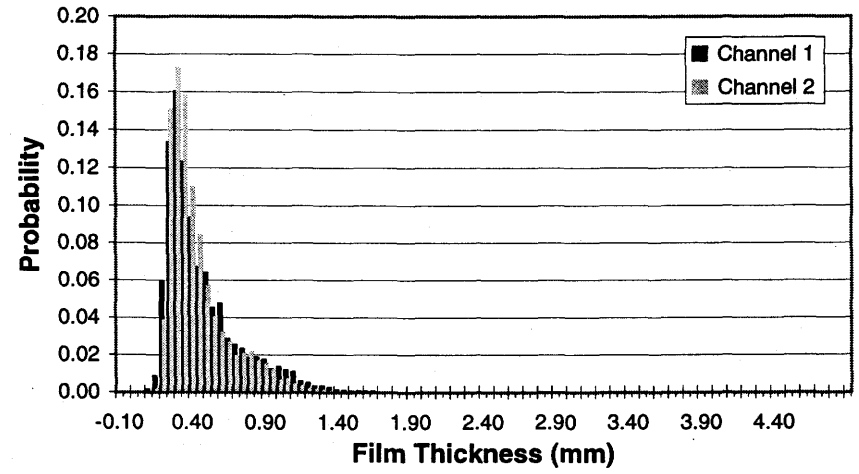

Figure D.24 - Film thickness PDF for 96F2P10 - A.

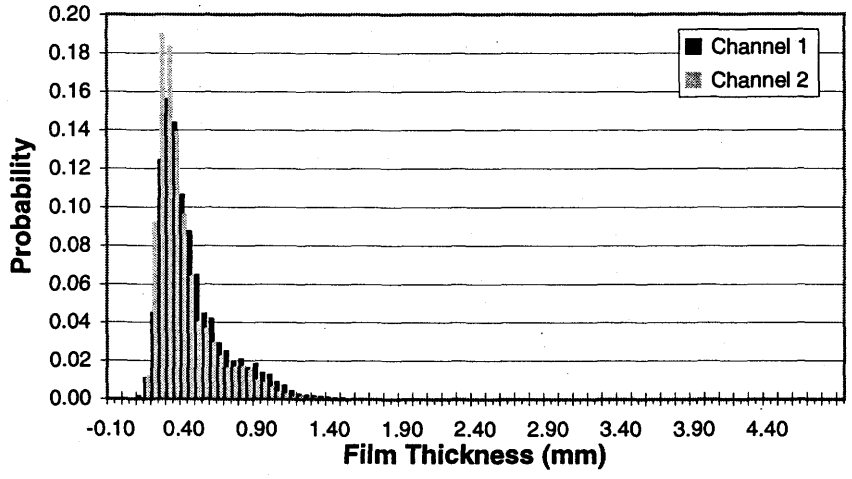

Figure D.25 - Film thickness PDF for 96F2P11 - A.

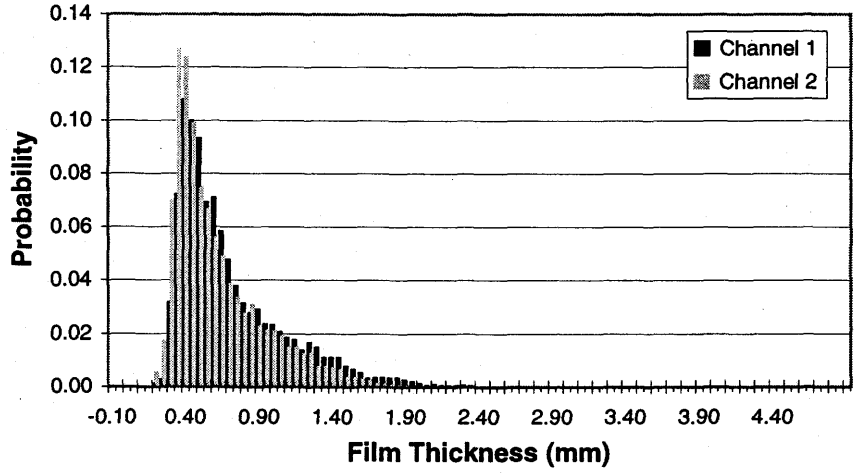

Figure D.26 - Film thickness PDF for 96F2P12 - A.

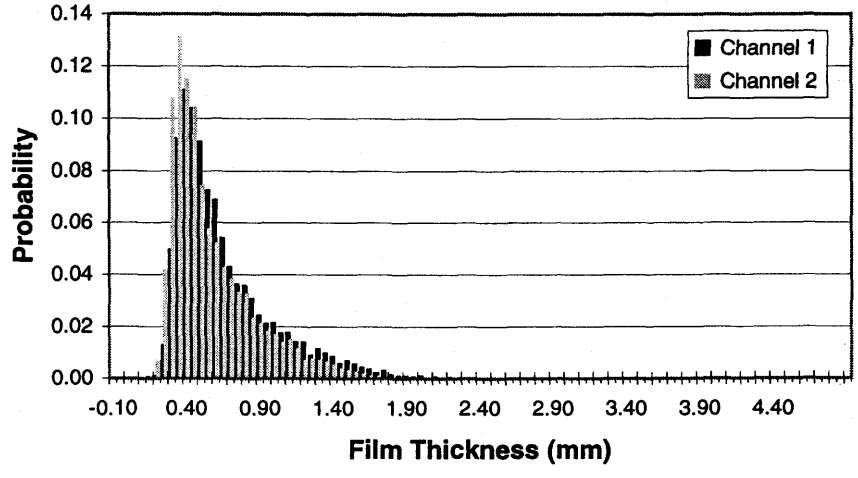

Figure D.27 - Film thickness PDF for 96F2P13 - A.

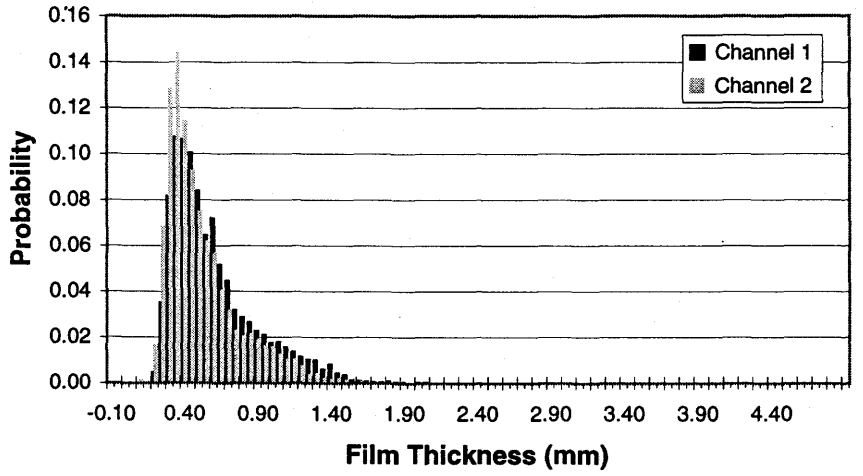

Figure D.28 - Film thickness PDF for 96F2P14 - A.

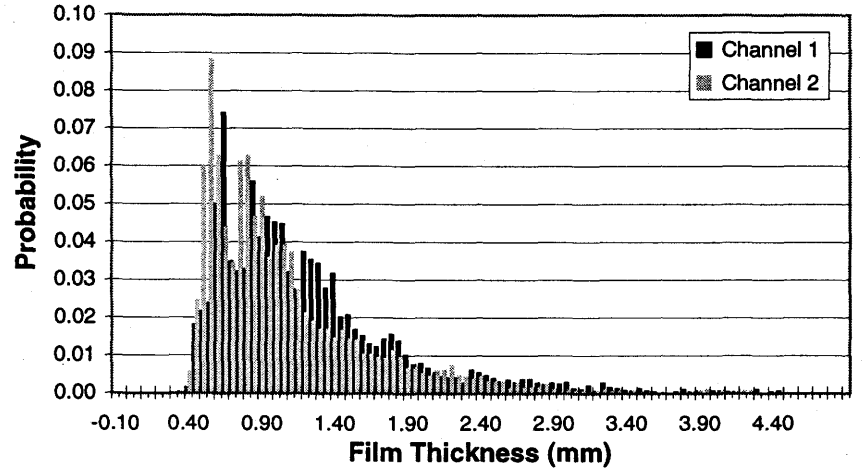

Figure D.29 - Film thickness PDF for 96F2P15 - T.

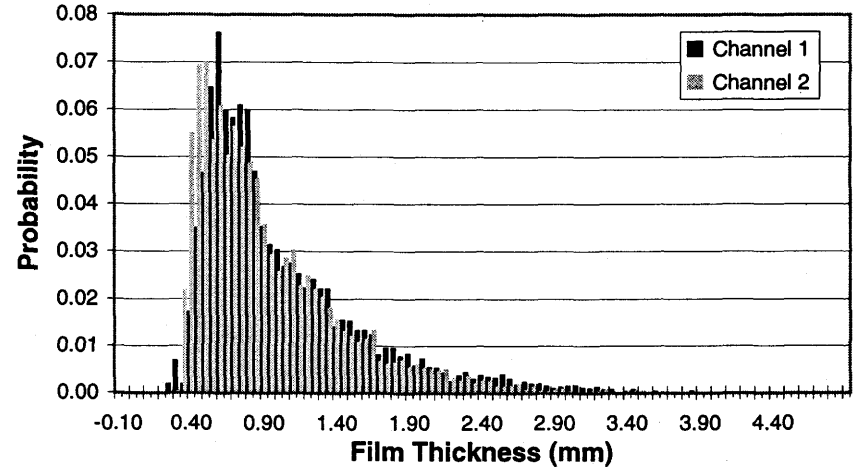

Figure D.30 - Film thickness PDF for 96F2P16 - T.

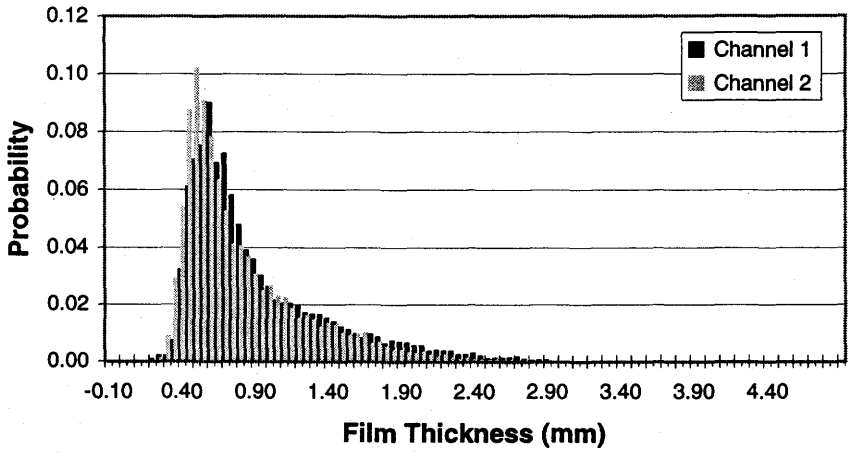

Figure D.31 - Film thickness PDF for 96F2P18 - T.

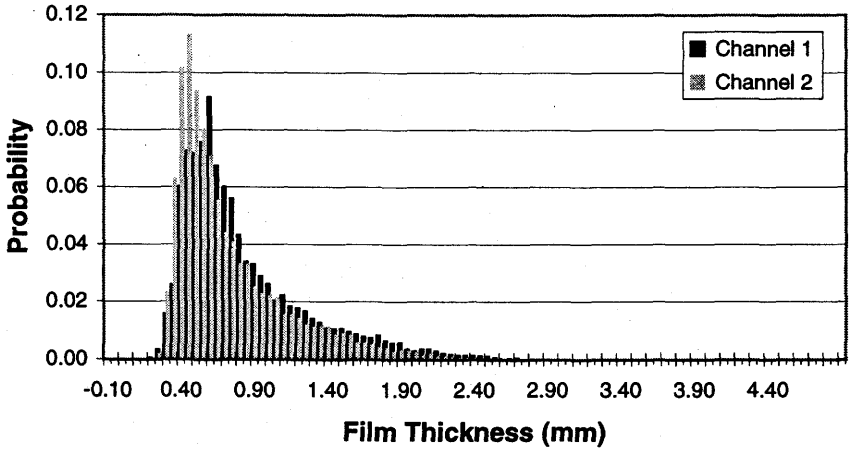

Figure D.32 - Film thickness PDF for 96F2P19 - T.

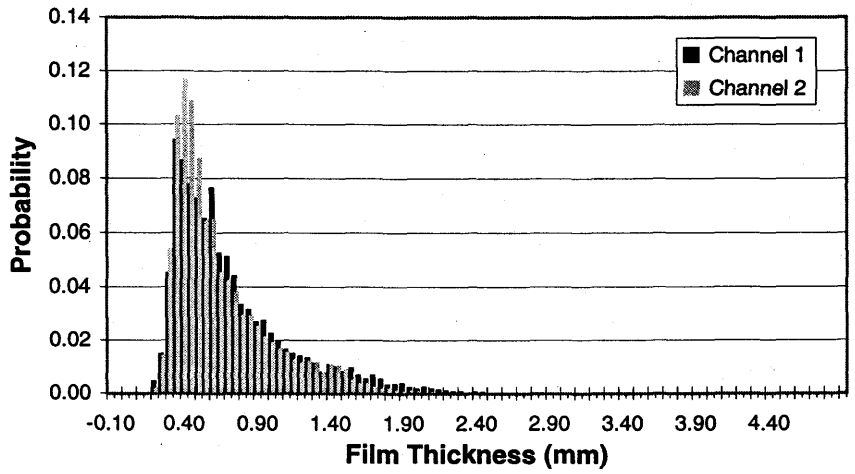

Figure D.33 - Film thickness PDF for 96F2P20 - T-A.

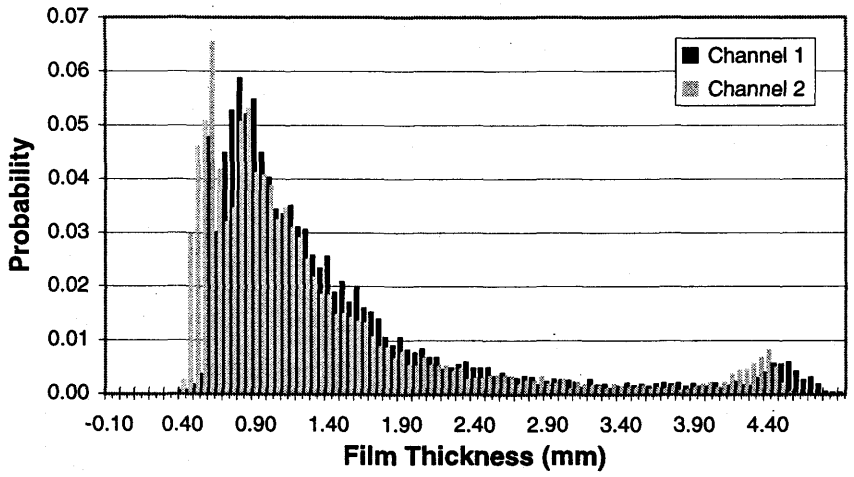

Figure D.34 - Film thickness PDF for 96F2P21 - T.

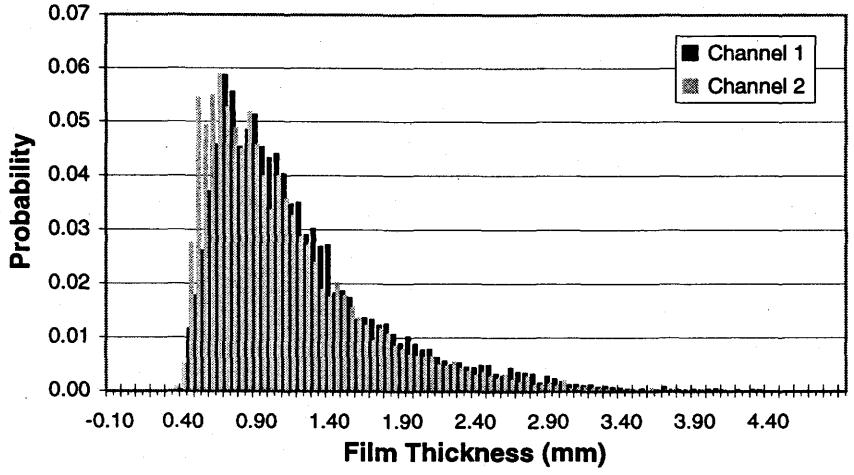

Figure D.35 - Film thickness PDF for 96F2P22 - T.

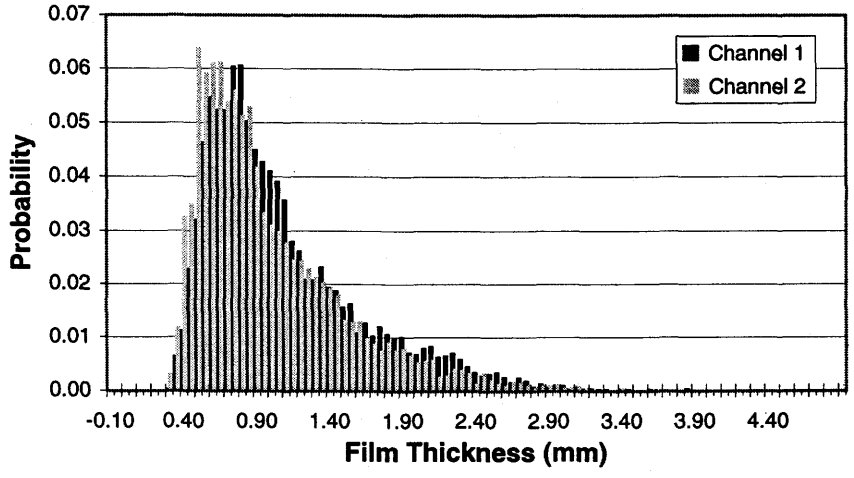

Figure D.36 - Film thickness PDF for 96F2P23 - T.

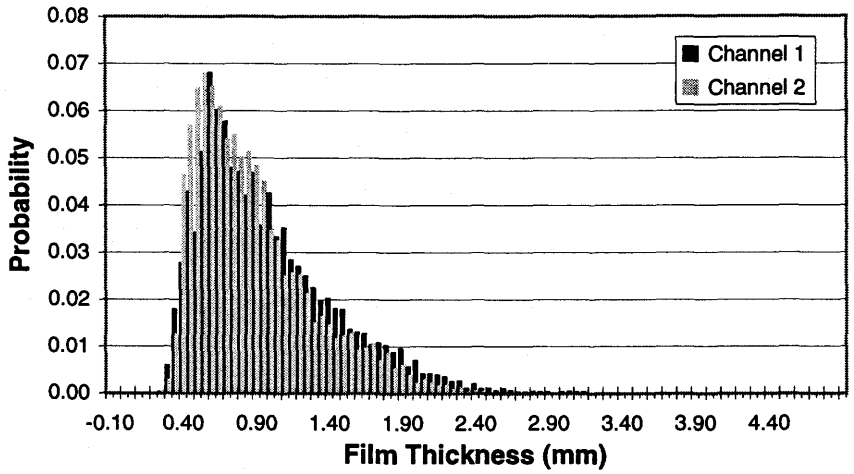

Figure D.37 - Film thickness PDF for 96F2P24. - T.

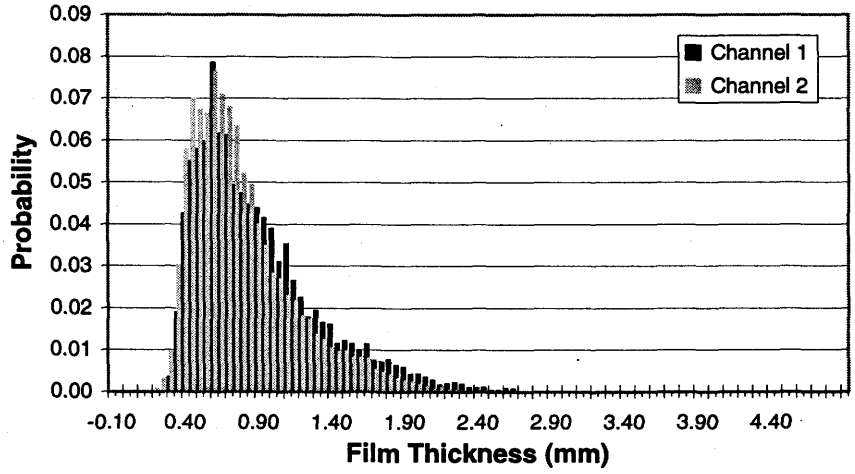

Figure D.38 - Film thickness PDF for 96F2P26 - T.

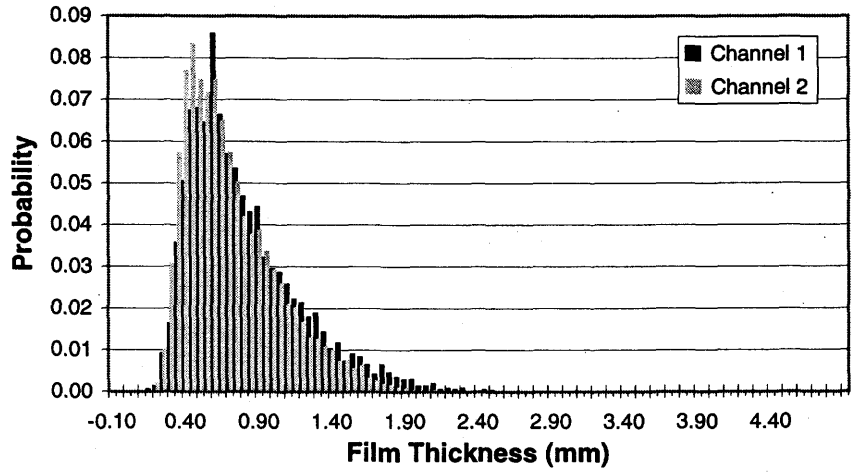

Figure D.39 - Film thickness PDF for 96F2P27 - T-A.

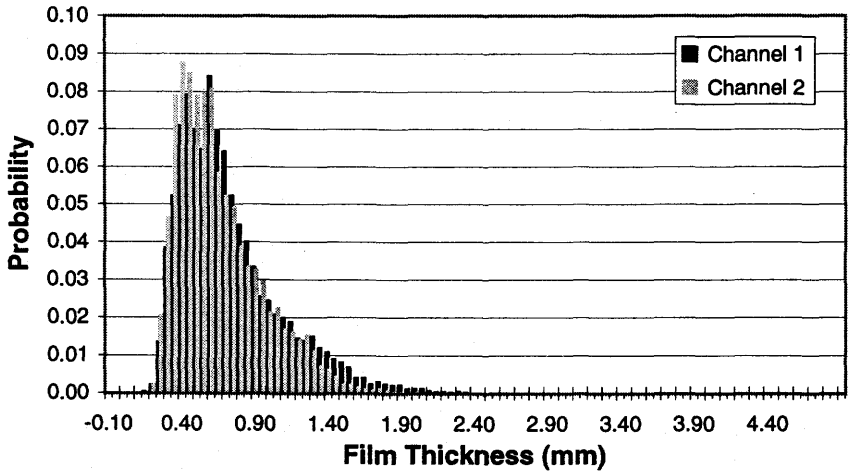

Figure D.40 - Film thickness PDF for 96F2P28 - A.

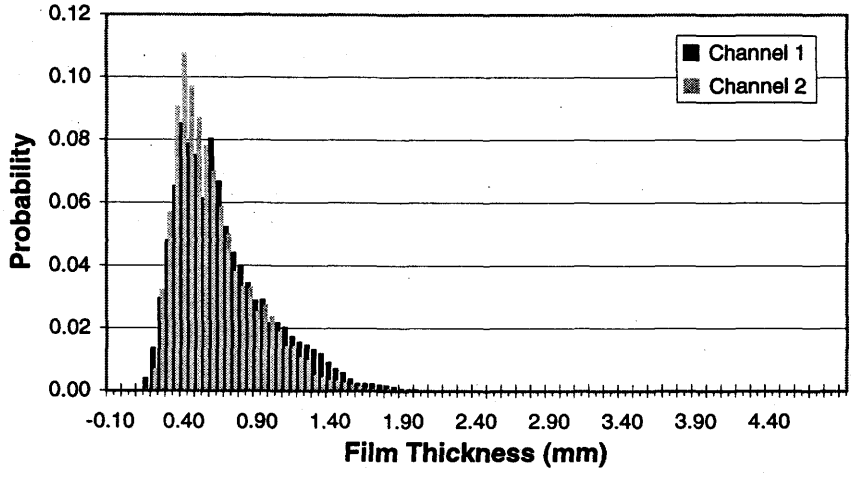

Figure D.41 - Film thickness PDF for 96F2P29 - A.

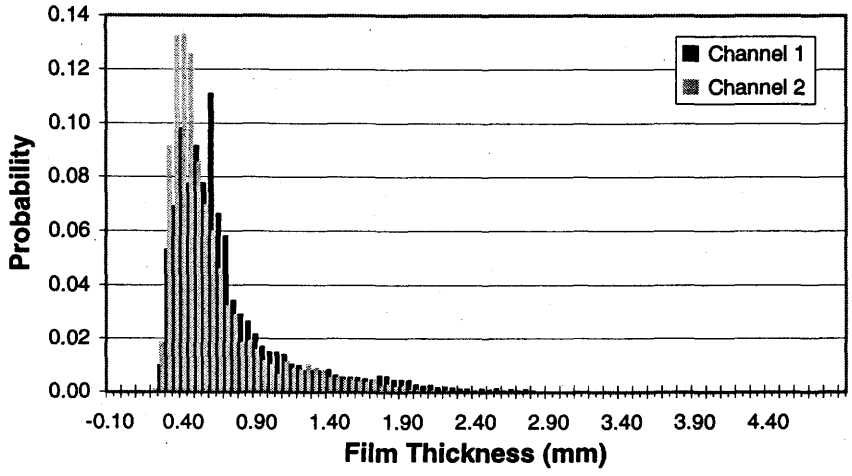

Figure D.42 - Film thickness PDF for 96F2P32 - T-A.

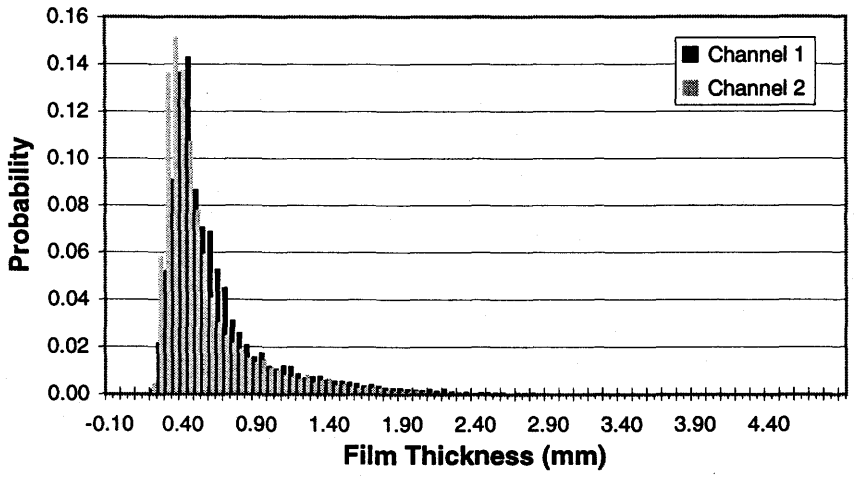

Figure D.43 - Film thickness PDF for 96F2P34 - A.

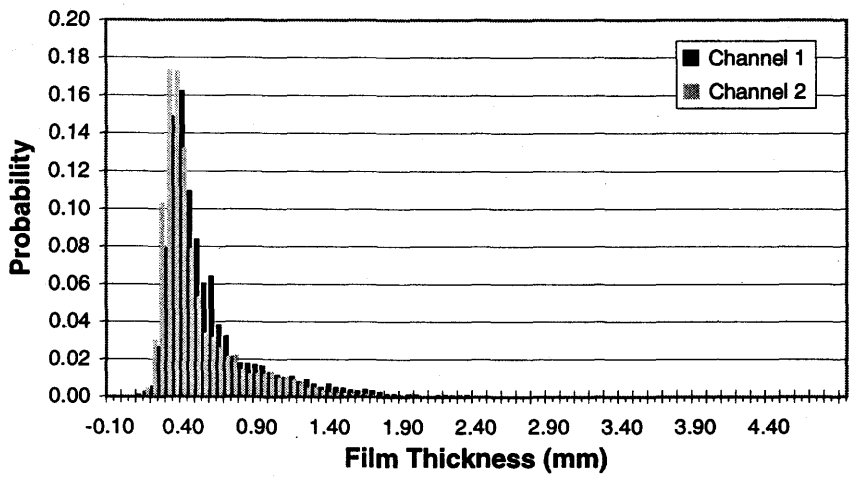

Figure D.44 - Film thickness PDF for 96F2P35 - A.

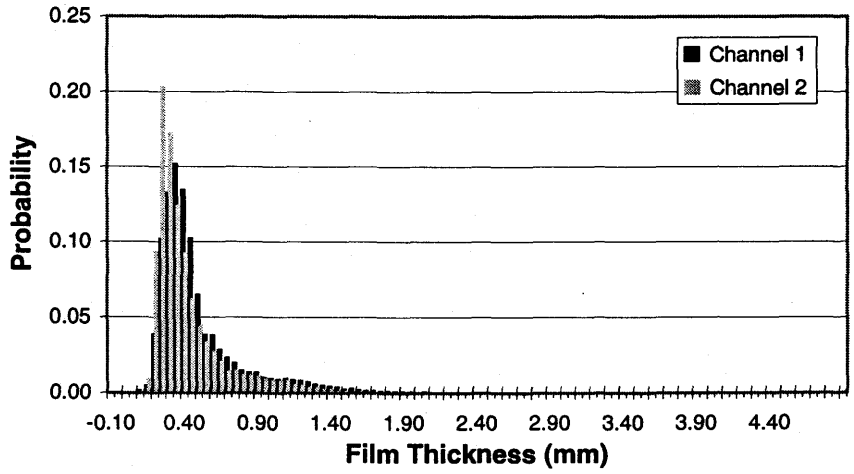

Figure D.45 - Film thickness PDF for 96F2P36 - A.

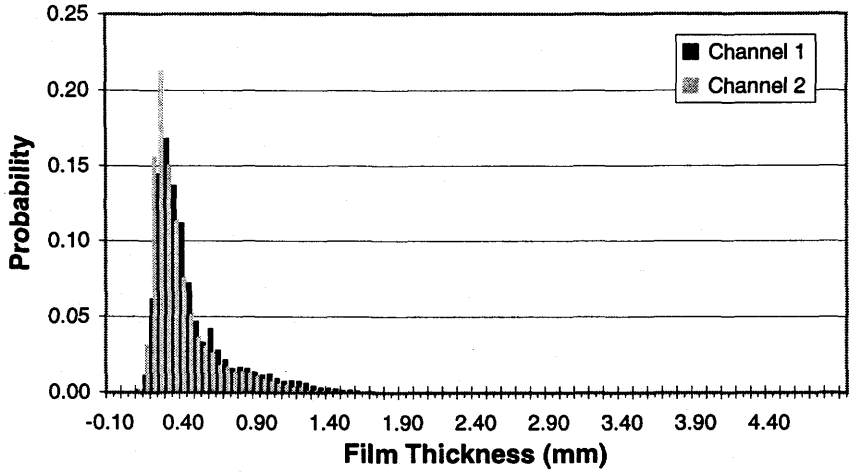

Figure D.46 - Film thickness PDF for 96F2P37 - A.

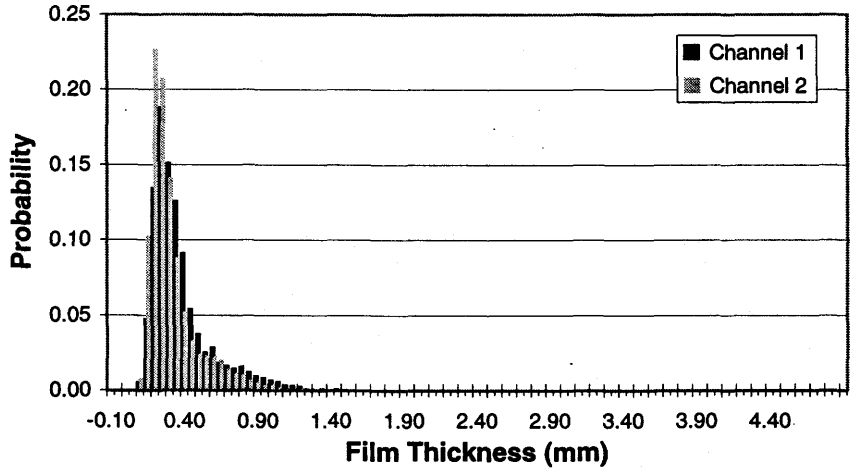

Figure D.47 - Film thickness PDF for 96F2P39 - A.

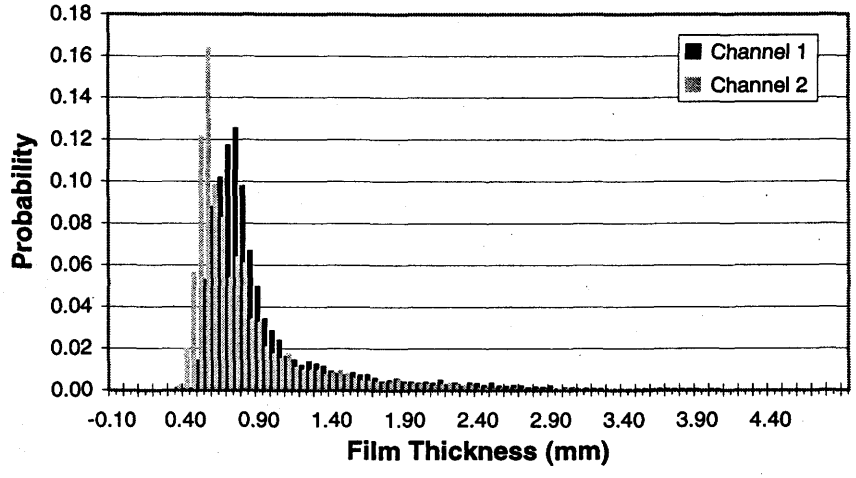

Figure D.48 - Film thickness PDF for 96F2P40 - T.

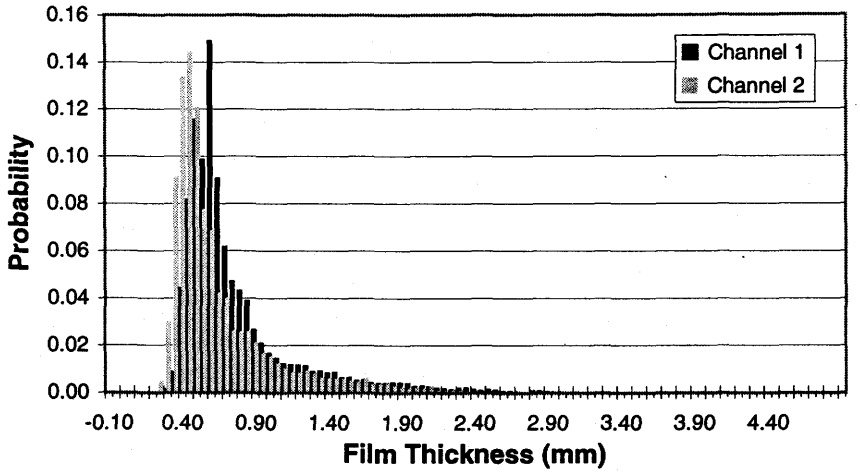

Figure D.49 - Film thickness PDF for 96F2P42 - T.

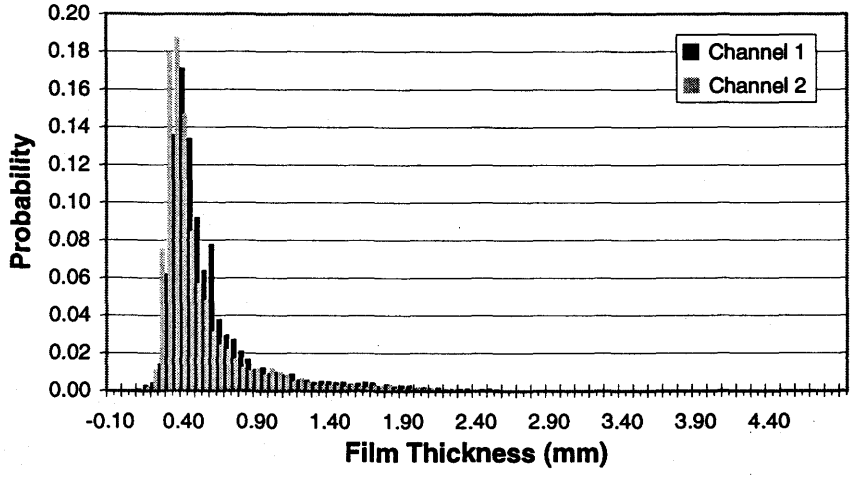

Figure D.50 - Film thickness PDF for 96F2P43 - A.

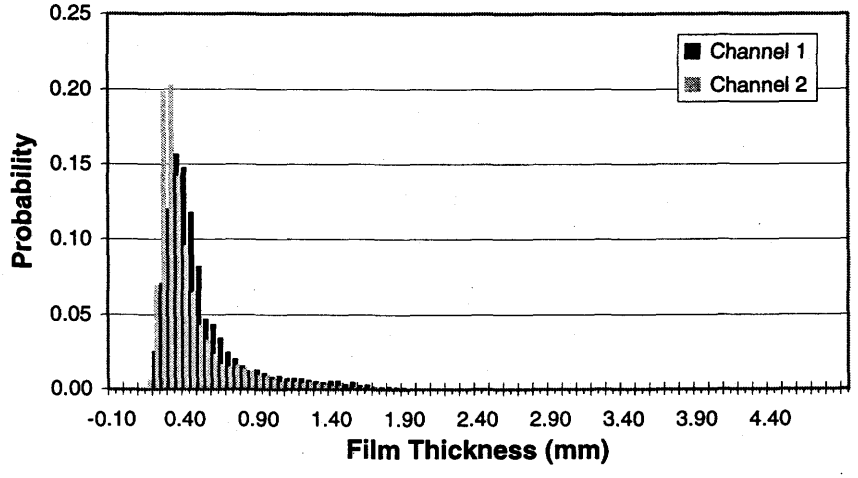

Figure D.51 - Film thickness PDF for 96F2P44 - A.

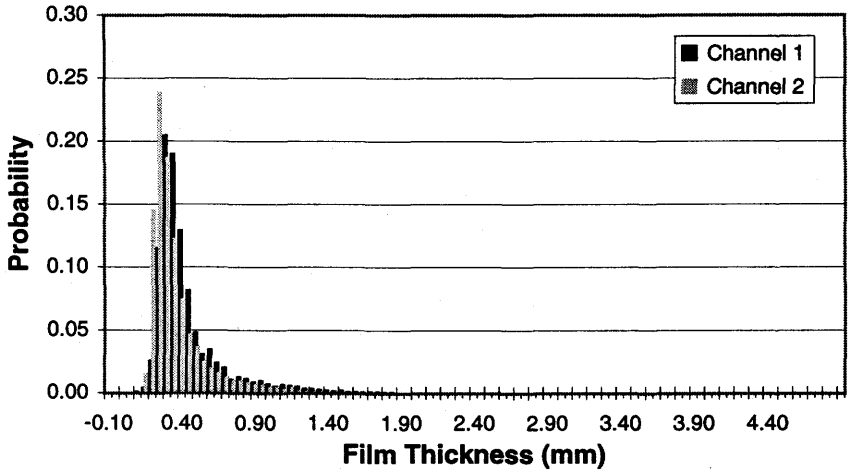

Figure D.52 - Film thickness PDF for 96F2P45 - A.

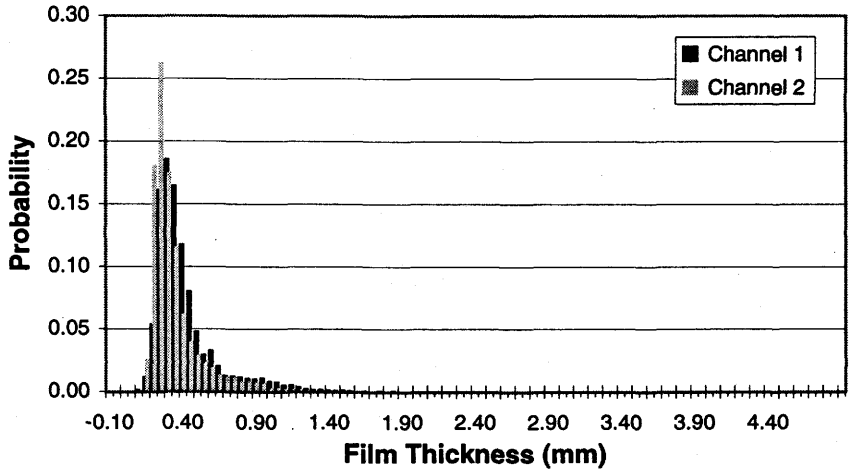

Figure D.53 - Film thickness PDF for 96F2P46 - A.

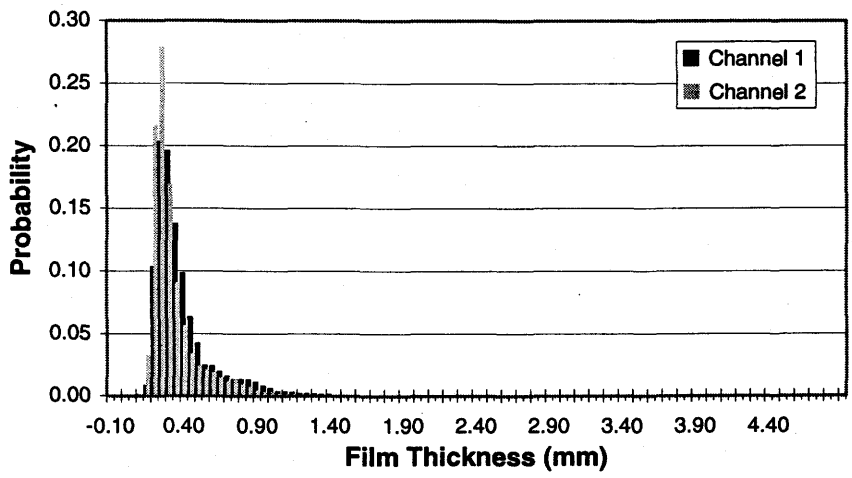

Figure D.54 - Film thickness PDF for 96F2P47 - A.

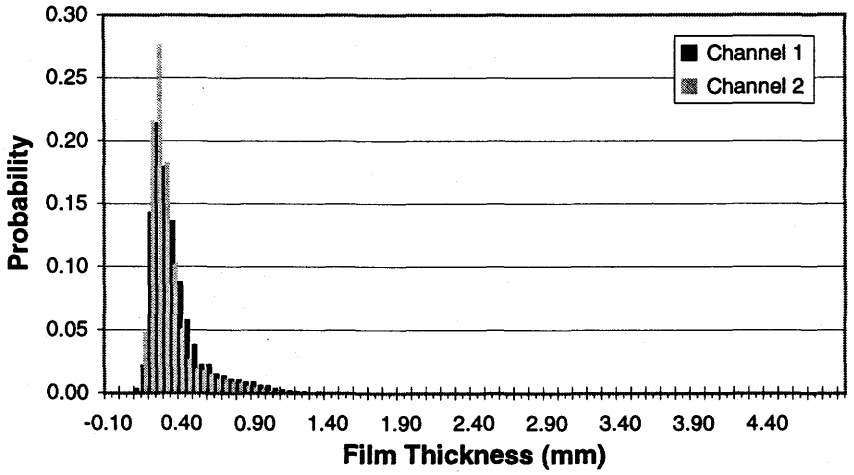

Figure D.55 - Film thickness PDF for 96F2P48 - A.

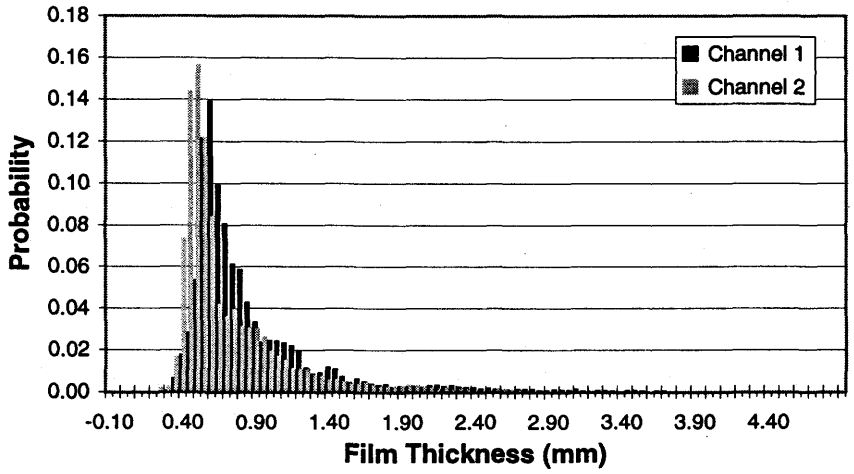

Figure D.56 - Film thickness PDF for 96F2P50 - T.

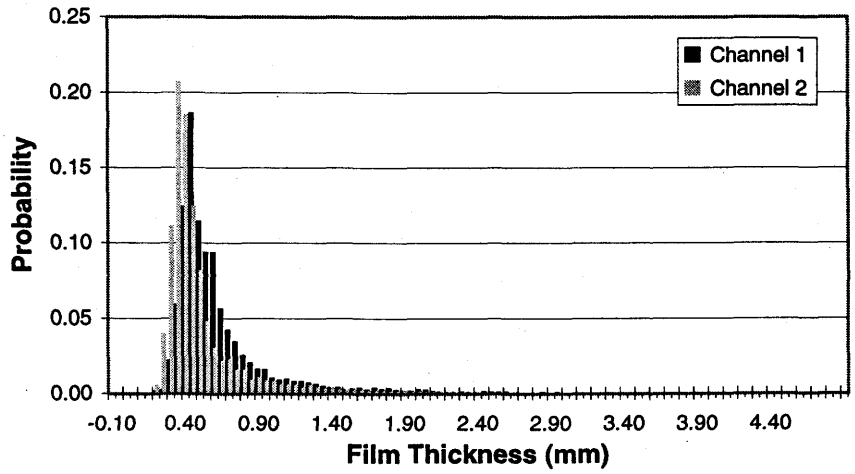

Figure D.57 - Film thickness PDF for 96F2P51 - T-A.

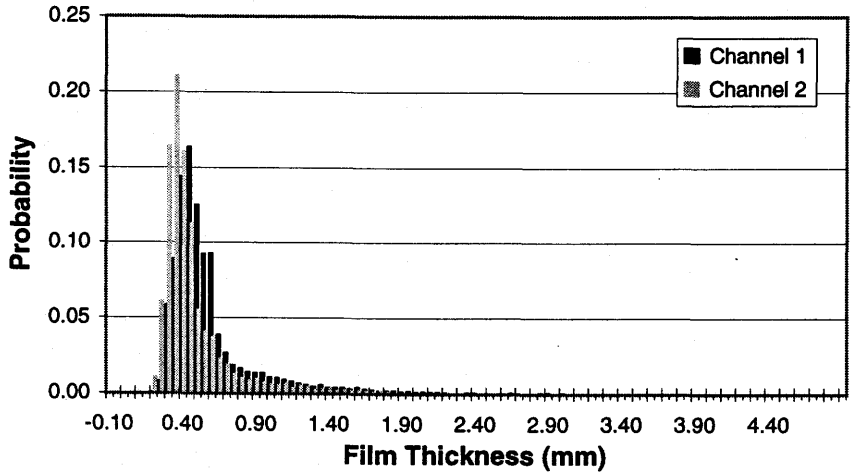

Figure D.58 - Film thickness PDF for 96F2P52 - A.